Energy Time Ptychography for Mössbauer Resonances

Dissertation

zur Erlangung des Doktorgrades

an der Fakultät für Mathematik, Informatik und

Naturwissenschaften

Fachbereich Physik
der Universität Hamburg

vorgelegt von
Ankita Negi

Hamburg, 2024

Gutachter der Dissertation:	Prof. Dr. Ralf Röhlsberger Prof. Dr. Christina Brandt
Zusammensetzung der Prüfungskommision:	Prof. Dr. Michael Potthoff Prof. Dr. Henry Chapman Prof. Dr. Ralf Röhlsberger Prof. Dr. Christina Brandt Priv.-Doz. Dr. Guido Meier
Vorsitzende der Prüfungskommision:	Prof. Dr. Michael Potthoff
Datum der Disputation:	15. April 2024
Vorsitzender des Fach-Promotionsausschusses PHYSIK:	Prof. Dr. Markus Drescher
Leiter des Fachbereichs PHYSIK:	Prof. Dr. Wolfgang J. Parak
Dekan der Fakultät MIN:	Prof. Dr.-Ing. Norbert Ritter

Abstract

Mössbauer spectroscopy studies atomic-level properties of an object by probing how atomic nuclei interact with their local magnetic and chemical environments. With the advent of advanced synchrotron sources, a time-domain version of this technique has emerged, which relies on the recoil-less resonant scattering of synchrotron radiation by Mössbauer nuclei. This method, called nuclear resonant scattering (NRS), detects the nuclear excitations in the object as beat patterns in time. NRS serves both as a tool for atomic characterization in material science and as a means to study the fundamental interaction between light and matter.

Time-domain NRS measurements provide several advantages over traditional energy-domain Mössbauer spectroscopy, including better energy resolution, sensitivity, and reduced measurement times. These benefits stem from the superior focus, coherence, and brilliance of synchrotron radiation compared to lab-based sources. However, analyzing and fitting time-domain NRS data is non-trivial and typically requires complex physical models and simulation software. To address this, recent research has focused on developing synchrotron Mössbauer sources for energy-domain measurements. Since these sources are difficult to fabricate, stabilize and replicate, we propose to shift the challenge to the computational realm. Instead of relying on synchrotron Mössbauer sources, we aim to extract the scattering magnitude and phase in the energy domain from time-domain measurements using their Fourier relationship. This involves solving a non-linear, non-convex inverse problem, which is inherently difficult due to its one-dimensional nature.

Our approach is based on Ptychography, a scanning coherent diffraction imaging technique, with two main steps: First, we take multiple overlapping time-domain measurements of the object with an energy shifted illumination window of a probe, creating an energy-time ‘ptychogram’. Then, we use an optimization framework, called a ptychography engine, to reconstruct the complex object from the ptychogram using

computer algorithms. Numerical tests demonstrate the robustness of our approach in reconstructing the complex object, even with noise and reduced overlap in the ptychogram. Furthermore, we validate the method through practical implementations in proof-of-concept experiments. The experiments involve reconstructing the complex energy domain response of an iron foil enriched with the Mössbauer isotope ^{57}**Fe**, employing two distinct probes: a thick ^{57}**Fe**-enriched stainless steel foil and an enriched stainless steel nanofilm embedded in an X-ray cavity. Our results underscore the importance of understanding and mitigating incoherent effects in experimental setups, as well as longer bunch spacing of the synchrotron radiation for successful phase retrieval.

Exploring NRS ptychography with modern X-ray FEL sources holds promise due to their high coherence and unique time structure. Additionally, applying the technique for other Mössbauer isotopes, e.g. tin (^{119}**Sn**), presents an exciting opportunity for further research.

Zusammenfassung

Die Mössbauer-Spektroskopie erforscht die Eigenschaften eines Objekts auf atomarer Ebene, indem sie untersucht, wie Atomkerne mit ihrer lokalen magnetischen und chemischen Umgebung wechselwirken. Mit dem Aufkommen fortschrittlicher Synchrotronquellen ist eine Zeitdomänenversion dieser Technik entstanden. Sie beruht auf der rückstoßfreien Resonanzstreuung von Synchrotronstrahlung an Mössbauer-Kernen. Bei dieser Methode, die als Kernresonanzstreuung (NRS) bezeichnet wird, werden die Kernanregungen im Objekt als Schwebungsmuster in der Zeit nachgewiesen. NRS dient sowohl als Werkzeug zur atomaren Charakterisierung in der Materialwissenschaft als auch als Mittel zur Untersuchung der grundlegenden Wechselwirkung zwischen Licht und Materie.

NRS-Messungen im Zeitbereich bieten mehrere Vorteile gegenüber der herkömmlichen Mössbauer-Spektroskopie im Energiebereich, darunter eine bessere Energieauflösung, Empfindlichkeit und kürzere Messzeiten. Diese Vorteile ergeben sich aus dem überlegenen Fokus, der Kohärenz und der Brillanz der Synchrotronstrahlung im Vergleich zu laborgestützten Quellen. Die Analyse und Anpassung von NRS-Daten im Zeitbereich ist jedoch nicht trivial und erfordert in der Regel komplexe physikalische Modelle und Simulationssoftware. Um dieses Problem zu lösen, hat sich die jüngste Forschung auf die Entwicklung von Synchrotron-Mössbauer-Quellen für Messungen im Energiebereich konzentriert. Da diese Quellen nur schwer herzustellen, zu stabilisieren und zu reproduzieren sind, schlagen wir vor, die Herausforderung in den Bereich der Berechnungen zu verlagern. Anstatt sich auf Synchrotron-Mossbauer-Quellen zu verlassen, wollen wir die Streustärke und Phase im Energiebereich aus Messungen im Zeitbereich extrahieren, indem wir ihre Fourier-Beziehung nutzen. Dazu muss ein nichtlineares, nichtkonvexes inverses Problem gelöst werden, das aufgrund seiner eindimensionalen Natur von Natur aus schwierig ist.

Unser Ansatz basiert auf der Ptychographie, einem Verfahren zur scannenden ko-

härenten Beugungsabbildung, der zwei Hauptschritte umfasst: Zunächst nehmen wir mehrere sich überlappende Messungen des Objekts im Zeitbereich mit einem energetisch verschobene Beleuchtungsfenster einer Referenzprobe und erstellen so ein Energie-Zeit-"Pychogramm". Anschließend verwenden wir einen Optimierungsmodel, eine so genannte Ptychographie-Engine, um das komplexe Objekt mithilfe von Computeralgorithmen aus dem Ptychogramm zu rekonstruieren. Numerische Tests zeigen die Robustheit unseres Ansatzes bei der Rekonstruktion des komplexen Objekts, selbst bei Rauschen und geringer Überlappung im Ptychogramm. Darüber hinaus validieren wir die Methode durch praktische Implementierungen in Proof-of-Concept-Experimenten. Die Experimente beinhalten die Rekonstruktion der komplexen Energiedomänenantwort einer mit dem Mössbauer-Isotop ^{57}**Fe** angereicherten Eisenfolie, wobei zwei verschiedene Referenzproben verwendet werden: eine dicke ^{57}**Fe**-angereicherte Edelstahlfolie und ein angereicherte Edelstahlfolie-Nanofilm, der in eine Röntgenstrahlenkavität eingebettet ist. Unsere Ergebnisse unterstreichen, wie wichtig es ist, inkohärente Effekte in Versuchsaufbauten zu verstehen und abzuschwächen, und wie wichtig ein längerer Bunch-Abstand der Synchrotronstrahlung für eine erfolgreiche Phasengewinnung ist.

Die Erforschung der NRS-Ptychographie mit modernen Röntgen-FEL-Quellen ist aufgrund ihrer hohen Kohärenz und einzigartigen Zeitstruktur vielversprechend. Darüber hinaus bietet die Anwendung der Technik auf andere Mössbauer-Isotope, z.B. Zinn (^{119}**Sn**), spannende Möglichkeiten für weitere Forschungen.

Contents

1. Introduction

Observation is the empirical foundation of all scientific investigation. In our daily lives, we rely on our eyes to perceive the world through light. However, what about objects too minuscule for our naked eyes to see? We illuminate them with light waves of small enough wavelength (or equivalently, high enough energy). The tiny X-ray wavelengths make their interaction with matter a potent tool to investigate objects at the molecular, atomic, or even nuclear scale. However, the higher energy and momentum of X-ray photons lead to more significant recoil effects in the interaction compared to visible light photons. (When one opens the window on a sunny day, the sunlight does not knock one backward!)

In 1958, Rudolf Mössbauer first observed the *recoilless* emission and absorption of X-ray photons by atomic nuclei in an object. This 'Mössbauer effect' occurs only when the emitting and absorbing nuclei are embedded in a solid lattice such that their effective recoil mass is increased and kinetic energy is transferred to the lattice. The difference in the nuclear energy levels is precisely matched (i.e. resonant) with the energy of the emitted or absorbed X-ray photons. The nuclear transitions have a very small natural linewidth Γ compared to the transition energy E_0. As a result, the quality factor (E_0/Γ) of Mössbauer resonances is several orders higher than electronic resonances. For example, the quality factor for the nuclear resonance of $^{57}\mathbf{Fe}$ is 10^{12}, or the equivalent of the diameter of a sand particle compared to the diameter of the sun. This exceptionally sharp sensitivity of the resonance makes it possible to detect the tiny 'hyperfine' interactions between the atomic nucleus and its environment using the resonant nuclear absorption (or scattering) of X-rays.

Nuclear resonance scattering (NRS) with synchrotron radiation combines the outstanding properties of the Mössbauer effect with those of synchrotron radiation, namely the high brilliance, coherence, linear polarization and pulsed time structure. As a resonant synchrotron pulse travels through an object, the entire nuclear ensemble can

be involved in the scattering of a single X-ray photon - forming the hybrid light-matter quasiparticle termed the nuclear *exciton-polariton* [Smi99; HT99; Smi+05]. At the detector, we can measure the coherent decay of the nuclear exciton-polariton over time, but this measurement is limited to the intensity of the elastically scattered X-ray wavefield. In quantum mechanics, the exciton-polariton state is fully represented as a complex-valued wavefunction that encodes both the magnitude and phase. Consequently, the X-ray wavefield scattered by the coherent nuclear ensemble also experiences a phase shift–which is lost in the measurement process. This poses a 'phase problem' for two main reasons.

Firstly, the phase is required to determine the energies and relative strengths of the Mössbauer transitions from the time response. The extremely high-quality factors of the nuclear resonances can be used for hyperfine spectroscopy to study the chemical and magnetic structure, dynamics, and phase transitions of materials with exceptional precision. Time response measurements of NRS have been used in a variety of fields encompassing physics, chemistry, material science, and geology. For example, NRS has been used to explore magnetic ordering in materials such as FeRh [Len+22] and SmS [Bar+04], as well as measure hyperfine fields in compounds with rare earth elements [Zha15]. It has been utilized in optical pump-X-ray probe studies to explore spin state changes of iron-containing spin-crossover complexes [Sad+19] and the evolution of magnetism under high pressure in multiferroic candidates [Pra+22]. However, the time response measurements are difficult to interpret for complicated objects, even though considerable effort has been spent on the simulation and fitting of the hyperfine parameters using theoretical models [HT99; Shv99] and sophisticated software packages [Stu00; Boc23]. Different hyperfine field configurations may also lead to the same temporal beating pattern [Röh05]. If we had the phase, we could instead employ the inverse Fourier transform to reconstruct the complex energy domain response of the object from the temporal measurements, without the need of a physical model.

Secondly, phase is an important quantity for quantum optics. The nuclear exciton-polariton has longer coherence times than its electronic counterpart[1] and can display unique quantum behaviors depending on the spatial distribution of the nuclei [RE21].

[1] We make comparisons to exciton-polaritons formed in materials with strong electron-hole interactions, such as semiconductor quantum wells or 2D materials like graphene. They have quality factors ranging from a few hundred to several thousand.

Specifically, Mössbauer nuclei embedded in X-ray cavity structures have emerged as promising candidates for exploring quantum optics with hard X-rays–which take advantage of the high quantum efficiency and low noise of X-ray detection. For example, they have been used to demonstrate 'collective' Lamb-shift phenomena [Röh+10] and electromagnetically induced transparency [Röh+12]. The long lifetime of the excited nuclear states also opens up the possibility to design almost two-level systems using these cavity structures [DLE22]. Measuring the phase of the nuclear exciton-polariton (e.g. in the cavity structures) provides insights into the state's coherence and superposition, which are essential for understanding and manipulating quantum systems [Hee+15; PKE09]. The importance of phase in coherent control of a quantum system has also been experimentally demonstrated [Hee+21; Boc+21].

A 'direct' measurement of the complex field of light beyond infrared frequencies was not reported until the groundbreaking 2004 experiment by Goulielmakis *et al.*. Using attosecond extreme ultraviolet (XUV) laser pulses as an ultrafast sampler, they were able to directly measure how the electric field built up and disappeared for a short, few-cycle pulse of 3.9×10^{14} Hz (769 nm) laser light. Performing such experiments in the X-ray regime is impractical due to the extremely high frequencies of X-ray oscillations (beyond 10^{19} Hz), requiring hypothetical zepto-second pulse sources. One can, in principle, build an X-ray interferometer to indirectly measure the phase shift. Time-domain interferometry of two nuclear resonant scattering samples using a triple Laue interferometer was first carried out in Refs. [Has+94; Izu+95]. They could use the interference pattern of the two samples to estimate their relative phase shift as a function of time delay after resonant excitation with the synchrotron radiation pulse. However, the unique properties of X-rays, such as their extremely short wavelengths and almost unity refractive index of most materials in the X-ray regime, make the design and stabilization of such interferometers challenging. Currently, a few phase retrieval approaches for NRS involve replacing the interferometer with a reference sample on a Doppler drive. Here, the Doppler drive acts as the phase shifter while the object and the reference act as interferometer arms, but with "radiative coupling" [Pot+01; vBür+02; Smi+05] between them. Examples of these schemes include Heterodyne Phase Reconstruction (HPR) [Cal+05] and Frequency-Frequency Correlation (FFC) [WE23]. However, both HPR and FFC are effective only when the radiative coupling effects between the object and the reference are negligible. Furthermore, these techniques require a

thin, single-line reference which is ideally a two-level quantum system. Fabricating a nuclear reference close to these ideal characteristics is challenging and poses many practical difficulties [Vel21]. None of these methods give a complete solution to the phase problem.

In the 1980s, computational phase retrieval emerged as a method to indirectly reconstruct X-ray phase shifts using algorithms. These algorithms rely on additional information about the object to constrain the reconstruction process. For instance, in coherent diffraction imaging (CDI), a computational imaging algorithm replaces the need for a high-quality lens. One common constraint in CDI is the object's isolation from its surroundings. If the object's extent is known or estimated, a "support constraint" can be applied, as seen in Fienup's hybrid input-output (HIO) algorithm [Fie82], to reconstruct the X-ray wave field's attenuation and phase shift from the object's diffraction pattern. Another approach involves constraining the object by taking multiple intensity measurements, forming the basis of the widely used phase retrieval technique called ptychography [t(Λ)I'kogræfi/ t(a)i-KO-graf-ee], named after the ancient Greek word πτυκή *(ptyché)* , which means *to fold*[2]. Ptychography requires an optical system with a probe element for localized illumination and a mechanism to move the object relative to the illumination. By probing different parts of the object, valuable information about the phase is collected in the measurements. The choice of probe positions ensures sufficient overlap of the illuminated parts of the object. This overlap introduces redundancy in the measurements, making the reconstruction algorithm robust. In some cases, ptychography can reconstruct more than just the phase shift of the object; it can correct uncertainties in the probe [MR09] and its positions [Dwi+18] and allow the retrieval of coherence properties of the illuminating probe [TM13].

We propose a ptychographic approach using multiple overlapping nuclear resonance scattering measurements to address the phase retrieval problem. Backward and forward Fourier propagation between the real space and the reciprocal space is integral to ptychography in X-ray imaging. For NRS, the Fourier transform connects the energy and time domains. As shown in Fig. 1.1, we employ a Doppler shift mechanism to shift (detune) the probe with respect to the object in the energy domain. The intensity of the

[2] or *Faltung* in German, which is also the mathematical term for convolution.

measured wavefield at the detector at time t is expressed as

$$I^{(j)}(t) = |\mathcal{F}\{\hat{P}(\omega + \Delta\omega_j) \cdot \hat{O}(\omega)\}|^2. \tag{1.1}$$

Here, $\hat{P}$ and $\hat{O}$ represent the energy domain complex scattering responses of the probe and the object, respectively. $\Delta\omega_j$ is the Doppler detuning applied to the probe, and $\mathcal{F}$ denotes the Fourier transform.

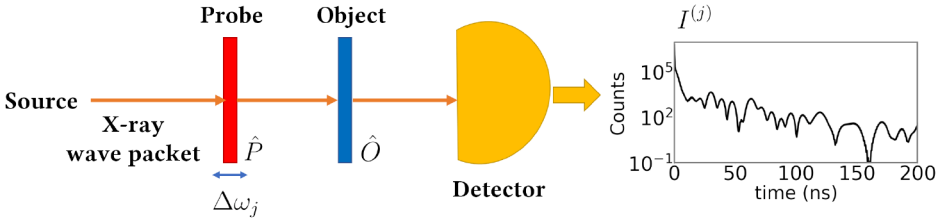

Figure 1.1.: A ptychographic measurement for a nuclear resonant scattering system. The synchrotron radiation is first scattered by the probe $\hat{P}$ and then the object $\hat{O}$. The temporal decay pattern $I^{(j)}$ at the detector changes with the Doppler detuning $\Delta\omega_j$ of the probe with respect to the object.

The set of ptychography measurements for various Doppler detunings is termed the "ptychogram." Solving the phase problem involves the non-linear inverse task of reconstructing $\hat{O}$ from the ptychogram, given the complex energy response $\hat{P}$ and Doppler detunings of the probe are known. It is a one-dimensional problem as we aim to reconstruct the phase of the object with respect to only one parameter ω, representing the energy of the incident X-rays. The ptychogram is a two-dimensional dataset, with one dimension being time and the second dimension being the Doppler detuning $\Delta\omega_j$ between the probe and the object.

To reconstruct the object from the ptychogram, we have developed a "ptychography engine" for nuclear resonance scattering (NRS). This iterative solver operates on an automatic differentiation framework, employing various gradient-based algorithms. The engine treats the phase retrieval problem as a non-convex cost minimization problem. We enhance the gradient-based algorithms with regularization techniques and methods for selecting hyperparameters. This improves their convergence efficiency and ability to navigate local minima. Despite ptychography's widespread success, its mathematical

foundation lacks comprehensive proof, except for a few simplified model cases [BP17; Mel+21]. To address this gap, we rigorously test and heuristically demonstrate the engine using simulated and experimentally measured ptychograms. The analysis helps draw crucial insights into the limitations and requirements of NRS ptychography.

Outline

The rest of the thesis is organized as follows. In **chapter 2**, we cover the theoretical background of nuclear resonance scattering (NRS), including how the dynamical theory can be applied to describe coherent elastic scattering by Mössbauer atoms. We focus on the special case of nuclear forward scattering and discuss the synchrotron radiation properties and hyperfine interactions that contribute to the scattering response in time and energy. We then introduce the one-dimensional phase retrieval problem in NRS and highlight its ill-posedness in contrast to higher-dimensional cases like crystallography.

In **chapter 3**, we introduces ptychography as a 'lens-less' computational imaging technique for high-resolution phase and magnitude reconstruction in X-ray imaging. Therafter, we extend the ptychography principles to NRS for recovering magnitude and phase responses in the energy domain from time-domain intensity measurements. We discuss the discretized one-dimensional ptychographic phase retrieval problem for NRS, framing it as a non-convex cost minimization problem with potentially multiple local minima.

In **chapter 4**, we describe the iterative phase retrieval process using the NRS ptychography engine. We then emphasize the advantages of gradient-based algorithms, likelihood models (Poisson, Gaussian, mixed Poisson-Gaussian) and regularization techniques employed in the engine. We also cover practical tweaks in the phase-retrieval implementation, such as the incoherent forward model (Sec. 4.3.5) in the case of a partially incoherent probe.

In **chapter 5**, we conduct numerical tests on the noiseless and noisy ptychographic phase retrieval using simulated data. We do a quantitative and qualitative analysis of the different algorithms and cost functions, the impact of overlap between the measurements and total variation regularization for stabilization. We also examine the effect of time windowing in NRS on energy resolution of the reconstruction.

In **chapter 6**, we report results from ptychography experiments at the dynamics beamline P01 at DESY to reconstruct the complex energy domain scattering response of a reference foil of ^{57}**Fe**. We describe experimental setups with illumination from two different probes - transmission from a thick stainless steel foil and specular reflection from a nanothin stainless steel film in an X-ray cavity. We then compare phase retrieval results from experimental and simulated ptychograms to demonstrate inco-

herent effects.

Lastly, in **chapter 7**, we summarize the main outcomes of the thesis, discuss open problems, and suggest potential directions for future research.

2. Nuclear resonant scattering

An atomic nucleus can absorb an X-ray photon if its energy is equal to the energy difference between two states of the nucleus. This process is called resonant absorption. A nucleus can also emit an X-ray photon when it undergoes a transition from an excited high energy state to a lower energy ground state. The width of the absorption and emission spectral lines is governed by various factors, including Doppler shifts caused by the random motion of the atoms and natural line broadening Γ due to the fundamental nature of the quantum process.

If the nucleus is *free*, it also recoils due to the conservation of momentum. The total energy of the emitted X-ray is then given as

$$E_\gamma = E_0 - E_R \tag{2.1}$$

where E_0 is the energy of the nuclear transition and $E_R = E_\gamma^2/(2Mc^2)$ is the kinetic energy lost to recoil. E_R depends on the energy of the photon E_γ and the mass M of the recoiling nucleus. This is shown in Fig. 2.1. For example, a free ^{57}**Fe** nucleus undergoing an energy transition of 14.41 keV has a recoil energy $E_R \approx 2$ meV – which is six orders greater than the natural transition linewidth of $\Gamma = 4.66$ neV. Therefore, the emitted X-ray photon does not have enough energy to be absorbed by another nucleus of the same type undergoing a transition between the same states, and resonant absorption can not occur.

However, if the atomic nuclei are bound in a solid, they have a much greater effective mass. In a solid lattice, the motion of atoms are superpositions of quantized vibrational modes i.e. the phonons. The recoil energy can only be transferred to the lattice if it is an integral multiple of the phonon energy $\hbar\omega_\mathrm{p}$. If the recoil energy $E_R < \hbar\omega_\mathrm{p}$, then either zero or one phonon of vibrational energy may be transferred to the lattice. In this case, the probability of occurrence of recoil-less (zero-phonon transfer) events becomes

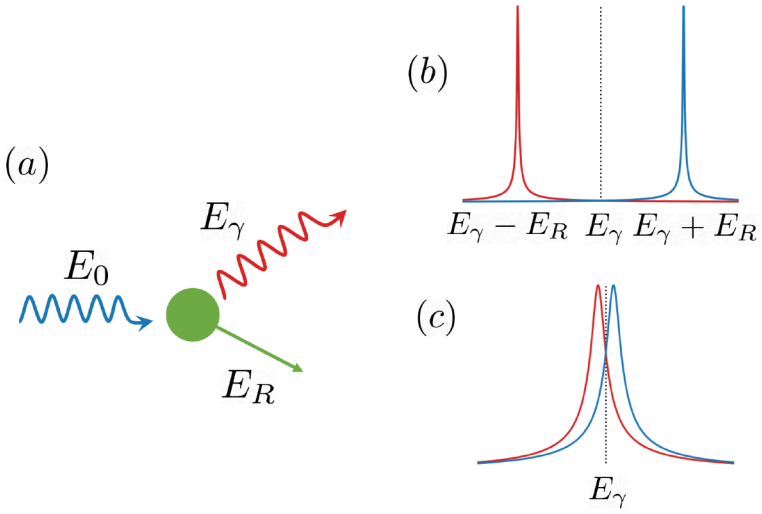

Figure 2.1.: (a) X-ray photon scattering by a free nucleus. (b) The emission (red) and absorption (blue) lines of free nuclei do not overlap. When drawn to scale, the separation between the two lines is about 4×10^5 Γ, where Γ is the natural linewidth. (c) Overlap of emission and absorption lines occurs in bonded solids where the recoil energy E_R is smaller (Mössbauer effect).

non-zero such that resonant absorption can be observed. The fraction of the events leading to the recoilless resonant absorption - the Mössbauer effect - is given by the Lamb-Mössbauer factor [Mös76],

$$f_{LM} = \mathrm{e}^{-k_\gamma^2 \langle x^2 \rangle}. \tag{2.2}$$

Here, $k_\gamma = E_\gamma/(hc^2)$ is the wave vector of the emitted X-ray photon and $\langle x^2 \rangle$ is the mean square displacement of the thermally vibrating nucleus in the direction of the incident X-ray photon. The Lamb-Mössbauer factor (and hence the strength of the signal) is strongly dependent upon the incident X-ray energy. Therefore, the Mössbauer effect is measurable only for nuclei with small energy differences between the ground and the excited state. Also, the energy resolution of the recoil-less resonant measurement depends on the natural lifetime of the excited nuclear state. To date, 45 isotopes have been found to exhibit a measurable Mössbauer effect (e.g., ^{57}**Fe**, ^{119}**Sn**, ^{121}**Sb**).

Nuclear resonant X-ray scattering (NRS) is based on the Mössbauer effect. Contrary to the original experiments of Mössbauer, NRS uses synchrotron radiation which has high coherence, brightness and collimation compared to a conventional lab X-ray source. Since the discovery of the Mössbauer effect, the theory for NRS was developed in the 1970s and 1980s. The first reliably successful measurement of the Mössbauer scattered radiation was achieved in 1984 by a group based in Hamburg, Germany, on thin, single crystal films of Yttrium iron garnet (YIG) [Ger+85]. The measurements were conducted at an experimental station in the HASYLAB located at the storage ring DORIS (DESY, Hamburg). The technique flourished in the 1990s with the arrival of highly brilliant and coherent third-generation synchrotron sources and the development of high-resolution monochromators and ultra-fast detectors. Presently, NRS beamlines are available at the following synchrotron sources around the world:

- P01 at PETRA III, DESY, Hamburg, Germany
- ID14 at ESRF, Grenoble, France
- BL35XU at SPring 8, Harima Science Park City, Hyogo, Japan
- Sector 3-ID, Sector 30-ID and HPCAT (16-ID) at APS, Argonne National Laboratory, Illinois, USA

A further contemporary review of the field can be found in Ref. [RC21].

Given the extensive use of ^{57}**Fe** in the Mössbauer physics community, this thesis specifically focuses on NRS experiments with this iron isotope. Compared to most other Mössbauer isotopes, has a nuclear magnetic dipole resonance at a low transition energy (14.41 keV) between the ground state with nuclear spin $I_g = 1/2$ and the excited state with nuclear spin $I_e = 3/2$. The lifetime of the nuclear excited state is 141.11 ns. The values of the scattering cross section (2558 kbarn) and the Lamb-Mössbauer factor (0.78) are also quite high at room temperature. The required technology and instrumentation for the isotope is also well established.

In the upcoming sections of this chapter, we will explore the key components of nuclear resonant scattering theory relevant to understanding how coherent X-ray fields interact with nuclear ensembles. Most of the subsequent discussion is presented in its original form in Refs. [Smi99] and [SG94].

2.1. Dynamical scattering theory

Under quantum electrodynamic theory, the light-matter interactions are studied by quantizing the electromagnetic field to photons. However, due to the low density of photon modes of common X-ray sources, it is sufficient to describe the X-ray field classically as a coherent, linear superposition of plane waves. The propagation of the X-rays in a medium without any free charges is described by the inhomogeneous wave equation,

$$\left(c^2\nabla^2 - \frac{\partial^2}{\partial t^2}\right)\mathbf{E} = \frac{1}{\epsilon_0}\frac{\partial^2 \mathbf{P}}{\partial t^2} \tag{2.3}$$

where $\mathbf{E}$ is the driving electric field of the X-rays, $\mathbf{P}$ is the polarization induced by $\mathbf{E}$ in the medium. c and ϵ_0 are the speed of light and the electric permittivity in vacuum, respectively. The propagating X-ray field is given by space and time-harmonic plane waves of frequency ω as

$$\mathbf{E}(\mathbf{r}, t) = |\mathbf{E}|\, \mathrm{e}^{\mathrm{i}(\omega t - \mathbf{k}\cdot\mathbf{r})} \tag{2.4}$$

such that

$$(|\mathbf{k}|^2 - |\mathbf{K}|^2)\mathbf{E} - \mathbf{k}(\mathbf{k}\cdot\mathbf{E}) = |\mathbf{K}|^2 \frac{1}{\epsilon_0}\mathbf{P}. \tag{2.5}$$

Here, $\mathbf{k}$ is the wave vector inside the medium and $\mathbf{K}$ is the wave vector in vacuum ($|\mathbf{K}| = \omega/c$). If we only retain the linear term for the dependence of $\mathbf{P}$ on $\mathbf{E}$[1], i.e.,

$$\mathbf{P} = \epsilon_0 \underline{\boldsymbol{\chi}}\mathbf{E}, \tag{2.6}$$

then Eq. (2.5) simplifies to

$$(|\mathbf{k}|^2 - |\mathbf{K}|^2)\mathbf{E} - \mathbf{k}(\mathbf{k}\cdot\mathbf{E}) = |\mathbf{K}|^2\, \underline{\boldsymbol{\chi}}\mathbf{E} \tag{2.7}$$

where $\underline{\boldsymbol{\chi}}$ is the electric susceptibility of the medium.

Two theories are widely used to describe the interaction of X-rays with matter. The

[1] At high radiation intensities which are comparable to the intensity of the electric field between atoms in the medium (10^9 V/m), it becomes possible for light photons to interact non-linearly with each other – leading to changes in their energy and momentum. The induced polarization thus has a non-linear dependence on the electric field and can be expressed as a power series, $\mathbf{P} = \sum_i \epsilon_0 \underline{\boldsymbol{\chi}}^{(i)}\mathbf{E}^i$ [Hoe20]. Non-linear interactions in the X-ray regime are virtually unexplored due to their extremely small cross-sections. The development of the X-ray free-electron laser (XFEL) sources in recent years has opened the door to the research field.

first is the so-called kinematical theory, which assumes that the atoms in the propagation medium only scatter the incoming wave of X-rays once. Following the 'single-scattering' events, the scattered wave intensities are summed, accounting for their phase differences, to produce the transmitted and reflected channel intensities. Thus, the kinematical theory only focuses on the first-order term in the expansion of the scattering wave function (also known as the *first Born approximation*). This approximation works effectively for scattering from surfaces and thin films with a small amount of interacting material.
However, in the case where the X-ray waves traverse large regions of space filled with atoms, further interaction between the single-scattered waves and the atoms cannot be disregarded. To explain observed phenomena that defy kinematical theory and go beyond the Born approximation, it is necessary to take the multiple scattering of waves inside the medium into account.

According to the dynamical scattering theory, as X-rays propagate through a medium, they excite currents in the atoms, emitting their waves. These re-emitted waves constructively interfere with the incident waves and give rise to modified scattered waves. A medium's total X-ray field is thus a coherent superposition of multiple scattering channels coupled by atomic currents. In the steady state, a dynamic equilibrium is established between the field and the atomic currents. The total field produced by the atomic currents is exactly equal to the field that produced them.

To find a self-consistent solution for the radiation field in all scattering channels, all orders of multiple scattering have to be taken into account. In an optically active medium with periodicity, there can be multiple eigenwaves corresponding to different polarization states and different propagation vectors. The Maxwell wave equation thus splits into a set of coupled linear differential equations with constant coefficients. These 'dynamical' wave equations connect the eigenwave in the system to each other and are given as

$$\left(\frac{|\mathbf{k}_d|^2}{|\mathbf{K}|^2} - 1\right) E_d^\theta = \sum_{d'\theta'} \chi_{dd'}^{\theta\theta'} E_{d'}^{\theta'}. \tag{2.8}$$

The index d denotes the direction of propagation of the eigenwave component E_d^θ along the polarization direction θ. The parameters $\chi_{dd'}^{\theta\theta'}$ are related to the probability

amplitude of scattering from eigenstate (θ', d') to (θ, d). They form the susceptibility tensor $\underline{\boldsymbol{\chi}}$. The rank of the susceptibility matrix increases with the number of eigenwaves (or scattering channels) allowed in the scattering system:

- In a disordered (i.e. non-crystalline) and optically isotropic medium, the only scattering channel allowed is in the forward direction, and $\underline{\boldsymbol{\chi}}$ is just a complex scalar χ_0.

- In a disordered but optically active, anisotropic medium, the scattering channels in the forward direction can be of different polarization states. $\underline{\boldsymbol{\chi}}$ then equals a 2×2 matrix of second rank with components $\chi^{\theta\theta'}$.

- In an ordered, crystalline, but optically inactive medium diffraction can occur. In the case of a single Bragg reflection, $\underline{\boldsymbol{\chi}}$ equals a 2×2 matrix of second rank with components $\chi_{dd'}$ for forward and Bragg scattering directions. The matrix size increases with the number of allowed Bragg reflections.

We have thus laid out the general formalism of the dynamical scattering theory [Smi99], which provides an algebraic structure that can be applied to a multitude of problems. Knowing $\underline{\boldsymbol{\chi}}$, the dynamical wave equations [Eq. (2.8)] can be solved using boundary conditions to find the propagation vectors, polarization states, and amplitudes of all constituent eigenwaves of the X-ray field in the medium. The physics of the interaction between the X-ray field and the medium is contained in the scattering amplitudes of the scatterers in the medium. The following sections continue the discussion relevant to the case of nuclear resonance scattering.

2.2. Coherent elastic scattering by a medium of Mössbauer atoms

The interaction of photons of a light field with the electromagnetic currents of atoms in a medium can be described as a scattering process. It may take place coherently or incoherently, depending on whether or not the state of the scattering system is unchanged thereafter. In most cases, coherence implies that the energy of the system does

not change, i.e., the scattering is elastic[2].

The scattering behavior of a single atom can be described in QED theory. For a coherent, elastic scattering process in a medium with multiple scattering atoms, it is not possible to determine which particular atom was involved. The single incident photon creates a *delocalized* intermediate excited state shared by the entire ensemble of scatterers [Smi99]. The corresponding scattering amplitude is thus derived as a quantum mechanical average over the ensemble. [3] In this case, the scattering amplitude of an atom can be represented by a 2×2 complex matrix $\hat{\mathbf{A}}(\omega)$ to include the dependence on the polarization state θ of the X-rays. It relates the magnitudes and phases of the energy (ω) components of the incident and scattered radiation to each other as

$$\hat{E}_s^{\theta}(\omega) = \sum_{\theta'} \hat{A}^{\theta\theta'}(\omega)\hat{E}_i^{\theta'}(\omega) \tag{2.9}$$

where $\sum_{\theta'}$ corresponds to the sum over the linearly independent polarization states. We break down the contributions to the scattering amplitude into the electronic part and the nuclear part, i.e.,

$$\hat{A}^{\theta\theta'}(\omega) = \hat{A}_e^{\theta\theta'}(\omega) + \hat{A}_N^{\theta\theta'}(\omega). \tag{2.10}$$

2.2.1. Electronic scattering amplitude

Far off the resonances of the electron shell, electronic scattering is slowly varying in energy and conserves the polarization of the incoming photon. The electronic scattering amplitude $\hat{\mathbf{A}}_e$ is given as [SG94; Röh05],

$$\hat{A}_e^{\theta\theta'} = -\delta_{\theta\theta'} \cdot 2\pi f_{DW} \cdot \left(f_e(q) \cdot r_e + \mathrm{i}\frac{k}{4\pi}\sigma_t \right) \tag{2.11}$$

[2] An exception is when delocalized quasi-particle excitations like phonons are created and annihilated during the scattering process, that transfer energy to and from the scattered photons. This is an inelastic process that does not violate the condition of coherence. However, in the case of NRS, the lifetime of thermal phonons is very short ($\sim 10^{-12}$ s) compared to the nuclear lifetimes ($\sim 10^{-9}$ s). The spatial coherence of the waves scattered by the phonons is preserved for only a very short time and over inter-atomic length scales (i.e. the vibrations of neighboring atoms are not correlated). The observation of coherent, inelastic NRS is therefore extremely difficult [Röh05].

[3] The dimension of the scattering amplitude is length. Therefore it is sometimes also referred to as the scattering length.

where δ is the Kronecker delta, r_e is the classical electron radius, and σ_t is the total absorption cross section at energy ω. The latter is typically calculated as the sum of the Klein-Nishina cross-section [KN29] and the photoelectric cross-section. $f_{DW} < 1$ is the Debye-Waller factor which describes the attenuation in elastic scattering of atoms due to thermal vibrations in their lattice. f_e is the form factor of the electron shell for momentum transfer q. When no momentum transfer occurs during the scattering process, the form factor f_e equals the atomic number Z. Note that the definition in Eq. (2.11) might differ by a factor of 2π depending on the author.

2.2.2. Nuclear scattering amplitude

The excitation of the nucleus in the coherent ensemble is described as an oscillating multipole radiation. For a single-bound nucleus, assumed to have no hyperfine splittings, the scattering amplitude is given as a complex Lorentzian line [Smi99] such that

$$\hat{A}_N^{\theta\theta'} = -\delta_{\theta\theta'} \frac{\Gamma/2\hbar}{\omega - \omega_0 - \mathrm{i}\Gamma/2\hbar} \cdot a \cdot f_{LM} \cdot \frac{K}{4\pi} \cdot \sigma_r. \tag{2.12}$$

where a is the abundance or isotopic enrichment of the sample, K is the magnitude of the wave vector of the incident photon and $\hbar$ is the reduced Planck's constant. $f_{LM} < 1$ is the Lamb Mössbauer factor representing the probability of recoilless scattering of the nuclear resonant X-rays and σ_r denotes the resonance cross-section of the nucleus,

$$\sigma_r = \frac{2\pi}{K^2} \cdot \frac{1}{1+\alpha} \cdot \frac{2I_e + 1}{2I_g + 1} \tag{2.13}$$

The meaning of the other symbols and their values for ^{57}**Fe** are listed in Table 2.1.

[4] as given in [Joh70]

Γ	natural linewidth	4.66 neV
ω_0	resonance energy	14.4125 keV
α	internal conversion coefficient	8.19 ± 0.18 [4]
I_g	nuclear spin of ground state	1/2
I_e	nuclear spin of excited state	3/2
σ_t	total electronic resonance cross section	5.75 kbarn
σ_r	nuclear resonance cross section	2557.67 kbarn

Table 2.1.: Table of symbols and their values for ^{57}**Fe** at the nuclear resonance.

2.3. Nuclear forward scattering

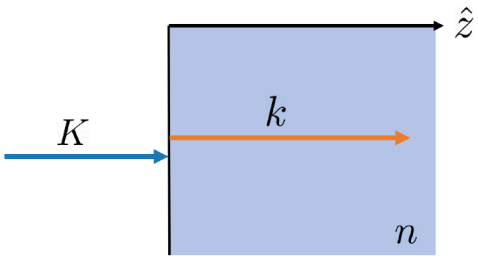

Figure 2.2.: Geometry of forward scattered wave propagation through an isotropic medium of refractive index n.

Let us consider the electric field of an arbritarily polarized incident wave propagating along the $+z$ axis of a sample with Mössbauer atoms, i.e.,

$$E_i = E_0 e^{i(\omega t - Kz)}. \tag{2.14}$$

If the sample is disordered (i.e. with no prefered crystalline orientations), the waves scattered in the medium coherently superimpose with each other only in the forward direction (as discussed in Sec. 2.1). Inside the sample, the propagation vector is given as $\mathbf{k} = k\hat{\mathbf{z}}$, where $\hat{\mathbf{z}}$ is the unit vector along z. If the sample is also optically inactive, the 'forward' scattering of the X-rays can be described with just one dynamical equation

and a complex scalar susceptibility χ_0 such that

$$\left(\frac{|\mathbf{k}|^2}{|\mathbf{K}|^2} - 1\right) E = \chi_0 E. \tag{2.15}$$

For coherent elastic scattering, the internal state of the scattering system is unmodified in the scattering process. The macroscopic ensemble of scatterers can be replaced by a continuous medium with a refractive index [5]

$$n(\omega) = 1 + \frac{4\pi}{K^2}\rho\hat{A}(\omega) \tag{2.16}$$

where ρ is the number density and $\hat{A}$ is the scattering length of the atoms in the medium. The refractive index is complex and deviates only slightly from unity such that

$$n = 1 - \delta + \mathrm{i}\beta = 1 - \xi. \tag{2.17}$$

The real part δ accounts for the change in phase velocity while the imaginary part β accounts for the attenuation of X-rays in the medium. ξ is a very small complex number. By definition, the refractive index connects the propagation vectors of the wave inside and outside the medium:

$$n = \frac{|\mathbf{k}|}{|\mathbf{K}|} \tag{2.18}$$

Substituting Eq. (2.18) in Eq. (2.15), we get:

$$\chi_0 = n^2 - 1 \tag{2.19}$$

$$= (1 - \xi)^2 - 1 \tag{2.20}$$

$$\approx -2\xi = \frac{8\pi}{K^2}\rho\hat{A} \tag{2.21}$$

Therefore, the total susceptibility depends on the scattering length of the atoms in the medium $\hat{A}$. Using Eq. (2.11) and Eq. (2.12) we can write

$$\chi_0(\omega) = \epsilon - \frac{\mu}{K}\frac{\Gamma/2\hbar}{\omega - \omega_r - \mathrm{i}\Gamma/2\hbar} \tag{2.22}$$

[5] This is the so-called index of refraction model.

where $\mu = \sigma_r f_{LM} \beta \rho$ is the nuclear linear absorption coefficient. The electronic susceptibility varies slowly in the range of nuclear resonance energies and can be taken as a complex-valued constant ϵ.

At the incidence boundary, $|E| = E_0$, the electric field of the scattered (transmitted) wave at propagation distance z in a medium is given as,

$$E_s = E_0 e^{i(\omega t - Kn(\omega)z)} = E_i e^{-i\chi_0(\omega)Kz/2} \tag{2.23}$$

with transmitted intensity $I_s = E_i^2 e^{\Im(\chi_0)Kz}$.

If the sample is thin (i.e. $z = \Delta z$ and $\chi_0 K \Delta z \ll 1$), we can neglect the coupling of the nuclei with the scattered radiation. In this kinematical approximation limit, we can Taylor expand the exponential in Eq. (2.23) to the first order. The total scattered radiation is then given as

$$E_s \approx E_i (1 - i\frac{\chi_0(\omega)}{2} K \Delta z). \tag{2.24}$$

We can interpret the first term as corresponding to transmission through the sample without interaction and the second term as the coherent forward scattering by the sample. Similar to the refractive index, the susceptibility χ_0 in the forward scattering term is a complex quantity (see Fig. 2.3). Its imaginary part $\Im(\chi_0)$ is encoded in the attenuation of the transmitted intensity while the real part $\Re(\chi_0)$ gives rise to a phase shift in the transmitted wave relative to the incident wave.

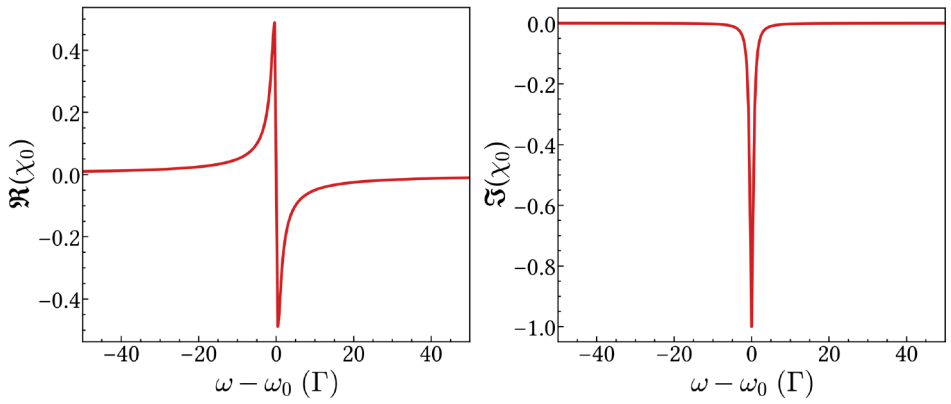

Figure 2.3.: Real and imaginary parts of the susceptibility calculated assuming $\mu/K = 1$. The units of ω is in Γ. At exact resonance, $\omega = \omega_0$, i.e., the energy of the incident X-rays matches the energy of the nuclear transition and $\Re(\chi_0) = 0$. No phase shift takes place and the absorption is strongest. In the wings of the resonance, the X-ray absorption is weak and there is a phase shift depending on the thickness of the traversed medium.

2.4. Nuclear forward scattering with synchrotron radiation

The nuclear resonant scattering experiments in this thesis were carried out at synchrotron facilities. Synchrotron X-ray pulses were incident on the samples that contain the resonant nuclei. The coherent, elastically scattered photons from the sample were then detected together with their time of arrival relative to the time of the pulse excitation (i.e. their time delay). This section describes the relevant properties of synchrotron radiation and the detected nuclear resonant scattering spectra.

2.4.1. Synchrotron radiation

Synchrotron radiation is produced when charged particles, such as electrons, are accelerated to nearly the speed of light and are forced to move in a curved path by a magnetic field. The emitted radiation has a very broad spectrum, ranging from infrared to X-rays, depending on the energy and velocity of the charged particles. The synchrotron radia-

tion source used in our experiments at PETRA III is a storage ring – where individual packets or 'bunches' of $\sim 4.8 \times 10^{12}$ electrons are stored and steered on a circular path along the ring with the help of strong bending and focusing magnets [HAS24].

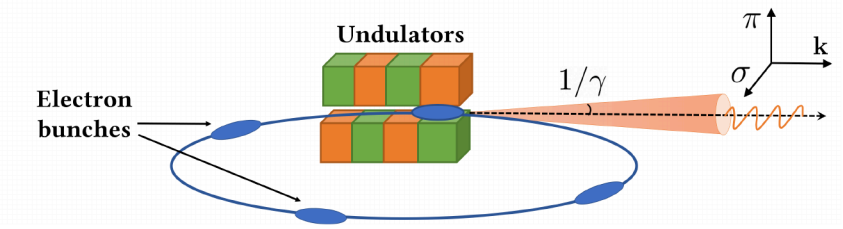

Figure 2.4.: Emission of linearly polarized synchrotron radiation in the lab frame from electron bunches in a storage ring.

The electron bunches circulate in the storage ring emitting photons, passing through radio frequency (RF) cavities until they reach energy levels of around 6 GeV. Since this energy is very large compared to the electron rest mass energy (0.511 MeV), relativistic effects cause the emitted radiation to be strongly collimated into a sharp forward cone along the instantaneous direction of the electrons [Win95]. The opening angle of this cone is given by γ^{-1} where γ is the Lorentz factor. At 6 GeV, the opening angle is around 0.1 mrad. The emitted light is linearly polarized in the orbit plane of the electrons (i.e. along σ in Fig. 2.4).

To make the light even more brilliant and collimated, undulators containing arrays of alternating magnets are used. The radiation produced in an undulator is very intense, highly coherent, and concentrated in narrow energy bands ($\sim$ 100 eV) around a specific fundamental wavelength. However, this bandwidth is still too broad compared to the energy linewidth of the nuclear resonances. Before hitting the sample, the synchrotron radiation passes through a high resolution monochromator system specially designed for nuclear resonant scattering experiments. The resulting energy bandwidth B is from 0.5 to 1 meV - which is still broad compared to the Mössbauer splitting of the nuclear resonance of ^{57}**Fe** (few 100 neV). We can assume that all spectral components of the synchrotron radiation have an equal magnitude within the energy bandwidth B, given as

$$E_0 = \sqrt{\frac{I_0}{\mathrm{B}}}, \tag{2.25}$$

where I_0 is the total intensity of the synchrotron radiation.

2.4.2. Time response of the nuclear resonant system

In a nuclear resonant scattering experiment, the synchrotron radiation emitted by the electron bunches arrives at the sample in the form of short (< 100 picoseconds) X-ray pulses. Each of these pulses leads to a collective excitation of the nuclear ensemble - the nuclear *exciton-polariton* [Röh05; HT99]. The time response of a disordered, optically inactive sample excited by an incoming synchrotron radiation pulse from the monochromator can be obtained by integrating over all energies of the scattered wave Eq. (2.23), i.e.,

$$E_s(t) = \frac{E_0}{2\pi} \int_{-\infty}^{\infty} \mathrm{e}^{\mathrm{i}(\omega t - Kn(\omega)z)}\, d\omega \tag{2.26}$$

$$= \frac{E_0}{2\pi} \int_{-\infty}^{\infty} \mathrm{e}^{-\mathrm{i}\chi_0(\omega)Kz/2} \cdot \mathrm{e}^{\mathrm{i}\omega t}\, d\omega. \tag{2.27}$$

Substituting the value of χ_0 from Eq. (2.22), the electric field at depth z of the sample can be calculated as [Smi99],

$$E_s(z,t) = E_0 \mathrm{e}^{-\frac{\mu_e z}{2}} \left[\delta(t) - \frac{\mu z}{2t_r} \cdot \mathrm{e}^{\mathrm{i}\omega_0 t - bt/2t_r} \cdot \Theta(z,t)\right] \tag{2.28}$$

where

$$\Theta(z,t) = \frac{J_1(\sqrt{\mu z t/t_r})}{\sqrt{\mu z t/t_r}}\,, \quad t \geq 0. \tag{2.29}$$

Here, δ is the Dirac delta function, μ_e is the relevant electronic absorption length of the sample (such that $\epsilon = \mu_e/K$ in Eq. (2.22)), μ is the nuclear absorption length as defined in Eq. (2.22), $t_r = \hbar/\Gamma$ is the natural lifetime of the nuclear transition and J_1 is the Bessel function of the first kind of first order. The function $\Theta(z,t)$ contains the space-time structure of the scattered wave. We have also included a term b to denote the inhomogeneous broadening of the resonance due to thermal effects and the non-uniformity of the environments of the resonant nuclei - while assuming that it preserves the Lorentzian line shape.

The first term in Eq. (2.28) describes the *prompt* part of the transmitted wave packet

due to the electronic scattering occurring at sub-picosecond time scales. The second term represents the *delayed* forward scattered radiation due to nuclear scattering which occurs at longer timescales of around $\sim 10 - 10^3$ ns. Nuclear scattering events are thus usually separated from electronic scattering events by gating in time.
If we assume that the sample is thin, the kinematical approximation in Eq. (2.24) can be taken. In this case, the time response of the thin film can be calculated using Cauchy's formula [Smi99],

$$E_s(t) \approx \frac{E_0}{2\pi} \int_{-\infty}^{\infty} (1 - \mathrm{i}\frac{\chi_0(\omega)}{2} K\Delta z)\, d\omega \tag{2.30}$$

$$= E_0 \left[\delta(t) \cdot \left(1 - \frac{\mu_e}{K}\right) - \frac{\mu\Delta z}{4t_r} \cdot \mathrm{e}^{\mathrm{i}\omega_r t - qt/(2t_r)} \right], \; t \geq 0. \tag{2.31}$$

The delayed time response of a thin sample has a sinusoidal component of frequency ω_r which decays exponentially with time.

2.4.3. Properties of the time response

The time response of the nuclear exciton exhibits interesting effects of coherence, namely quantum beating patterns and accelerated radiative decay.

Dynamical beats

From Eq. (2.25) and (2.28), the intensity of the forward scattered wave can be calculated as

$$I_s(t) = |E_s(t)|^2 = \frac{I_0}{\mathrm{B}} \cdot \mathrm{e}^{-\mu_e z} \cdot \frac{(\mu z)^2}{4t_r} \mathrm{e}^{bt/t_r} \cdot \Theta^2(z,t). \tag{2.32}$$

If we use the effective thickness $\zeta_{\mathrm{eff}} = \mu z$ and reduced time $\tau = t/t_r$ as our dimensionless space-time units, we can use their dot product $\tau\zeta_{\mathrm{eff}}$ to monitor the stages of the decay of the forward scattered intensity in time as follows:

- For $\tau\zeta_{\mathrm{eff}} = 0$, $\Theta = 1/2$ and Eq. (2.32) approaches the kinematical approximation given in Eq. (2.30). Therefore, for small times ($\tau\zeta_{\mathrm{eff}} \ll 1$), a thick sample behaves like a thin one.

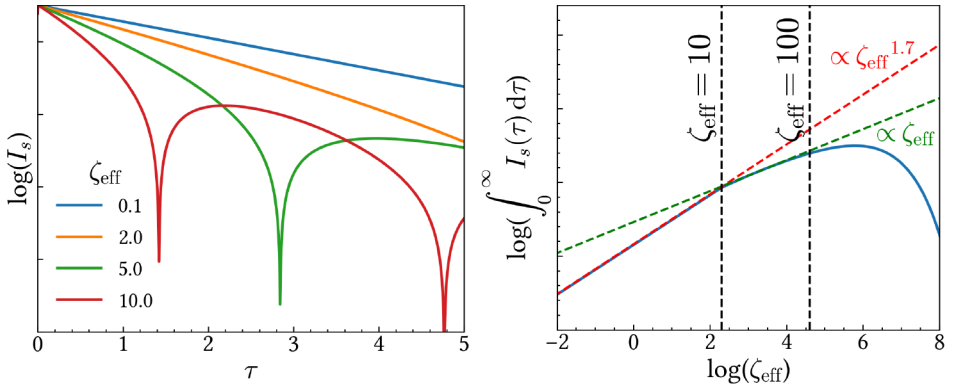

(a) (b)

Figure 2.5.: (a) The time response of an enriched ^{57}**Fe** foil simulated at different effective thicknesses (with absorption coefficients $\mu \sim 15.5\ \mu\text{m}^{-1}$, $\mu_e \sim 0.05\ \mu\text{m}^{-1}$) by assuming no hyperfine splitting. For the larger effective thicknesses of the foil, we see dynamical beats in the time response. The time responses have been normalized to the same maximum intensity. (b) The total transmitted intensity through a sample is plotted against its effective thickness. The red dotted line is proportional to $\zeta_{\text{eff}}^{1.7}$ while the green dotted line is proportional to ζ_{eff}. Due to an increase in the number of nuclear scatterers, the total transmitted intensity increases for thicknesses up to $\zeta_{\text{eff}} = 100$. For larger thicknesses, electronic absorption in the sample decreases the transmitted intensity.

- For initial times where $\tau\zeta_{\text{eff}} \approx 3$, $\Theta \approx \frac{1}{2}e^{-\tau\zeta_{\text{eff}}/8}$. The scattering intensity is given as

$$I_s \propto \zeta_{\text{eff}}^2 e^{-\tau(b+\zeta_{\text{eff}}/4)}. \tag{2.33}$$

  It is enhanced by a factor proportional to $\zeta_{\text{eff}}^2 = (\mu z)^2 \propto (nz)^2$, where n is the number density of nuclei and z is the distance travelled by the beam in the sample. This *superradiant*[6] emission is a quantum interference effect known as Dicke's superradiance [Dic54]. We also see another factor $e^{-\tau(b+\zeta_{\text{eff}}/4)}$ which leads to a *speed-up* of the decay of the forward scattered intensity in time (see Fig. 2.5(a)). This is because quantum coherence also accelerates the evolution of the super-

[6]Due to the high degree of coherence between them, the emission phase of the different nuclei in the ensemble is correlated. The secondary radiation emitted by them can interfere constructively, enhancing the radiation emission. As a result, the radiation is emitted coherently and with a higher intensity than would be spontaneously emitted by independent nuclei ($\propto n$).

radiant system, according to the law of conservation of energy. This speed-up depends on the effective thickness of the sample and the radiative coupling between the nuclei.
The effect of the inhomogenous broadening factor b is also an acceleration of the decay speed. However, if b is a purely incoherent broadening, the speed up is due to the loss of the coherent channel intensity to the incoherent channel intensity. This is opposed to the superradiant speed-up where the total emitted coherent intensity is enlarged.

- For longer times and thick samples ($\tau\zeta_{\text{eff}} > 3$), the effects of multiple scattering of the photons by the nuclei become evident. At finite depths within the sample, the nucleus is first illuminated by the primary ('prompt') radiation pulse and then by the delayed forward scattered radiation from the upstream part of the sample. The nuclei in different depths along the beam path of the sample thus experience different radiation fields. The amplitude of the nuclear scattering in the sample is now a function of both space and time. The corresponding function Θ has a node-antinode structure, thus leading to *dynamical beats* in the intensity spectrum I_s (see Fig. 2.5(a)). The dynamical beats reveal sequential absorption and re-emission of radiation by nuclei. The number of antinodes shows the number of scattering events in the observation window for the given sample [Smi99].

Although the electronic absorption of the incident radiation decreases the intensity of the nuclear scattering signal, its effect on thin samples is neglectable. In Fig. 2.5(b) we see that the total transmitted intensity is approximately proportional to $\sim \zeta_{\text{eff}}^{1.7}$ and drops to a linear $\sim \zeta_{\text{eff}}$ dependence for thicker samples as the electronic absorption starts to dominate.

Quantum beats

So far, our discussion was focused on a single nuclear transition. However, due to electric and magnetic interactions between the nucleus and its surrounding electrons, nuclear energy can split into several closely spaced levels, each with a slightly different energy. These 'hyperfine' interactions are small ($\sim$ μeV) in comparison to the energy levels of the nucleus (in keV), but they can be observed due to the extreme energy res-

olution of the Mössbauer effect. To study the nucleus, we make a multipole expansion of its Hamiltonian. No magnetic monopoles exist in the Standard Model. The electric dipole moment of the nucleus is also zero under the parity (P) and time reversal (T) symmetry. The hyperfine structure of the nucleus is thus influenced by three major interactions:

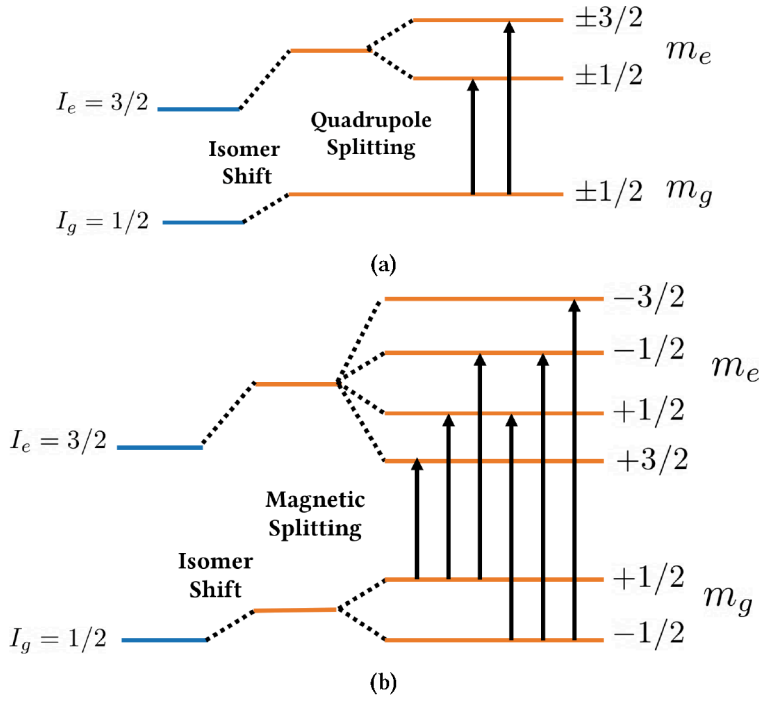

Figure 2.6.: Energy level diagram illustrating (a) the isomer shift and quadrupole splitting for the $I = 1/2$ to $3/2$ transition and (b) magnetic (Zeeman) splitting in ^{57}**Fe**. Compounds such as iron oxides (e.g., magnetite Fe_3O_4) or iron sulfides (e.g., pyrite FeS_2), exhibit a combination of both effects in their response, corresponding to the different Zeeman sub-levels and quadrupole-split states.

1. **The electric monopole interaction (isomer shift)**: The electric monopole or Coulombic interaction between the atomic nucleus and the s-electron cloud causes a renormalization of the energy of the nucleus. The nuclei in the excited and ground state are isomers - they have the same number of protons and neu-

trons but different energies due to the different internal configuration of the nucleons. Hence, they have a difference in their corresponding electric monopole potentials and get normalized by different amounts. This causes a slight shift in the energy required to transition between the ground and excited state, as shown in Fig. 2.6. The isomer shift thus induces a 'global' displacement of the lines in the energy spectrum away from zero. The amount of shift depends on the chemical environment of the nucleus and can be used, e.g., to distinguish between compounds with different valence states iron (II) and iron (III).

2. **The electric quadrupole interaction (quadrupole splitting)**: The quadrupole splitting occurs when the nuclear electric quadrupole moment interacts with the electric-field gradient due to an asymmetrically distributed electron cloud. Only the excited state of ^{57}**Fe** with nuclear spin I > 1/2 can have this asymmetry. Figure 2.6(a) shows the splitting for the first excited state in ^{57}**Fe**. The effect of quadrupole splitting on the energy and time response of a sample can be seen in Fig. 2.7.

3. **The magnetic dipole interaction (nuclear Zeeman effect)**: The interaction of the magnetic dipole moment of the ground and excited states of the nucleus with the local magnetic field causes a magnetic hyperfine splitting. This results in the energy and time response shown in Fig. 2.8. The local magnetic hyperfine field is a combination of the externally applied magnetic field and the magnetic field generated by the unpaired electrons in the vicinity of the nucleus. In ^{57}**Fe**, only states with nuclear spins I > 0 can be magnetically split, as shown in Fig. 2.6.

In the presence of the above interactions, the nuclear susceptibility splits into several terms with different transition energies

$$\chi_0(\omega) \propto \sum_j c_j \frac{\Gamma/2\hbar}{\omega - \omega_j - i\Gamma/2\hbar}, \tag{2.34}$$

where c_j and $\hbar\omega_j$ are respectively the weight and the energy of the j-th resonance transition. In a nuclear scattering experiment, the incident synchrotron pulse is energetically broad enough to excite all the hyperfine split nuclear levels. The scattered components can interfere constructively or destructively with the original incident ra-

diation pulse, depending on their relative phases. As a result, the intensity of the scattered radiation can oscillate as a function of time, and *quantum beats* are observed in the spectrum. The frequency of the beating due to a pair of split resonances corresponds to the energy difference between the two nuclear resonances. The complexity of the quantum beat pattern increases drastically with the number of interfering transitions. The weighting coefficient c_j depends on the orientation of the magnetic field and the polarization of the incident radiation. Since synchrotron pulses are highly polarized, the observed beat pattern is very sensitive to slight variations in the magnitude and orientation of hyperfine field parameters.

Therefore, as shown in Fig. 2.9, the time response measured in a nuclear resonant scattering experiment contains a combination of both quantum and dynamical beat patterns due to the hyperfine structure of the nuclei and the thickness of the sample.

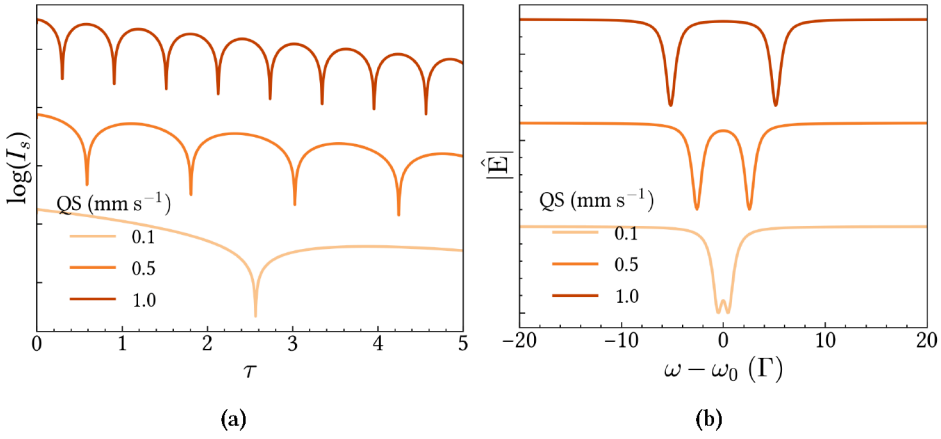

Figure 2.7.: Effect of a quadrupole splitting (QS) with isotropic angular distribution in a ^{57}**Fe** foil with $T_{\text{eff}} = 2.0$ assuming no isomer shift or magnetic splitting. As QS increases, (a) the period between two minima in the time response becomes smaller and (b) the susceptibility in the energy domain splits into two line which spread away from each other. The responses for the different QS values have been plotted with an offset for clarity.

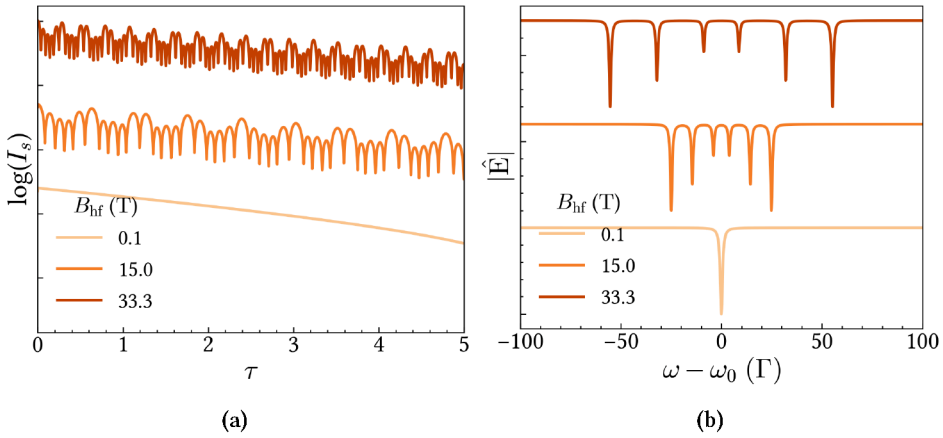

Figure 2.8.: Splitting due to a magnetic hyperfine field (B_{hf}) with random angular distribution in a ^{57}**Fe** foil with T_{eff} = 2.0 assuming no isomer shift or quadrupole shift. The B_{hf} values are given in Tesla (T). (a) The period of the beating structure in the time response becomes shorter and (b) the susceptibility in the energy domain splits into six peaks which spread away from each other as B_{hf} increases. The responses for the different B_{hf} values have been plotted with an offset for clarity

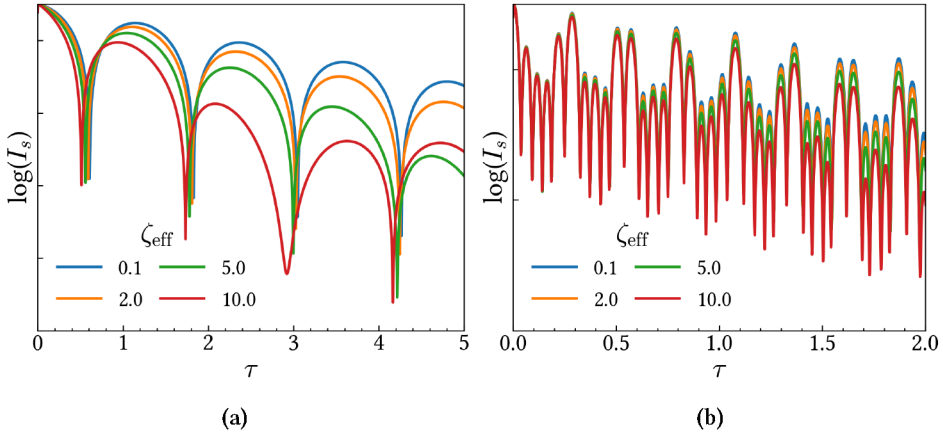

Figure 2.9.: Time responses of different thicknesses of a ^{57}**Fe** foil in the presence of (a) only a quadrupole splitting of 0.5 mm s^{-1} and (b) only magnetic splitting with B_{hf} = 33.3 T. The time response of the thicker foils decays faster than the thin foils. It is difficult to distinguish between the dynamical and the quantum beats for the thicker samples.

2.5. Energy domain methods based on Mössbauer effect

Aside from nuclear resonant scattering, lab-based conventional Mössbauer spectroscopy can be used to study the hyperfine structure of nuclei. This involves a process where a radioactive source emits X-ray radiation onto the sample, while a detector measures the intensity of the beam that passes through it. Both the emitting source and the sample must have high Lamb-Mössbauer factors to obtain a measurable signal. For ^{57}**Fe** samples, ^{57}**Co** is commonly used as a source (see Fig. 2.10(a)). It first decays by electron capture to an excited state of ^{57}**Fe** and then to a ground state of ^{57}**Fe** with a series of X-ray emissions – including the one that corresponds to the nuclear resonance in ^{57}**Fe**. While doing the measurement, the source and the sample are moved with respect to each other so that the emitted photons in the observer (sample) frame are 'detuned' by $\Delta\omega$ due to the Doppler effect. The energy of the photon emitted by the source moving with velocity v is given as[7]

$$\omega_{\mathrm{v}} = \omega_0 \sqrt{\frac{1 + \mathrm{v}/c}{1 - \mathrm{v}/c}} \tag{2.35}$$

where ω_0 is the energy of the photon emitted by the source at rest. For $\mathrm{v}/c \ll 1$,

$$\omega_{\mathrm{v}} \approx \omega_0 \left(1 \pm \frac{\mathrm{v}}{c}\right) \tag{2.36}$$

$$\text{and} \qquad \Delta\omega = \omega_{\mathrm{v}} - \omega_0 = \pm \frac{\mathrm{v}}{c} \omega_0. \tag{2.37}$$

The Doppler-shifted photons are thus used to 'scan' the sample at energies around the nuclear transitions. Since the energy differences between hyperfine nuclear levels are in fractions of μeV, the source is typically moved at a velocity of a few mm s^{-1}. The transmitted intensity from the sample is then plotted against the velocity of the source and absorption peaks are seen at the detunings corresponding to the resonance energies. Conventional Mössbauer spectroscopy is quite established and finds applications across all natural sciences. Most notably, it has used to demonstrate the gravitational red-shift

[7] Here, we neglect the second-order Doppler shift ($\propto \mathrm{v}^2$), a relativistic correction to the first-order Doppler shift formula, when the velocity v of the nucleus approaches relativistic speeds. This usually happens at higher temperatures, around a few hundred kelvin, due to thermal motion of the atoms.

[CSW60]. Unlike NRS, it directly measures nuclear transitions in a sample with incident photon energies. However, it has several drawbacks:

- Producing radioactive sources for Mössbauer spectroscopy can be challenging. NRS utilizes synchrotron radiation as a source, offering high-energy tunability and a broad spectrum, enabling access to a diverse range of Mössbauer nuclei. This advancement has significantly broadened the scope of possible materials that can be examined.
- Compared to the radiation emitted from a radioactive source, synchrotron radiation is highly brilliant and focused. As a result, measurement times for nanostructured samples such as thin films with a low amount of resonant material are significantly reduced, from several days to just a few hours or even minutes.
- Radioactive sources emit incoherent radiation and the corresponding Mössbauer spectra are therefore incoherent absorption measurements. On the contrary, synchrotron radiation is coherent, with a pulsed time structure. This allows time-resolved studies of coherent phenomena due to the nuclear excitations and dynamic processes in materials
- Due to the high degree of polarization of the incident synchrotron radiation. the NRS signal is more sensitive to the relative strengths of the frequency components of the resonance and the slight variations in the hyperfine interaction parameters.
- NRS is also more sensitive to the thickness of the sample. While the effect of increasing thickness in the Mössbauer transmission spectrum is only observed as a broadening of the peaks, the NRS time spectra of thick samples exhibit dynamical beats.
- The highly polarized and brilliant synchrotron radiation allows access to a wider range of experimental geometries not possible in the conventional Mössbauer spectroscopy due to low counts, e.g., nuclear Bragg diffraction [Rüf+91].

On the other hand, the most obvious drawback of NRS is that it probes the magnetic and electronic structure of Mössbauer nuclei as beating patterns in time (Sec. 2.4.3). As the complexity of the sample structure increases, the analysis of the detected time response $[I(t)]$ gets more difficult. This task is often performed with extensive theoretical

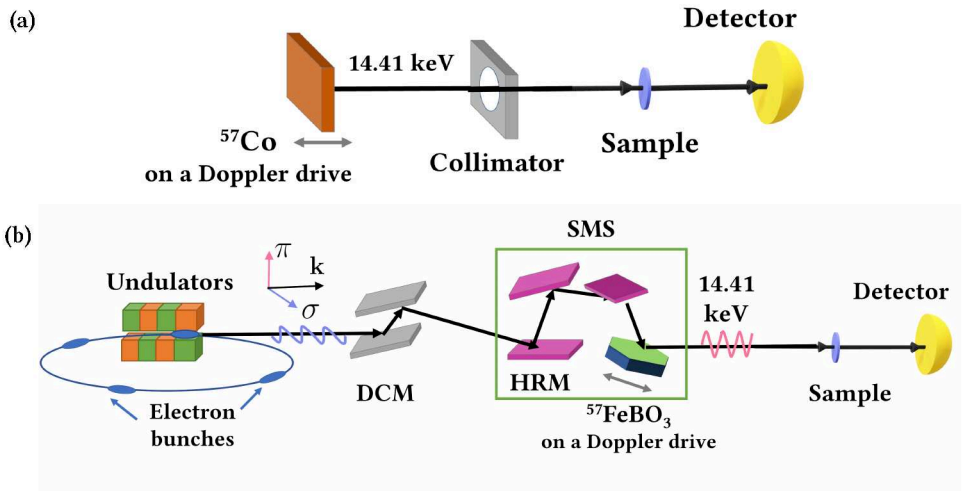

Figure 2.10.: (a) Mössbauer spectroscopy of a sample with ^{57}**Fe** nuclei. The ^{57}**Co** source emits incoherent radiation of 14.41 keV which is then collimated and incident on the sample. The detector records the number of photons at each Doppler detuning of the source relative to the sample. (b) Synchrotron Mössbauer spectroscopy of a sample with ^{57}**Fe** nuclei (at ESRF, Grenoble, France). A silicon double crystal monochromator (DCM) and a high resolution monochromator (HRM) narrows the bandwidth of the synchrotron beam to a small range of few meV around 14.41 neV. The beam is then incident on the $^{57}FeBO_3$ crystal which gives a pure nuclear reflected π-polarized beam at 14.41 keV with a bandwidth of 3–6 Γ. The crystal is kept inside a heating furnace and mounted on a Doppler drive. The detector records the number of photons at each Doppler detuning of the crystal relative to the sample.

modeling using specific software tools like CONUSS [Stu00] and NEXUS [Boc23]. The interpretation of the time spectra would be greatly simplified if its Fourier counterpart in the energy domain [$I(\omega)$] could be obtained simultaneously.

One way to get such an energy spectrum for ^{57}**Fe** is to use a synchrotron Mössbauer source (SMS) [Smi+97] which uses pure nuclear Bragg reflections from a ^{57}**Fe**BO_3 crystal (see Fig. 2.10(b)). In this regard, there exist some experimental challenges. A good source requires a high-quality crystal, kept at good temperature stability. To achieve a high energy resolution, the reflection is tuned to a narrow energy bandwidth, which is typically 3–6 Γ. However, the more spectrally narrow the bandwidth, the smaller the photon flux on the sample. Getting both a high resolution and high intensity in some experiments becomes very difficult [YC22]. Also, as shown in Fig. 2.11, the motion of the crystal on the Doppler drive can lead to the illumination of different spots on the crystal, causing differences in the reflected beam due to crystal imperfections.

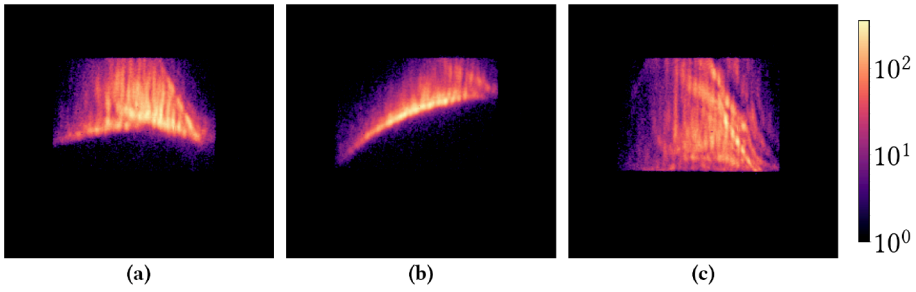

Figure 2.11.: The two-dimensional profile of the reflected beam at the same angle of incidence from different resonant spots (a), (b), (c) on the ^{57}**Fe**BO_3 crystal used in the synchrotron Mössbauer source at ESRF. At all three spots, the beam profile does not look like a Gaussian resembling a single Bragg reflection. The intensities have been plotted on a log scale. The data was collected in a beamtime in May 2023, courtesy Leon Merten Lohse *et al.*.

As opposed to countering the experimental difficulties in these energy-domain measurement methods, one can think of mathematically reconstructing the energy spectrum from the time response obtained from the NRS. As we will see in the next section, this is less straightforward than a simple Fourier transform. One needs to tackle the 'phase problem'.

2.6. The phase problem in NRS

In nuclear resonant scattering experiments, avalanche photodiodes (APDs) are used to detect the scattered photons by converting them into electron currents. They measure the photon counts, which are proportional to the magnitude squared (intensity) of the complex electromagnetic field averaged over the detector time resolution (typically from 0.3 - 1 ns). There is no way to detect the X-ray field oscillations on a time scale of $1/\nu$, where $\nu > 10^{19}$ Hz at 14.41 keV. Consequently, the phase information of the X-ray field is lost. This 'phase problem' exists not only for NRS but also Mössbauer spectrocopy and SMS measurements.

While the detector can only measure changes in the intensity, the phase of the X-ray field is inevitably changed as it passes through the sample. To completely characterize the quantum processes in the sample, both the magnitude and relative phase of the scattering must be known. From Eq. (2.26), we can write the scattered field at the detector as[8]

$$E(t) = \frac{E_0}{2\pi} \int_{-\infty}^{\infty} \mathrm{e}^{\mathrm{i}(\omega t - Knz)}\, d\omega \tag{2.38}$$

$$= \frac{E_0}{2\pi} \int_{-\infty}^{\infty} \mathrm{e}^{-\mathrm{i}\chi_0 Kz/2} \cdot \mathrm{e}^{\mathrm{i}\omega t}\, d\omega \tag{2.39}$$

$$= E_0 \cdot \mathcal{F}\{\hat{O}(\omega)\} \tag{2.40}$$

$$= \mathcal{F}\{\hat{E}(\omega)\}. \tag{2.41}$$

Here, E_0 is a constant given by Eq. (2.25), $\mathcal{F}$ denotes the Fourier transform while $\hat{O}(\omega) = \mathrm{e}^{-i\chi_0(\omega)Kz/2}$ is the response of the object scattering the incident X-rays as a function of energy. The scattering response is complex-valued and is given as

$$\hat{O}(\omega) = \left|\hat{O}(\omega)\right| \mathrm{e}^{i\phi(\omega)} \tag{2.42}$$

with a magnitude part $\left|\hat{O}(\omega)\right|$ and a phase part $\phi(\omega)$. The intensity of the wave field scattered by the object in time is given as

$$I(t) = |E(t)|^2, \tag{2.43}$$

[8] we drop the subscript 's' in $E_s(t)$ for improved readability

where the scattered field $E(t)$ is also complex and has an amplitude $E(t)$ and a phase $\eta(t)$ such that

$$E(t) = |E(t)|\, \mathrm{e}^{i\eta(t)} \tag{2.44}$$

The scattered field in time and the response of the object in energy are related to each other via a Fourier transform. In the one-dimensional, continuous setting, the phase retrieval problem can be stated as follows:

P 1.0 : The phase problem in NRS

Find a function $\hat{E} : \mathbb{R} \to \mathbb{C}$ from $\left|\mathcal{F}\{\hat{E}\}\right|$ where $\mathcal{F}$ denotes the Fourier transform of $\hat{E}$.

Points to Note:

- Since we are not interested in the global scaling factor for the intensity (E_0), the problem to retrieve $\hat{E}(\omega)$ or $\hat{O}(\omega)$ is equivalent.

- **P 1.0** is called a phase problem because, generally, one cannot uniquely obtain the object $\hat{E}(\omega)$ from the measured intensity $I(t)$ without the phase information. By retrieving the phase $\phi(\omega)$ or $\eta(t)$, one can perform the inversion $\hat{E}(\omega) = \mathcal{F}^{-1}\{\sqrt{I(t)}\mathrm{e}^{\mathrm{i}\eta(t)}\}$ to recover the scattering response of the object.

- The measured intensity is related to the autocorrelation of the object by the Wiener-Khinchin theorem, i.e.,

$$\mathcal{F}^{-1}\{I(t)\} = \int_0^\infty I(t)\mathrm{e}^{-\mathrm{i}\omega t}\, dt \tag{2.45}$$

$$= \int_0^\infty |E(t)|^2\, \mathrm{e}^{-\mathrm{i}\omega t}\, dt \tag{2.46}$$

$$= (\hat{E} \star \hat{E})(\omega) \tag{2.47}$$

  where $\star$ denotes the autocorrelation. Therefore, knowing the object's Fourier intensity is equivalent to knowing its autocorrelation.

Challenges in 1-D phase retrieval

The continuous phase retrieval problem in Sec. 2.6 is a one-dimensional inverse problem. With only a single $I(t)$ measurement, it is *underdetermined*. Since the phase $\eta(t)$ is lost, the problem lies in finding a good guessing strategy for it, which is an impossible task from a single $I(t)$ measurement. Unless we have some prior knowledge about the complex object, any choice of $\eta(t)$ will generate a valid solution that can be far from the original $\hat{E}(\omega)$. To further constrain the problem, it is necessary to impose additional conditions on $\hat{E}$, e.g., $\hat{E}$ having compact support, i.e., the area outside of which the field is known to be identically zero, and having sparsity [BP17]. However, the continuous one-dimensional phase problem can still have an infinite number of solutions even under the said conditions [Wal63] and is unstable [GKR20].

Let us focus on the discrete version of the phase problem in the subsequent discussion. We consider the one-dimensional complex object function $(\hat{E}[n])_{n\in\mathbb{Z}}$ defined on an energy grid discretized with resolution $\Delta\omega$. The object function has a finite support of length $N \in \mathbb{N}$ such that $\hat{E}[n] = 0$ for $n < 0$ and $n \geq N$.
On discretizing Eq. (2.38), we get the expression for the corresponding complex field of the object in the time domain

$$E[q] = \sum_{n=0}^{N-1} \hat{E}[n] \mathrm{e}^{-\mathrm{i}nq\Delta\omega\Delta t} \tag{2.48}$$

where Δt is the time resolution of the detector.

Since the time and energy domains in nuclear resonant scattering are connected via a Fourier transform, the object in the energy domain and the field at the detector are also connected via the (discrete) Fourier transform, i.e.,

$$E[q] = \sum_{n=0}^{N-1} \hat{E}[n] \mathrm{e}^{-\mathrm{i}nq\frac{2\pi}{N}} \tag{2.49}$$

Therefore, the resolution of the object grid and the detector are connected as

$$\Delta\omega\Delta t = \frac{2\pi}{N}$$

The intensity of the scattered radiation from the object is given as $I[q] = |E[q]|^2$. It is measured at N time points at the detector such that $q = 0, 1, 2, \cdots N-1$ i.e. the intensity vector $(I[q])_{q=0}^{N-1}$ is given.

There are some properties of the object that are irretrievably lost when the phase is lost because the discrete phase retrieval problem has trivial ambiguities, such that

1. the rotated object $(\mathrm{e}^{i\alpha}\hat{E}[n])$; $\alpha \in [-\pi, \pi)$,
2. the translated object $(\hat{E}[n + n_0])$; $n_0 \in \mathbb{Z}$, and
3. the reflected object $(\hat{E}[-n])$

all map to the same intensity I. Hence, information about the absolute position, inversion at the origin, and a global phase factor of $\hat{E}$ cannot be recovered, although this is usually of little practical significance. Complex objects obtained by any combination of these operations are considered equivalent, and in our case, it is good enough if any equivalent objects are recovered. This is because the phase of the incoming photon is not known at all.

The difficult task is to tackle the non-trivial ambiguities of the phase retrieval problem. These can be described by zeros and poles of the Z-transform of the autocorrelation function in the energy domain. The autocorrelation signal in the time domain is given as

$$c[q] = \sum_{l \in \mathbb{Z}} \overline{E[q]}\hat{E}[q + l]. \tag{2.50}$$

Here, the overline '$-$' symbol indicates complex conjugation. For complex objects, $c[q]$ is conjugate-symmetric i.e. $c[q] = \overline{c[-q]}$. For an object of support N, the autocorrelation signal $c[q]$ is supported on $m = -N + 1, \cdots, N - 1$. The corresponding autocorrelation function in the energy domain is given as $(\hat{C}[n])_{n \in \mathbb{Z}}$, where

$$\hat{C}[n] = \sum_{q=-N+1}^{N-1} c[q]\mathrm{e}^{inq\frac{2\pi}{N}}. \tag{2.51}$$

The autocorrelation function $\hat{C}$ is thus a non-negative trigonometric polynomial of degree $N - 1$. It is shown in Ref. [BP15] that for the one-dimensional discrete phase retrieval problem from the given real, non-negative autocorrelation polynomial $\hat{C}$, the

number of nontrivial solutions may vary from 1 up to 2^{N-2}. It is also shown that the number of ambiguities does not reduce even with the assumption that $\hat{E}$ is real and non-negative. The problem is thus highly *ill-posed* in one dimension.

In phase retrieval problems for crystallography or coherent diffraction imaging, the natural objects of interest correspond to two or three-dimensional fields. In these higher dimensional cases, the discrete phase retrieval problem rarely presents non-trivial ambiguities, and almost every object is uniquely identified by its Fourier magnitude up to trivial ambiguities [BBE17]. This is because, unlike single-variable polynomials, multi-dimensional polynomials are generally not factorable [HM82]. The set of factorable multi-dimensional polynomials is extremely small so that almost all polynomials in two or more variables are irreducible. Therefore, the multidimensional autocorrelation polynomial cannot be reduced to linear factors corresponding to zeros and poles - making the phase retrieval problem *uniquely* solvable [9].

Another way to think about it is that higher-dimensional measurements enhance the amount of information about the object field encoded in its autocorrelation, making phase retrieval easier. It has been shown in Ref. [KEO17] that the two-dimensional phase retrieval problem corresponds to a one-dimensional problem with additional constraints, which almost always guarantee uniqueness.

[9] In some cases, such as crystallography, the autocorrelation can be factorized into reducible polynomials of small degree [Wal63]. This makes the phase retrieval non-unique but with fewer ambiguities than the one-dimensional case.

3. Ptychography

Why not just build an interferometer?

-Me, at the start of this project,
probably.

The traditional method to measure the phase response of an object is to modulate the path difference between two coherent beams passing through the object and a reference/probe. Such a scheme was proposed by Sturhahn *et al.* [Stu01] for nuclear resonant scattering experiments and is shown in Fig. 3.1. Let us denote the scattering response of the object and the probe with time as $O(t)$ and $P(t)$, respectively. As described in Sec. 2.6, the scattered field is a complex quantity. Therefore, we denote $O(t) = |O(t)|\, e^{i\eta_O(t)}$ and $P(t) = |P(t)|\, e^{i\eta_P(t)}$.
In Figs. 3.1(a) and 3.1(b), the time spectrum of the object $|O(t)|^2$ and the probe $|P(t)|^2$ are measured, respectively. Figure 3.1(c) corresponds to measuring the intensity of the interference between the object and the probe,

$$|O(t) + P(t)|^2 = |O(t)|^2 + |P(t)|^2 + 2\,|P(t)O(t)| \cos\left(\eta_O - \eta_P\right). \tag{3.1}$$

To also get information about the sign of the phase, in Fig. 3.1(d), the interference is measured again but with introducing an additional phase shift of e.g. $\pi/2$ such that the intensity is

$$|O(t) + iP(t)|^2 = |O(t)|^2 + |P(t)|^2 + 2\,|P(t)O(t)| \cos\left(\eta_O - \eta_P - \pi/2\right). \tag{3.2}$$

If the magnitude $|P(t)|$ and phase $\eta_P(t)$ of the probe field are known, the four time-domain measurements - $|O(t)|^2$, $|P(t)|^2$, $|O(t) + P(t)|^2$ and $|O(t) + iP(t)|^2$ - can be used to solve Eqs. (3.1) and (3.2). One can thus reconstruct the object's phase and, subse-

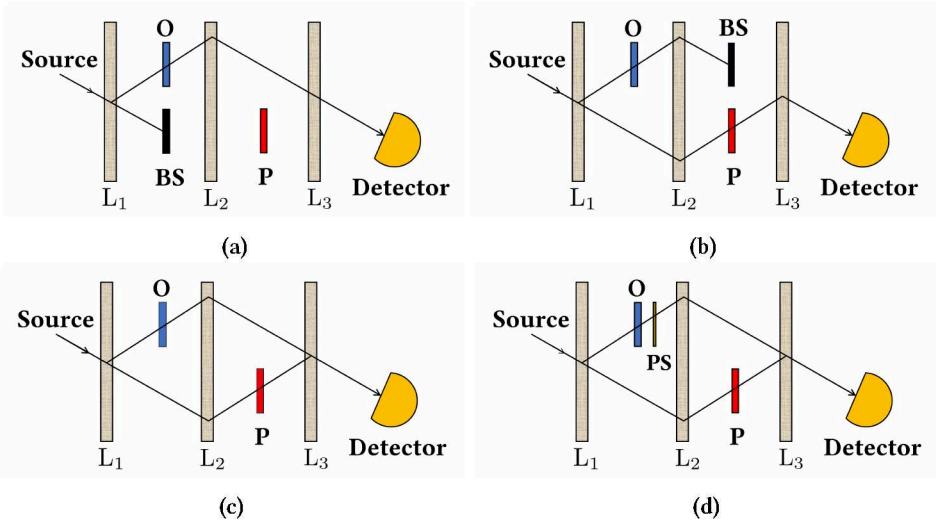

Figure 3.1.: Time domain interferometry to measure the phase of an object. **O**, **P**, **BS** and **PS** label the object, the probe, a beam-stop and a phase-shifter, respectively. The X-ray beam comes from the source and hits the different lamellas (L_1, L_2, L_3) of the LLL-interferometer and the elements in its path. The corresponding intensities in each case are measured with respect to time at the detector. The figure is adapted from [Stu01]. (a) Only the X-rays passing through the object are detected. (b) Only the X-rays passing through the probe are detected. (c) The X-rays passing through both the object and the probe are interfered with and detected. (d) The X-ray beam passing through the object is shifted in phase by **PS** and then its interference with the probe beam is detected.

quently, its energy domain response.

To build the interferometer, however, the two path lengths must be stabilized at the sub-Ångström level to match the wavelengths corresponding to the nuclear resonance energies (~10 keV). Also, since almost no material has an index of refraction that differs from unity by more than 10^{-5}, the optical elements used in the hard X-ray regime are designed based on dynamical diffraction with perfect single crystals made of silicon or germanium[1]. X-ray optics composed of single crystals are complicated and expensive to fabricate, in addition to experiencing 'diffraction loss' or 'glitches'[2]. The crystal interferometer must also be mounted without stress, external vibrations must be suppressed, and the surrounding temperature must be stable and homogeneous. Additionally, the proposed scheme requires the object to be kept between two lamellas of the interferometer - which is impractical in most experiments.

Similar problems are encountered when manufacturing good-quality refractive lenses (with low magnification and high numerical aperture) for hard X-ray diffraction imaging. Zone plates are the predominant lensing technology in the soft X-ray regime - but constructing them requires extreme manufacturing precision - otherwise, aberrations or phase errors are introduced in the diffracted radiation before it re-interferes to form the image. Consequently, alternative measurement schemes that couple with computer algorithms to tackle the phase problem have recently become prominent in the X-ray imaging community. Ptychography is one of these 'computational imaging' methods.[3] As shown in Fig. 3.2, it is based on replacing traditional lens optics with an encoder-decoder scheme [RM19].

[1] The triple Laue or LLL X-ray interferometer [BH65], which is the X-ray equivalent of the Mach-Zehnder interferometer, comprises three thin crystal lamellas (LLL) at which the X-rays are split up, deflected, and then superposed for interference via Bragg reflection. Because the wavelength of the X-rays and the lattice parameter are of comparable order, the splitting angles are relatively large, and the interference pattern reacts strongly to the relative movements of the crystal lamellas.

[2] At some energy of the X-rays, some crystalline planes satisfy diffraction conditions and part of the beam is diffracted in another direction leading to drop of intensity in the primary beam. The probability of observing such 'parasitic' diffraction is rather high, especially for hard X-rays. [Kli+22].

[3] It should be noted that ptychography is not restricted to the use of X-rays - coherent visible light can also be utilized [FR04].

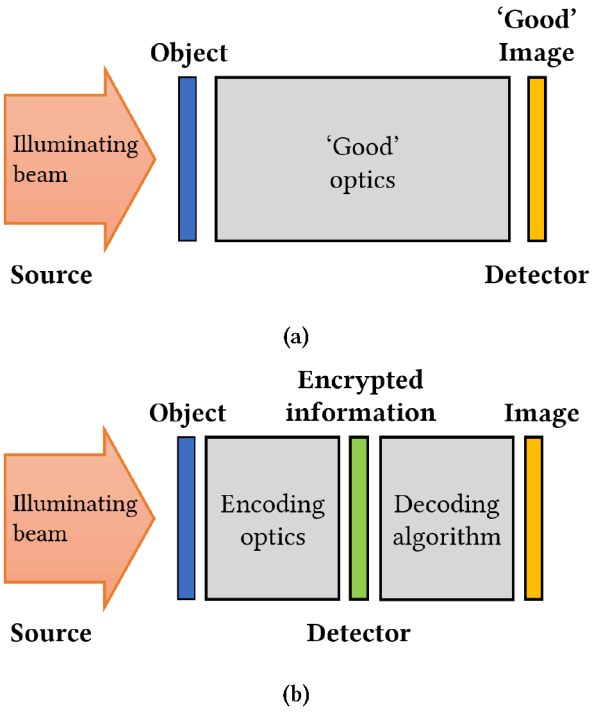

Figure 3.2.: The different imaging paradigms. (a) A conventional imaging setup relies solely on maufacturing high-quality optics to get a high-resolution image. (b) A computational imaging setup is a tight integration of the detection system and the computation to form the images of interest. Optics in the experiment are used to encrypt the information in the object and forward it to the detector. The measurement is then decoded to reconstruct the final image. The quality of the final image can be improved by algorithmic developments.

3.1. Ptychography for X-ray imaging

Crystallographers in the twentieth century used X-ray diffraction patterns to investigate periodic structures on the atomic scale. If the phase of the diffraction could also be captured alongside the intensity, the diffraction pattern could be inverse Fourier transformed to reveal the crystal structure. Hoppe and Hegerl realized that rather than trying to address this 'phase problem' using only one diffraction pattern[4], it is easier to record multiple diffraction patterns for different illumination conditions and use them to reduce the ambiguities in the problem. In 1969, they demonstrated a method to determine the phase of a crystal's Bragg reflections from their convolution with the Fourier transform of the illumination function [Hop69], which they later named ptychography.

As described in Refs. [GT21] and [Pfe17], there exist many modern variants of the ptychographic phase retrieval scheme. Nevertheless, one can generally lay down the following defining properties [RM19]:

(a) There exists an optical system, i.e. a 'probe' element, that allows for illuminating localized regions of the object and defines the illumination function.

(b) It must be possible to move the object with respect to the illuminating beam from the probe.

(c) The illumination on the object is (sufficiently) coherent.

(d) The radiation scattered from the probe-object setup creates an interference pattern (usually - but not always - a diffraction pattern) on the optical domain of the detector. The detector only measures the intensity of the scattered radiation.

(e) The probe or the object is moved to at least two position offsets such that the detector collects at least two interference patterns.

(f) The measured interference patterns can be put into a computational algorithm to estimate the phase and amplitude changes that have been imposed on the incident radiation by the presence of the object, enabling one to reconstruct an 'image' of the object.

[4] Algorithms to do phase retrieval from a single diffraction pattern existed (e.g. Gerchberg-Saxton [Ger72], Hybrid input-output [Fie78]), but were not feasible with the computational power at the time.

Looking back at Fig. 3.2(b) and making comparisons, the encoder block for ptychography is the measurement scheme mentioned in points (a) to (e). The decoder block is comprised of the computational algorithm in (f) that extracts the phase of the object from the measured interference patterns.

Hoppe's ptychography ansatz, initially designed for periodic objects, can also be applied to image non-periodic objects of arbitrary size if the change in illumination involves a simple shift of the probe relative to the object. This principle is employed in coherent diffraction imaging (CDI), a prominent X-ray microscopy technique using coherent radiation. Unlike conventional lens-based imaging where the numerical aperture of the lens limits the angular resolution, CDI utilizes a 'lensless' setup to directly detect the intensity of the diffraction pattern of an object. However, CDI faces challenges due to phase loss in measurements, especially for complex objects (i.e. which introduces both amplitude and phase changes to the illuminating beam), affecting algorithm convergence. Of course, non-absorbing objects (e.g. biological cells) which only introduce phase shifts in the radiation cannot be imaged by the technique either. Ptychography addresses this phase problem by enhancing the computational process through modified encoding optics and capturing object information with greater richness via multiple measurements.

3.1.1. The forward (encoder) model

The interaction between X-rays and matter leading to the contrast formation in CDI is also studied in the scattering theory framework. Like nuclear forward scattering[5], it is typically enough to use the refractive index to characterize the light-matter interaction. CDI is generally implemented as a 2-D method under the projection approximation, assuming that no multiple scattering occurs inside the object volume, and hence phase and intensity variations in the radiation at the object's exit surface arise only from its projected complex refractive index. The 3-D description of the object can then be replaced by a 2-D response function,

$$\hat{O}(x,y) = \mathrm{e}^{-\mathrm{i}(n(x,y)-1)K\Delta z} = \mathrm{e}^{\mathrm{i}\delta(x,y)K\Delta z} \cdot \mathrm{e}^{\beta(x,y)K\Delta z} \tag{3.3}$$

[5] See Sec. 2.3.

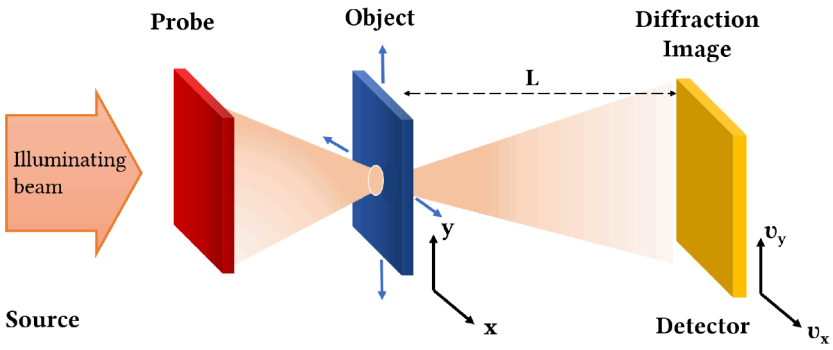

Figure 3.3.: A ptychography setup for CDI. The illuminating beam is focused by the probe onto the object and is then diffracted by the object onto the detector placed at a distance L which lies in the Fraunhofer (far-field) regime. The detector records the intensity of the diffraction pattern. The object is then moved transverse to the illuminating probe beam to collect diffraction patterns from different parts of the object.

where $n = 1 - \delta + i\beta$ is the complex refractive index of the object, K is the wave vector of the incident X-rays and Δz is the thickness of the object in the direction of X-ray propagation. The first multiplicative term in Eq. (3.3) forms the 'phase contrast' image while the second term forms the 'absorption contrast' image of the object.

Let us consider a simple setup for X-ray CDI with ptychography, as shown in Fig. 3.3. We assume the case of the propagation of light in a homogeneous medium, neglecting any polarization effects. A coherent illuminating beam passes through some focusing optics/aperture and is used as a 'probe' for the object. The 'probe' function is the 2-D profile of the focused beam's wave field. To also model the object as a 2-D function, we must ensure that the projection approximation is valid by keeping the object 'optically thin', i.e., the following condition must be fulfilled:

$$\Delta z < \frac{\Delta x \Delta y}{\lambda} \tag{3.4}$$

where Δz is the thickness of the object in the direction of X-ray propagation, and $(\Delta x, \Delta y)$ is the resolution of the object reconstruction[6].

The 2-D probe and object response functions are modeled as $(\hat{P}[n_x, n_y])_{n_{(x,y)} \in \mathbb{N}}$ and

[6]A more refined object thickness limit for ptychography was tested in Ref. [Tsa+16] using numerical

$(\hat{O}[n_x, n_y])_{n_{(x,y)} \in \mathbb{N}}$ on a discrete grid of spatial resolution $(\Delta x, \Delta y)$ where $0 \leq n_x < N_x$ and $0 \leq n_y < N_y$. This discretization is done such that the number of steps in the spatial grid matches the number of pixels $(N_x \times N_y)$ at the detector. For each $j-$th measurement, the probe is shifted by $(m_x^{(j)}, m_y^{(j)})$ pixels to a new position with respect to the object by moving the object transverse to the beam direction such that

$$\hat{P}^{(j)}\left[n_x, n_y\right] = \hat{P}\left[n_x - m_x^{(j)}, n_y - m_y^{(j)}\right],$$

as is indicated by the blue arrows in Fig. 3.3.

The combined response of the probe and the object can be modeled by the complex element-wise product (Hadamard product) of the two responses, generating an exit wavefield

$$\hat{Z}^{(j)} = \hat{P}^{(j)} \cdot \hat{O}. \tag{3.5}$$

The exit wave from the object propagates to the Fraunhofer diffraction domain at the far-field, where it is recorded on a detector with $N_x \times N_y$ pixels. The $j-$th measurement, i.e., the intensity of the detected diffraction pattern $(I^{(j)}\left[q_x, q_y\right])^{N_x \times N_y}$ is thus discretized in the reciprocal space with resolution $(\Delta v_x, \Delta v_y)$. Fraunhofer propagation of X-rays can be described by the Fourier transform up to a constant phase pre-factor [Goo05]. The intensity can thus be written with the help of the 2-D discrete Fourier transform,

$$I^{(j)}\left[q_x, q_y\right] = \left|\mathbb{F}(\hat{Z}^{(j)}[n_x, n_y])\right|^2 \tag{3.6}$$

$$= \left|\sum_{n_x, n_y} \hat{Z}^{(j)}\left[n_x, n_y\right] \mathrm{e}^{-\mathrm{i}2\pi\left(\frac{q_x n_x}{N_x} + \frac{q_y n_y}{N_y}\right)}\right|^2. \tag{3.7}$$

The above equation thus gives us the forward (encoder) model of the ptychographic CDI experiment. Now that the encoder model is ready, the second half of the problem is to invert it.

experiments and is given as $\Delta z \leq 5.2\frac{\Delta x \Delta y}{\lambda}$.

3.1.2. The inversion (decoding) scheme

The collection of intensity measurements for different 'j' probe positions is referred to as a *ptychogram* [GT21]. It contains information on the phase of the object. For a 2-D object, the ptychogram is a 4-D data set, with the four dimensions being the real space dimensions (x, y) of the object and the reciprocal space dimensions (v_x, v_y) of the measured diffraction patterns. In 1992, Bates and Rodenburg [RB92] showed that a ptychogram can be continuously modeled as a convolution of the Wigner distributions of the probe and the object. They proposed a direct, linear inversion algorithm called the Wigner distribution deconvolution method (WDDM) to extract the complex object from the ptychogram using the knowledge of the probe. The drawback of the method is that to discretize the model one needs to satisfy the Nyquist sampling theorem, i.e., the probe needs to be moved in scanning steps which had to be at least as small as the sought resolution of the reconstruction.

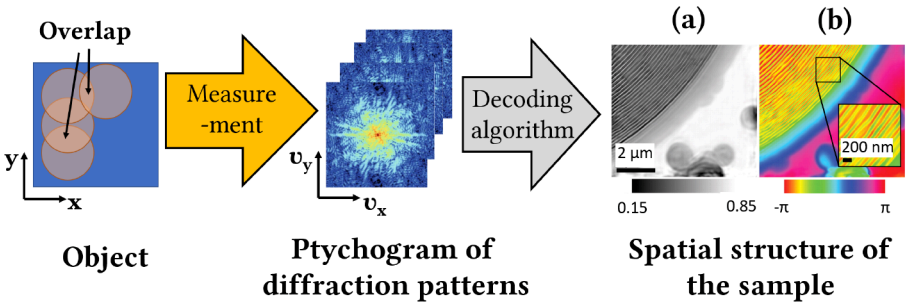

Figure 3.4.: We adopt the above diagram with experimental results in [Thi+08] where CDI ptychography with 6.8 keV X-rays was used alongside a decoding algorithm to reconstruct the (a) amplitude and (b) phase of the object. The reconstruction shows details of the nanostructures in the object with a resolution $\sim$ 20 nm which is several times smaller than the size of the probe beam (about 300 nm).

When the above sampling condition is not satisfied, there exist non-linear approaches to solve the problem. For each j-th probe position, one can compare the modeled intensities to the measured intensities in the ptychogram, and refine the unknown complex object until they match. This is the approach taken by the iterative class of algorithms, particularly all variants of the ptychographic iterative engine (PIE) [FR04], which is the

widely regarded standard algorithm of choice in the X-ray imaging community. As shown in Fig. 3.4, the sampling for these methods can be done with step sizes much larger than the WDDM method as long as the position offsets are chosen such that there is some degree of overlap between the adjacent illuminated areas. The resulting ptychogram can be used to recover the complete structural information (including the phase) of the object since the structure of the unknown object function $\hat{O}$ gets expressed in the multiple measurements. The search space for an object solution that is consistent with the multiple measurements with the exactly known illumination positions and their area of overlap is drastically reduced.

3.1.3. Solution to the phase problem

By following the described encoder-decoder scheme, CDI ptychography allows for the reconstruction of both the magnitude and the phase of the object, thus solving the phase problem. This is important to improve the resolution of our 'lensless' X-ray microscope. Many CDI ptychography setups technically do involve lenses, especially as the probe element. It is still called 'lensless' because the resolution of the scheme is not limited by the aperture of the focusing element or the pinhole that is used as the probe. The real space resolution (assuming that the wave field $\hat{Z}$ is fully coherent) is inversely proportional to the maximum diffraction angles (θ_x, θ_y) measured by the detector in the x and y directions,

$$(\Delta x, \Delta y) = \left(\frac{\lambda}{2 \sin \theta_x}, \frac{\lambda}{2 \sin \theta_y} \right). \tag{3.8}$$

Here

$$(\theta_x, \theta_y) = \left(\frac{\lambda}{2 \sin \left(\arctan \left(N_x p_x / 2L \right) \right)}, \frac{\lambda}{2 \sin \left(\arctan \left(N_y p_y / 2L \right) \right)} \right) \tag{3.9}$$

where L denotes the distance of the object from the detector and (p_x, p_y) denote the detector pixel sizes. For the large L (i.e. Fraunhofer) limit, the small angle (paraxial) approximation is valid, and $\tan \theta \approx \sin \theta$. The resolution of the reconstructed object is thus given as

$$(\Delta x, \Delta y) \approx \left(\frac{\lambda}{2\theta_x}, \frac{\lambda}{2\theta_y} \right) = \left(\frac{\lambda L}{N_x p_x}, \frac{\lambda L}{N_y p_y} \right). \tag{3.10}$$

and is inversely proportional to the size of the detector. By solving the phase problem, the resolution of ptychographic X-ray imaging routinely improves upon the lens-based

X-ray imaging with the development of better detectors, model refinements, cleverer algorithms and more computational power.

3.2. Ptychography for NRS

In CDI ptychography, we reconstruct $\hat{O}(x, y)$ and thereby the complex index of refraction n of a thin object in the spatial domain as

$$\hat{O}(x, y) = \mathrm{e}^{-\mathrm{i}(n(x,y)-1)K\Delta z} = \mathrm{e}^{\mathrm{i}\delta(x,y)K\Delta z} \cdot \mathrm{e}^{\beta(x,y)K\Delta z}. \tag{3.11}$$

The retrieved phase contrast δ and absorption β images are intrinsic properties that can be used to reconstruct the structural information in the object. The real space where the CDI object resides and the reciprocal space where the detected diffraction patterns reside are Fourier connected. In nuclear resonant scattering, we have an analogous Fourier relationship between the scattering response of the object in the energy domain and the detected temporal decay patterns, as shown in Fig. 3.5. The scattering response of the object can be related to its susceptibility as

$$\hat{O}(\omega) = \mathrm{e}^{-\mathrm{i}(n(\omega)-1)Kz} = \mathrm{e}^{-\mathrm{i}\chi_0(\omega)Kz/2}. \tag{3.12}$$

As given in Eq. (2.22), the complex susceptibility term χ_0 contains both the magnitude and phase of the nuclear transitions in the object - or the full description of the nuclear exciton-polariton. Reconstructing the complex $\hat{O}$, and in turn χ_0, would mean we can reconstruct both the Mössbauer energy spectrum and the temporal decay pattern of the object.

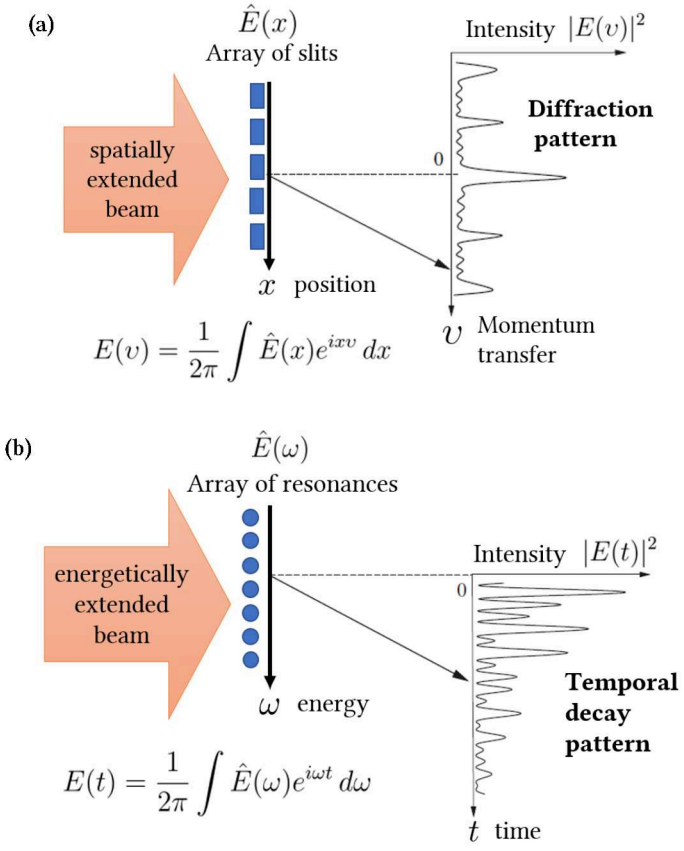

Figure 3.5.: The analogy between CDI and NRS. In the CDI measurement of a one-dimensional object in real space (e.g. an arrangement of slits), we detect its diffraction pattern in the reciprocal space. In a nuclear resonant scattering measurement of an object, its hyperfine structure is detected as a beat pattern when the excited nuclei decay with time. The figure is adapted from [Röh05].

Conjecture: *If ptychography works between the real and reciprocal space, is it possible to do ptychography in time and energy? If yes, then what kind of probe is required?*

For CDI, the probe is typically a lens/aperture that focuses the illumination to a spot on the object. The point spread function and the modulation transfer function are used to describe the properties of the lens. The point spread function describes the diffraction spread of an infinitely small point source as it passes through the lens and reaches the object. The modulation transfer function of a lens is given by its ability to transfer modulation/contrast[7] from the object to the image and is given as a function of spatial frequency.
If our CDI probe is a perfect lens (i.e. free from any aberrations) or a uniformly illuminated circular aperture, the probe function is described by the 'Airy disk' diffraction pattern, as shown in Fig. 3.6. The point spread function (PSF) of an Airy disk is given as [Gre04]

$$\mathrm{PSF} = 4\left|\frac{J_1\left(\frac{2\pi a\sqrt{x^2+y^2}}{\lambda S}\right)}{\frac{2\pi a\sqrt{x^2+y^2}}{\lambda S}}\right|^2, \tag{3.13}$$

where J_1 is the Bessel function of the first order, a is the radius of the aperture/lens, S is the distance between the probe and the illuminated object and λ is the wavelength of the illuminating light. If we plot it along one spatial dimension, the PSF of the diffraction limited probe can be approximated by a Gaussian function. The cutoff spatial frequency where the contrast reaches zero is $2 \cdot \mathrm{NA}/\lambda$, where NA is the numerical aperture of the lens. For NRS, we need a probe that confines the illuminating beam to an energy range comparable to the hyperfine response of the object. An ideal "lens" in this case would then be a sample with a single-line nuclear resonant scattering response i.e. a "clean" hyperfine structure with no splitting of the excited or ground state levels due to magnetic dipole or electric quadrupole interactions. For example, a stainless steel foil with

[7] The contrast or modulation transfer function can be defined as $\mathrm{MTF} = \frac{I_{\max} + I_{\min}}{I_{\max} - I_{\min}}$ where $I_{\max}$ is the maximum intensity and $I_{\max}$ is the minimum intensity in the pattern.

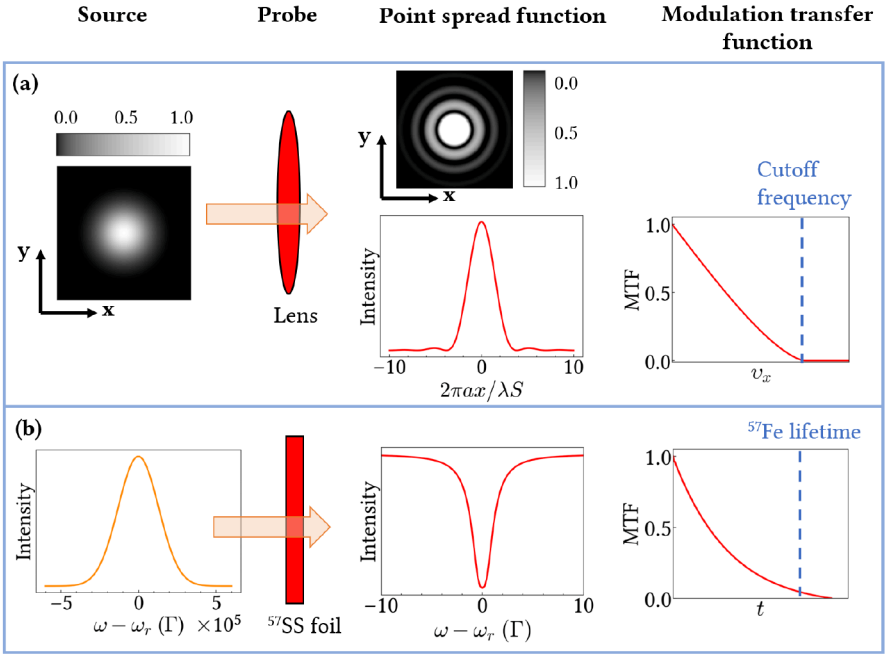

Figure 3.6.: The point spread function and modulation transfer function (MTF) of an ideal circular 'lens' for (a) coherent diffraction imaging (CDI) and (b) nuclear resonance scattering (NRS). In CDI experiments, the synchrotron source gives a beam with a roughly Gaussian spatial profile. The perfect lens or circular aperture will diffract each point in the beam into an Airy disk function in each spatial dimension. For NRS experiments at PETRA III, the synchrotron beam is monochromatized to a Gaussian with full-width half maximum of roughly 1 meV or 2×10^5 Γ. In this case, a nanometer thin paramagnetic stainless steel foil with ^{57}**Fe** nuclei and no quadrupole splitting would have a single Lorentzian-like response.

no quadrupole splitting would give a Lorentzian-like point spread function, as seen in Fig. 3.6. If the foil has low effective thickness, it will give an exponentially decaying modulation transfer function with time (with no dynamical beats). Such an ideal thin film could be directly used to raster scan the object in the energy domain to obtain a Mössbauer-like spectrum, with resolution determined by the energetic width of the Lorentzian[8]. Unfortunately, preparing such stainless steel nanofilms with a sharp, single-line energy response is difficult due to the electric field gradients at the boundaries of the constituent nanometer-sized crystallites [Sah+11]. Also, as the films get thinner, the photon count rates in the experiments become lower.

However, as we have discussed in the context of CDI, ptychography relaxes the requirement of an ideal probe in the setup. Therefore, to probe the object, we can take a stainless steel foil with some hyperfine structure, assuming we can model the transitions to good accuracy. In fact, to get sufficient 'overlap' between consecutive measurements (Fig. 3.7), a broader probe response in energy is even better. This can be achieved by increasing the thickness of the foil. We can then algorithmically deconvolve the complex probe response and the complex object response.

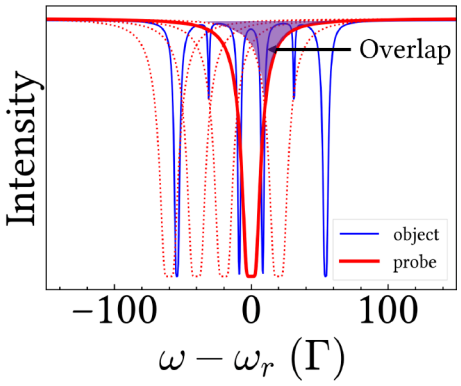

Figure 3.7.: Ptychographic scanning of a ^{57}**Fe** foil (object) using a thick stainless steel foil as a probe. Like CDI, the probe is moved with respect to the object, but in the energy domain. The different probe positions are indicated by dotted lines.

In the following sections, we discuss how we can use a two-sample system to do

[8]We assume that in this ideal case, there is no time windowing (see Sec. 5.4) of the data during measurement.

ptychography in the energy-time domain.

3.2.1. Nuclear resonant scattering by a two-sample system

Suppose we perform a nuclear resonant scattering experiment on two spatially separated samples. For simplicity, we assume that the incoming synchrotron radiation is linearly polarised in an arbitrary direction. The scattered radiation from the upstream sample P is further scattered by the downstream sample O before reaching the detector. From linear response theory, the combined scattering response of the two samples in time is given by the convolution of their respective responses, i.e.,

$$Z(t) = \int_{-\infty}^{\infty} O(t-t')H(t-t')P(t')H(t')\,dt' \tag{3.14}$$

$$= \int_{0}^{t} O(t-t')P(t')\,dt'. \tag{3.15}$$

The running time t' in the integral is the time of emission of radiation from P and the excitation in O. $H(t')$ is the unit step function, which is zero for a negative argument. Neglecting the electronic absorption, the expressions for $P(t)$ and $O(t)$ can be written in the shortened forms

$$P(t) = \delta(t) - R_P(t) \tag{3.16}$$

$$\text{and} \quad O(t) = \delta(t) - R_O(t) \tag{3.17}$$

where $R_P(t)$ and $R_O(t)$ contain the 'delayed' nuclear-scattered responses of the samples. As shown in Fig. 3.8, the scattering from the two samples is the coherent superposition of four optical paths i.e.

$$Z(t) = \int_{0}^{t} (\delta(t-t') - R_O(t-t'))(\delta(t') - R_P(t'))\,dt' \tag{3.18}$$

$$= \delta(t) + R_P(t) + R_O(t) + R_{PO}(t). \tag{3.19}$$

[9] Small compared to the bandwidth of the radiation input to the monochromator but large enough to excite all the allowed hyperfine nuclear transitions in the sample.

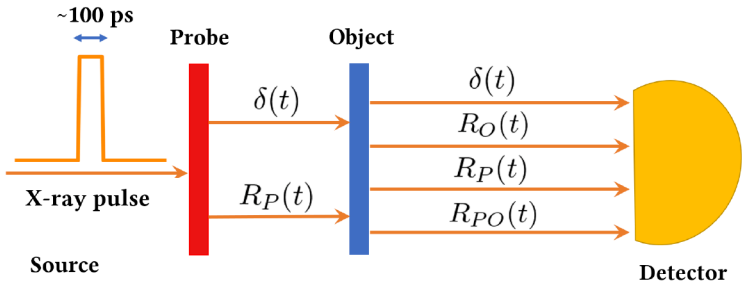

Figure 3.8.: Scattering of synchrotron radiation by a probe-object system. The synchrotron radiation arrives in short picosecond long pulses. The source is monochromatized to a small bandwidth of $\sim$ 1 meV around the nuclear resonance frequency ω_r[9]. The instantaneous $\delta(t)$ scattering channel is due to pure electronic scattering. The channels R_P and R_O correspond to nuclear scattering by only the sample P and O, respectively. The channel R_{PO} corresponds to the case where the nuclear scattered radiation from P is further scattered buy the nuclei in O.

The first term is for the events when the incident X-rays do not interact with the nuclei in the samples. The second term and third term refer to nuclear-scattering events from only one sample at a time. The last term is called the 'radiative coupling' term and is defined as

$$R_{PO}(t) = \int_0^t R_O(t - t')R_P(t')\,dt'. \tag{3.20}$$

It refers to the events where the X-rays get nuclear scattered from both samples. The spatially separated nuclei are coupled by the forward scattered radiation and act as one coherent ensemble. In Eq. (3.20), we omit the constant phase factor = $e^{i2\pi S/\lambda}$ induced by the propagation of the beam in the distance S between the probe and the object.

3.2.2. Interferometry with a two-sample system

Let us keep the object at rest and suddenly perturb the probe in the beam direction, e.g. with the help of a piezo-electric foil. The motion introduces an additional time-

dependent phase shift in the radiation scattered by the first sample in the beam

$$\varphi(t) = \frac{2\pi}{\lambda} \int_0^t \mathrm{v}(t')\, dt' \tag{3.21}$$

where v is the velocity of the motion and λ is the wavelength of the X-rays. In the energy domain, this corresponds to a detuning in the response of the two samples, as given in Eq. (2.37). Due to the induced phase shift, the coupling term depends on the sample sequence [Smi+05]. When the moving probe is placed in front of the object, the coupling term is given as

$$R_{PO}(t) = \int_0^t R_O(t-t')\mathrm{e}^{\mathrm{i}\varphi(t')} R_P(t')\, dt'. \tag{3.22}$$

When the object is placed first in front of the beam and the moving probe is placed second, the coupling term is given as

$$R_{OP}(t) = \int_0^t R_O(t-t')\mathrm{e}^{\mathrm{i}\varphi(t)}\mathrm{e}^{-\mathrm{i}\varphi(t-t')} R_P(t')\, dt'. \tag{3.23}$$

The two-sample system is therefore no longer commutative. However, if the velocity of the relative motion changes slowly compared to the nuclear lifetimes, we can consider it as a constant during the scattering process. In this case, the detuning between the response of the two samples does not change as the scattering happens and the induced phase shifts in the coupling term are equal even on inverting the samples, i.e., $R_{PO} = R_{OP}$. This can be done, e.g., by mounting the probe on a Doppler drive operated at a frequency ~ 25 Hz, as shown in Fig. 3.9. The detuned energy response of the probe moving with a constant velocity v_j can be written as

$$\hat{P}^{(j)}(\omega) = \hat{P}(\omega + \Delta\omega_j) \tag{3.24}$$

where from Eq. (2.37)

$$\Delta\omega_j = \omega_0 \frac{\mathrm{v}_j}{c} = \frac{2\pi}{\lambda}\mathrm{v}_j. \tag{3.25}$$

and $\omega_0 = 2\pi c/\lambda$ is the angular frequency of the incident X-ray photon. In the time domain, the Doppler detuning causes an additional phase shift $\varphi_j(t)$ in the electric field

scattered by the probe P, such that

$$R_P^{(j)}(t) = e^{i\varphi_j(t)} R_P(t), \tag{3.26}$$

where

$$\varphi_j(t) = \frac{2\pi}{\lambda} v_j t = \Delta\omega_j t. \tag{3.27}$$

Changing v_j changes the detuning between the samples. If v_j is sufficiently high such

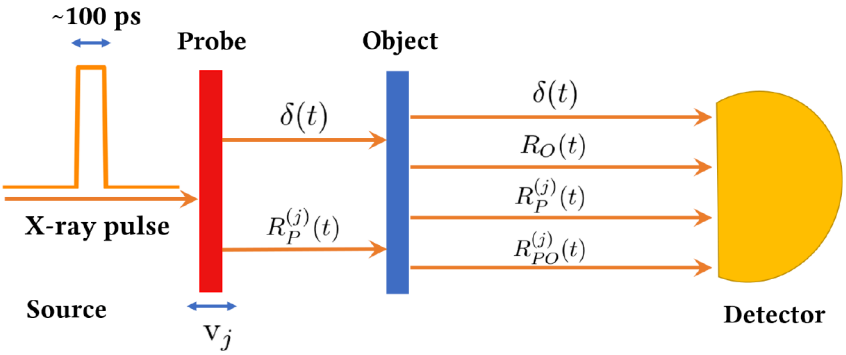

Figure 3.9.: Scattering of synchrotron radiation by a probe-object system when the probe is moved with a constant velocity v_j with respect to the object.

that the probe and the object response are completely detuned, the radiative coupling term in Eq. (3.19) can be neglected and we only get the interference term in their combined response, i.e.,

$$Z(t) \approx \delta(t) + R_P^{(j)}(t) + R_O(t). \tag{3.28}$$

In this case, the setup in Fig. 3.9 is similar to the time domain version of the interferometer shown in Fig. 3.1(d), where the Doppler drive serves as a phase shifter and the two samples act as the two arms of the interferometer. Neglecting the $\delta(t)$ term from the electronic scattering, the intensity of the interference pattern at velocity v_j of the

probe can be written as,

$$\begin{aligned} I^{(j)}(t) &\approx \left| R_P^{(j)}(t) + R_O(t) \right|^2 \\ &\approx |R_P(t)|^2 + |R_O(t)|^2 + 2\,|R_P(t)|\,|R_O(t)| \cos\left(\eta_P(t) + \eta_O(t) + \Delta\omega_j t\right) \\ &\approx I_P(t) + I_O(t) + 2\sqrt{I_P(t) I_O(t)} \cos\left(\eta_P(t) + \eta_O(t) + \Delta\omega_j t\right) \end{aligned} \tag{3.29}$$

where $I_P(t)$ and $I_O(t)$ are the intensities of the probe and the object. In an interferometer, besides these two intensity measurements, at least two more measurements at different detunings $\Delta\omega_j$ are required to uniquely determine the phase $\eta_O(t)$ of the object. However, $\eta_O(t)$ is fast oscillating in time, and determining it can be difficult using just two measurements. Therefore, several measurements at different velocities v_j are taken by moving the Doppler drive at a continuously changing velocity [Cal+05]. For each photon hitting the detector, both its time of flight and the velocity of the probe on the Doppler drive are recorded. This collection of intensity measurements is essentially the ptychogram (Sec. 3.1.2) for our 1-D object. The ptychogram is a 2-D data set with one dimension being time and the other being the Doppler detuning of the probe (see Fig. 3.10(b)). It is very similar to a spectrogram - which is widely used in signal processing to represent the variation of a signal's frequency content with time.

To get the phase of the object from the ptychogram, one can fit the model

$$f_n(\Delta\omega_j) = A_n + B_n \cos\left(C_n + \Delta\omega_j t_n\right) \tag{3.30}$$

where

$$\begin{aligned} A_n &= I_P(t_n) + I_O(t_n) \\ B_n &= 2\sqrt{I_P(t_n) I_O(t_n)} \\ C_n &= \eta_P(t_n) + \eta_O(t_n) \end{aligned}$$

to the measured intensities at fixed time slices $t = t_n$. The fitted parameters alongside the intensity measurements $I_P(t)$ and $I_O(t)$ and the phase response of the probe $\eta_P(t_n)$ can be used to reconstruct the complex response function[10] of the object in the time domain. This is the so-called heterodyne phase reconstruction (HPR) scheme which has also been mentioned in mathematical papers like [RDN13]. However, it has two

[10] If the object is optically active, the above steps have to be repeated for the other polarization direction by rotating the polarization of the incoming beam or by rotating the sample.

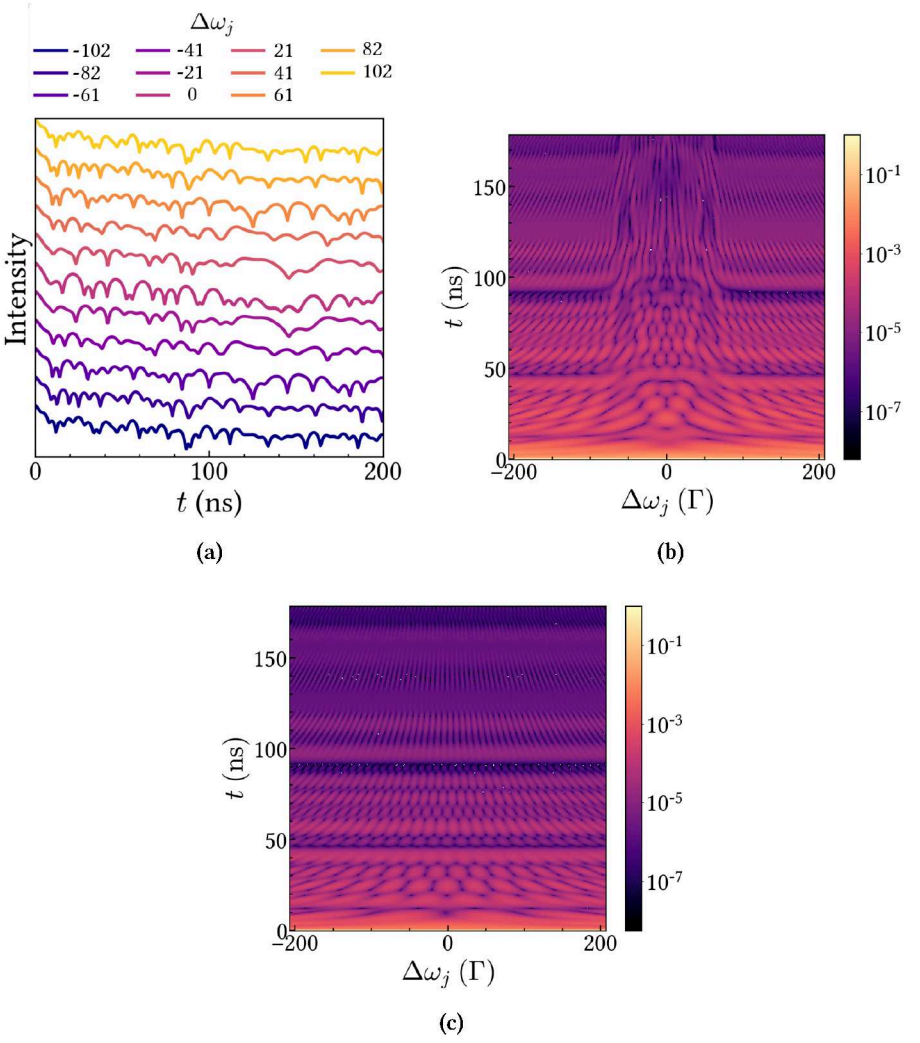

Figure 3.10.: (a) Different temporal decay patterns at the detector for different Doppler detunings $\Delta\omega_j$ of the probe relative to the object. The intensities of the decay patterns have been normalized from 0 to 1 and plotted with a constant offset for clarity. (b) The decay patterns are plotted as a 2-D ptychogram with color-coded intensities. (c) Ptychogram simulated by ignoring the coupling between the probe and the object such that only interference between the probe and the object is present, according to (Eq. (3.29)). On comparing (b) and (c), we can see that the radiative coupling term is small at large Doppler detunings.

main drawbacks:

1. The HPR model assumes the interference condition in Eq. (3.28). Therefore, only the measurements in the ptychogram for which the resonance lines of the probe and the object are highly detuned can be used (see Fig. 3.10). Moreover, close to the minima of the quantum beats of $I_O(t)$ and $I_P(t)$, the cosine term in Eq. (3.29) becomes ~ 0 and the effect of the coupling can no longer be neglected. This significantly reduces the region of the dataset that can be utilized and fitted with the model in Eq. (3.30).

2. There are proposed schemes to extend the HPR model, e.g., the extended heterodyne phase reconstruction (xHPR) model in Ref. [Ger21]. However, xHPR relies on modeling the probe energy response as a thin, single line such that one may write its phase response as $\eta_P(t_n) = \omega_P t_n$. One can then reconstruct the phase response of the object as

$$\eta_O(t_n) = C_n - \omega_P t_n \tag{3.31}$$

   where ω_P is the resonance frequency of the probe. The problem of fabricating such a probe for NRS is analogous to the case of an ideal, perfect lens for imaging. Therefore, in practice, even with the xHPR model one retrieves the convolution of the probe's response with the object. The features of the reconstructed object would be distorted or washed out if the probe is not single line or has a broad energy response. Even for a single line, the Nyquist sampling conditions apply, i.e., the Doppler detuning steps determine the resolution of the reconstruction.

3.2.3. Ptychography with a two-sample system

An alternative approach to solving the phase problem in NRS is to relax the requirement of the ideal single-line probe altogether. We can use the ptychographic principles discussed in Sec. 3.1 to deconvolute the probe response from the object and make the phase retrieval 'probe-less'.

The forward (encoder) model

Let us go back to the scattering response of a two-sample system as given in Eq. (3.14). Suppose we keep the probe on a Doppler drive and the object at rest. By the Fourier

convolution theorem, convolution in the time domain equals point-wise multiplication in the energy domain, i.e., the combined scattering response of the probe and the object in the energy domain is given as

$$\begin{aligned}\hat{Z}^{(j)}(\omega) &= \hat{P}^{(j)}(\omega) \cdot \hat{O}(\omega) \\ &= \hat{P}(\omega + \Delta\omega_j) \cdot \hat{O}(\omega).\end{aligned} \tag{3.32}$$

Here $\hat{P}$ and $\hat{O}$ are the scattering responses of the probe and the object while $\Delta\omega_j$ is the induced energy shift in the probe response corresponding to the velocity v_j of the Doppler drive. The intensity at the detector at any time is proportional to the squared magnitude of the combined wave field, i.e.,

$$\begin{aligned}I^{(j)}(t) &= \left|Z^{(j)}(t)\right|^2 \\ &= \left|\mathcal{F}\{\hat{P}(\omega + \Delta\omega_j) \cdot \hat{O}(\omega)\}\right|^2.\end{aligned} \tag{3.33}$$

This is the one-dimensional, continuous ptychographic forward model for our setup. It is non-linear due to the presence of the absolute ($|.|$) operation in the measurement.

For our numerical applications, we would now approximate the continuous ptychographic problem by a discrete problem. We consider the one-dimensional complex object function $(\hat{O}[n])_{n\in\mathbb{N}}$ and probe function $(\hat{P}[n])_{n\in\mathbb{N}}$, supported on $0 \leq n < N$ and defined on a discrete grid of energy resolution $\Delta\omega$. Equation (3.33) can be discretized as

$$\begin{aligned}I^{(j)}[q] &= \left|\sum_n \hat{P}^{(j)}[n] \cdot \hat{O}[n] \mathrm{e}^{-\mathrm{i}\frac{2\pi}{N}qn}\right|^2 \\ &= \left|\mathbb{F}\{\hat{P}^{(j)} \cdot \hat{O}\}[q]\right|^2.\end{aligned} \tag{3.34}$$

This is the one-dimensional discrete forward model for our NRS ptychography setup.

3.3. The inverse problem in NRS ptychography

Let us now pause and make an important switch in notation here. So far we have been treating the phase problem by addressing $\hat{O}$ and $\hat{P}$, i.e., the discretized versions of the continuous object and probe response functions in the energy domain. Since our detectors and computers will treat these discrete functions as data arrays or matrices, they have to be finite in size. We are assuming that the discrete object and probe functions are compactly supported on N. We now express these functions as 1-D arrays $\hat{\boldsymbol{O}} \in \mathbb{C}^{N\times 1}$, $\hat{\boldsymbol{P}}_j \in \mathbb{C}^{N\times 1}$. The intensity in the time domain is measured at N points with a fixed time resolution and is given as $\boldsymbol{I}_j \in \mathbb{R}^{N\times 1}$. The index $j = \{0, 1, 2 \cdots M-1\}$ corresponds to the velocities of the Doppler drive. Such an approximation is a valid representation of the physical experiment when the peaks in the probe's energy response lie within the bandwidth allowed by the time resolution of the detector.

The discrete ptychographic phase problem can then be framed in a variety of ways. Setting this mathematical framework properly is important for discussing its properties and the possible solution schemes.

3.3.1. Ptychography as a constraint projection problem

First, the phase problem can be framed as a projection problem:

Pr. 2.1 : The phase problem in NRS ptychography

Find $\hat{\boldsymbol{O}} \in X \subseteq \mathbb{C}^{N\times 1}$ subject to the constraints

$$\boldsymbol{I}_j = \left|\mathbf{F}\cdot\hat{\boldsymbol{Z}}_j\right|^2 \quad , \quad j = \{0, 1, \ldots, M-1\} \tag{3.35}$$

$$\text{and} \qquad \hat{\boldsymbol{Z}}_j = \text{diag}\left(\hat{\boldsymbol{P}}_j\right)\cdot\hat{\boldsymbol{O}}. \tag{3.36}$$

Here, $\hat{\boldsymbol{Z}}_j \in \mathbb{C}^{N\times 1}$ is the exit wave from the object at velocity v_j of the probe on the Doppler drive. $\mathbf{F} \in \mathbb{C}^{N\times N}$ is the discrete Fourier transform matrix, and $\text{diag}\left(\hat{\boldsymbol{P}}_j\right) \in \mathbb{C}^{N\times N}$ is a diagonal matrix. In this framework, we can use set-projection operators to

extract the object from an exit wave matrix

$$\hat{\mathbf{Z}} = \begin{pmatrix} \hat{\boldsymbol{Z}}_0 \\ \hat{\boldsymbol{Z}}_1 \\ \vdots \\ \hat{\boldsymbol{Z}}_{M-1} \end{pmatrix} \tag{3.37}$$

that lies at the intersection of the constraints on the problem. These constraints can arise, e.g., from additional prior knowledge. In the case of ptychography, the following constraints on the problem are imposed by the measurement scheme itself:

1. **Fourier modulus constraints**: We have time domain measurements of the intensities ($\boldsymbol{I}_j$) at the detector for each Doppler detuning [Eq. (3.35)]. The projection operator to these constraints can be defined as [Thi+09]

$$\Pi_{\mathcal{F}}\{\hat{\mathbf{Z}}\} : \hat{\boldsymbol{Z}}_j \rightarrow \mathbf{F}^{\dagger} \cdot \mathrm{diag}\left(\frac{\sqrt{\boldsymbol{I}_j}}{\left|\mathbf{F} \cdot \hat{\boldsymbol{Z}}_j\right|}\right) \cdot \mathbf{F} \cdot \hat{\boldsymbol{Z}}_j \qquad \forall j. \tag{3.38}$$

   i.e. we propagate each exit wave to the detector domain ($\mathbf{F} \cdot \hat{\boldsymbol{Z}}_j$) and then replace its magnitude with the measured magnitude ($\sqrt{\boldsymbol{I}_j}$) - while preserving the phase information. Geometrically, this means projecting $\hat{\boldsymbol{Z}}_j$ on a circle of radius $\sqrt{\boldsymbol{I}_j}$ in the complex plane. The Fourier constraint set is *non-convex* since the interior region of the circle is not included. This means that one can find two points in the set where the line segment joining the two points leaves the set and the projection algorithms can get stuck in local minima.

2. **Overlap constraint**: The overlap constraint is based on the idea that X-rays passing through overlapping illuminated areas of the object (see Fig. 3.7) must carry shared information. To satisfy the overlap constraint, one can look for a solution that best describes all measurements in each iteration. For example, as given in Ref. [Thi+09], one can solve the least-squares problem

$$\min_{\hat{O}} \sum_j \left\| \hat{\boldsymbol{Z}}_j - \mathrm{diag}\left(\hat{\boldsymbol{P}}_j\right) \cdot \hat{\boldsymbol{O}} \right\|^2 \tag{3.39}$$

which gives the updated object

$$\hat{O}' = \frac{\sum_j \mathrm{diag}\left(\hat{P}_j\right)^\dagger \cdot \hat{Z}_j}{\sum_j |\hat{P}_j|^2}. \tag{3.40}$$

The projection to the overlap constraint in 3.36 is then given as

$$\Pi_O\{\hat{Z}\} : \hat{Z}_j \rightarrow \mathrm{diag}\left(\hat{P}_j\right) \cdot \hat{O}' \qquad \forall j \tag{3.41}$$

i.e. at each velocity of the Doppler drive, the exit wave is composed of the dot product of the probe and the updated object response.

In the feasibility framework, a natural question arises about the *uniqueness* of the solution to the ptychographic phase retrieval problem[11]. As discussed previously in Sec. 2.6, the general one-dimensional phase problem is *ill-posed*. How many constraints do we then need to make the ptychographic phase retrieval problem in **Pr. 2.1** necessarily *well-posed* and solve it uniquely?

The oversampling conjecture: For general phase retrieval of every object in $\mathbb{C}^N$, it was conjectured in Ref. [Ban+14] that the number M of necessary measurements is $M \geq 4N - 4$. This was proven in Ref. [Con+15]. However, due to some counter-examples [Vin15], the precise lower bound is still an open question, i.e., it is not proven whether or not a unique solution exists in the case when the number of measurements $M < 4N - 4$. On the other hand, the Miao [MSC98] oversampling conjecture is based on the suggestion that a system of equations can in principle have a solution if the number of equations exceeds the number of unknowns. Therefore, one needs at least $M = 2N$ measurements to reconstruct a one-dimensional object in $\mathbb{C}^N$ uniquely.

The oversampling requirement is tied to the number of Fourier modulus constraints - which is only one aspect of the ptychographic phase retrieval problem. The structure

[11] Note that we only talk about uniqueness with respect to the non-trivial ambiguities here. The trivial ambiguities described in Sec. 2.6 hold for the discrete ptychographic phase retrieval because it is a special case of the phase retrieval problem. Any questions on the uniqueness of the solution always include uniqueness up to a global phase shift.

of the probe in the energy domain has a significant impact on the accuracy of the reconstruction. This is because the overlap constraint is also essential for the measurement scheme. Without it, the ptychographic problem splits into several separate standard phase retrieval problems. However, the optimum overlap between measurements is still unproven. Additionally, the majority of results in mathematical literature are empirically tested for the two- and three-dimensional problems and do not necessarily imply a similarity to the one-dimensional problem.
The theoretical uniqueness of the solution has only been proven via numerical experiments with extremely high overlap conditions and oversampling, such as in [IVW15]. In a real ptychography setup, such an ideal measurement scheme is definitely neither possible nor practical due to the required experimental effort. Therefore, the uniqueness of the retrieved solution remains mathematically unclear.

3.3.2. Ptychography as a non-convex minimization problem

The phase problem can also be framed as a non-convex minimization of a cost function ρ that represents the distance between the measured ptychogram and the forward model on the object:

Pr 2.2 : The phase problem in NRS ptychography

Minimize cost function $\rho : X \to [0, \infty)$ given as

$$\rho(\hat{\boldsymbol{O}}) = \sum_j \mathcal{D}\left(\boldsymbol{b}_j \,, \left|\mathrm{F} \cdot \mathrm{diag}\left(\hat{\boldsymbol{P}}_j\right) \cdot \hat{\boldsymbol{O}}\right|^2\right) \tag{3.42}$$

where $\hat{\boldsymbol{O}} \in X \subseteq \mathbb{C}^{N\times 1}$. The distance map $\mathcal{D} : X \times X \to [0, \infty)$ is a metric between the intensity measurements $\boldsymbol{b}_j$ and the modeled intensity of the exit wave from $\hat{\boldsymbol{O}}$, when the probe detuning is $\Delta\omega_j$.

Since the problem has a large number of variables, only local search algorithms can be used to find the solution to **Pr. 2.2**. Note that both formulations **Pr. 2.1** and **Pr. 2.2** of the problem are equivalent. The optimization problem is also non-convex. Hence, for practical ptychography implementation, the theoretical uniqueness of the solution is

not the main concern but rather the existence of local minima to Eq. (3.42) as shown in Fig. 3.11. Tackling the local minima is another one of the few mathematical questions remaining in phase retrieval.

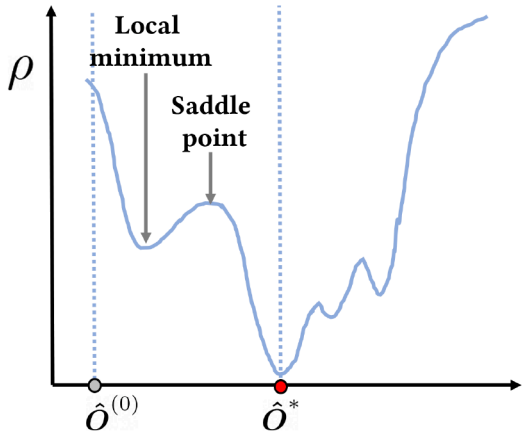

Figure 3.11.: Phase retrieval as a cost-function minimization problem. The solution $\hat{O}^*$ lies at the global minimum of the cost function ρ. Since ρ is non-convex, local minima and saddle points exist and might hinder the local optimization algorithms from reaching the solution from the starting guess $\hat{O}^{(0)}$.

In this chapter, we have thus established the theoretical framework for ptychography in energy and time and its parallels with real space ptychography in coherent diffraction imaging. By solving the phase problem for a nuclear resonant scattering object, we can reconstruct its complex scattering response or susceptibility which contains information about nuclear transitions in the object and fully describes the quantum state of the nuclear ensemble. In the ptychographic experimental setup, the phase information of the object is captured in a 2-D ptychogram, which is a time-energy measurement of the scattered field from the object. The ptychogram is measured by detuning a probe with respect to the object using a Doppler drive and then measuring the intensity of the scattered field of the two-sample system in time. By viewing ptychography as a non-convex optimization problem, we can invert the ptychogram if it has the "overlap constraint", i.e., the probe is detuned such that the illuminated parts of the object are overlapped in energy. The probe for NRS ptychography, therefore should be a sample

with a broader energy response (e.g., a thick stainless steel foil) so that it can interact with larger part of the beam illuminating the object, and measure with sufficient overlap along the energy axis. This is an advantage over the existing phase reconstruction methods - where the probe needs to be ideally thin and moved in small detuning steps to improve the resolution of the reconstruction.

4. The ptychography engine

To tackle the one-dimensional phase problem in Sec. 3.3, we introduce the decoding unit for our ptychography setup. The inversion algorithm or the ptychography engine is one part of the decoder pipeline (Fig. 4.1). Some common notation for this chapter is supplemented in the glossary at the end of the appendix.

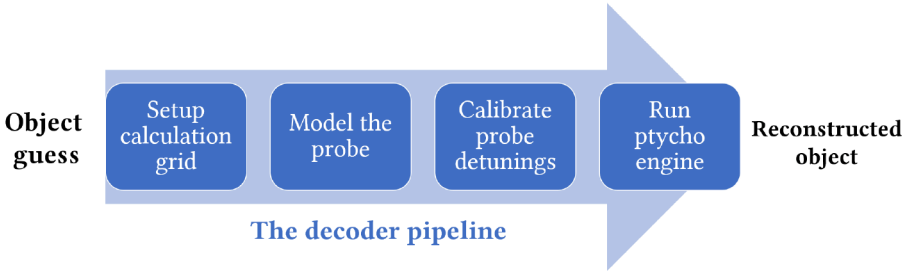

Figure 4.1.: The reconstruction pipeline of the object from the measured ptychogram.

In the feasibility framework of the phase problem (**Pr. 2.1**), projection algorithms like Hybrid Input-Output [Fie82], Difference Map [Els03] and Relaxed Averaged Alternating Reflections (RAAR) [Luk04] can be directly applied. Their successful usage has been shown for two-dimensional CDI ptychography [Thi+09]. The projection algorithms start with an initial guess on the object $\hat{O}^{(0)}$ and repeatedly apply a mapping $\mathcal{M}$ such that

$$\hat{O}^{(i+1)} = \mathcal{M}(\hat{O}^{(i)}). \tag{4.1}$$

When one reaches a *fixed* point

$$\hat{O}^{**} = \mathcal{M}(\hat{O}^{**}) \tag{4.2}$$

the algorithm is then said to have converged[1]. However, our ptychographic engine is based on the optimization approach (**Pr. 2.2**) to the problem. This has several advantages:

1. The optimization framework allows us to flexibly model the noise in our data by choosing a cost function ρ according to the maximum likelihood scheme and adding regularization terms (Sec. 4.1).

2. State-of-the-art gradient-based algorithms which are popular in the machine learning community can be used to minimize the non-convex cost function ρ. These algorithms are highly tunable and can be integrated with several acceleration strategies.

3. Gradient-based algorithms minimize ρ by making use of $\nabla_{\hat{\boldsymbol{O}}}\rho$, i.e., the derivative of ρ with respect to the object. Instead of calculating the gradient analytically, one can use automatic differentiation (Sec. 4.3.4).

The pseudo-code for a (deterministic) gradient-based algorithm for our ptychography engine is given in Algorithm 1. The DETUNE ($\hat{\boldsymbol{P}}$, $\Delta\omega_j$) step refers to the detuning of the probe by $\Delta\omega_j$ with respect to the object. We use linear interpolation to do this. The STEPSIZE_SELECTION and ACCELERATION_SCHEME steps depend on the choice of the gradient-based algorithm. For example, the simplest gradient-based algorithm is steepest gradient descent (GD) with a constant stepsize and no acceleration. We list the other algorithms in detail with their pseudocodes in Appendix A. The working of the engine can be understood as a five-step process and is shown in Fig. 4.2.

Algorithm 1 Deterministic gradient algorithm for NRS ptychographic engine

1: $max\_iter \leftarrow$ *maximum number of engine iterations*
2: $\boldsymbol{b}_0, \boldsymbol{b}_1 \cdots \boldsymbol{b}_{M-1} \leftarrow$ *measurements*
3: $\Delta\omega_0, \Delta\omega_1 \cdots \Delta\omega_{M-1} \leftarrow$ *Dopper detunings*
4: $\hat{\boldsymbol{P}} \leftarrow$ *probe* $\in \mathbb{C}^N$
5: *Initialize:* $\hat{\boldsymbol{O}} \leftarrow \hat{\boldsymbol{O}}^{(0)} \in \mathbb{C}^N$, $\alpha \leftarrow \alpha^0 \in (0, 1)$, $i \leftarrow 0$
6: **repeat**

[1]Note again that it is not mathematically guaranteed that $\hat{\boldsymbol{O}}^{**} = \hat{\boldsymbol{O}}^*$, i.e., the fixed point is the solution $\hat{\boldsymbol{O}}^*$ to the problem, because we are working with a non-convex problem and local optimization methods.

Initialize: $\rho \leftarrow 0$, $\nabla_{\hat{O}}\rho \leftarrow 0$
for $j \in \{0, 1, \ldots M-1\}$ **do**
Forward:
$\hat{\boldsymbol{P}}_j \leftarrow \text{DETUNE}\ (\hat{\boldsymbol{P}}, \Delta\omega_j)$
$\hat{\boldsymbol{Z}}_j \leftarrow \text{diag}\left(\hat{\boldsymbol{P}}_j\right) \cdot \hat{\boldsymbol{O}}$
Compare and calculate gradient:
$\rho \leftarrow \rho + \text{dist}(\boldsymbol{b}_j\ , |\mathbf{F} \cdot \hat{\boldsymbol{Z}}_j|^2)$
$\nabla_{\hat{O}}\rho \leftarrow \nabla_{\hat{O}}\rho + \nabla_{\hat{O}}\text{dist}(\boldsymbol{b}_j\ , |\mathbf{F} \cdot \hat{\boldsymbol{Z}}_j|^2)$
end for
Accelerate:
$\alpha \leftarrow$ STEPSIZE_SELECTION
$\boldsymbol{d} \leftarrow$ ACCELERATION_SCHEME (α, $\nabla_{\hat{O}}\rho$)
Update: $\hat{\boldsymbol{O}} \leftarrow \hat{\boldsymbol{O}} + \boldsymbol{d}$
if $i = max\_iter$ **then**
Stop the engine.
else
$i \leftarrow i + 1$
end if
until CONVERGED
return $\hat{\boldsymbol{O}}$

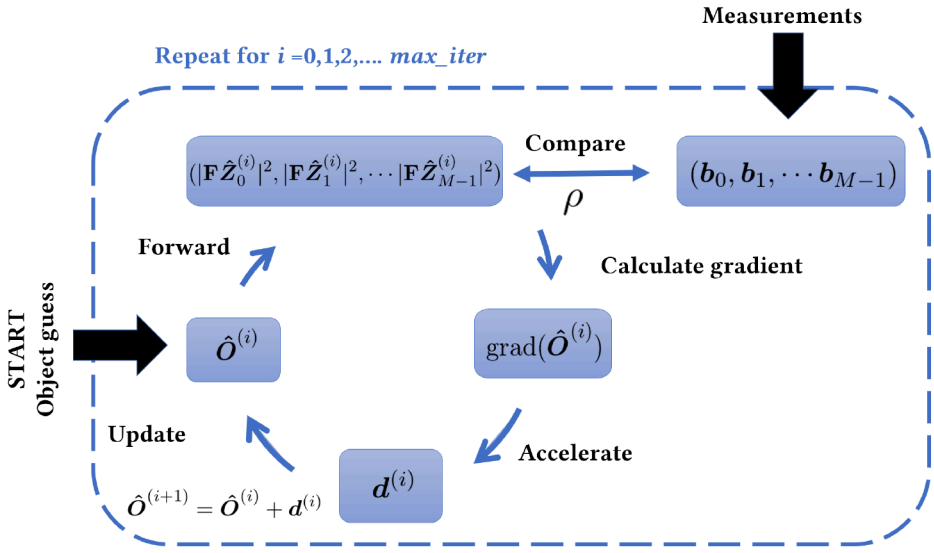

Figure 4.2.: The five steps of the deterministic ptychography engine. (1) At each engine iteration i, the current object guess $\hat{\boldsymbol{O}}^{(i)}$ is passed through the **forward** model to the detector. At the detector, the intensities at different probe detunings $\Delta\omega_j$ are calculated. (2) The calculated intensities are **compared** to the actual measured counts $\boldsymbol{b}_j$ via a cost function ρ. (3) The **gradient** $\nabla_{\hat{O}}\rho$ is calculated. (4) The gradient is used to generate an **update** vector $\boldsymbol{d}^{(i)}$ based on an **acceleration** scheme (depending on the choice of algorithm). (5) The object is updated for the next engine iteration. The engine is stopped either when a convergence criterion is met or a maximum number of engine iterations (max_iter) is reached.

4.1. Choosing the cost function

The gradient descent algorithms need a cost function ρ to minimize. It has been widely reported in X-ray ptychography literature how the choice of a cost function can affect the retrieval [Yeh+15; KCU18], especially in the presence of noise in the measurements.

The noisy ptychographic phase retrieval problem is *ill-posed* [For+20], i.e., it does not have a provably unique solution. To deal with the noisy form of the problem, we would first use the framework of maximum likelihood estimation, as shown in Ref. [TG12].

4.1.1. Maximum likelihood estimation

In the maximum likelihood estimation scheme, we aim to formulate a cost function that incorporates some knowledge of the noise model in the experiment to yield a superior reconstruction. In further discussion, we would use the short-hand notation $\boldsymbol{x}_q$ to denote $\boldsymbol{x}[q]$, i.e., the value of the vector $x \in \mathbb{C}^{N\times 1}$ at the q-th time point. The phase problem then becomes as follows:

Pr. 3.0 : The phase problem in ptychographic NRS

Maximize the joint likelihood function $\mathcal{L} : \mathbb{C}^{N\times 1} \to [0, \infty)$ given as

$$\mathcal{L}(\hat{\boldsymbol{O}}) = \prod_j \prod_q p(\boldsymbol{b}_{jq}|\hat{\boldsymbol{O}}) \tag{4.3}$$

where $p(\boldsymbol{b}_{jq}|\hat{\boldsymbol{O}})$ is the Bayesian probability of measuring $\boldsymbol{b}_{jq}$ counts at the detector at time $(q-1)\Delta t$ and probe detuning $\Delta\omega_j$, given the object's energy domain response is $\hat{\boldsymbol{O}}$.

The likelihood function is a statistical metric for the consistency of the forward model with the measurements. If the model is changed to make the measurements more probable, the likelihood increases, indicating that the model is better. We try to find an object $\hat{\boldsymbol{O}}$ that maximizes the likelihood $\mathcal{L}$ or, equivalently, minimizes the negative log-likelihood. The cost function is thus given as

$$\rho(\hat{\boldsymbol{O}}) = -\log(\mathcal{L}(\hat{\boldsymbol{O}})). \tag{4.4}$$

The probabilities in Eq. (4.3) have to include modeling of all sources of noise in the forward process. Let us assume that each measurement can be modeled as

$$\boldsymbol{b}_j = \text{Poisson}(\boldsymbol{I}_j) + \boldsymbol{n}_j \tag{4.5}$$

where $\boldsymbol{I}_j = |\mathbf{F} \cdot \text{diag}\left(\hat{\boldsymbol{P}}_j\right) \cdot \hat{\boldsymbol{O}}|^2$ i.e. the noiseless modeled intensity, Poisson$(\cdot)$ denotes sampling the measurement from a Poisson distribution based on the modeled intensi-

ties[2] and $\boldsymbol{n}_j$ is a random noise vector sampled from a Gaussian distribution $\mathcal{N}(0, \boldsymbol{\sigma}_j^2)$. We evaluate the likelihood functions for the following three noise cases:

1. **Poisson likelihood**: Suppose there are no sources of random noise present in the experiment ($\boldsymbol{n}_j = 0$). Since the photon counting process at the detector is a Poissonian process, the probabilities can be written with a Poisson distribution model, i.e.,

$$p(\boldsymbol{b}_{jq}|\hat{\boldsymbol{O}}) = \frac{I_{jq}^{\boldsymbol{b}_{jq}} \cdot \mathrm{e}^{-I_{jq}}}{\boldsymbol{b}_{jq}!}. \tag{4.6}$$

The cost function to be minimized is now given as Eq. (4.4)

$$\rho(\hat{\boldsymbol{O}}) = -\log\left(\prod_j \prod_q p(\boldsymbol{b}_{jq}|\hat{\boldsymbol{O}})\right) \tag{4.7}$$

$$= \sum_j \sum_q -\boldsymbol{b}_{jq} \cdot \log(\boldsymbol{I}_{jq}) + \boldsymbol{I}_{jq} + \log(\boldsymbol{b}_{jq}!). \tag{4.8}$$

If we make a Taylor expansion of $\log(\sqrt{\boldsymbol{I}_{jq}})$ around $\sqrt{\boldsymbol{b}_{jq}}$ to the second order, i.e.,

$$\log(\sqrt{\boldsymbol{I}_{jq}}) \approx \log(\sqrt{\boldsymbol{b}_{jq}}) + \frac{\sqrt{\boldsymbol{I}_{jq}} - \sqrt{\boldsymbol{b}_{jq}}}{\sqrt{\boldsymbol{b}_{jq}}} - \frac{(\sqrt{\boldsymbol{I}_{jq}} - \sqrt{\boldsymbol{b}_{jq}})^2}{2\boldsymbol{b}_{jq}} \tag{4.9}$$

and neglect the constant terms that only depend on $\boldsymbol{b}_{jq}$, we get an approximation of the cost function in Eq. (4.8) as

$$\rho(\hat{\boldsymbol{O}}) \approx 2 \sum_j \sum_q (\sqrt{\boldsymbol{I}_{jq}} - \sqrt{\boldsymbol{b}_{jq}})^2 = 2 \sum_j \left\| |\mathbf{F} \cdot \mathrm{diag}\left(\hat{\boldsymbol{P}}_j\right) \cdot \hat{\boldsymbol{O}}| - \sqrt{\boldsymbol{b}_j} \right\|^2. \tag{4.10}$$

The Poisson log-likelihood cost function is thus approximately proportional to the '**amplitude-based**' cost function popular in the ptychography community [Yeh+15; ZSC16].

One advantage of the gradient-based methods is that the reformulated problem **Pr. 3.0** can now be flexibly solved by using the gradient of the cost function in

[2] or 'applying' Poisson noise to the model.

Eq. (4.8). We can calculate the gradient of ρ with respect to the complex object $\hat{\boldsymbol{O}}$ using Wirtinger calculus [Hun07] as

$$\nabla_{\hat{O}}\rho = 2\sum_j \mathrm{diag}\left(\hat{\boldsymbol{P}}\right)_j^{\dagger} \cdot \mathbf{F}^{\dagger} \cdot \mathrm{diag}\left(\mathbf{F}\cdot\hat{\boldsymbol{Z}}_j\right)\cdot\left(1-\frac{\sqrt{\boldsymbol{b}_j}}{|\mathbf{F}\cdot\hat{\boldsymbol{Z}}_j|}\right) \tag{4.11}$$

$$= 2\sum_j \mathrm{diag}\left(\hat{\boldsymbol{P}}\right)_j^{\dagger} \cdot \left(\hat{\boldsymbol{Z}}_j - \mathbf{F}^{\dagger}\cdot\mathrm{diag}\left(\frac{\sqrt{\boldsymbol{b}_j}}{|\mathbf{F}\cdot\hat{\boldsymbol{Z}}_j|}\right)\cdot\mathbf{F}\cdot\hat{\boldsymbol{Z}}_j\right) \tag{4.12}$$

where $\hat{\boldsymbol{Z}}_j = \mathrm{diag}\left(\hat{\boldsymbol{P}}_j\right)\cdot\hat{\boldsymbol{O}}$.

2. **Gaussian likelihood**: If $\boldsymbol{n}_j \neq 0$ (e.g. due to electronic noise at the APDs [LTP13]) and the photon counts are high[3], the probabilities can be written with the Gaussian model

$$p(\boldsymbol{b}_{jq}|\hat{\boldsymbol{O}}) = \frac{1}{\sqrt{2\pi\boldsymbol{\sigma}_{jq}^2}}\mathrm{e}^{-(I_{jq}-\boldsymbol{b}_{jq})^2/(2\boldsymbol{\sigma}_{jq}^2)}. \tag{4.13}$$

In this case, the cost function can be written as (up to a constant)

$$\rho(\hat{\boldsymbol{O}}) = \sum_j\sum_q \frac{(\boldsymbol{I}_{jq}-\boldsymbol{b}_{jq})^2}{2\boldsymbol{\sigma}_{jq}^2} = \sum_j \frac{1}{2}\left\|\frac{|\mathbf{F}\cdot\mathrm{diag}\left(\hat{\boldsymbol{P}}_j\right)\cdot\hat{\boldsymbol{O}}|^2-\boldsymbol{b}_j}{\boldsymbol{\sigma}_j^2}\right\|^2. \tag{4.14}$$

Note that for a unit noise variance at each time point in each measurement, i.e., $\boldsymbol{\sigma}_j = 1\ \forall\ j$, the cost function takes the familiar form of the mean square error,

$$\rho(\hat{\boldsymbol{O}}) = \frac{1}{2}\sum_j \left\||\mathbf{F}\cdot\mathrm{diag}\left(\hat{\boldsymbol{P}}_j\right)\cdot\hat{\boldsymbol{O}}|^2-\boldsymbol{b}_j\right\|^2. \tag{4.15}$$

In this case, the gradient is given as

$$\nabla_{\hat{O}}\rho = \frac{1}{2}\sum_j \mathrm{diag}\left(\hat{\boldsymbol{P}}\right)_j^{\dagger}\cdot\mathbf{F}^{\dagger}\cdot\mathrm{diag}\left(\mathbf{F}\cdot\hat{\boldsymbol{Z}}\right)\cdot(|\mathbf{F}\cdot\hat{\boldsymbol{Z}}_j|^2-\boldsymbol{b}_j). \tag{4.16}$$

[3]For higher mean photon counts, the Poisson distribution reaches the Gaussian distribution.

The mean square error Eq. (4.15) is also dubbed as an '**intensity-based**' cost function in ptychography literature.

3. **Mixed Poisson-Gaussian likelihood**: In the limit of low photon counts and the presence of random noise, one has to address a mixed Poisson-Gaussian noise model. Calculating the exact $p(\boldsymbol{b}_{jq}|\hat{\boldsymbol{O}})$ for this case would be inefficient since every $\boldsymbol{b}_{jq}$ exhibits an infinite Gaussian mixture distribution. Hence, we use an approximation to the model as described in Ref. [ZSD17].

   It can be shown that the maximum likelihood estimation scheme can be used to construct a ρ that makes the probability distribution of each pixel of the measured data the same (i.e. stabilizes the variance) regardless of its intensity [KCU18]. We can do this by applying the variance-stabilizing Generalized Anscombe transform ($\mathcal{G}$) to the data [SMB98; MF13; ZSD17]. For a real vector $\boldsymbol{x}$ sampled from a Poisson-Gaussian distribution, the transform is given as

$$\mathcal{G}(\boldsymbol{x}) = \begin{cases} 2\sqrt{\boldsymbol{x}_q + \frac{3}{8} + \boldsymbol{\sigma}_q^2} & \text{if } \boldsymbol{x}_q > -\frac{3}{8} - \boldsymbol{\sigma}_q^2, \\ 0 & \text{otherwise.} \end{cases} \tag{4.17}$$

   Here $\boldsymbol{\sigma}_q^2$ is the variance at the q-th pixel of the object $\boldsymbol{x}_q$. Applying $\mathcal{G}$ to the data makes each measured intensity pattern approximately Gaussian distributed with a $\sigma_j^2 = 1$. The noise can now be removed using the same approach for additive white Gaussian noise [4]. The corresponding cost function is given as

$$\rho(\hat{\boldsymbol{O}}) = \sum_j \sum_q \frac{[\mathcal{G}(\boldsymbol{I}_j)_q - \mathcal{G}(\boldsymbol{b}_j)_q]^2}{2} \tag{4.18}$$

$$= \frac{1}{2} \sum_j \left\| \mathcal{G}(|\mathbf{F} \cdot \mathrm{diag}\left(\hat{\boldsymbol{P}}_j\right) \cdot \hat{\boldsymbol{O}}|^2) - \mathcal{G}(\boldsymbol{b}_j) \right\|^2 . \tag{4.19}$$

A comparison of these noise models on simulated NRS ptychography datasets with different noise levels is done in Sec. 5.2.

[4] Note that for the case of no Gaussian noise ($\sigma_j^2 = 0 \; \forall j$), Eq. (4.17) reduces to the Anscombe Transform [Ans48] used for handling Poisson noise.

4.1.2. Regularization

Noise modeling might not be enough to deal with the ill-posedness of the inverse problem, especially at low degree of overlap between the measurements. To make the optimization algorithm more stable and robust, we can use regularization techniques. We introduce prior knowledge into the algorithm by adding extra penalty terms in the regularized cost function,

$$\rho_R(\hat{\boldsymbol{O}}) = \rho(\hat{\boldsymbol{O}}) + \boldsymbol{u}R(\hat{\boldsymbol{O}}) \tag{4.20}$$

where $\boldsymbol{u}$ is the weighting of the regularization/penalty term $R(\hat{\boldsymbol{O}})$. In Sec. 5.3 and 5.4, we demonstrate the use of the following types of regularization for our phase retrieval problem:

1. **L1 regularization**: The regularization term can be written as

$$R_{\mathrm{L1}}(\hat{\boldsymbol{O}}) = \left\| 1 - \hat{\boldsymbol{O}} \right\|_1 \tag{4.21}$$

   where $\|\cdot\|_1$ denotes the L1-norm. This type of regularization promotes 'sparsity' in our solution by penalizing deviations of the object from the baseline (= 1 for a transparent object) at each energy point.

2. **Total variation (TV) regularization**: This type of regularization is widely used for denoising images [ROF92]. The regularization term can be formulated as the discrete approximation of the first order derivative of the 1-D object as

$$R_{\mathrm{TV}}(\hat{\boldsymbol{O}}) = \left\| \nabla\hat{\boldsymbol{O}} \right\|_1 \sim \left\| (\hat{\boldsymbol{O}})_{q+1} - (\hat{\boldsymbol{O}})_q \right\|_1 \tag{4.22}$$

   where $\|\cdot\|_1$ denotes the L1-norm [FW23]. TV regularization imposes sparsity in the reconstructed solution by penalizing the difference between the value of $\hat{\boldsymbol{O}}$ at adjacent energy points ω_{q+1} and ω_q.

4.2. Additional constraints on the object

Based on prior knowledge, we can incorporate additional constraints into the retrieval algorithm. Since the nuclear susceptibility of the object is made up of Lorentzians

(Eq. (2.34)), it decays to zero at infinity by definition. Therefore, we avoid applying any support constraint to the object. Positivity constraints also do not hold meaning for a complex object. For a forward scattering object it would be physical to apply the constraint that the absorption term of the object $0 \leq |\hat{\boldsymbol{O}}_p| <= 1 \; \forall \; p$. It is also possible to limit the object's phase response to a specific interval. However, because the phase shift is robust to fluctuations in intensity, it does not improve the reconstruction result. For a constraint C, if the projection operator Π_C can be analytically determined, we can easily implement it in the phase retrieval algorithm (Step 19 in Algorithm 2).

Algorithm 2 Projected gradient algorithm for NRS ptychographic engine

1: $max\_iter \leftarrow$ *maximum number of engine iterations*
2: $\boldsymbol{b}_0, \boldsymbol{b}_1 \cdots \boldsymbol{b}_{M-1} \leftarrow$ *measurements*
3: $\Delta\omega_0, \Delta\omega_1 \cdots \Delta\omega_{M-1} \leftarrow$ *Dopper detunings*
4: $\hat{\boldsymbol{P}} \leftarrow$ *probe* $\in \mathbb{C}^N$
5: *Initialize:* $\hat{\boldsymbol{O}} \leftarrow \hat{\boldsymbol{O}}^{(0)} \in \mathbb{C}^N$, $\alpha \leftarrow \alpha^0 \in (0, 1)$, $i \leftarrow 0$
6: **repeat**
7: *Initialize:* $\rho \leftarrow 0$, $\nabla_{\hat{\boldsymbol{O}}}\rho \leftarrow 0$
8: **for** $j \in \{0, 1, \ldots M-1\}$ **do**
9: *Forward:*
10: $\hat{\boldsymbol{P}}_j \leftarrow \text{DETUNE}\ (\hat{\boldsymbol{P}}, \Delta\omega_j)$
11: $\hat{\boldsymbol{Z}}_j \leftarrow \text{diag}\left(\hat{\boldsymbol{P}}_j\right) \cdot \hat{\boldsymbol{O}}$
12: *Compare and calculate gradient:*
13: $\rho \leftarrow \rho + \text{dist}(\boldsymbol{b}_j\ , |\mathbf{F} \cdot \hat{\boldsymbol{Z}}_j|^2)$
14: $\nabla_{\hat{\boldsymbol{O}}}\rho \leftarrow \nabla_{\hat{\boldsymbol{O}}}\rho + \nabla_{\hat{\boldsymbol{O}}}\text{dist}(\boldsymbol{b}_j\ , |\mathbf{F} \cdot \hat{\boldsymbol{Z}}_j|^2)$
15: **end for**
16: *Accelerate:*
17: $\alpha \leftarrow$ STEPSIZE_SELECTION
18: $\boldsymbol{d} \leftarrow$ ACCELERATION_SCHEME (α, $\nabla_{\hat{\boldsymbol{O}}}\rho$)
19: *Update:* $\hat{\boldsymbol{O}} \leftarrow \hat{\boldsymbol{O}} + \boldsymbol{d}$
20: *Project to constraint:* $\hat{\boldsymbol{O}} \leftarrow \Pi_C(\hat{\boldsymbol{O}})$
21: **if** $i = max\_iter$ **then**
22: *Stop the engine.*
23: **else**

24: $i \leftarrow i + 1$
25: **end if**
26: **until** CONVERGED
27: **return** $\hat{O}$

4.3. Practical ptychography implementation

4.3.1. Setting up the calculation grid in the energy domain

Rather than performing a fit of the object parameters, the ptychography engine reconstructs the shape of the response function of the object over an energy grid. The size and resolution of the calculation grid should be such that the energy response of the object and the probe can be sampled properly, as shown in Fig. 4.3.

According to the Nyquist theorem, the time resolution Δt of the detector should not be larger than twice the smallest quantum-beat period to be resolved. This is crucial to avoid aliasing. The sampling frequency of the signal is thus given as

$$\nu_s = \frac{1}{2\Delta t}. \tag{4.23}$$

From the Planck-Einstein relation, this corresponds to a maximum photon energy (in natural units) of

$$\omega_s = 2\pi\nu_s = \frac{\pi}{\Delta t} \tag{4.24}$$

such that the energy resolution of the calculation grid is given as

$$\Delta\omega = \frac{2\omega_s}{N_{\mathrm{FFT}}} = \frac{2\pi}{N_{\mathrm{FFT}} \cdot \Delta t}. \tag{4.25}$$

Here N_{FFT} corresponds to the number of points in the calculation grid of the FFT. For example, the highest energy ω_s that we can reconstruct with a detector resolution of $\Delta t = 0.5$ ns is $\sim 886\ \Gamma$, where Γ is the linewidth of ^{57}**Fe**.
To speed up the FFT calculations, N_{FFT} can be chosen such that it is a power of 2. If N_{FFT} is even, the energy grid is given as

$$\left(-\frac{N_{\mathrm{FFT}}}{2}, \cdots -1, 0, 1 \cdots, \frac{N_{\mathrm{FFT}}}{2} - 1\right) \cdot \Delta\omega \tag{4.26}$$

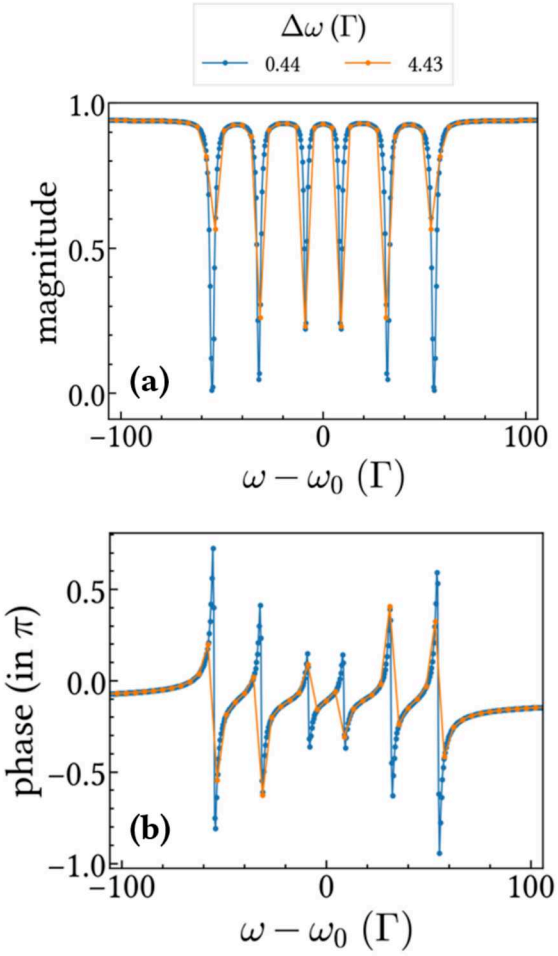

Figure 4.3.: The calculation of the (a) magnitude and the (b) phase of the energy response of an unmagnetized 2.5 µm ^{57}Fe foil on an energy grid with different resolutions. $\Delta\omega$ = 4.43 Γ is too big to correctly resolve the width and height of the peaks in the energy response.

else

$$\left(-\frac{N_{\mathrm{FFT}}-1}{2}, \cdots -1, 0, 1 \cdots, \frac{N_{\mathrm{FFT}}-1}{2}\right) \cdot \Delta\omega. \tag{4.27}$$

The corresponding calculation grid in the time domain is then given as

$$(0, 1, 2 \cdots, N_{\mathrm{FFT}} - 1) \cdot \Delta t. \tag{4.28}$$

4.3.2. Phase wrapping

Since the phase of the object is 2π-periodic, phase shifts of ϕ and $\phi + 2n\pi$ cannot be distinguished (where n is some integer) from each other. While retrieving $\hat{\boldsymbol{O}}$, our algorithm can choose any of the values of n at each energy. This may lead to phase jumps or "wrapping" in the reconstruction as soon as ϕ hits $-\pi$ or π. This is shown in Fig. 4.4. In this thesis, we have simply used the *numpy.unwrap* function to unwrap the phase, wherever necessary. However, noise in the reconstruction can sometimes make it difficult or even impossible. The more sophisticated approach would be to adopt the 'refractive' ptychography formalism as mentioned in [Wit+22]. This is discussed in Appendix C.1.

4.3.3. Stochastic algorithms

Algorithms **1** and **2** are deterministic algorithms which make use of the 'full-batch' gradient, i.e., we calculate the update on the object by taking into account the entire ptychogram. Stochastic algorithms, on the other hand, introduce an element of randomness to their computations and explore larger solution spaces than deterministic algorithms. The convergence properties of the stochastic implementation are usually noisier but it can escape saddle points and sharp local minima more easily [KLY18; MUZ21].

We can also implement the gradient algorithms in a stochastic manner, as shown in algorithm **3**. We shuffle and divide the ptychogram dataset into randomly sampled 'minibatches' of size s. In the inner **for** loop, we update the object in the direction determined by the cost of the k-th minibatch. The outer **for** loop is complete when all the minibatches of the ptychogram have been sequentially used to update the object $\hat{\boldsymbol{O}}$. This two-**for** loop process is repeated either until a convergence criterion is met

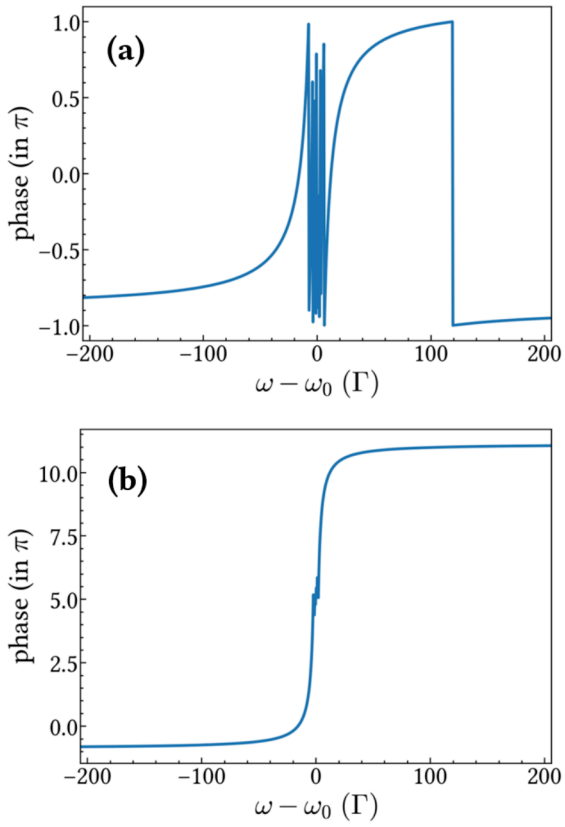

Figure 4.4.: The (a) wrapped and (b) unwrapped phase of the energy response of an enriched stainless steel foil of thickness 20 µm simulated using NEXUS [Boc23]. The wrapped phase has discontinuities and oscillates between $-\pi$ and π around 0.

or a maximum number of engine iterations is reached. The stochastic algorithms thus utilize the gradient of the 'minibatches' for updating the object.

Algorithm 3 Stochastic gradient-based algorithm for NRS ptychographic engine

max_iter ← *maximum number of engine iterations*
$\boldsymbol{b}_0, \boldsymbol{b}_1 \cdots \boldsymbol{b}_{M-1}$ ← *measurements*
$\Delta\omega_0, \Delta\omega_1 \cdots \Delta\omega_{M-1}$ ← *Dopper detunings*
$\hat{\boldsymbol{P}}$ ← *probe* $\in \mathbb{C}^N$
$s \in (1, M/2)$ ← *Size of a minibatch*
Initialize: $\hat{\boldsymbol{O}} \leftarrow \hat{\boldsymbol{O}}^0 \in \mathbb{C}^N$, $\alpha \leftarrow \alpha^0 \in (0,1)$, $i \leftarrow 0$
repeat
    Shuffle the measurements
    Split the measurements into M/s *minibatches:*
    for $k \in \{0, 1, \ldots, M/s - 1\}$ **do**
        Update object for k-th minibatch of size s:
        Initialize: $\rho \leftarrow 0$, $\nabla_{\hat{\boldsymbol{O}}}\rho \leftarrow 0$
        for $j \in \{ks, ks+1, \ldots (k+1)s\}$ **do**
            Forward:
            $\hat{\boldsymbol{P}}_j \leftarrow \text{DETUNE}\ (\hat{\boldsymbol{P}}, \Delta\omega_j)$
            $\hat{\boldsymbol{Z}}_j \leftarrow \text{diag}\left(\hat{\boldsymbol{P}}_j\right) \cdot \hat{\boldsymbol{O}}$
            Compare and calculate gradient:
            $\rho \leftarrow \rho + \text{dist}(\boldsymbol{b}_j\ , |\mathbf{F} \cdot \hat{\boldsymbol{Z}}_j|^2)$
            $\nabla_{\hat{\boldsymbol{O}}}\rho \leftarrow \nabla_{\hat{\boldsymbol{O}}}\rho + \nabla_{\hat{\boldsymbol{O}}}\text{dist}(\boldsymbol{b}_j\ , |\mathbf{F} \cdot \hat{\boldsymbol{Z}}_j|^2)$
        end for
        Accelerate:
        $\alpha \leftarrow$ STEPSIZE_SELECTION
        $\boldsymbol{d} \leftarrow$ ACCELERATION_SCHEME (α, $\nabla_{\hat{\boldsymbol{O}}}\rho$)
        Update: $\hat{\boldsymbol{O}} \leftarrow \hat{\boldsymbol{O}} + \boldsymbol{d}$
    end for
    if $i =$ *max_iter* **then**
        Stop the engine.
    else
        $i \leftarrow i + 1$

30: **end if**
31: **until** CONVERGED
32: **return** $\hat{O}$

4.3.4. Automatic differentiation

Automatic differentiation is a methodology for computing derivatives of functions by breaking them down into primitive elementary operations. The derivatives of these simpler operations can then be combined using the chain rule. The resultant derivatives are computed with machine precision while maintaining computational efficiency.

Once we provide the physics-based experimental forward model in the automatic differentiation framework, we can automatically calculate the first or higher-order derivatives of the cost function with respect to any required model variables. Furthermore, if we change the forward model, the changes are instantly transferred to the derivatives. This gives two significant benefits for ptychography. First, the derivatives of both the object and probe variables are easily accessible. Second, we can readily incorporate changes to model components such as the interaction mechanism or adding the regularization or noise terms into ρ. Since our ptychography engine consists of gradient algorithms based on calculating derivatives, we implement the bulk of it in *Pytorch* - which is a computing framework based on Python and C++. It uses automatic differentiation to efficiently compute gradients - enabling flexible and faster analysis of the phase problem.

4.3.5. Incoherent forward model

The solution of an inverse problem is as good as the validity of the forward model. The forward model used by the ptychography engine in Eq. (3.34) assumes that all photons measured at the detector are scattered via fully coherent processes. However, there are some possible incoherent contributions to the experimental data:

1. **Spatial incoherence**: In a nuclear forward scattering experiment, even a minimal thickness distribution in the probe has to be taken into account via an incoherent superposition model, as described in [Gol+18]. This is because the transverse coherence length of the setup is just a few nanometers (see Appendix B). The

nuclear resonant scattering signal is given as the incoherent sum of the intensities of the time response from the different thicknesses of the probe.

2. **Angular incoherence**: If an experiment is performed in a grazing incidence geometry, as in Sec. 6.5, there is a distribution in the incidence angles of the X-ray photons on the probe due to the divergence of the beam. This results in scattering from different incoherent parts of the beam, at length scales longer than the transverse coherence length. The time response of the probe is given by a sum of the intensities of the response from the different angles.

To get an incoherent forward model, we replace the fixed probe with a probe distribution. The intensity at the detector for Doppler detuning $\Delta\omega_j$ is given as

$$\boldsymbol{I}_j = \sum_m w_m |\mathbf{F} \cdot \mathrm{diag}\left(\hat{\boldsymbol{P}}_j^m\right) \cdot \hat{\boldsymbol{O}}|^2. \tag{4.29}$$

The extra index m runs over the different probe modes illuminating the object with relative weights w_m.

5. Numerical studies

We now demonstrate the testing and refining of the numerical algorithms that underpin our ptychography engine. Through a series of carefully crafted examples and case studies, this chapter aims to bridge the gap between theoretical concepts and practical application. We conduct detailed sensitivity analyses by systematically varying parameters and observing the performance of the phase retrieval.

Simulations facilitate benchmarking of the engine against known solutions or existing methods. Because the hyperfine structure of ^{57}**Fe** is well known, ^{57}**Fe** and stainless steel foils are routinely used as reference samples at nuclear resonant scattering beamlines. We simulate a simple nuclear forward scattering ptychography experiment as shown in Fig. 3.9 using NEXUS [Boc23]. We consider a stainless steel foil 95% enriched with ^{57}**Fe** and of thickness 20 μm as the probe. The magnitude of the energy response of the probe is a Lorentzian with full-width half maximum $\sim$ 10 Γ. As discussed in Sec. 3.2, the broad energy response of the probe ensures sufficient overlap between adjacent measurements. A 95% enriched ^{57}**Fe** metal foil of thickness 2.5 μm is taken as the object. The object foil has a hyperfine field of 33 T and is magnetized in the direction parallel to the polarization of the incident synchrotron radiation. The simulated energy response of the object and the probe are shown in Fig. 5.1 and Fig. 5.2, respectively. Because of the selection rules for the transitions, only four resonant lines appear in the energy response of the ^{57}**Fe** foil [Röh05].

The simulations are done on a 4096 point energy grid with $(\omega_{\min}, \omega_{\max}, \Delta\omega) = (-886.62, 886.19, 0.43)$ Γ. The probe and the object are defined on this grid and are therefore 4096×1 pixels in size. The noiseless ptychogram 'A' (Fig. 5.3(b)) is then obtained by detuning the probe at 512 different energies $\Delta\omega_j$ in the range of $(-200, 200)$ Γ, with equal steps of 0.78 Γ between them. Due to the broad energy response of the probe, this creates an overlap of ~90% between consecutive measurements. The detuning profile is plotted in Fig. 5.3(a). Linear interpolation is used to detune the real and

imaginary parts of the probe function.

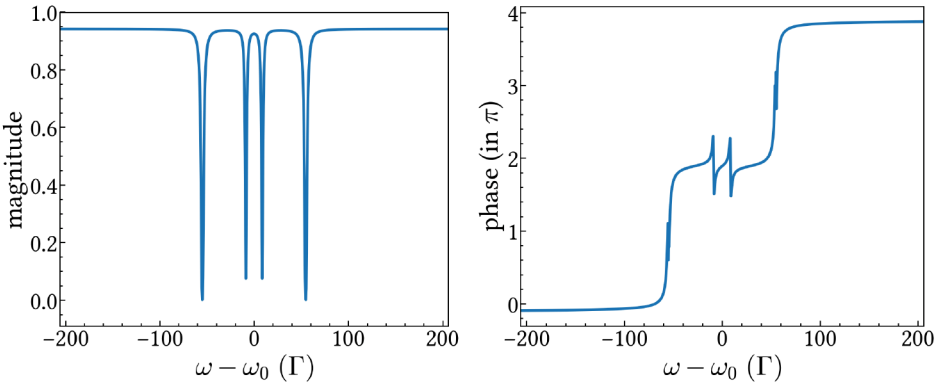

(a) (b)

Figure 5.1.: Magnitude (a) and phase (b) spectrum of the "true" object (^{57}**Fe** foil of thickness 2.5 µm).

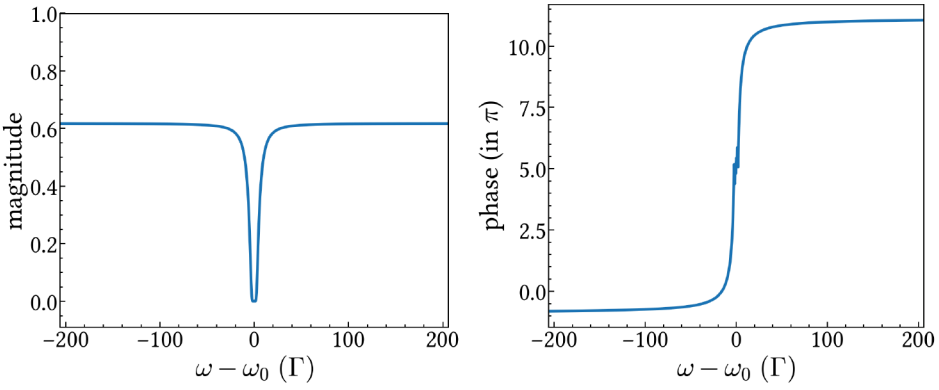

(a) (b)

Figure 5.2.: Magnitude (a) and phase (b) spectrum of the probe (enriched stainless steel foil of thickness 20 µm).

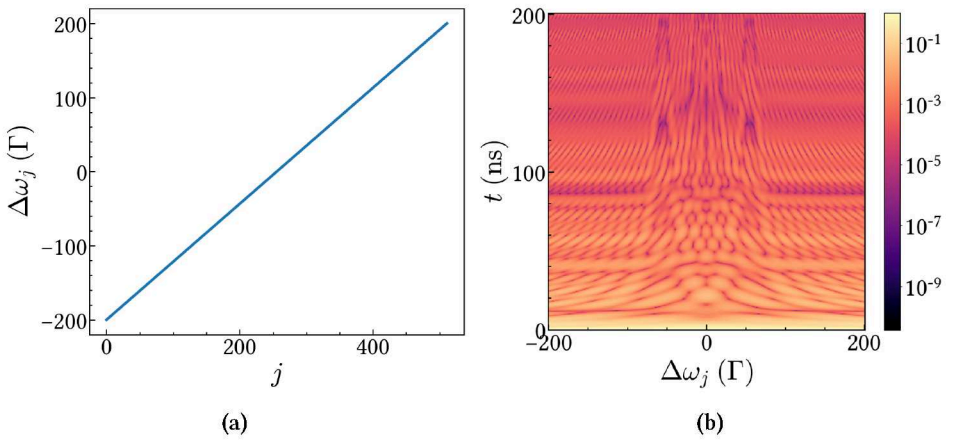

Figure 5.3.: (a) The detuning induced in the probe using the Doppler drive. (b) The normalized intensity of the ptychogram 'A' simulated in the noiseless case.

5.1. Comparing the different algorithms

We can implement phase retrieval from the ptychogram using different variants of the gradient-based algorithms. We therefore first compare the performance of different deterministic and stochastic algorithms tested during this work, which are listed with their run parameters in Table 5.1 and 5.2, respectively. All the algorithms have been described in detail with their pseudo-codes in Appendix A.

For each algorithm, we start with the prior knowledge that our object is mostly "transparent", i.e., the resonant energy lines of the foil are very sharp. Thus we initialize the object $\hat{\boldsymbol{O}}^{(0)}$ as a 4096×1 array of ones. The object is then updated at each iteration i as

$$\hat{\boldsymbol{O}}^{(i+1)} = \hat{\boldsymbol{O}}^{(i)} + \boldsymbol{d}^{(i)}. \tag{5.1}$$

To demonstrate the convergence of the algorithms, we track not only the cost function ρ but also the relative residual value

$$R_{\text{value}} = \frac{\left\|\hat{\boldsymbol{O}}^{(i)} - \hat{\boldsymbol{O}}^{*}\right\|}{\left\|\hat{\boldsymbol{O}}^{(0)} - \hat{\boldsymbol{O}}^{*}\right\|} \tag{5.2}$$

Algorithm	parameters	values
GD	(α)	(0.03)
aGD-CM 1	(α , β)	(0.003, 0.77)
aGD-CM 2	(α , β)	(0.003, 0.95)
aGD-NAG	(α , β)	(0.003, 0.95)
GD-backtrack	(α, η)	(1, 0)
GD-BB	(α, η)	(1, 0.77)
CGD-backtrack	(α)	(1)

Table 5.1.: Table of deterministic algorithms described in Appendix A.

Algorithm	parameters	values
SGD	(α, β, batch-size)	(0.003, 0, 20)
SGD-NAG	(α, β, batch-size)	(0.003, 0.77, 20)
ADAM	(α, β_1, β_2, batch-size)	(0.003, 0.9, 0.999, 20)

Table 5.2.: Table of stochastic algorithms described in Appendix A.

and the relative update

$$R_{\text{grad}} = \frac{\left\|\boldsymbol{d}^{(i)}\right\|}{\left\|\boldsymbol{d}^{(0)}\right\|} \tag{5.3}$$

of the object as the iteration number i progresses. Here $\hat{\boldsymbol{O}}^*$ denotes the true solution of the problem, which is the response of the ^{57}**Fe** foil shown in Fig. 5.1. To check the quality of the reconstruction, we calculate the mean square error (MSE) between the magnitudes of the final reconstructed object $\hat{\boldsymbol{O}}^r$ and the true solution $\hat{\boldsymbol{O}}^*$ as

$$\text{MSE} = \frac{1}{L}\sum_{q=0}^{L-1}(|\hat{\boldsymbol{O}}^r|_q - |\hat{\boldsymbol{O}}^*|_q)^2 \tag{5.4}$$

where $L = 4096$ is the length of $\hat{\boldsymbol{O}}^r$.

We first demonstrate how the different algorithms perform on the noiseless phase retrieval problem by applying them on the ptychogram 'A'. For all algorithms, we choose

Algorithm	GD	aGD-CM 1	aGD-CM 2	aGD-NAG	GD-backtrack	GD-BB	CGD-backtrack
MSE	0.105	0.091	0.092	0.091	0.092	0.097	0.092

Table 5.3.: Mean square error of the reconstructed object.

to minimize the amplitude cost function (similar to Eq. (4.10)),

$$\rho = \frac{1}{2L} \sum_j \left\| |\mathbf{F} \cdot \hat{\boldsymbol{Z}}_j| - \sqrt{\boldsymbol{b}_j} \right\|^2 . \tag{5.5}$$

where $L = 4096$ is the length of $\hat{\boldsymbol{O}}^r$. In Fig. 5.4, we see the object reconstructed by the different algorithms after 500 engine iterations. Both the magnitude and the phase are reconstructed almost perfectly in our region of interest (ROI) - which is the energy range of the Doppler detunings ($-200\ \Gamma$, $200\ \Gamma$). The MSE of the object reconstructed by the different algorithms is also calculated over the ROI and is given in Table 5.3.

Except for GD and GD-backtrack, all the algorithms converge to the true solution. We can also study the convergence behavior of the different algorithms in Fig. 5.5. In Fig. 5.5a, we see that for GD, the cost function decreases for the first ~ 60 iterations. After this, it plateaus and does not decrease. This could be characteristic of a local minimum or a saddle point in the landscape of ρ and is often encountered, e.g., in non-convex optimization of neural networks, especially when using GD on constant step-sizes [AS21].

The plateau phenomenon caused by vanishing gradients can be mitigated by using acceleration techniques. For example, by adding the β term in aGD-CM 1, we add 'classic' momentum to the gradient and overcome the plateau region faster than GD-backtrack. The 'classic' momentum approach, however, is less stable with respect to the increase in the β term. For example, the higher β setting aGD-CM 2 performs worse than aGD-CM 1. This is also evident in the oscillations of the corresponding R_{val} term of aGD-CM 2 in Fig. 5.5c. If the β term is too high, the algorithm starts to oscillate around the minimum. The more stable form of adding momentum to the optimizer is by using Nesterov's method [Nes83], as can be seen in the smoother convergence curves of aGD-NAG.

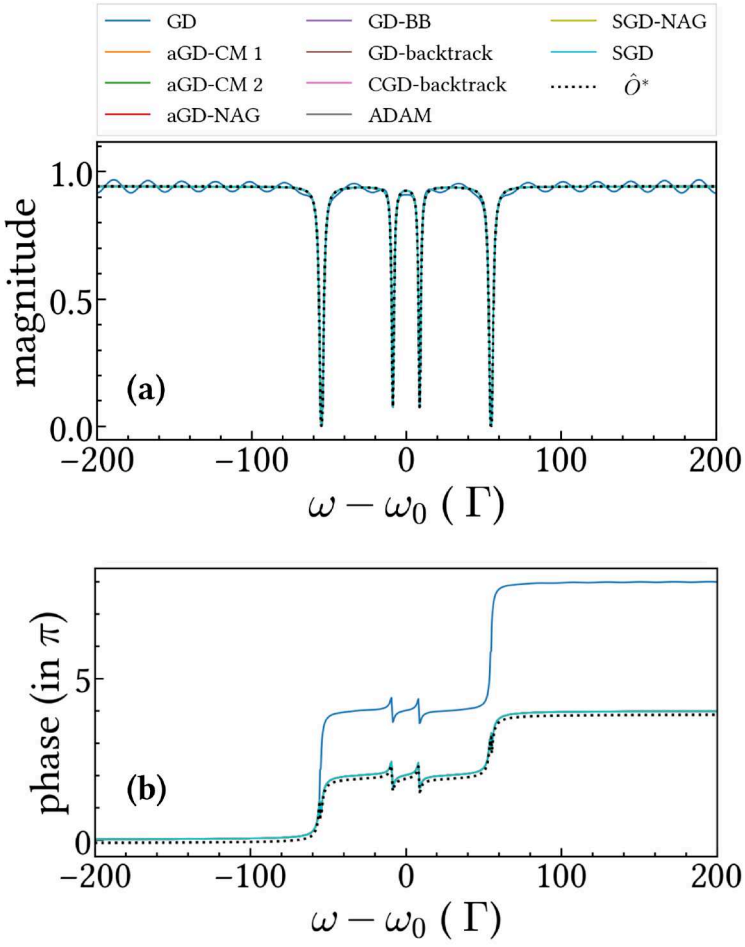

Figure 5.4.: The magnitude and phase spectrum of the object reconstructed by the different algorithms after 500 iterations. Aside from GD, most algorithms reconstruct the object perfectly in the absence of noise in the measurements.

Another way to accelerate gradient descent is to use a stepsize selection scheme. For example, if we apply Armijo backtracking to adapt the step size (GD-backtrack), we reach convergence faster. Backtracking at each step can be expensive, therefore we also demonstrate GD-BB which uses the Barzilai-Borwein (BB) method [TZ18] to select a stepsize and then backtracks in a non-monotonic fashion as described in Appendix A.2. The BB-stepsize selection is based on a scalar approximation of the second-order derivative (Hessian) from the difference in the gradient of the last two iterates. It generally converges faster than GD-backtrack[1].
We can also decide to choose a conjugate direction instead of the steepest descent direction for our algorithm. This is implemented in CGD-backtrack based on the Hager Zhang method [HZ05] and non-monotonic backtracking line search. Even with the best tuning of parameters, the number of backtracks required at each iteration is significantly higher than the other methods, and therefore each iteration takes longer. In our implementation, we "switch off" the backtracking after 50 iterations. The algorithm also takes longer than 500 iterations to converge. SGD, SGD-NAG and ADAM are stochastic algorithms that shuffle and divide the datasets in minibatches of size $s = 20$ at each iteration i. We derive the following conclusions from our algorithm tests:

- Among all the deterministic algorithms, GD-BB performs the best. It is only overtaken by the slower and more expensive CGD-backtrack after 200 iterations. The biggest advantage of our implementation of GD-BB is its adaptive nature - it does not require any tuning of parameters and is readily generalizable to any choice of ρ and regularization terms.

- Both stochastic methods SGD and SGD-NAG perform better than the deterministic methods. SGD-NAG is SGD with Nesterov acceleration and converges only in 20 engine iterations for our test problem.

[1] Since BB-stepsize selection is non-monotonic, its convergence is more usefully determined by checking if R_{grad} falls below a small threshold value.

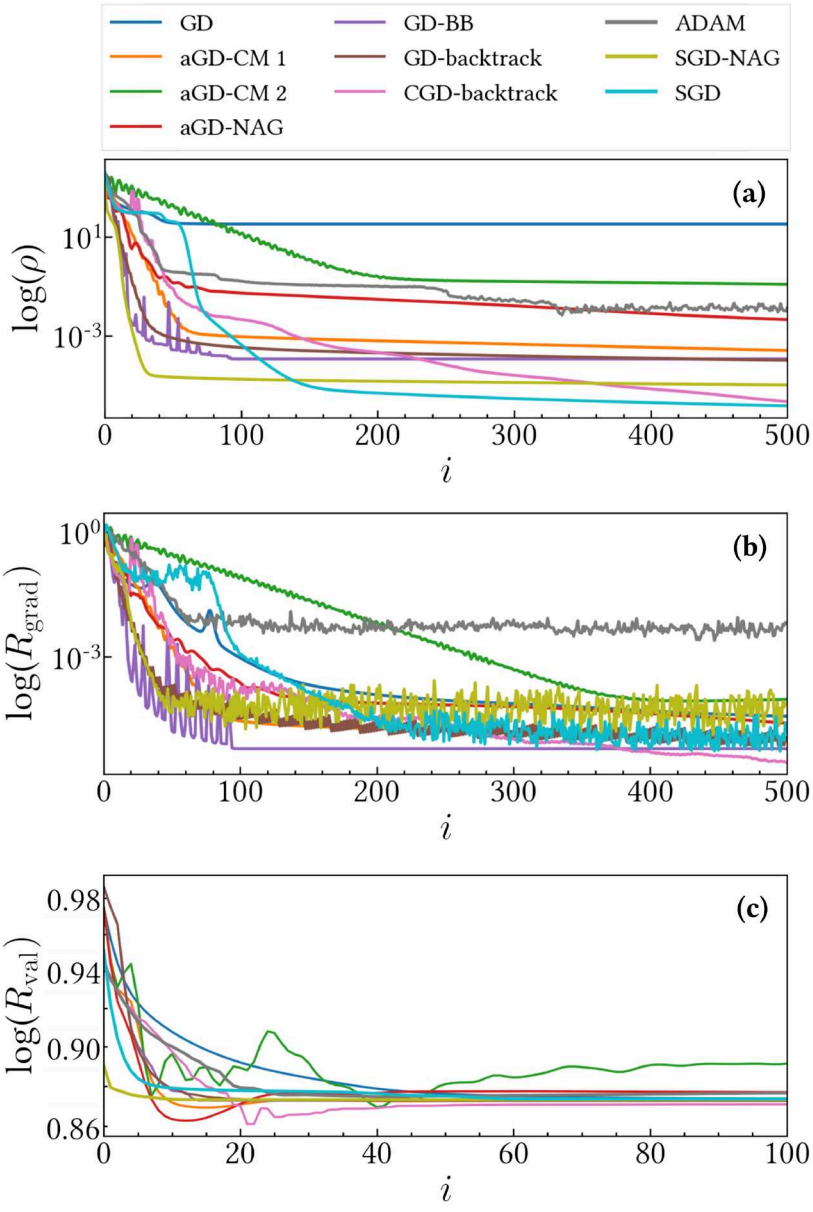

Figure 5.5.: The convergence curves of the different algorithms in Table 5.1 and 5.2.

5.2. Comparing the different noise cases

Till now we have been studying the noiseless ptychographic phase retrieval problem. In this section, we move to investigating the noisy form of the problem which is more relevant for phase retrieval from experimental data.

For our first series of tests, we simulate ptychograms with different levels of Poisson and Gaussian noise according to the noise model in Eq. (4.5). First, each pixel of the ptychogram is randomly sampled from a Poisson distribution given by Eq. (4.6) such that the total number of photons equals N_p. We choose N_p as some fraction of N_p^*, where $N_p^* \approx 3\times10^9$ is the total number of photons in the "ideal" noiseless histogram 'A' simulated using NEXUS. Thus, the ratio N_p/N_p^* gives the relative intensity of the noisy ptychogram. Thereafter, Gaussian noise of variance σ^2 is added to each pixel. In nuclear resonant scattering experiments, avalanche photodiode (APD) arrays are used to detect the scattered photons based on the photo-electric effect. An avalanche can be initiated not only by incident photons, but also by thermally generated carriers or band-to-band tunneling. These 'dark count rates' are very low for the high-quality APDs used in NRS at room temperature and are unlikely to contribute much noise to the measured data. The dominant sources of Gaussian noise are therefore assumed to be the very small readout noise generated by the thermal fluctuations in the many interconnected electronics components of the detection system and cosmic background, such that the Gaussian noise variance is very low. The signal to noise ratio (SNR) of the ptychogram can be defined as

$$\mathrm{SNR}_{jq} = \frac{\boldsymbol{b}_{jq}}{\sqrt{\boldsymbol{b}_{jq} + \sigma^2}}, \tag{5.6}$$

where $\boldsymbol{b}_{jq}$ is the intensity measured at time $q\Delta t$ and Doppler detuning $\Delta\omega_j$. Next, we perform phase retrieval using GD-BB for each of the three cost functions described in Sec. 4.1.1, i.e., the amplitude cost function [Eq. (4.10)], the intensity cost function [Eq. (4.15)] and the generalized Anscombe transform (GAT) cost function [Eq. (4.18)]. Since we only want to compare the three cost functions under different noise conditions, we use the true object $\hat{\boldsymbol{O}}^*$ as the starting guess to decrease the convergence runtime.
The accuracy of the phase retrieval is characterized by the mean squared error (MSE) [Eq. (5.4)] between the retrieved[2] and true object over the range of the Doppler de-

[2]Before the comparison, the retrieved object was scaled by N_p/N_p^*, i.e., the relative photon intensity in

tunings (−200 Γ, 200 Γ). Each MSE is computed over 50 realizations of the same noise setting in the ptychogram. We plot the MSE for the different noise cases in Fig. 5.6. The error bars indicate the standard deviation of the plotted MSE value. We conclude three main points from the noise plots:

- In Fig. 5.6 we see that for all three cost functions, the MSE decreases as the relative intensity in the ptychogram increases (i.e., $N_p/N_p^* \longrightarrow 1$). This is to be expected from the signal-to-noise ratio in Eq. (5.6).
- In low photon intensity regimes (low values of N_p/N_p^*), the noise in the ptychogram is more Poisson or mixed Poisson-Gaussian. As the photon intensity increases, the likelihood of the noise becomes more 'Gaussian'. Because it is based on a Gaussian likelihood, the intensity cost function performs comparably or slightly better for high photon count regimes while it performs worse in low photon count regimes than the amplitude and GAT cost functions.
- The GAT cost function does not have a significant advantage over the amplitude cost function at low photon intensity, even as the variance of the added Gaussian noise is increased. This might indicate that even with added random noise of variance $\sigma^2 = 10$ per pixel, the simulation follows the Poisson likelihood model.

Next, we take a qualitative look at the phase retrieval results for the ptychogram under different noise conditions (see Fig. 5.7):

1. Ptychogram B1, B2 and B3 are Poisson-sampled under high to low SNR conditions with $N_p/N_p^* = 1$, 0.01 and 0.001.
2. Ptychogram C1, C2 and C3 have Gaussian noise with variance σ^2= 0.1, 1 and 10 per pixel.
3. Ptychogram D1, D2 and D3 are Poisson-sampled under medium SNR conditions ($N_p/N_p^* = 0.01$) and have Gaussian noise with variance σ^2= 0.1, 1 and 10 per pixel.

In the subsequent analysis, we run the algorithms with the amplitude cost function in Eq. (5.5). The initial object guess ($\hat{\boldsymbol{O}}^{(0)}$) was taken as 4096×1 array of ones. Our region of interest (ROI) is the energy range from -200 Γ to 200 Γ.

the noisy histogram. This relationship is given by Parseval's energy theorem.

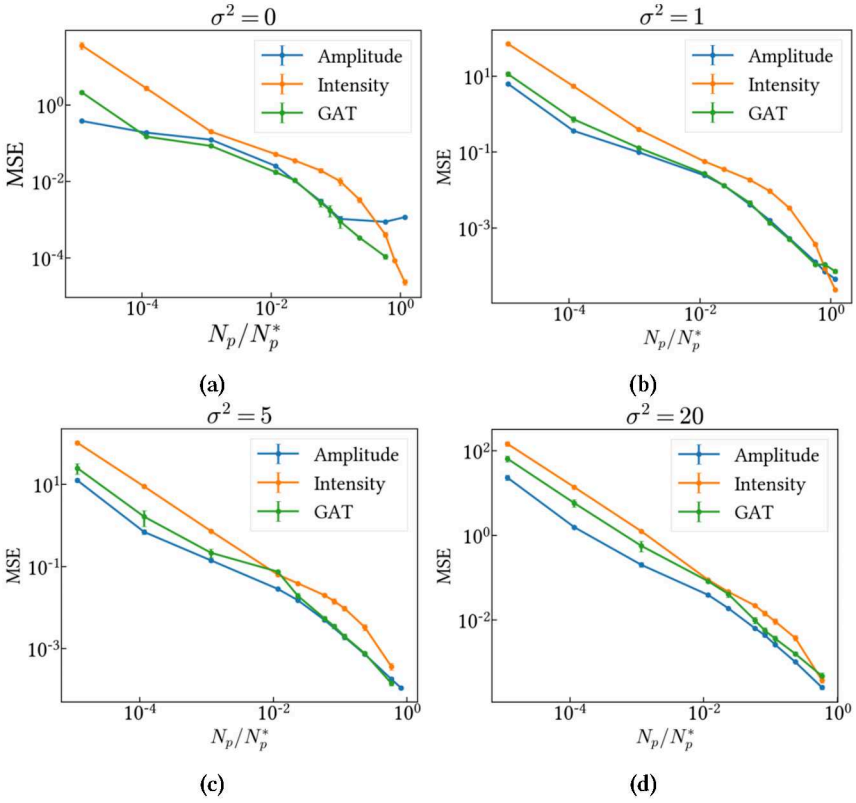

Figure 5.6.: Log-Log plot of the mean squared error (MSE) of the retrieved object for the different cost functions against N_p/N_p^* i.e. the relative photon intensity of the ptychogram compared to the ideal 'noiseless' case. The four plots represent different levels of Gaussian noise added to the ptychogram. GAT stands for the generalized Anscombe transform metric in Eq. (4.17).

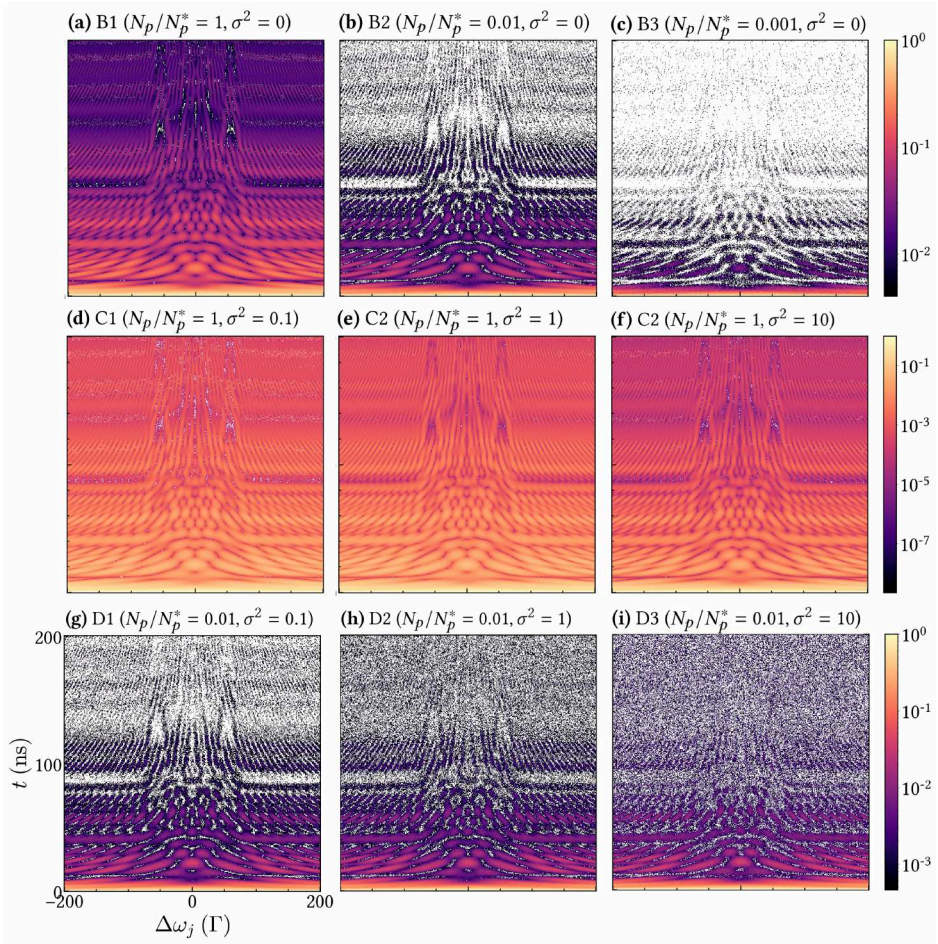

Figure 5.7.: The normalized intensity of the different noisy ptychograms used for object reconstructions. Ptychograms B1, B2 and B3 only have Poisson noise. Ptychograms C1, C2 and C3 have Gaussian noise added to the measurements. Ptychograms D1, D2 and D3 have a mixture of Poisson-Gaussian noise distribution.

5.2.1. Poisson noise

To demonstrate the effect of the Poisson noise in the measurements, we choose algorithms aGD-NAG, SGD-NAG, and GD-BB to run the ptychographic engine on pty-

chograms B1 (high SNR), B2 (medium SNR) and B3 (low SNR). Here, SGD-NAG 1 and SGD-NAG 2 are implementations of SGD-NAG with batch sizes 1 and 20, respectively. We show the convergence curves of the different algorithms in Fig. 5.8(a) and 5.8(b). For ptychogram B1, we see that algorithm SGD-NAG 1 converges at the lowest iteration number. However, it is not the fastest, since each iteration takes longer than SGD-NAG 2. The stochastic methods SGD-NAG 1 and SGD-NAG 2 converge at lower iteration numbers than the deterministic methods. Eventually, all the algorithms converge to the same object in the region of interest.

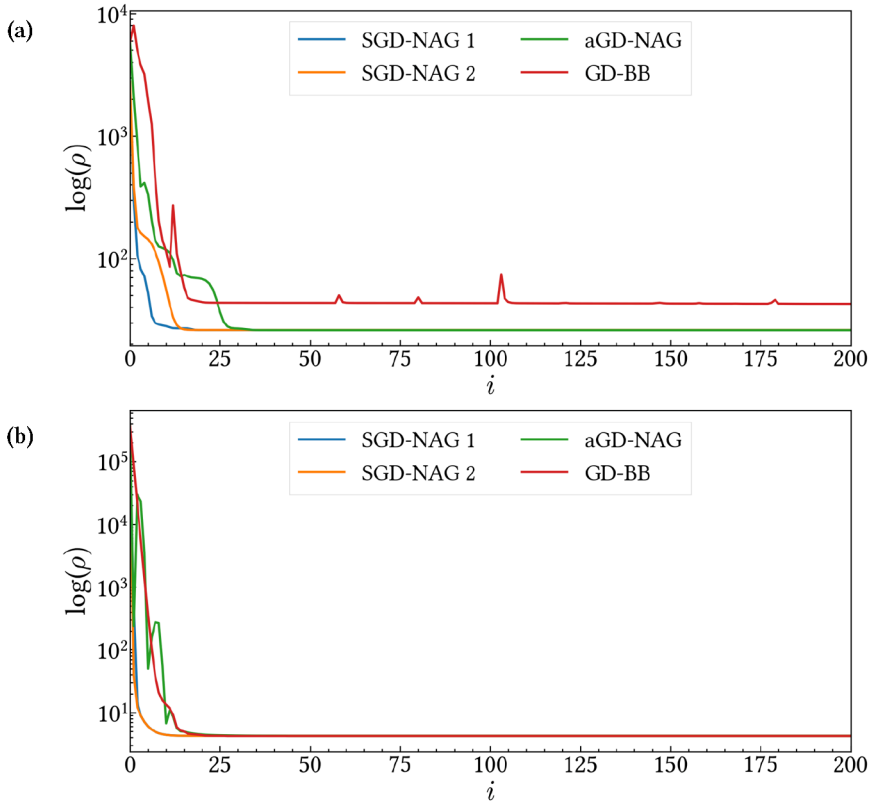

Figure 5.8.: (a) The convergence behavior of the different algorithms for ptychogram B1 (the high SNR case) and (b) ptychogram B3 (the low SNR case).

In Fig. 5.9 we see that the baseline of the magnitude of the reconstructed object has fluctuations that decrease as the relative photon intensity in the ptychogram increases. For low light conditions (see Fig. 5.9(c)) where $N_p/N_p^* = 0.001$, the reconstructed resonance peaks are broader, and the ratio between the heights of the peaks is not preserved. Nonetheless, the four peaks can be identified in their correct locations for all three cases. In an experiment, this means that to get a good estimate of the relative probabilities of the hyperfine transitions, we have to surpass the low light regime by counting for longer times.

On examining the phase response of the reconstructed object in Fig. 5.10, we see that it can be globally shifted. In some of the tests, e.g. in Fig. 5.10(c), the reconstructed phase is "wrapped" at the resonance lines. As explained in Appendix 4.3.2, the reconstructed phase can take any arbitrary value from $-\pi$ to π at the outer resonance lines where the object's scattering response is strongest and $|\hat{O}| = 0$. Thus, there is an ambiguity in the unwrapped phase shift of the object between the three cases. To unwrap the phase, we are using the *numpy.unwrap* function in *Python*.

We also plot the corresponding time response of each reconstructed object in Fig. 5.15(a). The response of the object reconstructed from the low count ptychogram B3 decays faster with time. We conclude that for the forward model with a fixed probe and low photon intensity in the measurements (higher Poisson "noise"), the ptychography engine reconstructs a "weakly" scattering object - with weaker phase shifts and lower peak contrast. The time response of the reconstructed object also has a lower overall intensity.

5.2.2. Gaussian noise

Next, we test the effect of adding Gaussian noise to the noiseless ptychogram 'A' by running the phase retrieval on ptychograms C1, C2 and C3. As the variance of noise per pixel increases from 0.1 to 10, the fluctuations in the baseline start increasing. However, the ratio of the peak heights and widths is maintained. The hyperfine magnetic field can also be correctly determined since the peaks are reconstructed at their correct positions. Additionally, we see in Fig. 5.12 that the reconstruction of the phase response is even more stable to the increase of the Gaussian noise.

From the temporal response of the reconstructed objects (Fig. 5.15(b)), we see that

the object reconstructed from ptychogram B3 has random noise beyond ~ 300 ns. The object reconstructed from ptychograms with smaller Gaussian noise (ptychogram B1 and B2) is correct for longer times. Therefore, there is a relation between the amount of background Gaussian noise in the ptychogram and the maximum time for which we can reconstruct the object's temporal response accurately.

5.2.3. Mixed Poisson-Gaussian noise

In the case of ptychogram D1, D2 and D3, we see in Fig. 5.13 that the magnitudes of the reconstructed objects have much noisier baselines compared to the ptychogram B2, with the same relative photon intensity but no Gaussian noise.

In this case, we have modeled the noisy ptychograms for the Poissonian measurement process with a lower relative intensity $N_p/N_p^* = 0.01$. Even though the peaks in the reconstructed object are visible at the correct positions, the peak ratio is not maintained. This is because at low photon counts, the nuclear transitions in the object with smaller peak heights in the energy spectrum do not get expressed in the ptychogram, since the probabilities of the associated scattering events is lower.

The effect of increasing Gaussian noise is also seen in the time response of the reconstructed object Fig. 5.15(c). Compared to ptychograms C1, C2 and C3, the relative photon intensity in the ptychograms D1, D2 and D3 is lower by a factor of 10^{-2}. We see that not only does the time response of the reconstructed objects decay faster (the Poisson 'noise' effect), but after some time a background Gaussian random noise takes over. The effect of the added Gaussian noise also sets in much quicker (at ~ 75 ns for the reconstruction from ptychogram D3).

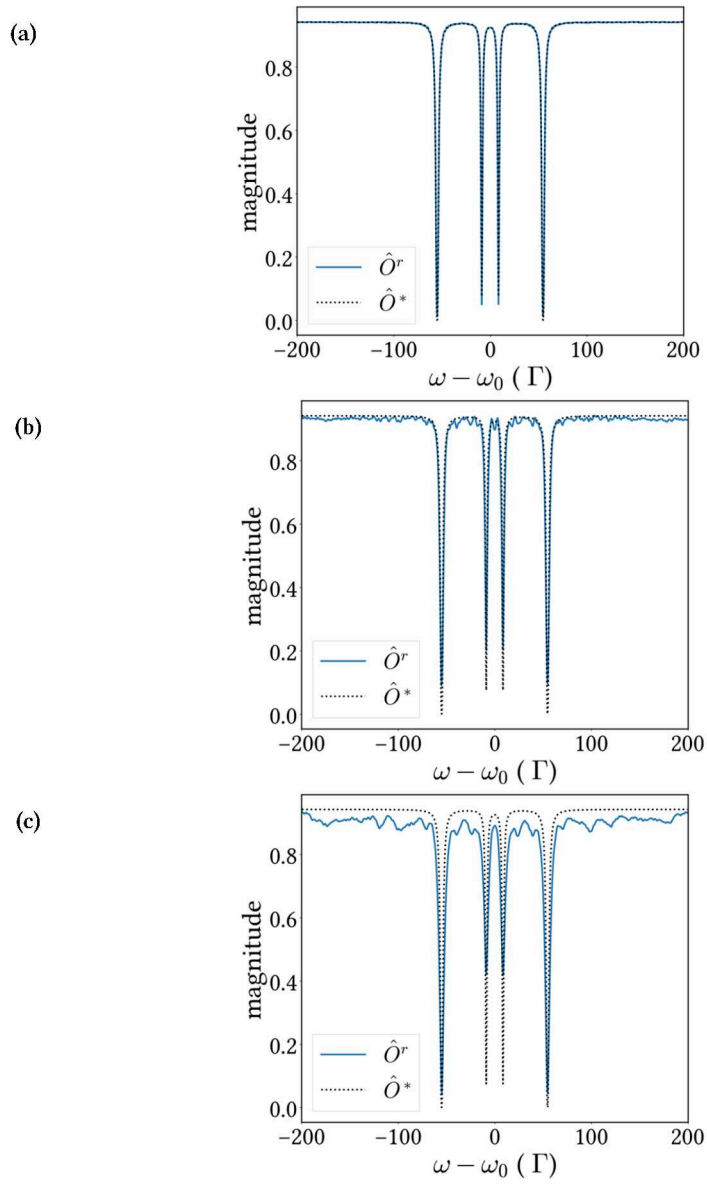

Figure 5.9.: The magnitude of the object $\hat{\boldsymbol{O}}^r$ reconstructed from ptychograms (a) B1 (b) B2 and (c) B3 with increasing Poisson noise. The dotted line represents the magnitude of the true object $\hat{\boldsymbol{O}}^*$.

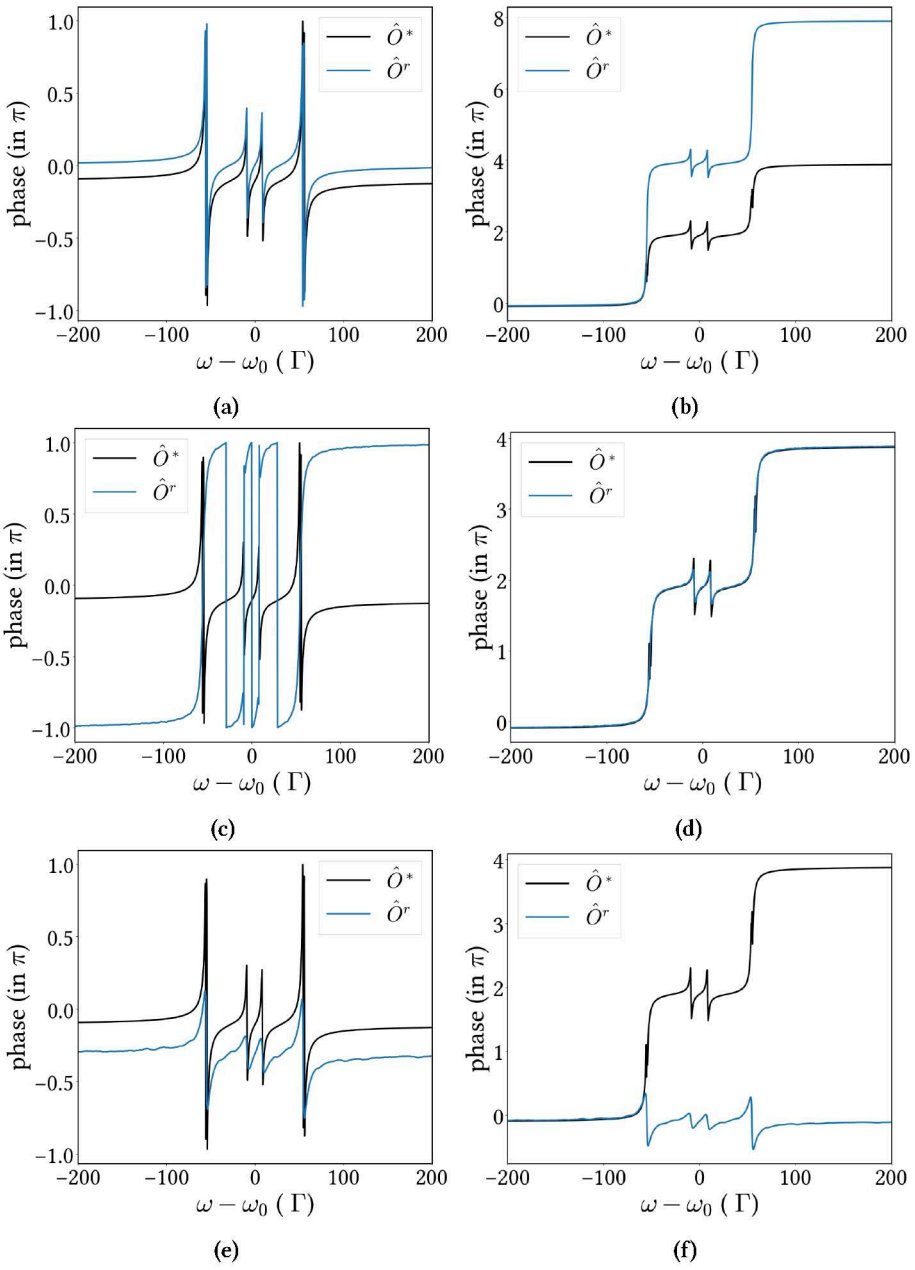

Figure 5.10.: The wrapped (a),(c),(e) and unwrapped (b),(d),(f) phase response of the objects reconstructed from ptychograms B1, B2 and B3, respectively. The black line represents the phase response of the true object $\hat{O}^*$.

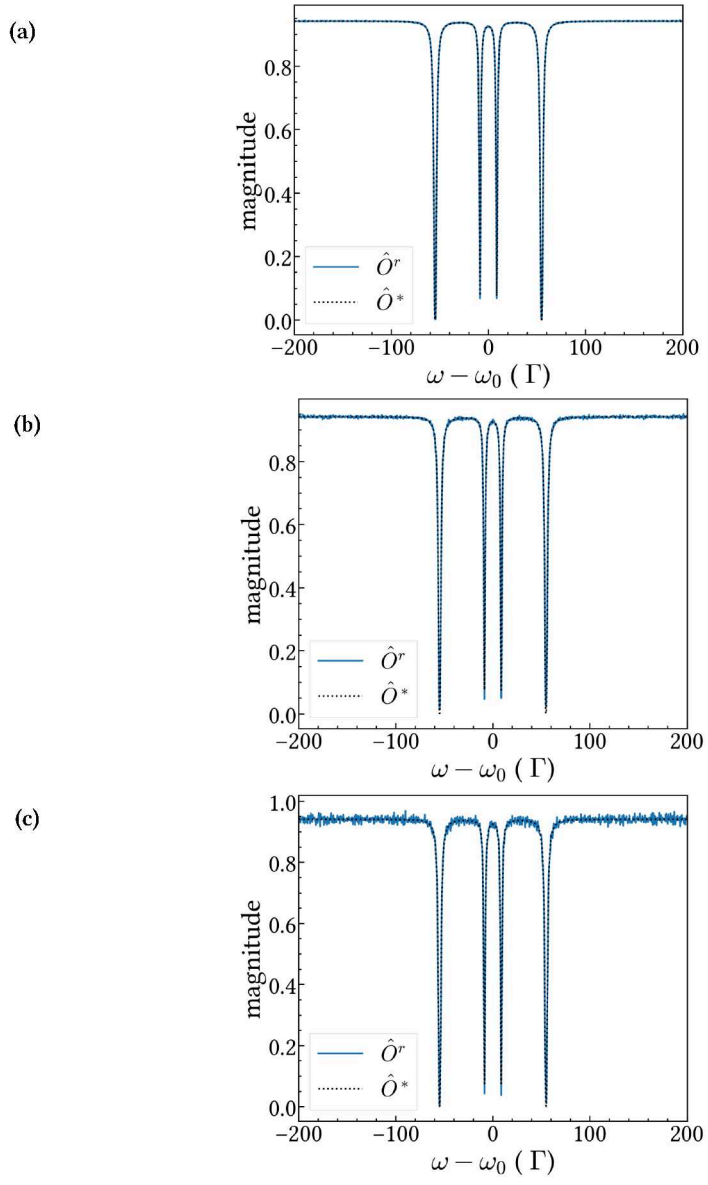

Figure 5.11.: The magnitude of the object $\hat{\boldsymbol{O}}^r$ reconstructed from ptychograms (a) C1 (b) C2 and (c) C3 with increasing Gaussian noise. The dotted line represents the magnitude of the true object $\hat{\boldsymbol{O}}^*$.

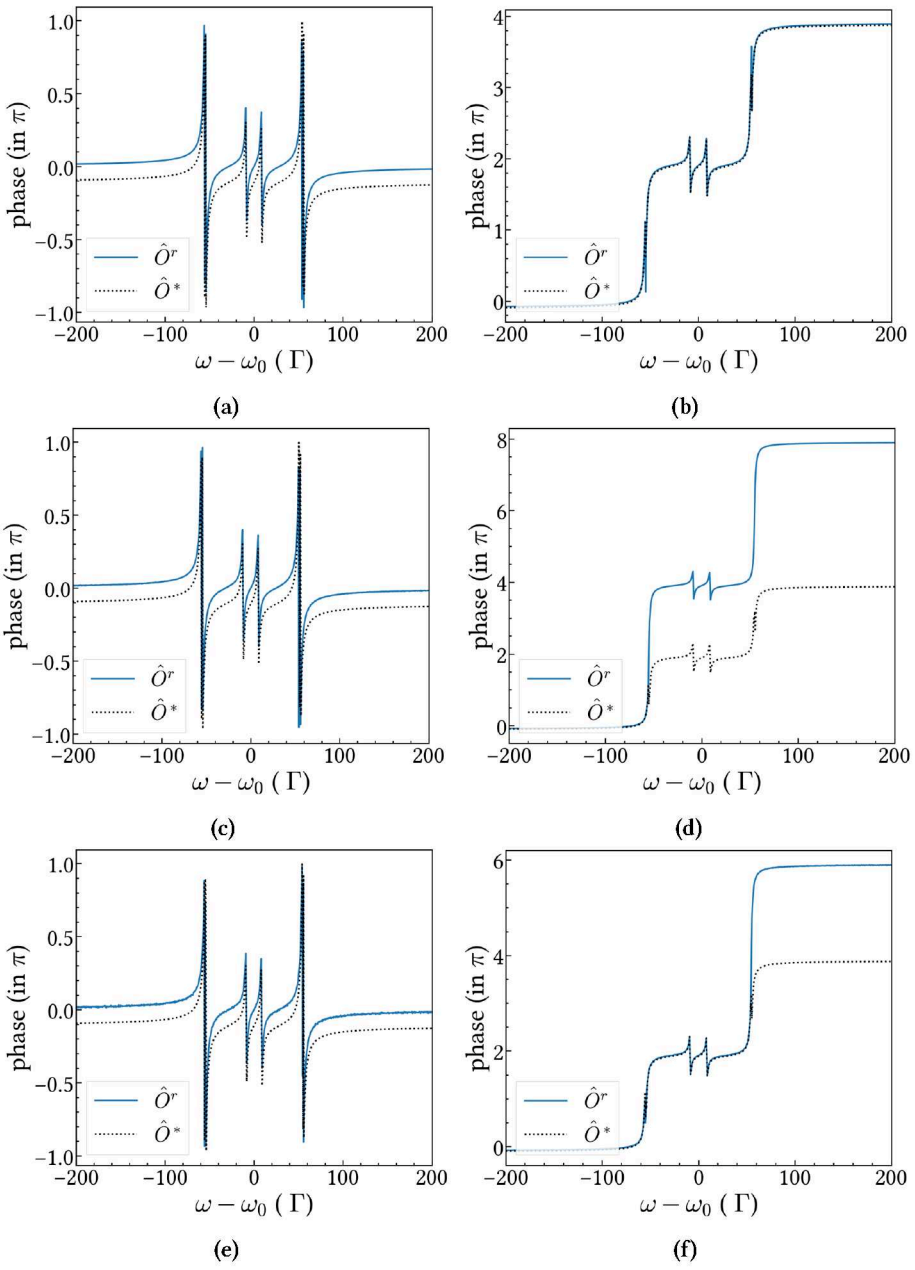

Figure 5.12.: The wrapped (a),(c),(e) and unwrapped (b),(d),(f) phase response of the objects reconstructed from ptychograms C1, C2 and C3, respectively. The black line represents the phase response of the true object $\hat{O}^*$.

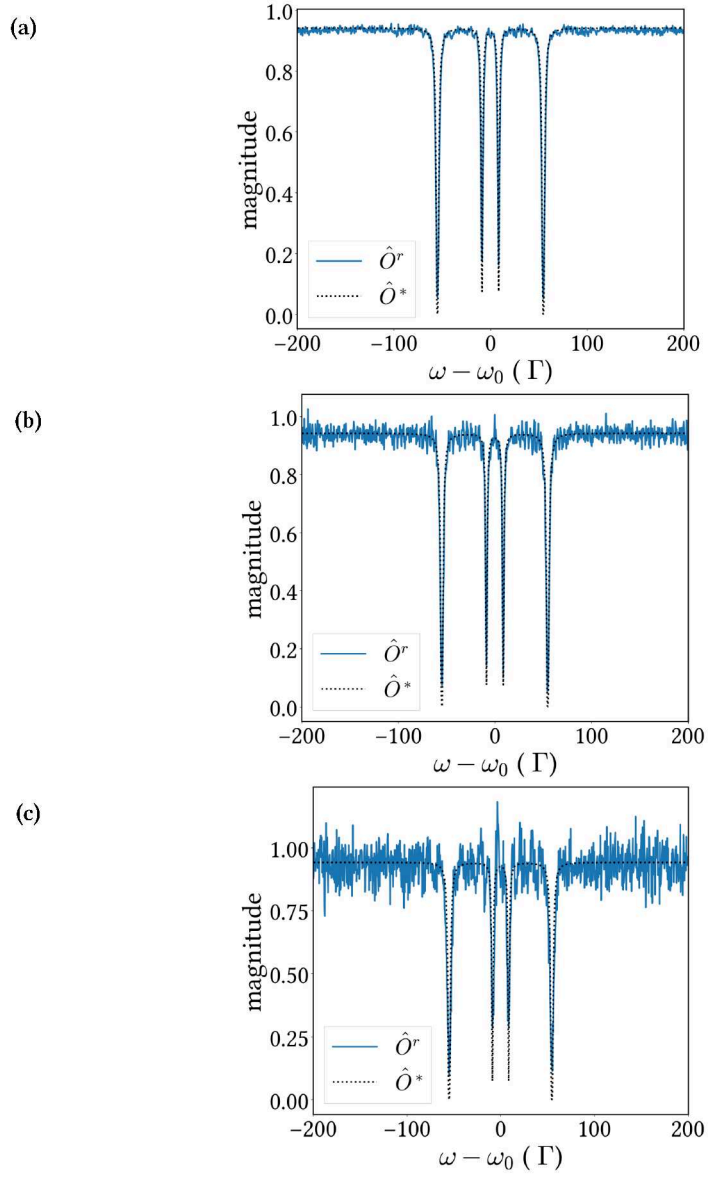

Figure 5.13.: The magnitude of the object $\hat{O}^r$ reconstructed from ptychograms (a) D1 (b) D2 and (c) D3 with increasing mixed Poisson-Gaussian noise. The dotted line represents the magnitude of the true object $\hat{O}^*$.

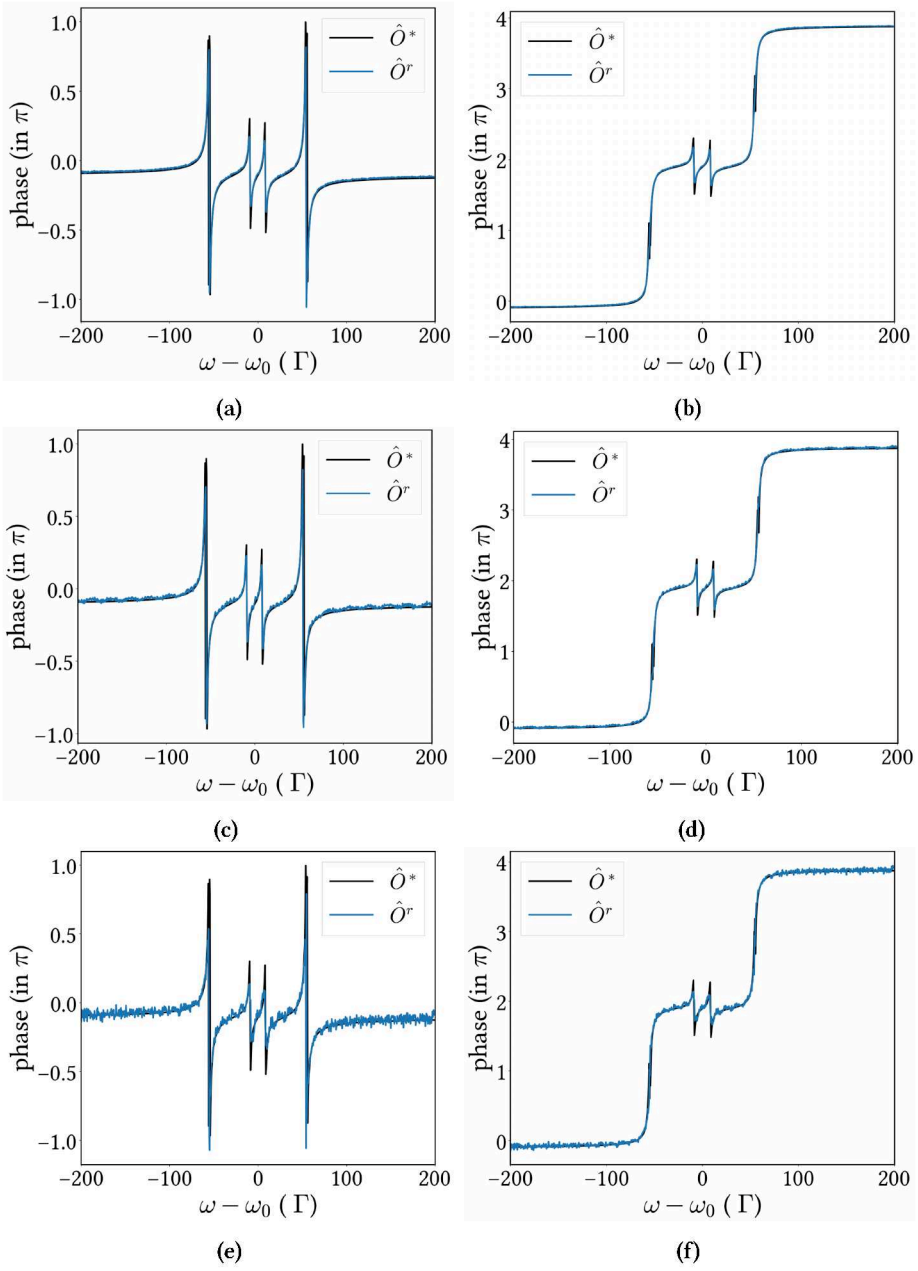

Figure 5.14.: The wrapped (a),(c),(e) and unwrapped (b),(d),(f) phase response of the objects reconstructed from ptychograms D1, D2 and D3, respectively. The black line represents the phase response of the true object $\hat{O}^*$.

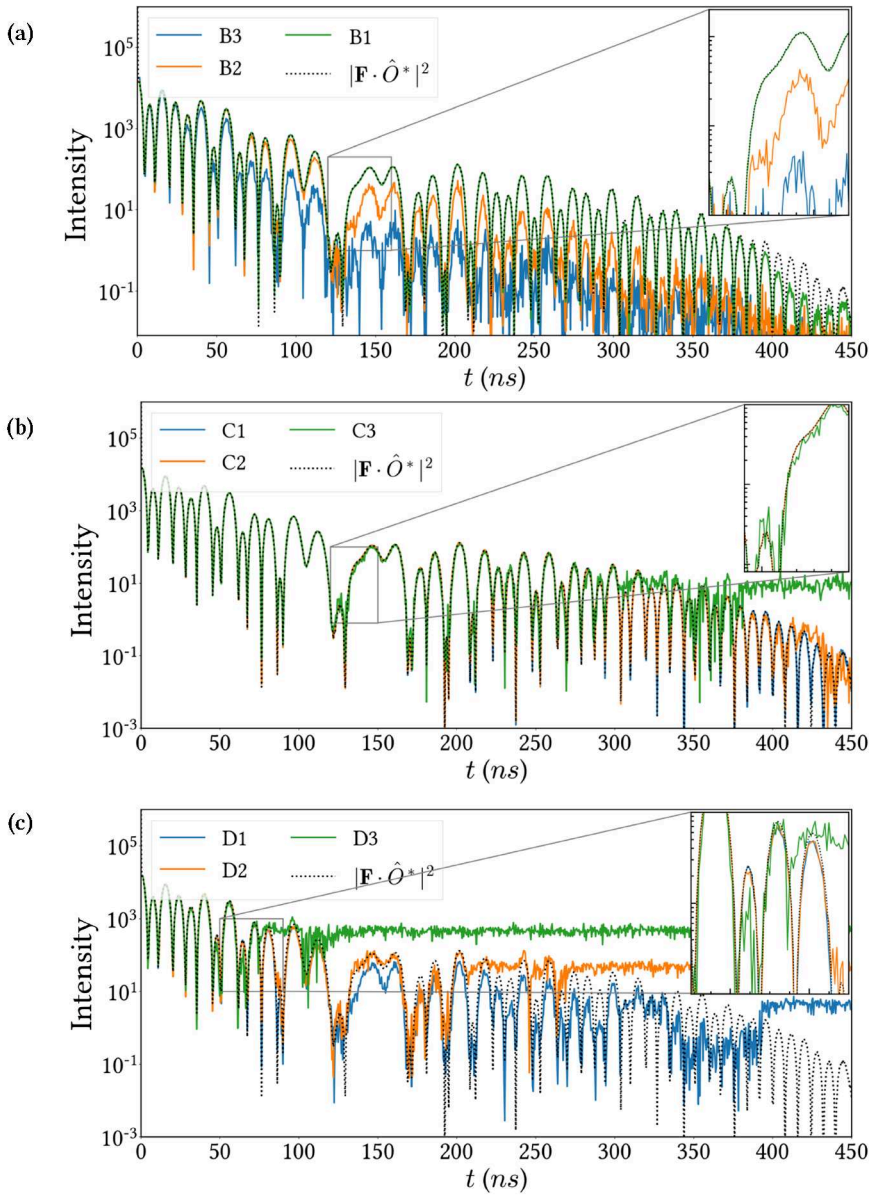

Figure 5.15.: *(see next page)*

Figure 5.15 ***(previous page)***: The time response of objects reconstructed using the noisy ptychograms. (a) For ptychograms B1, B2, and B3, we notice that the reconstructed temporal response of the object from the low photon intensity ptychogram B3 is most noisy and decays the fastest. (b) For ptychograms C1, C2, and C3, we observe that the time response of the object reconstructed from ptychogram C1 is the most noisy. Gaussian noise appears in the reconstruction as random sharp features in different parts of the time response. This is also illustrated in the inset. (c) For ptychograms C1, C2, and C3, increasing the added Gaussian noise has a significant effect on the time response of the reconstructed objects. In the inset figure, we can observe that the time response of the object reconstructed from ptychogram D3 not only "decays" at the second peak, but is also obscured by random noise after the third peak.

From the qualitative analysis in this section we can infer the following main points:

- Both Poisson and Gaussian noise in the ptychogram affect the reconstructed object, albeit differently. High levels of the Poisson noise in the ptychogram change the overall peak heights in the energy domain and their ratios. The peaks are also broadened and the time response of the object decays faster. The Gaussian noise affects the flat regions of the object in the energy domain. The noise also shows up in the background of the time response of the reconstructed object.
- The location of the peaks (i.e. the energies of the nuclear transitions) can be determined with a good accuracy even with low photon counts (high Poisson noise) and high levels of Gaussian noise in ptychogram D3.

The expected Gaussian noise in the NRS experiments is quite low, therefore, our main source of noise is due to the fundamental limit attributed to the Poisson process of the photon arrivals. This randomness is present even if the detectors are perfect, i.e., no read noise, no dark current, and a uniform response. This indicates that the only method to avoid noise in the experimental data is to have "good" counting statistics. The "goodness" of the statistics is empirically measured, although, for our simulated experiment, the total counts in the ptychogram should be $> 10^7$. Therefore, Poisson noise would make it difficult to efficiently reconstruct weakly scattered samples with low count rates.

5.3. Degree of overlap between measurements

Ptychography relies on making the phase retrieval problem well-posed by the constraints imposed by the overlapping region between neighbouring measurements (as shown in Fig. 3.7). As the overlap percentage decreases, the problem becomes more ill-posed, and the object cannot be recovered [She+21]. We define the percentage of overlap in our measurements as the ratio of the overlap area between the magnitudes at two consecutive probe positions and the area under the curve $|\hat{P}|$. In the experimental setup, the overlap percentage can be increased by decreasing the Doppler detuning between two consecutive measurements (Fig. 5.16). It also, of course, depends on the shape of the probe. To address the ill-posedness, we can use total variation (TV) and L1

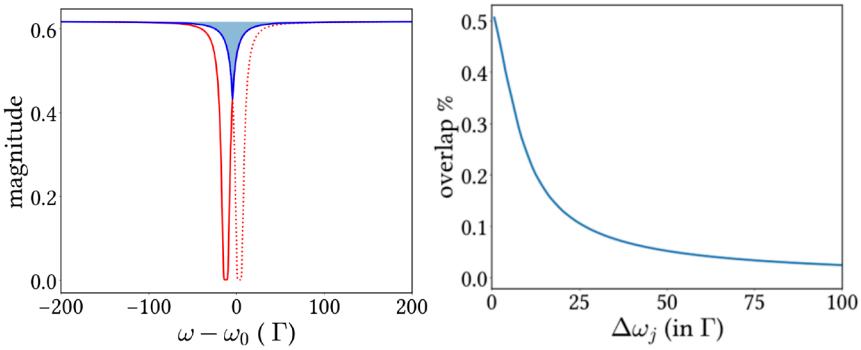

Figure 5.16.: (a) The overlap area between two consecutive measurements is shaded in blue.(b) The decrease in the percentage of overlap as the relative detuning between two probe positions increases.

regularization, as described in Sec. 4.1.2. For both total variation and L1 regularization, we first determined the best value of the weighting parameter u in Eq. (4.20) as 0.195 and 0.08, respectively. This was done by choosing the value of u with the smallest mean squared error (MSE) between the true object and the object reconstructed with regularization from measurements with 50% overlap (See Fig. 5.17). We use the same values of u for all the test cases in this section. In Fig. 5.18 we show the MSE of the reconstructed object as a function of overlap percentage for three cases - no regularization, total variation regularization and L1 regularization. The overlap ratio was reduced by reducing

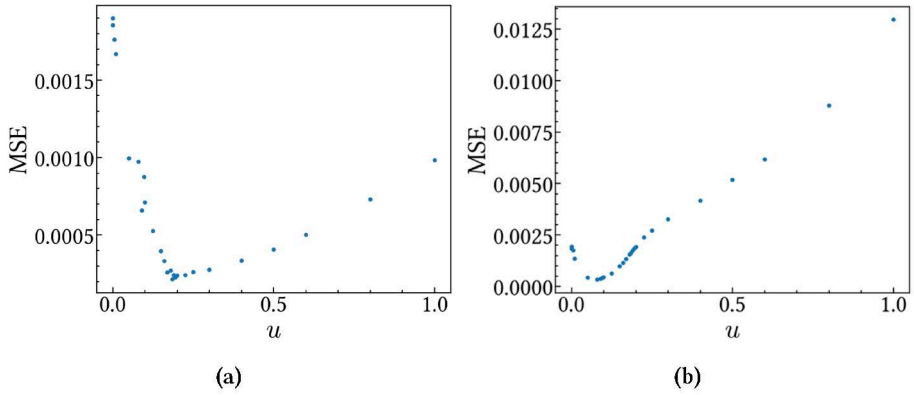

Figure 5.17.: MSE of the reconstructed object vs. the weighting parameter u for (a) total variation (TV) and (b) L1 regularization of the object.

the number of Doppler detuning points. In all cases, the MSE increases rapidly as the overlap between probe positions falls roughly below 25%. We also note that the MSE of the unregularized object is not strictly decreasing with increasing overlap because the ptychography engine sometimes converges to different local minima. MSE analysis indicates that both total variation and L1 regularization stabilize reconstructions as the overlap decreases.

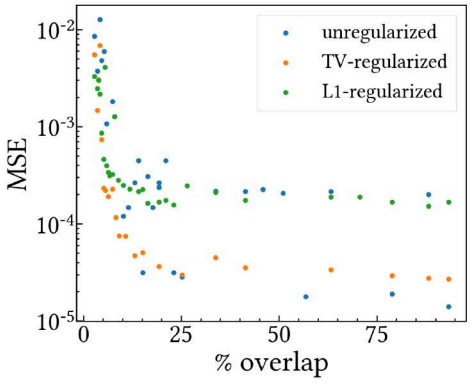

Figure 5.18.: The MSE of the object reconstructed with and without any regularization schemes.

For a qualitative analysis of the results we show the object reconstructed with and without a regularization term in Fig. 5.19 and 5.20. We have taken only the measurements from the noiseless ptychogram A which have 7.4% overlap between consecutive probe positions. We can summarize our findings as follows:

1. Under low overlap conditions, the unregularized object reconstruction has fluctuations in the baseline of its magnitude and phase response in the energy domain. These additional features likely arise because the probe positions are so far apart that the object is not illuminated uniformly at each energy.

2. Both the total variation and L1 regularized solutions are sparse in the energy domain.

3. In the time domain, the object's response has less noisy features for total variation regularization, although it also introduces a dampening to the spectrum at later times. For L1 regularization, the object's time response contains non-smooth artifacts.

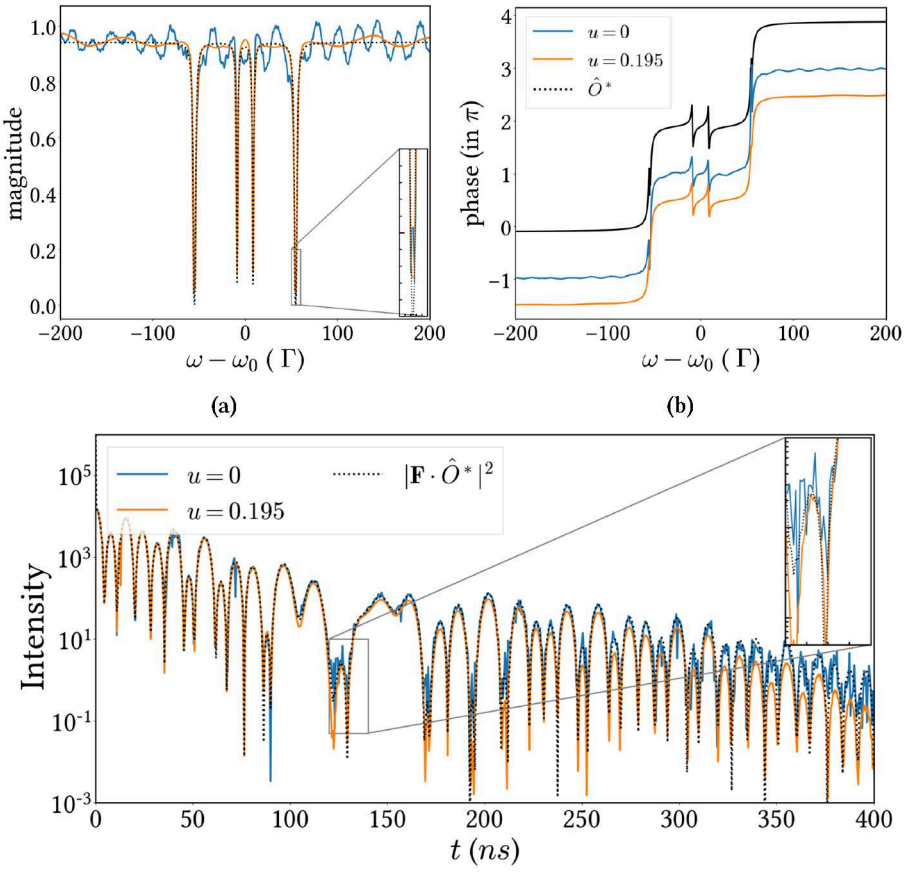

Figure 5.19.: (a) Magnitude, (b) phase and (c) time response of the unregularized ($u = 0$) and total variation (TV) regularized ($u = 0.195$) object reconstructed from a noiseless ptychogram measured with 7.4% overlap. The inset in (c) depicts that the time response of the regularized object is reconstructed without noisy features.

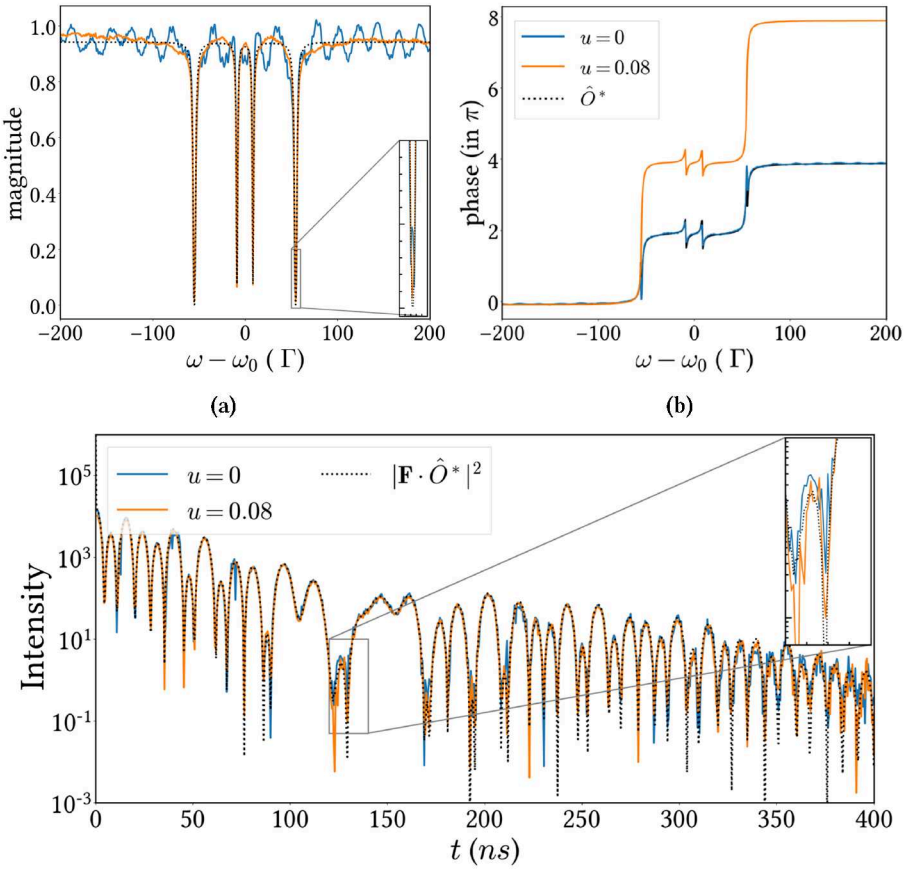

Figure 5.20.: (a) Magnitude, (b) phase and (c) time response of the unregularized ($u = 0$) and L1 regularized ($u = 0.08$) object reconstructed from a noiseless ptychogram measured with 7.4% overlap. The inset in (c) depicts that L1 regularization does not make the object's response less noisy in the time domain.

5.4. The time-windowing effect

As discussed in Sec. 4.3.1, we need an appropriate resolution of the energy grid for the ptychography engine calculations. However, the experiment has an inherent energy resolution which comes from the data measured at the detector. The X-ray pulses hitting the sample arrive with a period T_{bs} between them, depending on the bunch mode of the synchrotron operation (See Fig. 5.21). This information is given to us by the "bunch clock" signal from the synchrotron. In a forward scattering experiment, we typically get a "prompt" signal at the detector due to the electronic scattering in the sample–which happens at a much faster time scale (in picoseconds) compared to nuclear scattering (in nanoseconds). To prevent the prompt signal from saturating the detector electronics, a veto interval is typically placed around the bunch clock signal during which no data is recorded. This establishes a data acquisition time window from T_{min} to T_{max} for the nuclear scattering signal at the detector. For a maximum time of acquisition T_{max}, the

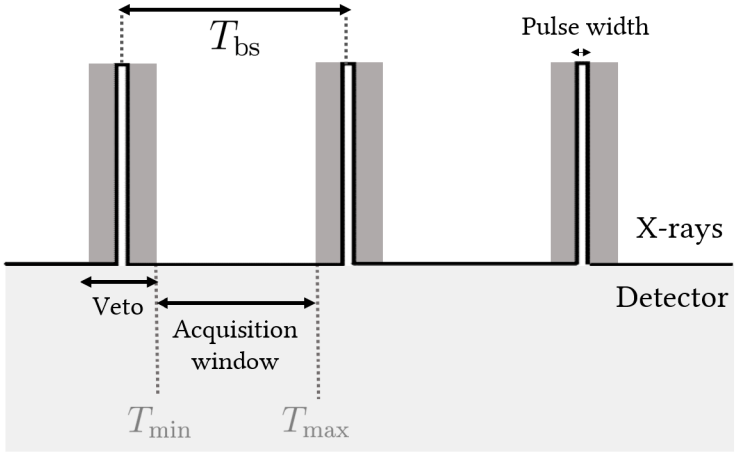

Figure 5.21.: The timing calibration of the experiment. The pulsewidth of the synchrotron X-ray pulses is in picoseconds while T_{bs}, T_{min} and T_{max} are in nanoseconds.

energies of the nuclear transitions are sampled with a resolution

$$\Delta\omega' = \frac{\hbar}{\Gamma} \cdot \frac{2\pi}{T_{\mathrm{max}}} \tag{5.7}$$

at the detector. For T_{max} = 200 ns, e.g., this corresponds to an inherent energy resolution of $\sim$ 4.4 Γ (see Fig. 4.3). We can name the upsampling ratio between the inherent resolution of the experiment and the resolution of the calculation grid as

$$M_{\text{factor}} = \frac{\Delta\omega'}{\Delta\omega} = \frac{N_{\text{FFT}}\Delta t}{T_{\text{max}}}. \tag{5.8}$$

For $M_{\text{factor}} = 1$, the energy resolution of the measured data $\Delta\omega'$ matches the energy resolution of the calculation $\Delta\omega$. For $M_{\text{factor}} > 1$, the resolution of the measured data $\Delta\omega'$ is less than $\Delta\omega$. For the calculations, the measured ptychogram is thus zero-padded in the time domain. It is to be stressed that the zero padding does not increase the amount of information we have in the measurements. The true energy resolution of NRS ptychography ($\Delta\omega$) is limited by the maximum measurable time length (field of view) at the detector. For a fixed T_{max}, increasing the M_{factor} just interpolates an already smeared out energy response function to a denser sampling grid [Bra86]. Since the time window of detection is rectangular, side lobes or 'wiggle' artifacts appear in the energy domain response due to sinc interpolation (see Fig. 5.22). For a qualitative analysis of the time

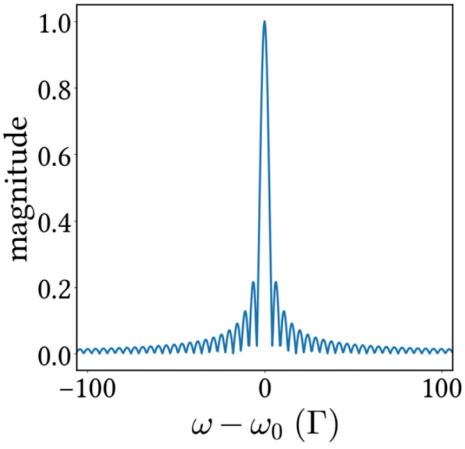

Figure 5.22.: The Fourier transform of a discrete rectangular window is a discrete sinc or Dirichlet kernel. Zero padding of the ptychogram is equivalent to applying a rectangular window in the time domain i.e. sinc interpolation between points in the energy domain by convolving it with the Dirichlet kernel.

window effect, we show the object reconstructed from the noiseless ptychogram with $T_{\text{min}} = 0$ and $T_{\text{max}} = 1024$ and 102.4 ns, respectively in Fig. 5.23. They correspond to $M_{\text{factor}} = 2$ and 20.

Ringing 'wiggle' artifacts (similar to spectral leakage [Les06]) appear in the energy domain magnitude and phase of the reconstructed object as the value of M_{factor} increases (see Fig. 5.23(a) and Fig. 5.23(b)). We can try to suppress the wiggle artifacts by adding regularization terms to our cost function. The reconstructed object is shown for total variation (Fig. 5.24) and L1 regularization (Fig. 5.25). While total variation regularization effectively reduces the artifacts, it favors 'step-like' features in the magnitude and phase of the reconstructed object. Nevertheless, the peak positions can be correctly identified and the peak ratios are effectively maintained.

L1 regularization tries to force the object to have a flat baseline and the ratio of the peak heights is not maintained. This is expected since in the regularization term (Eq. (4.21)) we force the object towards 1. Both regularization terms attempt to extrapolate the time response of the object beyond $T_{\text{max}} = 102.4$ ns to reduce the spectral leakage.

Instead of regularization terms, we can also alternately project the solution to the constraint $C : 0 \leq |\hat{\boldsymbol{O}}_p| \leq 1 \; \forall \; p$ as

$$\hat{\boldsymbol{O}}_p = 1 \qquad \text{if} \;\; |\hat{\boldsymbol{O}}_p| > 1 \tag{5.9}$$

by using projection gradient descent (Algorithm 2). However, as shown in Fig. 5.26, this does not significantly improve the quality of the result. The projection step induces other irregular artifacts in the baseline of the magnitude and phase of the reconstructed object.

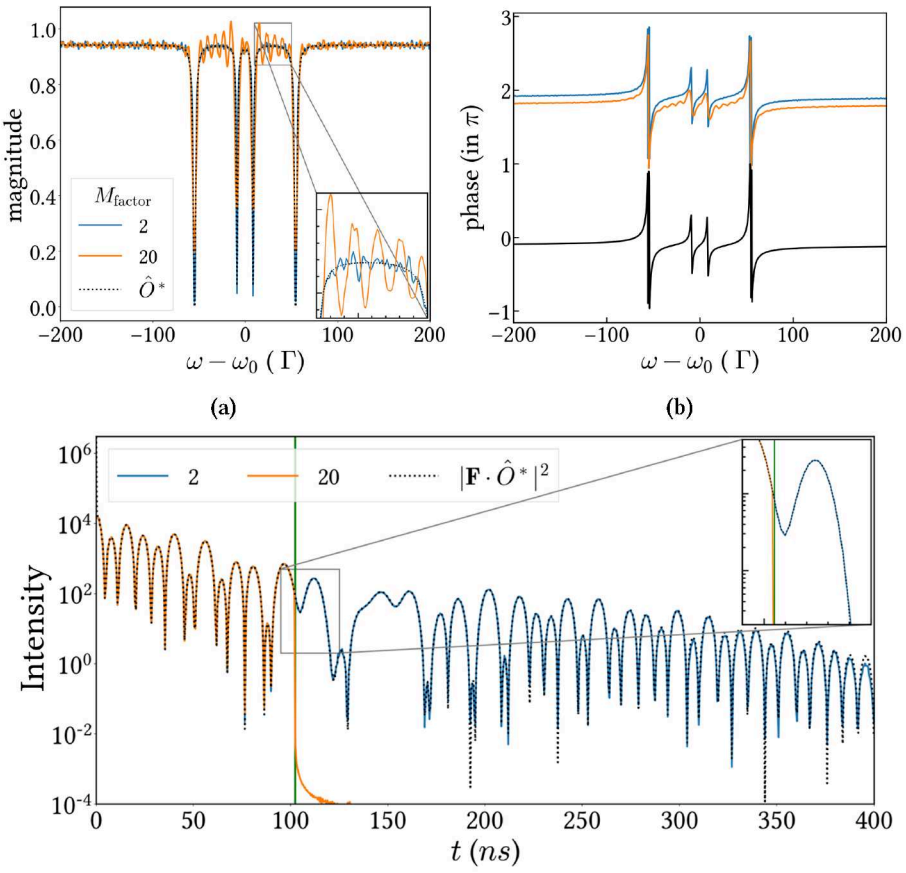

Figure 5.23.: (a) Magnitude, (b) phase, and (c) time response of the object reconstructed from the noiseless ptychogram A measured with different M_{factor} (different T_{max}) at the detector. The vertical green line in (c) is plotted at 102.4 ns. The time response of the object reconstructed from a ptychogram with T_{max} = 102.4 ns also drops to zero after T_{max} = 102.4 ns.

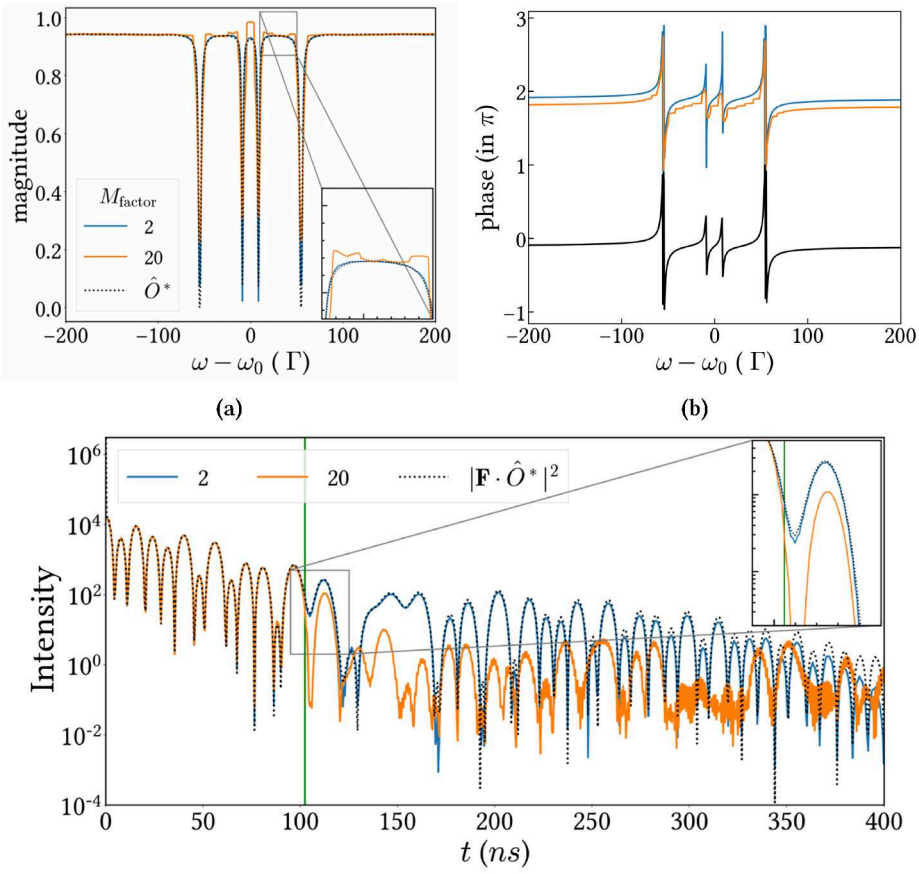

Figure 5.24.: (a) Magnitude, (b) phase and (c) time response of the total variation (TV) regularized object reconstructed from the noiseless ptychogram A measured with different M_{factor} at the detector. The TV regularized object is sparse and does not have the 'wiggles' of the unregularized object in the baseline. In (c), the vertical green line is plotted at 102.4 ns. The inset shows the smooth extrapolation of the regularized object beyond 102.4 ns.

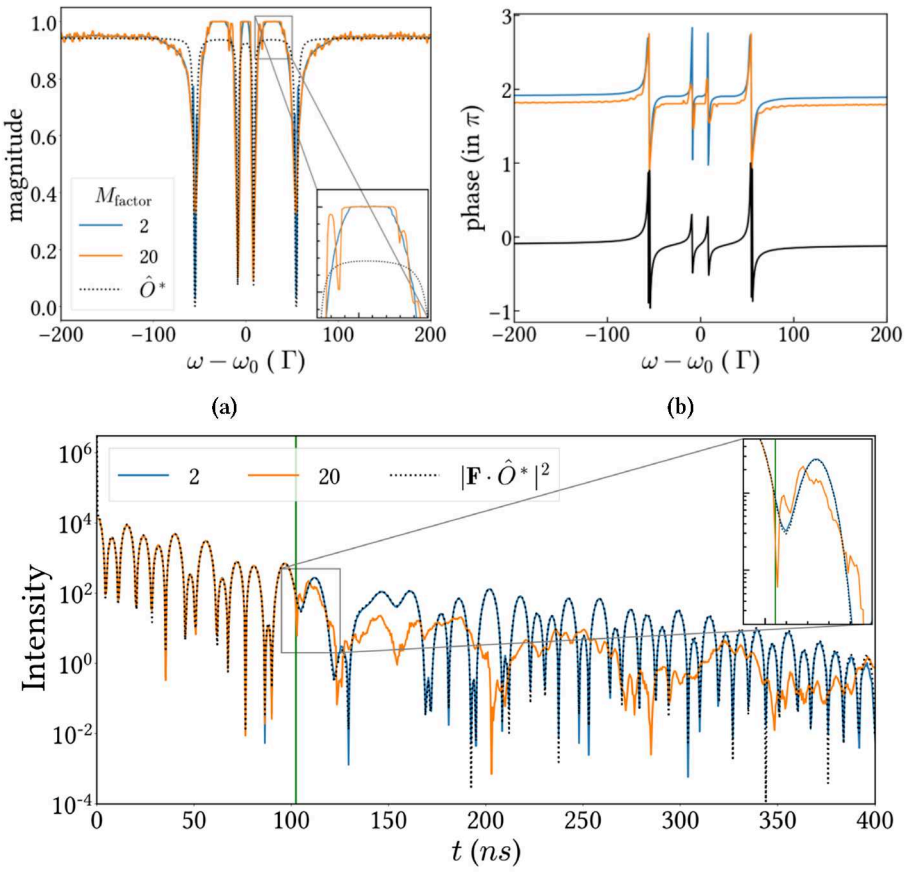

Figure 5.25.: (a) Magnitude, (b) phase and (c) time response of the L1 regularized object reconstructed from the noiseless ptychogram A measured with different M_{factor} at the detector. The L1 regularized object has fewer baseline fluctuations than the unregularized object. However, the L1 penalty term forces the object towards 1 at some energies. The inset in (c) shows the extrapolation of the regularized object beyond the vertical green line plotted at 102.4 ns.

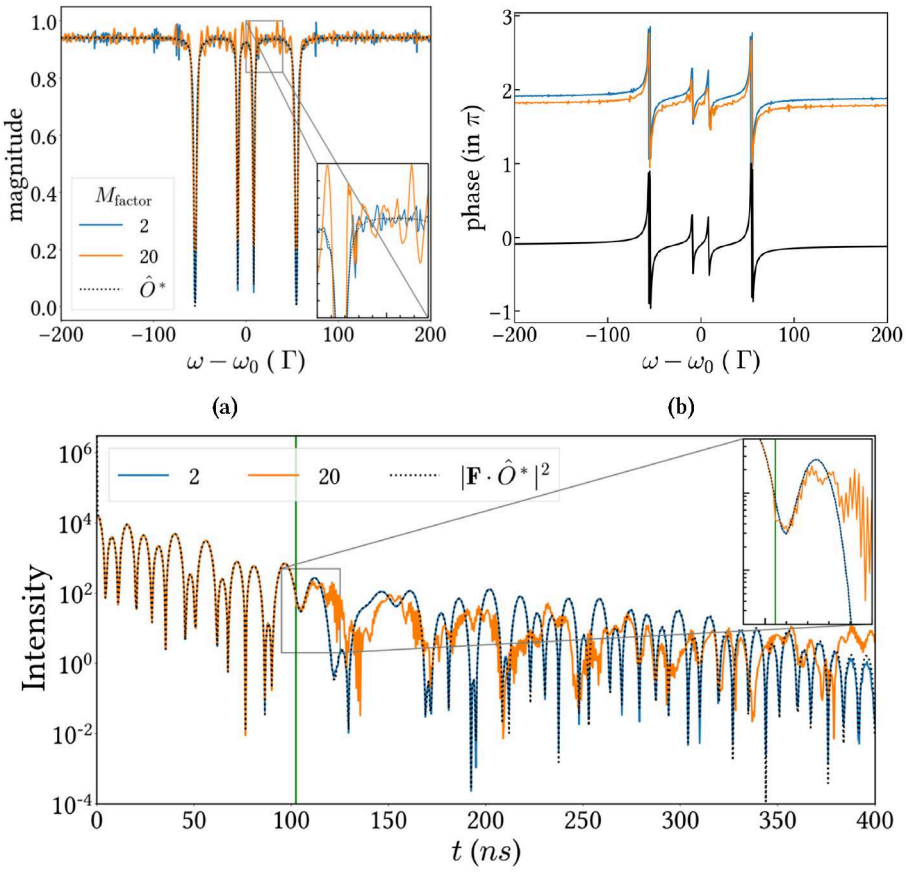

Figure 5.26.: (a) Magnitude, (b) phase and (c) time response of the object reconstructed from the noiseless ptychogram A measured with different M_{factor} at the detector using projection gradient descent. The magnitude of the reconstructed object is constrained between 0 and 1 compared to the unregularized object. In (c), we see that the projection step also extrapolates the time response beyond the vertical green line plotted at 102.4 ns.

For a quantitative analysis, we calculate and plot the MSE of the reconstructed object from the noiseless ptychograms with $T_{\text{min}} = 0$ and different values of M_{factor} (T_{max}) in Fig. 5.27(a). We see that the MSE of the reconstructed object increases rapidly for $1/M_{\text{factor}} < 0.2$. Note that the MSE of the regularized cases is higher than the unregularized cases because the regularization term tries to reduce the overfitting of the forward model.

The data loss between 0 and T_{min} is essentially equivalent to the beamstop often used in ptychographic imaging to block the primary beam which might damage the detector. In a ptychographic imaging system, the beam-stop size on the detector should not exceed the numerical aperture of the probe [Dej+24], otherwise the reconstruction error increases and the contrast drops.

In Fig. 5.27(b), we plot the MSE of the object reconstructed from ptychograms measured for $T_{\text{max}} = 200$ ns and different prompt pulse cut-off times T_{min}. The MSE increases slowly as T_{min} increases.

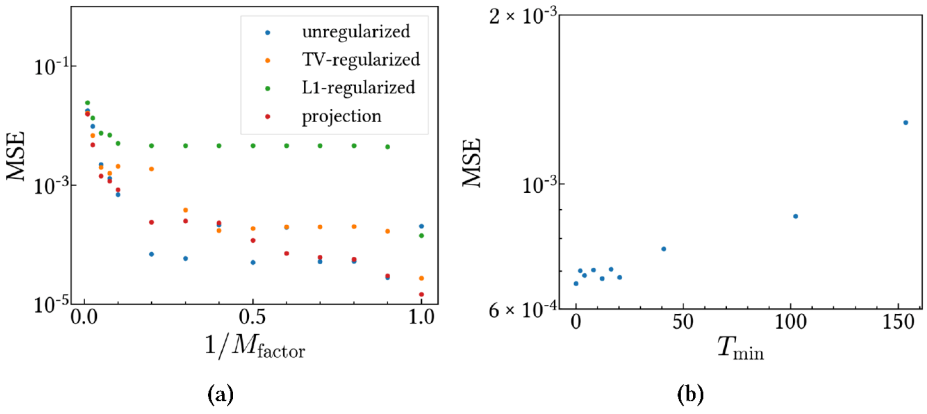

Figure 5.27.: The MSE of object reconstructed in the case of (a) $T_{\text{min}} = 0$ but increasing T_{max} under the various regularization term and unregularized projection gradient descent (in red). (b) The MSE of reconstructed object with fixed $T_{\text{max}} = 200$ ns but increasing prompt cut-off time T_{min}.

We summarize the main points of this section as follows:

- The inherent energy resolution in ptychography is improved by increasing the time window ($T_{\text{min}}, T_{\text{max}}$) introduced by the synchrotron's mode of operation.

- Zero-padding in the time domain is used for the calculations in the ptychography engine, which interpolates the energy response function to a higher-resolution grid. The upsampling ratio M_{factor} compares the resolution of the experiment ($\Delta\omega'$) to the resolution of the calculation grid ($\Delta\omega$).
- Increasing the M_{factor} introduces ringing 'wiggle' artifacts in the reconstructed energy response of the object. Introducing a total variation regularization term in the inversion algorithm performs the best in numerically reducing these artifacts.

6. Experimental details

The stability and success of ptychography are heavily based on the choice of the probe/illumination function since it determines the distribution of the photons in the measured region. It has been shown that the "condition number" [1] of the phase problem might be less for some types of probes than others [For+20; PS21]. As mentioned in Sec. 3.2, a sample with a thin, single-line Lorentzian scattering energy response is equivalent to a perfect lens with a circular aperture in scanning microscopy. For ptychography, we can relax these "ideal" conditions if our probe/lens has a broad energy response so that we can illuminate the object with sufficient overlap between consecutive measurements. In this chapter, we demonstrate proof-of-principle ptychography experiments with two alternative setups - one with a thick ^{57}SS foil and the second with a thin ^{57}SS nanofilm in a cavity as a probe. Here, ^{57}SS indicates stainless steel (Fe(55)Cr(25)Ni(20)) with its iron content enriched to 95% with the resonant ^{57}**Fe** isotope.

- **Thick ^{57}SS foil**: A stainless steel alloy with a weight composition (Fe:Cr:Ni) = (55:25:20) can be enriched with the ^{57}**Fe** isotope and annealed such that the iron is in the austenitic (face-centered cubic) phase, which is non-magnetic [Sah+11]. Such a paramagnetic stainless steel foil in transmission can resonantly absorb energies around the 14.41 keV Mössbauer transition of ^{57}**Fe** such that its absorption spectrum is a single line of an approximately Lorentzian shape. The full-width half maximum of the scattering response of the transmitting foil can be controlled by varying its thickness [MDF63]. Therefore, we can change the degree of overlap in ptychography experiments by choosing foils of different thicknesses.

[1] The condition number in the context of the phase problem refers to how sensitive the solution is to small changes or errors in the data. A higher condition number indicates that the phase problem is more ill-posed, meaning that slight errors or uncertainties in the measured data can lead to significant inaccuracies in the determined phases.

- **Thin ^{57}SS film in X-ray cavity**: Layers of resonant Mössbauer nuclei embedded into an X-ray cavity are also interesting structures used in X-ray quantum optics [Hee14; Hee+15; RE21; Hab+17]. If we sandwich a nanometer-thin stainless steel layer between a multilayer X-ray cavity, the nuclear ensemble can coherently interact with the X-ray wavefield entering the cavity at grazing incidence. The scattering response of the cavity can be controlled by changing the position of the embedded ^{57}SS layer and tuning the incidence angle on the cavity. Close to nuclear resonances, the properties of the combined system of cavity and nuclei lead to a strong polarization of the scattering X-rays. The electronic refractive index of the cavity materials also results in off-resonant scattering of the X-rays. We can suppress this electronic scattering by tuning to a waveguide mode of the cavity.

6.1. The experimental setup

All the experiments in this thesis were performed at the nuclear resonant scattering beamline P01 at Petra III. Their common parameters are listed in Table 6.1. The standard beamline setup to measure the time response of a sample in the transmission geometry is shown in Fig. 6.1. The X-ray beam is monochromatized to a bandwidth of about 1 meV around the nuclear resonance energy of ^{57}**Fe** at 14.41 keV. This is done with the help of a silicon double-crystal monochromator (DCM) and a high-resolution monochromator (HRM). An array of avalanche photodiodes (APDs) is operated in Geiger mode to detect the single photons scattered from the sample. Each APD is approximately 1 cm × 1 cm in size and can detect a photon flux of up to 10^7 ph s^{-1}. In the presence of higher flux from the sample, photon-absorbing foils were moved in front of the APDs to prevent them from getting damaged. The time resolution of the APDs is 0.5 ns. The storage ring was operated in the 40-bunch mode, leaving 192.125 ns between successive pulses.

The first experimental setup for NRS ptychography is shown in Fig. 6.2(a). The transmitted wavefield from a stainless steel (^{57}SS) foil was used to illuminate the object. In the second setup (Fig. 6.2(b)), the X-ray beam from the high-resolution monochromator first hit a thin film cavity at grazing incidence. The specularly reflected beam was then used to illuminate the object.

Parameter	Value
Energy	14.41 keV
FWHM Energy	1 meV
Maximum photon flux from the HRM	1×10^{10} ph s^{-1}
Beam spot size (Vert. × Horiz.)	40 µm × 1 mm
Detector pixel size with slits (Vert. × Horiz.)	0.2 mm × 4 mm
Detector distance	1 m
Detector time resolution	0.5 ns
Bunch clock time period (T_{bs})	192.125 ns (40-bunch mode)
Acquisition time window (T_{min}, T_{max})	(17 ns, 178 ns)

Table 6.1.: Parameters of the experiments at P01, Petra III.

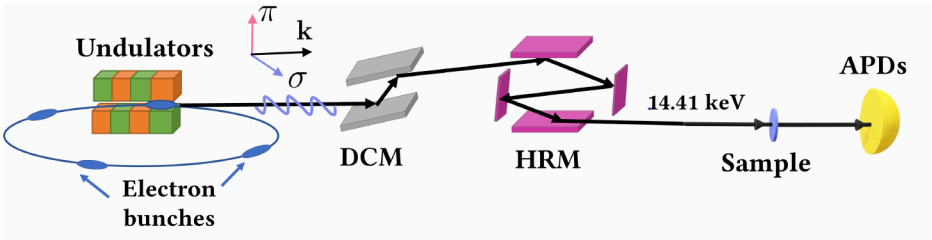

Figure 6.1.: The experimental station at P01, Petra III. The synchrotron X-ray pulses coming from the undulator are polarized along σ and pass through a double crystal monochromator (DCM) and a high-resolution monochromator (HRM). The monochromatized X-ray pulses have a bandwidth of 1 meV at 14.41 keV. The scattered signal from the sample is detected by an array of avalanche photodiodes (APDs).

In both setups, the object foil was mounted on a Doppler drive (Wissel MVT-1000) and its movement was precisely controlled with the help of the driving unit (Wissel MR-360). For the best accuracy of the driving electronics, the drive was moved sinusoidally with a frequency of about 27 Hz which is close to its natural resonance frequency (~25 Hz). The error in the velocity of the drive is 0.1-0.5% in the sinusoidal mode. A function generator (Wissel DFG-1000) was used to provide the sinusoidal input signal to the driving unit (Wissel MR-360).

To collect the ptychogram, we made use of a multi-event time digitizer (FAST ComTec MCS6A). The digitizer was synchronized to the bunch-clock signal (i.e. the timing sig-

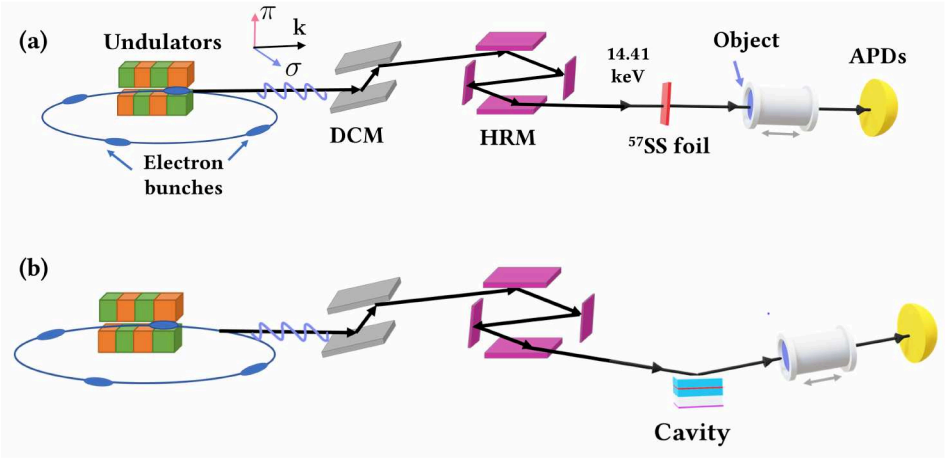

Figure 6.2.: The (a) transmission and the (b) grazing incidence ptychography setup at P01, Petra III. In both setups, the monochromatized X-ray pulses first hit the probe (the ^{57}SS foil in (a) and the cavity in (b)) and then the object. The scattered signal from the object is detected by an array of avalanche photodiodes (APDs).

nal of the electron bunches revolving in the synchrotron) and was connected to the APD array. The time of arrival of photons at the APDs can thus be recorded. To get information on the Doppler drive velocity, the MCS6A also receives signals from the digital function generator via a "Tag bit box". The Tag bit box samples the input signal given to the drive by the function generator into 1024 channels with equidistant time intervals. The channel values from the Tag bit box thus encode information about the velocity of the drive and the corresponding Doppler detuning between the probe and the object.

The MCS6A labels each scattered photon with its arrival time at the detector and the channel number. Using this event-based detection setup, we can measure a 2-D histogram of the photon counts, e.g., as shown in Fig. 6.14. This 2-D histogram contains information on the interference and coupling between the probe and the object and acts as our ptychogram.

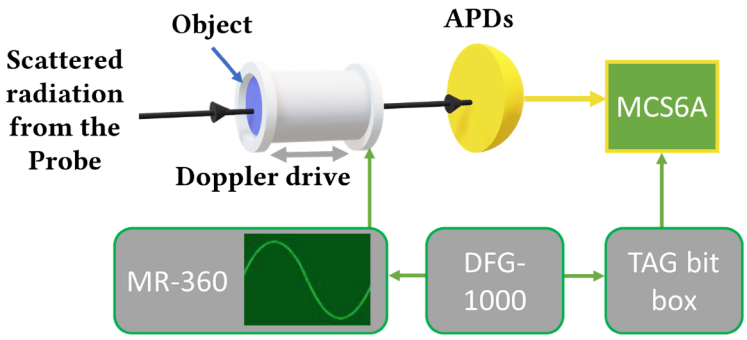

Figure 6.3.: The ptychogram measurement setup at P01, Petra III. The object is mounted on a Doppler drive and moved along the direction of the probing beam by the driving unit MR-360. A digital function generator DFG-1000 is used to give a sinusoidal velocity profile to the drive. The MCS6A collects the photon counts with their time of arrival at the APDs and the instantaneous velocity of the drive, and bins them into a 2-D histogram.

6.2. Characterization of the probes

To do phase retrieval with our ptychographic engine, it is important to know the complex energy response of the probe. Therefore, we first characterized the probes to extract their structural and hyperfine parameters.

6.2.1. The ^{57}SS foil

We measured the time response of the ^{57}SS foil alone in the beam (as shown in Fig. 6.1), and then fit the time response using NEXUS. The fitting procedure was performed with a differential evolution algorithm [Bis+21] in NEXUS along with a bunch spacing correction (see Appendix B.3) where $T_{\mathrm{bs}} = 192.125$ ns. The foil is assumed to have a Lamb-Mössbauer factor of 0.78 and a density of 7.8 g cm^{-3}.

The foil is thick enough to show dynamical beats with minima at around 45, 95 and 155 ns in its time response. Stainless steel in the austenitic phase does not display ferromagnetic order, so the ^{57}Fe isotopes have a single-line resonance at 14.413 keV with no Zeeman splitting. As shown in Fig. 6.4(b), the best fit to the time response is obtained

by assuming that the single line broadened by a mixture of coherent and incoherent processes. The coherent broadening could arise because we are measuring over many ^{57}**Fe** nuclei in the sample - each of which might be embedded in a slightly different electronic environment.[2] It is fitted as a Gaussian distribution of isomer shifts in the sample with a full width at half maximum (FWHM) of 0.23 mm s^{-1}. The incoherent broadening is fitted by assuming that the thickness of the foil is not uniform and can be estimated as a Gaussian distribution centered at 17.83 μm with a FWHM of 0.73 μm (See Fig. 6.5(c)). A thickness variation of this length scale was also observed in the atomic force microscopy image of the foil, as shown in Fig. 6.4(a).

The result of the best fit (Fit 3 in Fig. 6.4(b)) is given in Table 6.2. Using the fitted hyperfine parameters, we can simulate the complex energy domain response or "illumination" function of the ^{57}SS foil for different thicknesses. They are shown in Fig. 6.5.

Parameter	**Fit result**
Thickness	17.83 μm
FWHM Thickness	0.73 μm
FWHM Isomer shift	0.23 mm s^{-1}

Table 6.2.: Fitted parameters of the time response of the thick ^{57}SS foil, as shown in Fig. 6.4(b).

[2]The coherent broadening could also be due to a distribution of quadrupole splittings, i.e. the variations in the electronic field gradients over the sample- but there is no way to distinguish the two effects in the time response.

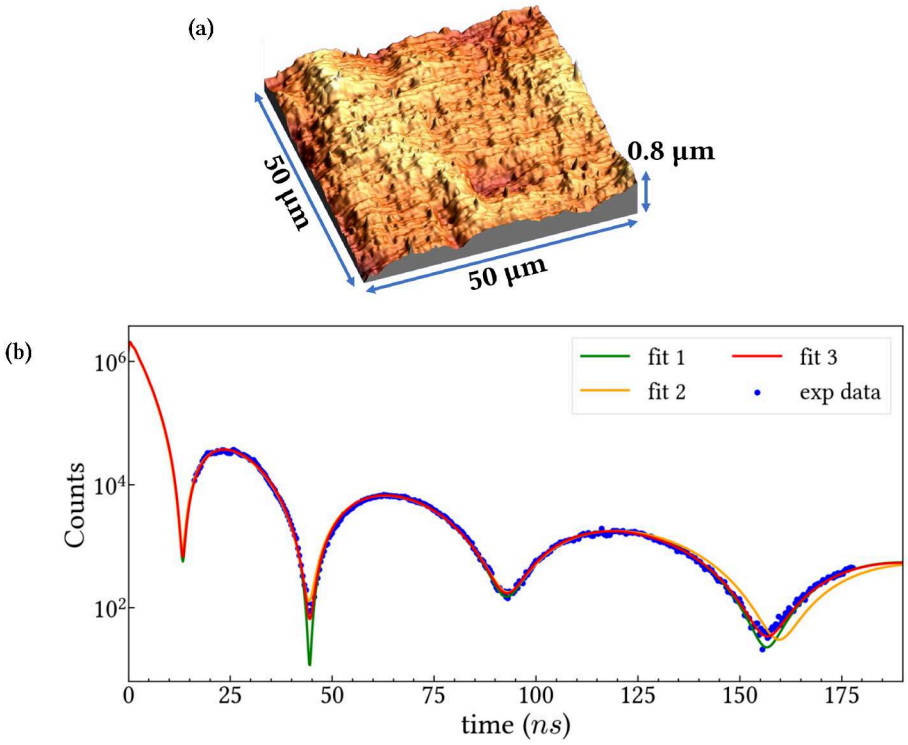

Figure 6.4.: (a) The atomic force microscopy image of the surface of the foil, taken over an area equivalent to the beam spot size on the foil. Several such images were taken over different spots on both sides of the foil, roughly at the center. The surface height variation was found to be 0.75 - 1.2 µm. (b) The time response of the foil measured between 17 and 178 ns (in blue) versus the fitted models. Fit 1 (in green) assumes 100% coherent broadening due to an isomer shift distribution. The minima at 45 ns and 155 ns are not correctly fitted. Fit 2 (in orange) assumes 100 % incoherent broadening due to only thickness distribution in the foil. The fit becomes worse after 125 ns. Fit model 3 (in red) performs the best - it assumes a mixture of coherent and incoherent line broadenings in the energy response of the foil.

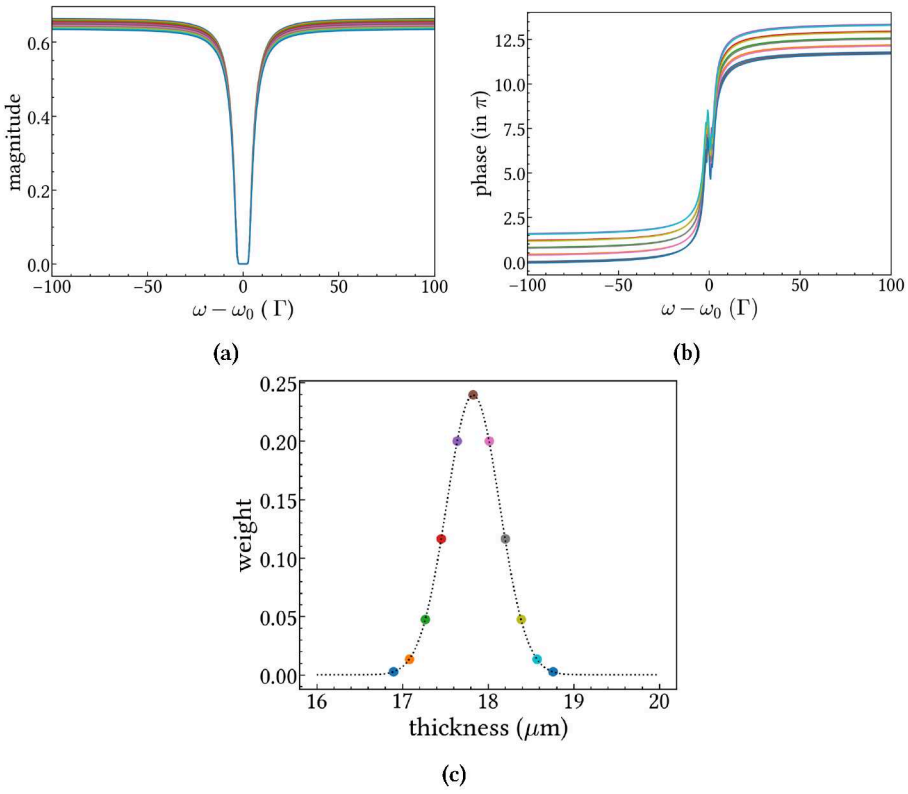

Figure 6.5.: (a) Magnitude and (b) phase response of the ^{57}SS foil. (c) The marked circles denote the thicknesses of the probes, which are chosen from a Gaussian distribution with FWHM 0.73 µm. The color code in all three subfigures is the same.

6.2.2. Thin ^{57}SS film in an X-ray cavity

A thin-film cavity can be formed by stacking an optically thin layer (of low Z and/or low material density and lower critical angle) between two optically dense layers (of high Z and/or high material density and higher critical angle) [Vel21; Hee14]. The refractive index of most materials in the X-ray regime is slightly less than 1. Therefore, total reflection of X-rays occurs at the smooth surface of a sample if the incidence angle is smaller than the critical angle of the material. The critical angle is directly proportional to the square root of the density and the atomic number Z of the material. The

higher-density layers are totally reflective and serve as "mirrors" within a certain angular range, while the lower-density layer serves as a "guiding layer" for the transmission of the X-ray wavefield. By embedding a layer of resonant Mössbauer nuclei in the cavity environment, their scattering response can be tailored beyond those offered by a foil.[DLE22]

A schematic of the cavity used in our experiments is shown in Fig. 6.6(a). It was fabricated by magnetron sputter deposition at DESY, Hamburg on a super-polished Si wafer, similar to as described in [Hab+17]. The guiding layer in the cavity is made of boron carbide (B_4C), whereas the mirror layers are made of platinum. In the center of the boron carbide layer, a 1.2 nm ^{57}SS layer is embedded. The silicon substrate used to prepare the cavity has a native oxide layer on top of about 2 nm thickness. The precise thickness and roughness of the constituent layers were determined by measuring the X-ray reflectivity of the cavity at different incidence angles and fitting the data using a differential evolution algorithm in the software GenX [GB22]. The fitted curve is shown in Fig. 6.6(b) and the fit parameters are given in Table 6.3. When the incidence angle of the X-ray beam on the cavity is larger than the critical angle of the top platinum layer ($\vartheta_c \sim 0.32°$), the beam is not only reflected but also refracted through the cavity layers. For incidence angles smaller than the critical angle, no refraction occurs. However, the X-ray reflectivity spectrum of the cavity exhibits distinct minima at certain angles below ϑ_c. It is at these angles that the cavity behaves like a waveguide - the X-ray field evanescently couples into the cavity, gets strongly amplified with the generation of a standing wave in the guiding layer, and couples out at the lateral boundaries of the cavity.

To calculate the energy response of the cavity, we need to determine the hyperfine parameters of the ^{57}**Fe** nuclei in the stainless steel layer precisely. To do so, we fit the time spectrum of the cavity measured at incidence angle $\vartheta = 0.53°$. Since this angle is far away from any waveguide mode, the time response is stable to any small angular perturbations during the measurement. As we are in grazing incidence, the nuclear scattering from the cavity can be treated in the forward-scattering approximation [Röh99]. The fitted model is shown in Fig. 6.7(b) and the fit parameters are given in Table 6.4. An isomer shift distribution in the sample effectively broadens the linewidth of the single line resonance of the paramagnetic stainless steel. The FWHM is given as 0.38 mm s^{-1}, which is approximately equivalent to 3.9 Γ. Bulk stainless steel does not

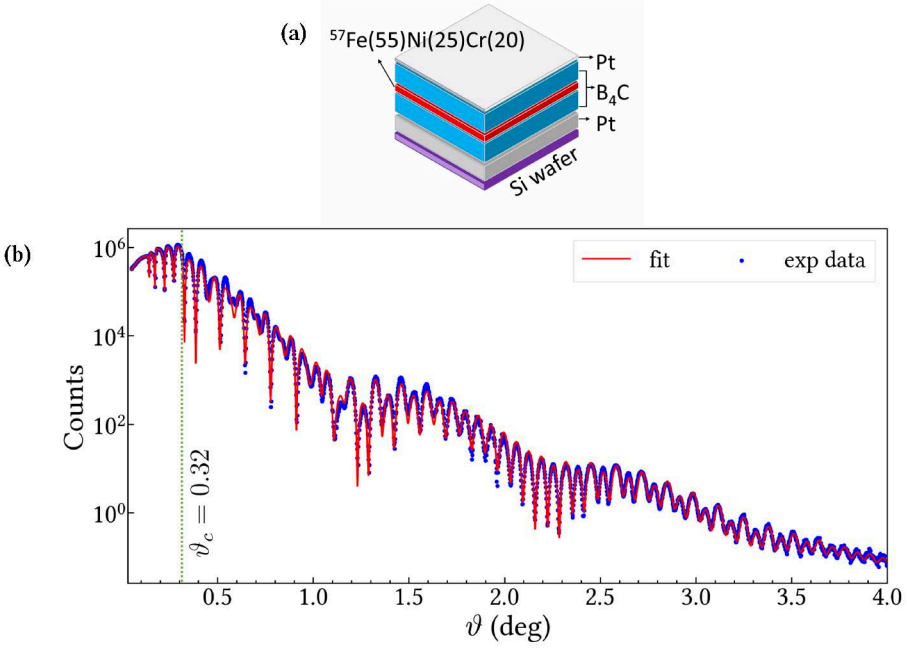

Figure 6.6.: (a) Layer structure of the thin film cavity. (b) X-ray reflectivity of the cavity was measured as a function of the angle of incidence ϑ. It is fitted using GenX to calculate the thicknesses and roughness of each layer in the cavity. The green dotted line marks the critical angle ϑ_c of the top platinum layer of the cavity.

Layer material	Thickness (nm)	Density (g/cm^3)	Roughness (nm)
Pt	2.23	21.45	0.22
B_4C	15.98	2.49	0.31
^{57}SS	1.20	7.03	0.29
B_4C	17.83	2.50	0.29
Pt	16.08	20.84	0.29
SiO_2	1.80	2.65	0.64

Table 6.3.: Layer parameters of the cavity from the GenX fit of the X-ray reflectivity shown in Fig. 6.6(b). The roughness values indicate the standard deviation of a Gaussian distribution around the layer thickness.

have any electric field gradients and exhibits no quadrupole splitting. However, our fitted model shows that the ^{57}SS layer has a quadrupole splitting of 0.64 mm s^{-1}. This has been measured previously for stainless steel films of nanometer range thicknesses [Sah+11]. The fit model assumes that the ^{57}SS layer has an isotropically distributed electric field gradient in 3-D with no preferred direction.

Parameter	Fit result
Quadrupole splitting	0.64 mm s^{-1}
FWHM Isomer shift	0.38 mm s^{-1}

Table 6.4.: Fit parameters of the time response of the cavity, as shown in Fig. 6.7(b).

Using the parameters in Table 6.4 and Table 6.3, we can also simulate the nuclear contribution to the X-ray reflectivity of the cavity. In Fig. 6.8, we plot the simulation alongside the measured nuclear reflectivity at different incidence angles of the beam.

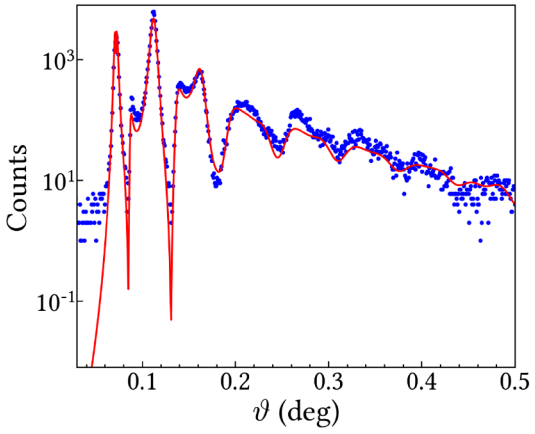

Figure 6.8.: The angular dependence of the nuclear reflectivity of the cavity. The experimental data is shown in blue while the curve simulated from the fitted hyperfine parameters is shown in red.

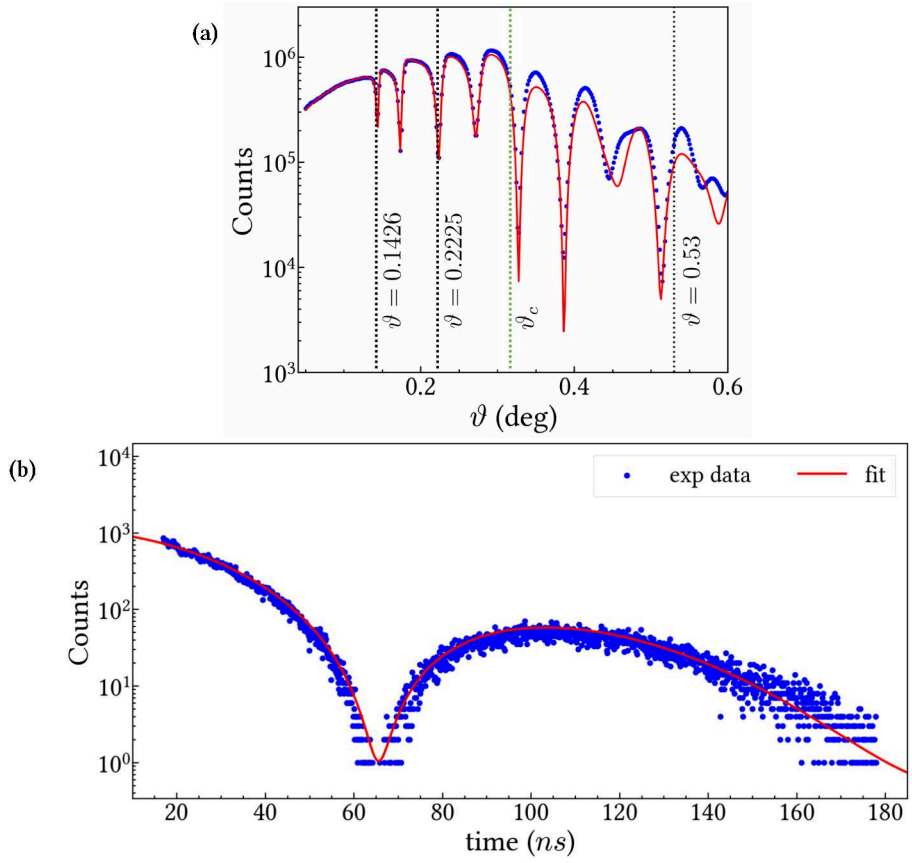

Figure 6.7.: (a) The electronic reflectivity of the cavity as a function of the angle of incidence. The experimental data is shown in blue while the GenX fit is shown in red. The measured X-ray reflectivity of the cavity has minima corresponding to the "waveguide" modes. The first and third-order waveguide modes of the cavity are at incidence angles $\vartheta = 0.1426°$ and $0.2225°$, respectively. (b) The time response of the cavity measured at $\vartheta = 0.53°$, between $T_{\text{min}} = 17$ ns and $T_{\text{max}} = 178$ ns. The model fitted using NEXUS is shown in red.

By varying the incidence angle of the beam, we can choose different waveguide modes of the cavity and tune the interaction between the incident X-rays and ^{57}**Fe** nuclei in the stainless steel layer. Different modes of the cavity have different field distributions and energy responses. We employ the cavity as a probe function at two different angles of incidence - the first-order waveguide mode $\vartheta = 0.1426°$ and the third-order waveguide mode $\vartheta = 0.2225°$. The field intensities in the cavity at the two angles is shown in Fig. 6.9. The corresponding complex scattering response of the cavity is shown in Fig. 6.10. We can see that the scattering response of the cavity around the first-order waveguide mode is relatively more sensitive to slight changes in the incidence angle compared to the third-order waveguide mode.

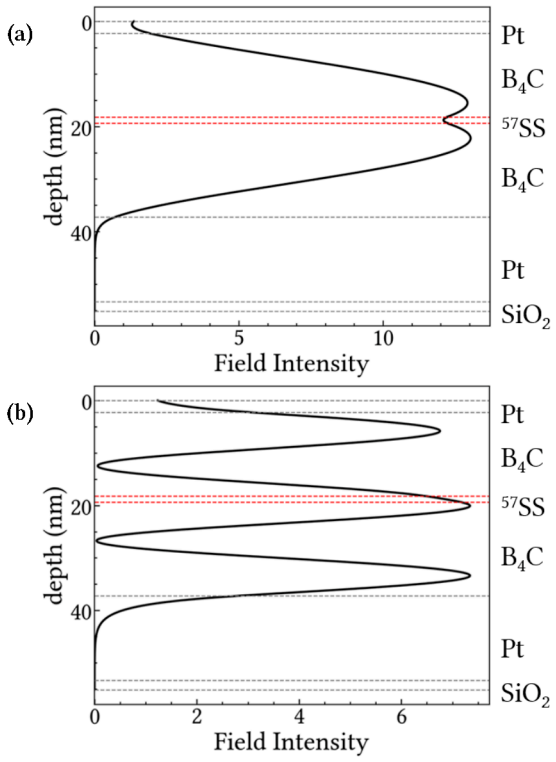

Figure 6.9.: The field intensity inside the cavity for the (a) first and (b) third-order waveguide mode. The small dip in field intensity at the center in (a) is due to interaction with the thin stainless steel layer.

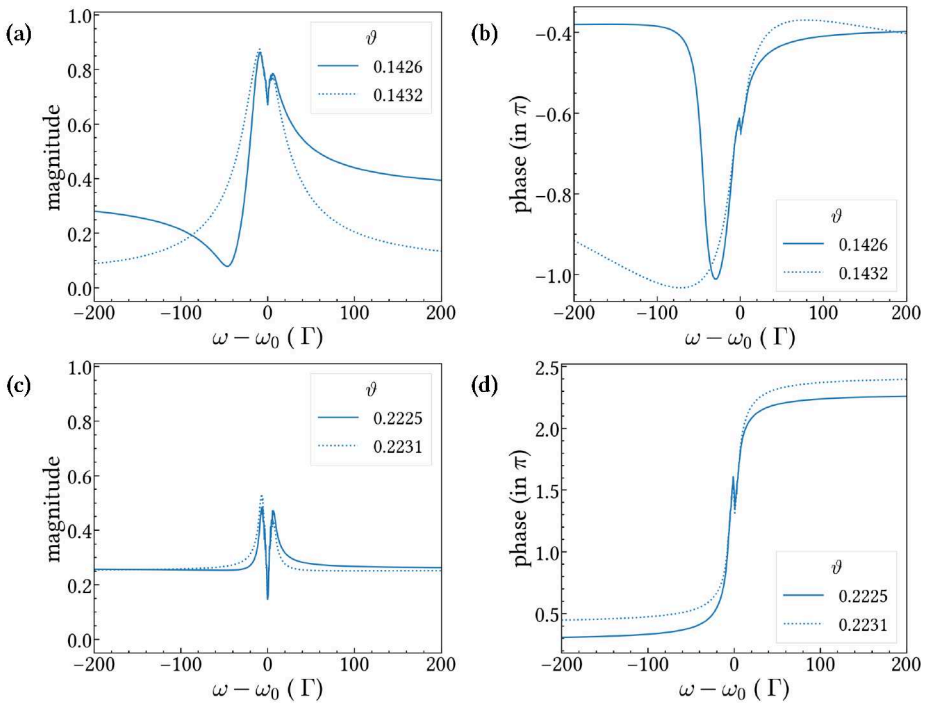

Figure 6.10.: The subfigures (a) and (b) respectively show the magnitude and phase of the scattering response of the cavity at the first-order waveguide mode while subfigures (c) and (d) respectively show the magnitude and phase of the scattering response of the cavity at the third-order waveguide mode. The dotted lines in all subfigures represent the scattering response in the presence of a slight angular perturbation of 0.0006°.

6.3. The reference object

To validate and benchmark the performance of our ptychography setups, we used them to reconstruct the complex energy domain scattering response of a reference object - an iron foil enriched to 95% with the resonant ^{57}**Fe** isotope.

To characterize its hyperfine parameters, we measured the time response of the ^{57}**Fe** foil alone in the beam. The scattering geometry of the experiment is shown as an inset in Fig. 6.11(b). An external magnetic field **B** = 0.12 T was applied to the foil along the σ direction, i.e., along the direction of the polarization of the synchrotron beam. We

fit the time response with a differential evolution algorithm using NEXUS. The Lamb-Mössbauer factor and density of the foil is taken as 0.796 and 7.874 g cm^{-3}, respectively. In the fit model, we assume two hyperfine sites per unit cell, corresponding to two different magnetic phases in the foil. Site 1 is magnetized along σ while site 2 has no preferred orientation of the magnetic field. The two magnetic phases can coexist due to the external magnetic field not being able to fully magnetize all nuclear spins in the same direction. Site 1 and site 2 both are also assumed to have a splitting due to quadrupole interaction with an isotropically distributed electric field gradient.

To describe the broadening of the lines we assume incoherent distributions in the thickness of the foil. The best fit (Fit 2 in Fig. 6.11(b)) was obtained for bunch spacing correction with $T_{bs} = 192.125$ ns. The parameters of the best fit are given in Table 6.5. As shown in Fig. 6.11(a), the foil has a Gaussian thickness distribution centered at 2.4 µm with a FWHM of 0.3 µm. The ratio of the two sites tells us that 93.6% of the ^{57}**Fe** nuclei in the foil are magnetized along the σ direction while the rest are randomly oriented. The mean hyperfine magnetic field B_{hf} at the nuclei in the two magnetic phases is slightly different, i.e., 32.7 T for sites oriented along the applied external field **B** and 32.4 T for the sites with random orientation. The mean quadrupole splitting of all sites was found to be 0.04 mm s^{-1}.

Parameter	**Fit result**
Thickness	2.4 µm
FWHM Thickness	0.3 µm
Weight site 1	93.6 %
B_{hf}	32.7 T
Quadrupole splitting	0.04 mm s^{-1}
Weight site 2	6.4 %
B_{hf}	32.4 T
Quadrupole splitting	0.04 mm s^{-1}

Table 6.5.: Fit parameters of the time response of the ^{57}**Fe** foil, as shown in Fig. 6.11(b).

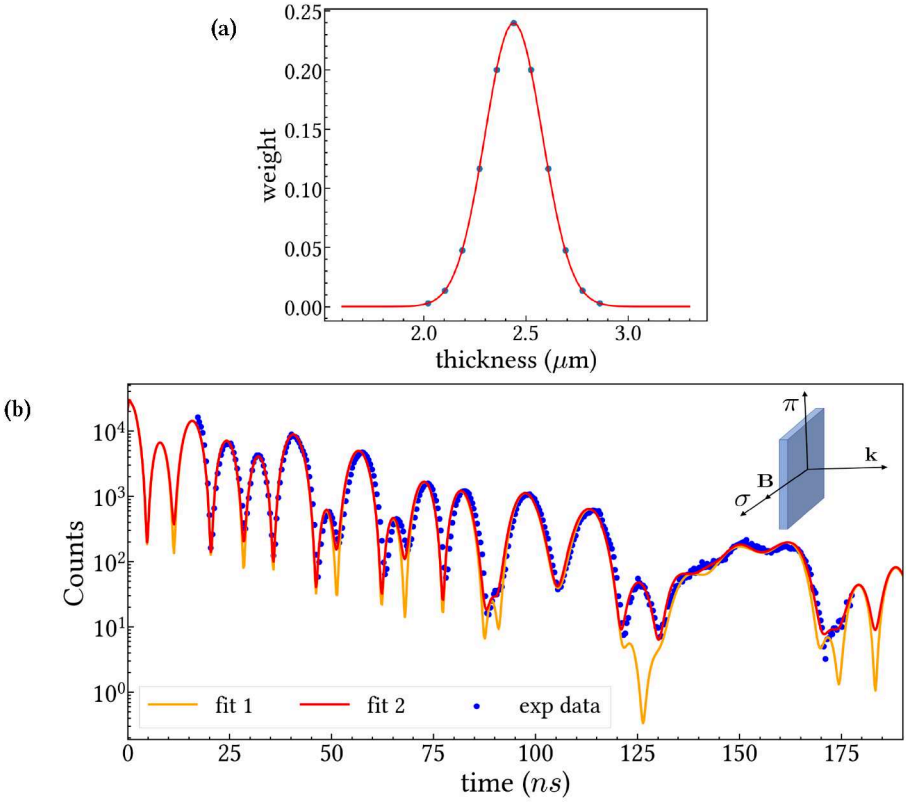

Figure 6.11.: (a) The fitted thickness distribution of the ^{57}**Fe** foil. (b) The time response of the ^{57}**Fe** foil measured between 17 and 178 ns (in blue) versus the fitted model with bunch spacing correction (in red) and without bunch spacing correction (in orange). The scattering geometry is shown as an inset. The incident synchrotron radiation from Petra III is σ polarized.

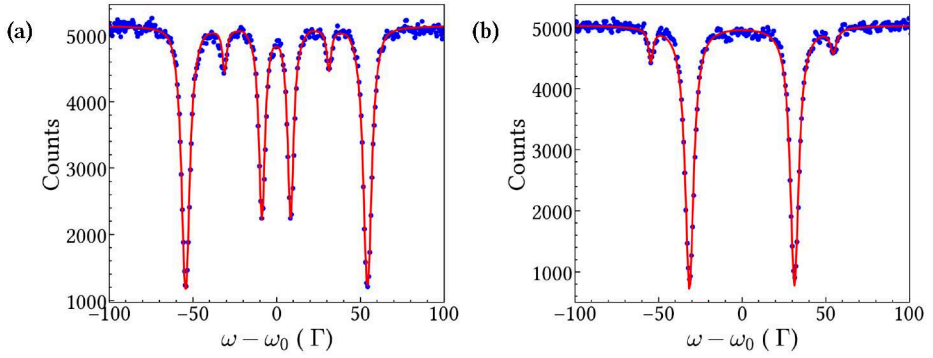

Figure 6.12.: The energy spectra of the ^{57}**Fe** foil measured using the synchrotron Mössbauer source (SMS) at ID-18, ESRF, France (in blue) is plotted alongside the energy spectrum simulated with parameters in Table 6.5 (in red). In (a), the magnetic field was applied along the direction of polarisation of the beam from the SMS, whereas in (b), it was applied perpendicularly.

We have thus characterized the ^{57}**Fe** foil and can simulate its complex energy response[3] using the fit parameters in Table 6.2, which we denote as $\hat{\boldsymbol{O}}^*_\infty$. The acquisition time at the detector is limited from T_{min} = 17 ns to T_{max} = 178 ns. By masking the pixels with the missing data, the ptychographic engine can reasonably extrapolate the missing intensities between 0 and 17 ns by taking advantage of the oversampled measurements. This is also done in ptychographic imaging in the presence of a beam stop [Dej+24; Rei+17]. For values beyond T_{max}, the extrapolation does not work so well. Therefore, to remove the reconstruction errors beyond T_{max}, we define a filtering window $\boldsymbol{H}$ in the time domain as

$$\boldsymbol{H}_q = \begin{cases} 1 & q\Delta t \leq T_{\text{max}} \\ 0 & \text{otherwise} \end{cases} \tag{6.1}$$

which is a Heaviside step function.[4] We can apply this filter to the complex energy response of the foil as

$$\hat{\boldsymbol{O}}^*_H = \mathbf{F}^{-1} \cdot \text{diag}(\boldsymbol{H}) \cdot \mathbf{F} \cdot \hat{\boldsymbol{O}}^*_\infty, \tag{6.2}$$

where $\mathbf{F}$ denotes the discrete Fourier transform matrix. Hence, we obtain $\hat{\boldsymbol{O}}^*_H$, which is the simulated energy response of the ^{57}**Fe** foil including the windowing effects. As shown in Fig. 6.13, the time domain filtering also introduces wiggle artifacts in the energy response of the object just like the measurement time window (see also Sec. 5.4). In most cases, we will compare our reconstruction results using this filtered object as the reference or the "ground truth".

[3] We ignore the small distribution in the thickness of the foil.

[4] Smoothening the step-function in $\boldsymbol{H}$ leads to a Gaussian-like smoothening of the artifacts in the energy response of the object, but the peaks of the resonances are broadened and their relative heights are not preserved.

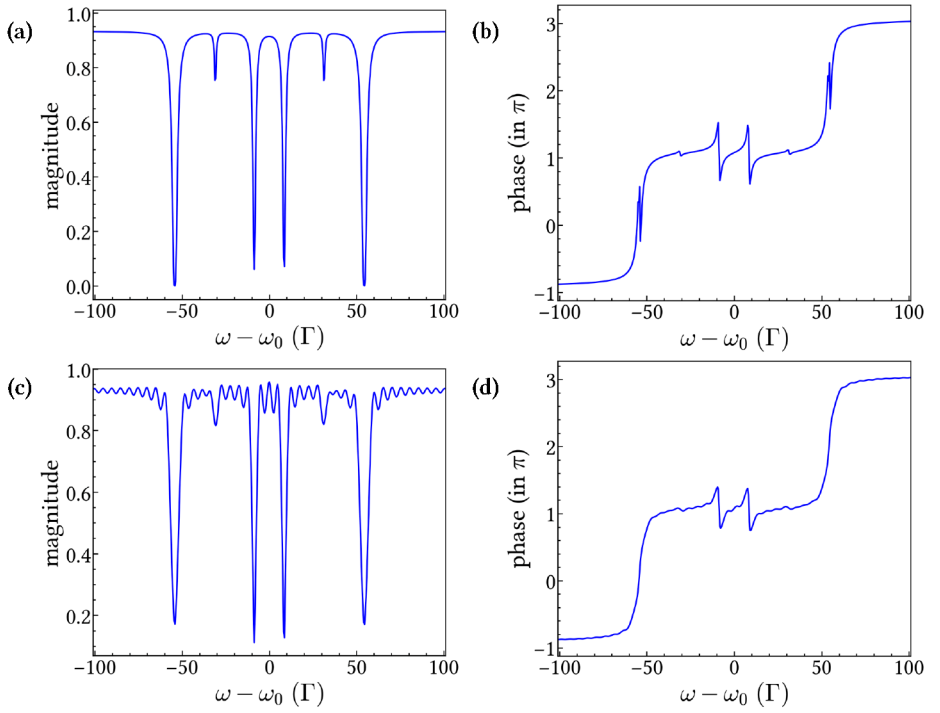

Figure 6.13.: (a) Magnitude and (b) phase response of the true object (^{57}**Fe** foil) $\hat{\boldsymbol{O}}_H^{\infty}$ without the time window ($T_{\max} = \infty$). (c) Magnitude and (d) phase response of the true object $\hat{\boldsymbol{O}}_H^{*}$ with the time window $\boldsymbol{H}$ where $T_{\max} = 178$ ns. Here, the external magnetic field is applied along the direction of σ polarization of the beam.

6.4. Transmission mode ptychography

The ptychography setup in the transmission geometry is shown in Fig. 6.2(a), where we employed the ^{57}SS foil as the probe. The object (^{57}**Fe** foil) was mounted on the Doppler drive and moved relative to the probe. We measured two ptychograms for the object by introducing an external magnetic field $\mathbf{B}$ = 0.12 T at two distinct orientations with respect to the direction of linear polarisation of the synchrotron beam (along σ). In the first case, we applied $\mathbf{B} \parallel \sigma$, i.e., along the direction of the beam's polarisation. In the second case, we used $\mathbf{B} \parallel \pi$, which is perpendicular to both the direction of polarisation of the beam and the wave vector $\mathbf{k}$. They are shown in Fig. 6.14. The velocity of the Doppler drive at each channel number of the MCS6A was calibrated via the procedure described in Appendix C.2.

The input parameters of the ptychography reconstruction are listed in Table 6.6. We always start the phase retrieval with a 4096×1 array of ones as our object guess. When the algorithm converges, we can do an additional post-processing step to remove any errors due to the finite T_{max} in the experiment. The reconstructed object $\hat{\boldsymbol{O}}^r$ is corrected by filtering out the later times as

$$\hat{\boldsymbol{O}}^r_H = \mathbf{F}^{-1} \cdot \text{diag}(\boldsymbol{H}) \cdot \mathbf{F} \cdot \hat{\boldsymbol{O}}^r \tag{6.3}$$

where $\boldsymbol{H}$ is defined in Eq. (6.1).

Parameter	Value
$(\omega_{\text{min}}, \omega_{\text{max}}, \Delta\omega)$	(-886.62, 886.19, 0.43) Γ
M_{factor}	11
Calculation grid size	4096×1
Acquisition time window (T_{min}, T_{max})	(17 ns, 178 ns)
Maximum velocity of the Doppler drive	20.7(1) mm s^{-1}
Algorithm	SGD-NAG
(α, β, batch-size)	(0.003, 0.66, 20)

Table 6.6.: Ptychography engine reconstruction parameters for the transmission mode experiment.

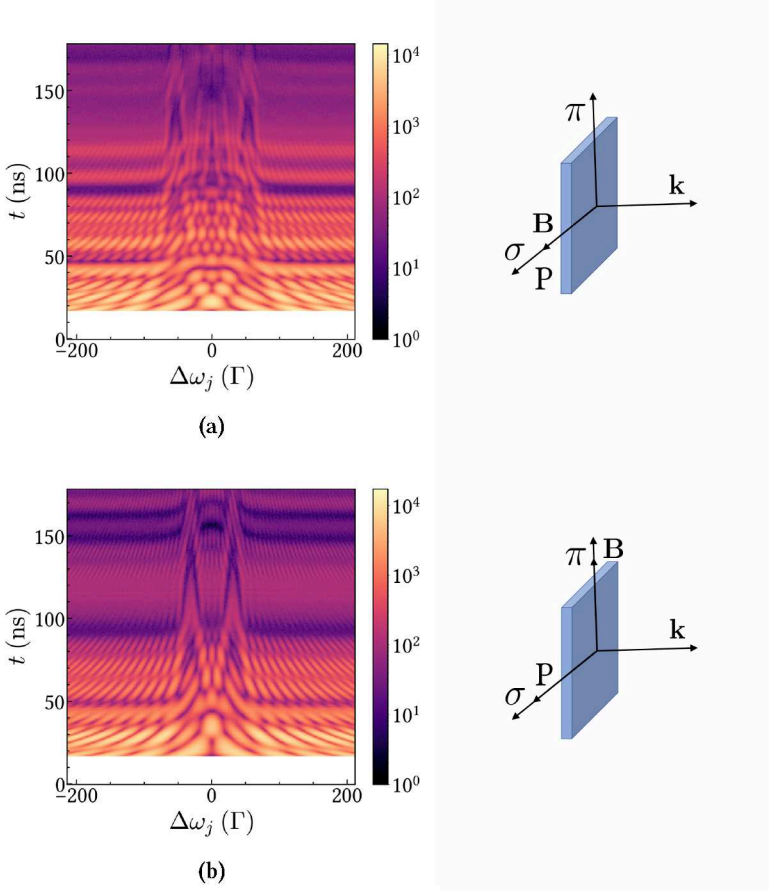

Figure 6.14.: The experimentally measured ptychogram when the external magnetic field is applied (a) parallel to the direction of polarization of the synchrotron beam (**B** $\parallel$ σ) and (b) perpendicular to the direction of polarization (**B** $\parallel$ π). Here **P** and **k** denote the polarization and propagation direction of the synchrotron beam, respectively.

6.4.1. Phase retrieval from simulated datasets

As previously described in the Sec. 4.3.5, the thickness distributions in the probe and the object lead to incoherent contributions in the experimental data. Additionally, there can be incoherent contributions to the measurements due to scattering from the previous synchrotron pulses, as described in Appendix B.3. To study how these incoherent contributions affect phase retrieval, we simulate the ptychography experiment where the ^{57}**Fe** foil was magnetized along the direction of the polarization of the beam ($\mathbf{B} \parallel \sigma$). All the parameters for the simulation are taken from Tables 6.2 and 6.5. The detector time window of (T_{min}, T_{max}) = (17, 178) ns is also taken into account.
The simulated ptychograms for the coherent and incoherent case are shown in Fig. 6.15. If we integrate the photon counts for each ptychogram over all Doppler detunings, we obtain an 'integrated time response' of the system. We can see in Fig. 6.15(d) that the integrated time response of the incoherent simulation describes the experiment more closely than that of the fully coherent simulation. Therefore, the results of phase retrieval from the incoherent simulation and the experimental data should be comparable.

To retrieve the phase and reconstruct the object, we have simulated the complex energy response of the probe at eleven distinct points sampled from its thickness distribution, as shown in Fig. 6.5. For the coherent simulation, we assume that only the probe mode corresponding to the mean thickness of the ^{57}SS foil interacts with the object. For the incoherently simulated ptychogram, we assume that all eleven probe modes interact with the object and their contributions to the measurement can be described by the incoherent forward model (Eq. (4.29)) of the ptychography engine. The ptychography engine converges to a solution in less than 200 iterations for both cases. As a post-processing step, we have filtered the reconstructed object according to Eq. (6.3). This gets rid of reconstruction noise from times beyond 178 ns (where the detector records no data) but introduces the artificial "wiggles" around the resonance peaks. We compare the filtered reconstructed object $\hat{\boldsymbol{O}}_H^r$ to the filtered ground truth object $\hat{\boldsymbol{O}}_H^*$ in Fig. 6.16. In both the coherently and incoherently simulated cases, the object is reconstructed very well in the region of interest $\Delta\omega_j \in (-70, 70)\ \Gamma$, except for a scaling factor in the magnitude (not shown). The scaling factor arises because we do not have information about the absolute intensity of the object due to the missing data in the ptychogram

before $T_{\text{min}} = 17$ ns. We can only force the engine to extrapolate the missing time response object between 0 and T_{min}, as shown in Fig. 6.17.
We also show the reconstruction of the object from the incoherent simulation with total variation (TV) regularization, where $u = 0.05$ in Eq. (4.20). This is shown in Fig. 6.18. We see that the wiggle artifacts in the reconstructed object are now replaced by blocky "staircase artifacts" [CMM00]. This is because TV regularization tends to force sparsity into the solution by converting the wiggles into piecewise constant regions while solving the cost minimization problem [Shi+19]. In Eq. (4.22), the regularization term only takes the first derivative of the object into account and ignores the higher-order smoothness of the solution.

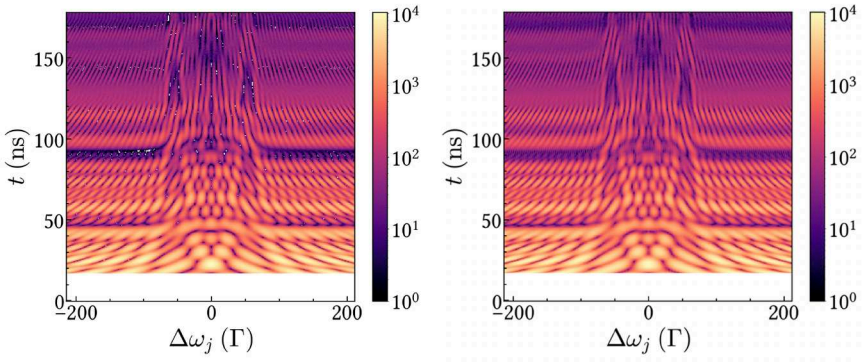

(a) Coherent simulation **(b)** Incoherent simulation

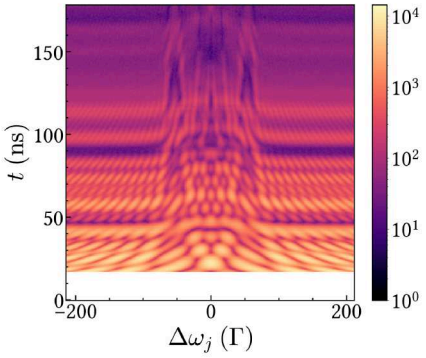

(c) Experimental data

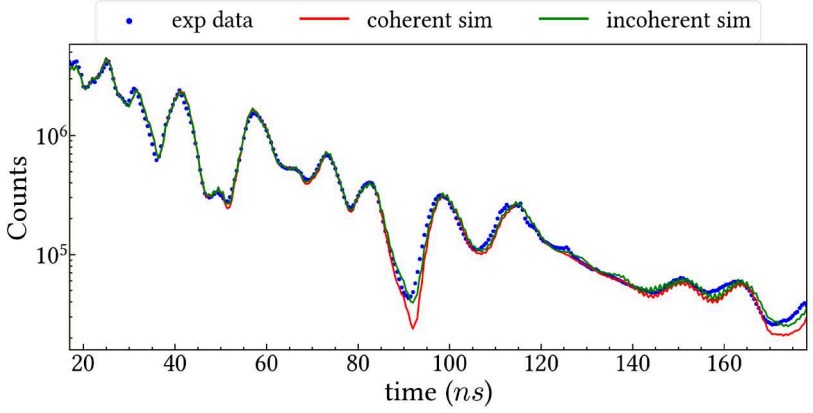

(d) Integrated time response of the probe-object system.

Figure 6.15.: *(see next page)*

Figure 6.15 ***(previous page)***: (a) The ptychogram simulated with the assumption that the iron foil and the stainless steel foil have a uniform mean thickness of 2.4 μm and 17.83 μm, respectively. (b) The incoherent simulation of the ptychogram via Monte Carlo sampling for the thickness distributions of the probe and the object foils. Incoherent contributions from the previous pulses are also included by assuming an electron bunch-spacing of 192.125 ns. (c) The ptychogram measured in the experiment. (d) The ptychograms can be used to generate the integrated time response of the probe-object system over all Doppler drive detunings. The mismatch between the coherent simulation and the experimental data is evident in the minima of the plots.

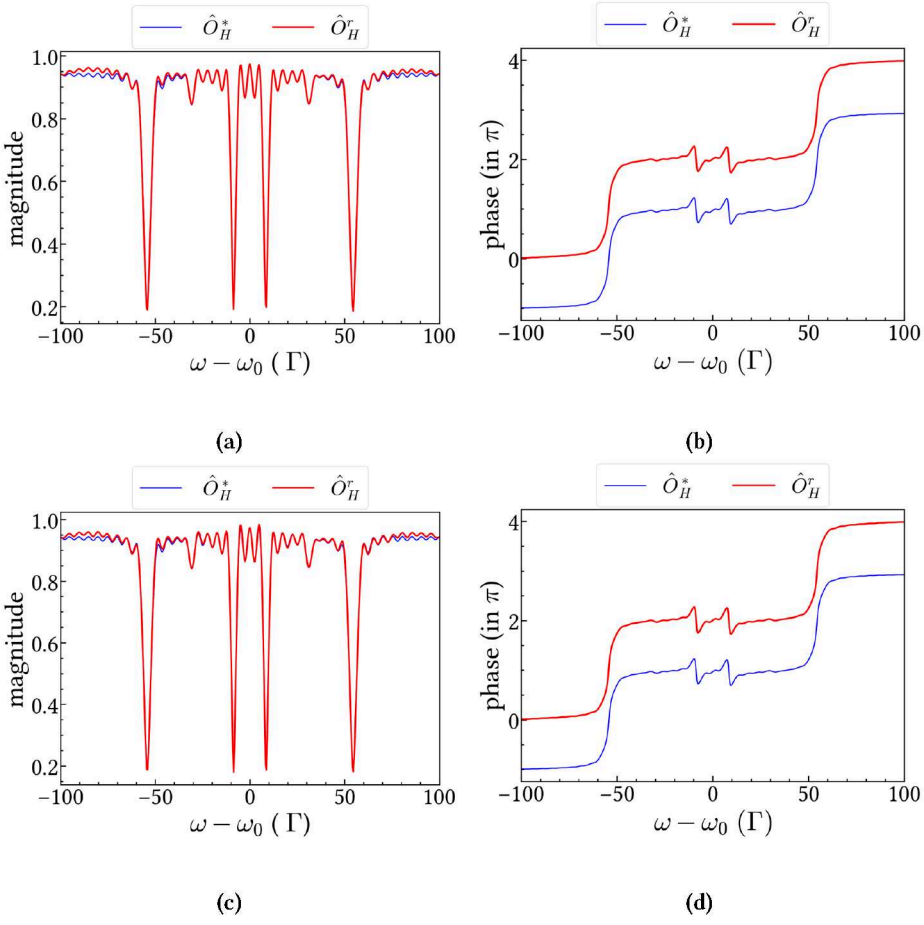

Figure 6.16.: The energy domain scattering response of the reconstructed object $\hat{\boldsymbol{O}}_H^r$ (in red) compared to the true object $\hat{\boldsymbol{O}}_H^*$ (in blue). Subfigures (a) and (b) show the object reconstructed from the coherently simulated ptychogram while (c) and (d) show the object reconstructed from the incoherently simulated ptychogram. Both the reconstructed and the true objects have been time windowed by $\boldsymbol{H}$ to filter out the extrapolation errors beyond $T_{\max}$. The reconstructed object has been scaled by a constant value to match the baseline of the true object for comparison.

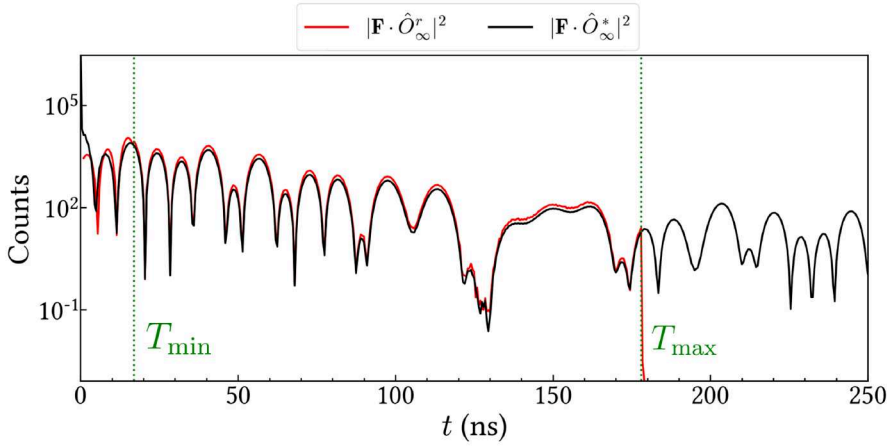

Figure 6.17.: The time response of the object reconstructed from the incoherent simulation (in red) and the true object (in black). The engine is unable to reconstruct the time response beyond $T_{\max}$ but is able to extrapolate the values between 0 and $T_{\min}$ quite well.

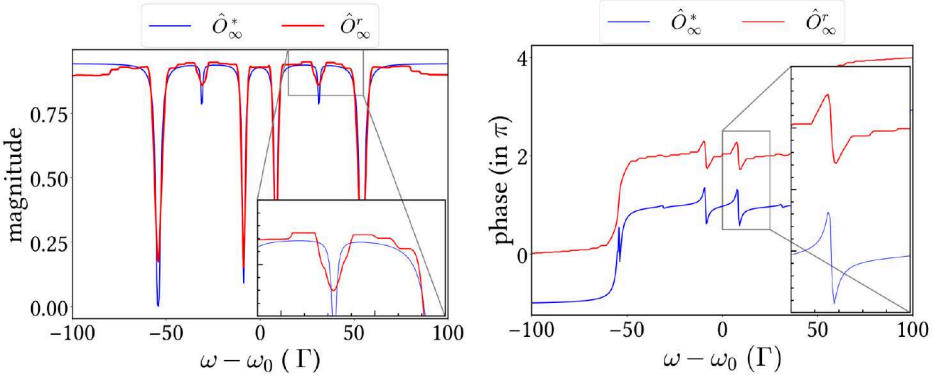

Figure 6.18.: (a) Magnitude and (b) phase response of the reconstructed object $\hat{\boldsymbol{O}}^r_\infty$ with TV regularization (in red) compared to the true object (in blue). The zoomed inset depicts "staircase effects" in the regularized solution.

6.4.2. Phase retrieval from the experimental datasets

From our tests on the simulated ptychograms in the previous section, we observed that even when the experimental data has some incoherent contributions, we may correctly retrieve the phase if we include the incoherence into the forward model of the ptychographic engine as in Eq. (4.29). In this section, we show the phase retrieval results from the experimentally measured ptychograms for the two orientations of the external magnetic field **B** on the ^{57}**Fe** foil (Fig. 6.14). We sample eleven probe modes from their distribution, similar to the incoherently simulated case in the previous section (Fig. 6.5).

As discussed in Fig. 3.10, the object and the probe are coupled for smaller Doppler detunings. If we select only the measurements in the range $\Delta\omega_j \in$ (-70 Γ, 70 Γ) from the ptychogram to retrieve the object, it improves the phase retrieval results from the experimental data (see Appendix C.3). The reasoning behind this is not clear. Outside this range, we mostly measure the interference signal. It could be that the interference signal is more susceptible to background noise, velocity drive calibration errors and incoherent contributions to the experiment.

For both ptychogram datasets, the reconstruction is run for 500 iterations. Their convergence behavior is shown in Fig. 6.19. For the first ptychography experiment where $\mathbf{B} \parallel \sigma$, we reconstruct the object with and without total variation (TV) regularization ($u = 0.05$). In both cases, the reconstructed object is globally shifted in energy relative to the true object by 0.49 Γ. The phase response of the reconstructed object also has a global phase shift of 0.33π relative to the true object. As described in Sec. 2.6, this is a trivial ambiguity in the ptychographic phase retrieval problem and is inevitable. When the global energy shift is taken into account, the positions of the four largest peaks in the magnitude of the object match with each other up to ± 0.2 Γ, which is comparable to the resolution of the calculation grid (0.43 Γ). The magnitude and phase of the reconstructed object are shown in Fig. 6.20. The object has been filtered in the time domain according to Eq. (6.3) and rescaled to match the height of the peaks of the true object $\hat{\boldsymbol{O}}^*_H$. The results of the peak position fits are shown in Table 6.7.
In the region of interest $\Delta\omega_j \in (-70, 70)$ Γ, the unregularized reconstructed object matches very well with the true object $\hat{\boldsymbol{O}}^*_H$. However, due to the wiggle artifacts, it is difficult to differentiate between the real and the artificial peaks in the magnitude of the object. In the SMS measurement of the foil (Fig. 6.12(b)a), we see that there are

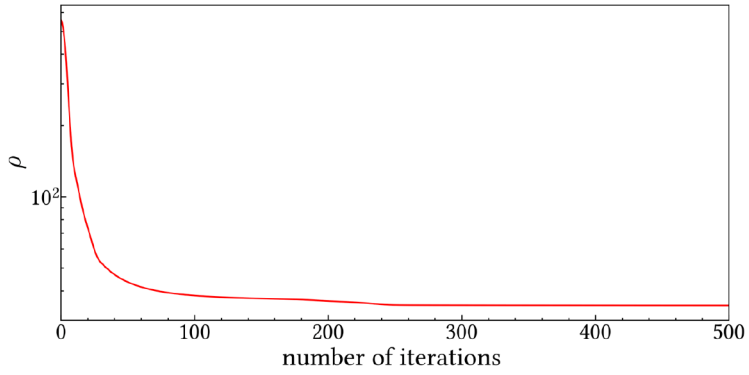

(a) B ∥ σ

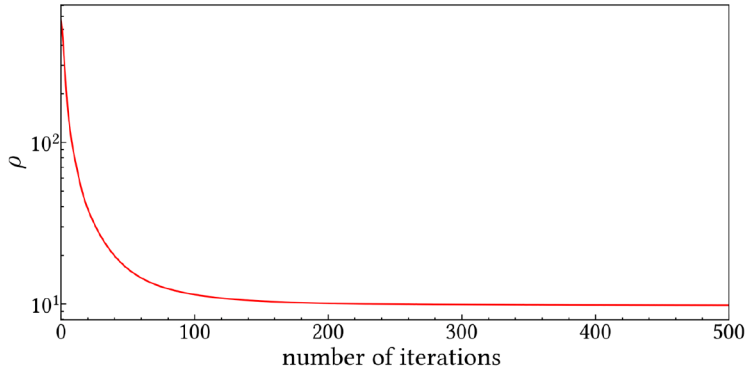

(b) B ∥ π

Figure 6.19.: The cost ρ of the reconstructed object decreases with the number of iterations of the ptychography engine. (a) The value of ρ decreases rapidly for the first 50 iterations and then the rate of decrease slows down. Between iterations 250-255, ρ decreases rapidly again but thereafter the curve plateaus. (b) The value of ρ plateaus after 200 iterations.

two additional smaller resonance peaks present in the energy spectrum at around ±31.5 Γ. These peaks are not clearly distinguishable in the energy response of the object retrieved from experimental data. Instead, we see additional peaks emerging at ±20 Γ due to the time windowing. In the total variation regularized solution, the wiggles are replaced by severe staircase artifacts. The quality of the reconstruction in this case is not improved by the regularizer.
The time domain response of the reconstructed object is shown in Fig. 6.21. We see that the engine has the most problem reconstructing the intensities of the object between 120 and 140 ns. This is likely due to the bunch spacing incoherence in the experimental data because of scattering from the previous pulses (see Fig. 6.11(b)). Since this incoherent contribution cannot be included in a differentiable way in the forward model, the ptychography engine cannot correct it while solving the inverse problem.

Peak	a	b	c	d
$\hat{\boldsymbol{O}}_H^*$	-54.22	-8.67	8.49	54.40
$\hat{\boldsymbol{O}}_H^r$	-54.20	-8.58	8.58	54.21

Table 6.7.: The positions of the peaks marked in Fig. 6.20 for the true and the reconstructed object. All values are given in units of Γ.

In the second case where $\mathbf{B} \parallel \pi$, the magnitude and phase of the reconstructed object $\hat{\boldsymbol{O}}_H^r$ is shown in Fig. 6.22. We compare it to the synchrotron Mössbauer source (SMS) spectrum of the ^{57}**Fe** foil magnetized perpendicular to the polarization of the source (Fig. 6.12(b)b). The magnitudes of the reconstructed object and the measured SMS spectrum have been normalized from 0 to 1 for comparison. While there are four nuclear resonance peaks in the SMS spectrum, our reconstructed object has two prominent peaks 'b' and 'c'. The positions of the peaks are given in Table 6.8. Once again, the wiggle artifacts in the unregularized reconstruction mask the smaller peaks 'a' and 'd' in the reconstruction. With the help of total variation regularization (with u = 0.05), we can impose sparsity in the object reconstruction. As shown in Fig. 6.22(c), this makes it easier to distinguish an energy contribution at the positions 'a' and 'd', even though the reconstructed object now has staircase artifacts.

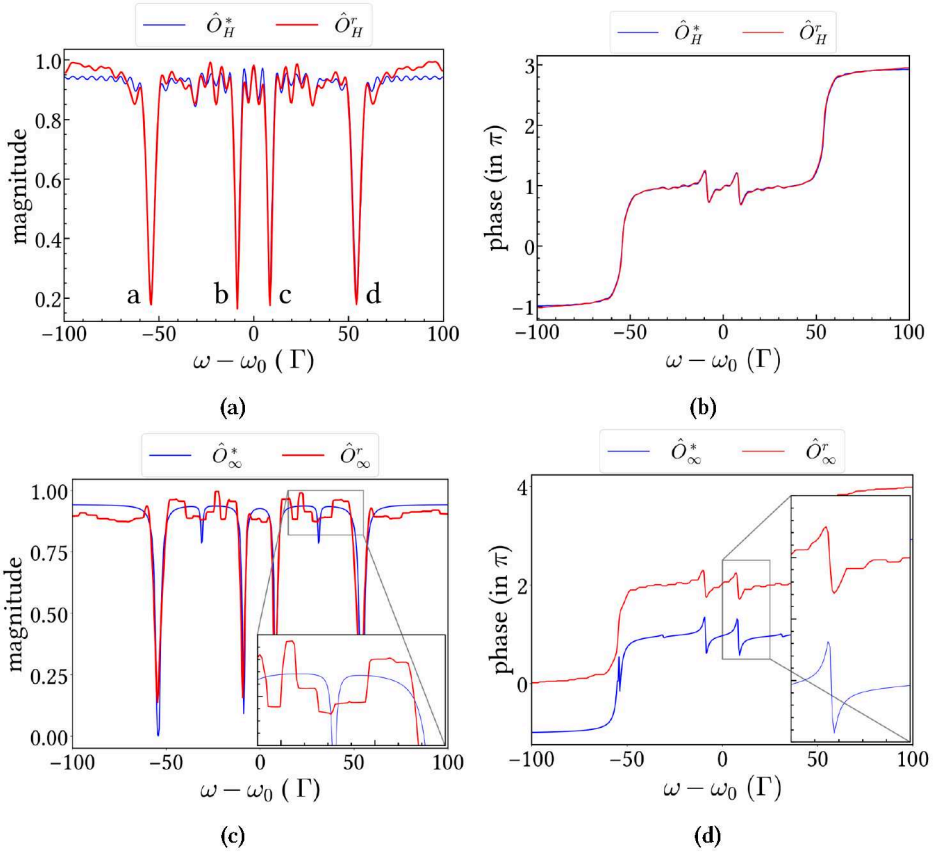

Figure 6.20.: Magnitude and phase response of the reconstructed object $\hat{\boldsymbol{O}}^r_H$ (in red) compared to the true object $\hat{\boldsymbol{O}}^*_H$ (in blue) from the ptychogram with $\mathbf{B} \parallel \sigma$. The global energy shift of 0.49 Γ and the global phase shift of -0.33π has been taken into account while plotting the reconstructed object. Subfigures (a) and (b) show the unregularized reconstruction while (c) and (d) show the total variation regularized reconstruction with $u = 0.05$.

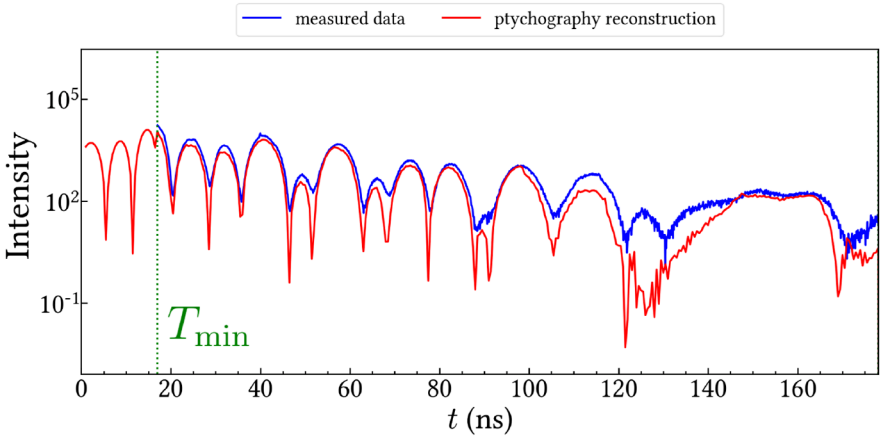

Figure 6.21.: The time response of the reconstructed object plotted against the experimentally measured time response of the ^{57}**Fe** foil for the same scattering geometry (**B** $\parallel \sigma$).

Peak	a	b	c	d
SMS spectrum	-54.47	-31.38	31.45	54.71
$\hat{O}^r_H$	-	-31.85	31.17	-

Table 6.8.: The positions of the peaks marked in Fig. 6.22 calculated from the SMS spectrum and the ptychographically reconstructed object. All values are given in units of Γ.

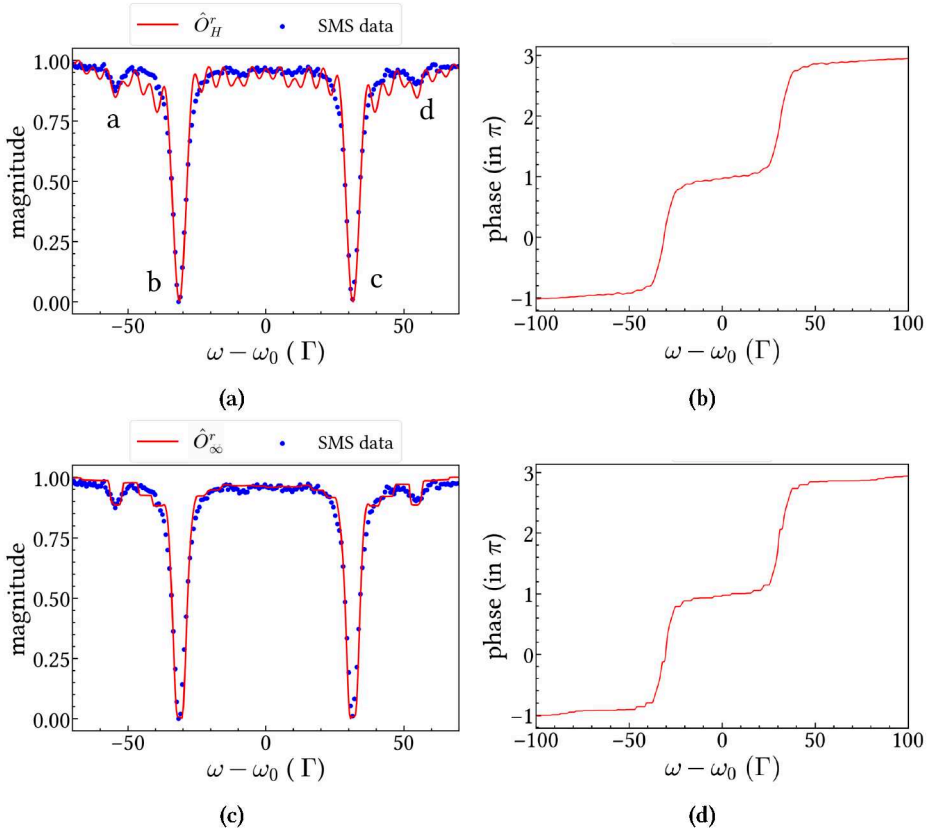

Figure 6.22.: The magnitude and phase of the object $\hat{O}^r_H$ reconstructed from the ptychogram with $\mathbf{B} \parallel \pi$ (in red) compared to the square root of the intensity spectrum measured at the SMS (in blue). Subfigures (a), (b) depict the results in the unregularized case while (c), (d) are for the total variation regularized case.

6.4.3. Conclusion

From the transmission mode ptychography experiment, we have shown that using a "known" nuclear resonant scattering probe like the ^{57}SS foil, the response of an object can be reconstructed in the energy domain. Ptychography can also be repeated for different scattering geometries to get the corresponding scattering responses. We have shown this by reconstructing specific hyperfine transitions in the ^{57}**Fe** foil by applying an external magnetic field. In principle, a polarizer-analyzer setup can also be utilized in the experiment to obtain the complex components of the scattering matrix of the object.

The incoherent effects due to the small thickness distribution of the probe were present in the experimental data. However, they could be taken into account in the forward model to improve the results. This approach is, in fact, equivalent to the "multi-modal ptychography" methods [Shi+18] employed in coherent diffractive imaging. The main bottleneck on the accuracy of the phase retrieval arises from the limited time window of the detection. It not only leads to the wiggle artifacts in the spectrum but also bunch spacing incoherence.

As shown in the example reconstructions from simulated and experimental ptychograms, it is possible to cosmetically remove the wiggles using regularization techniques like total variation. In Fig. 6.23, we see the time response of the ^{57}**Fe** foil with $\mathbf{B} \parallel \pi$, reconstructed with and without total variation (TV) regularization from the experimentally measured ptychogram. In both cases, the ptychography engine can smoothly extrapolate the response to times below T_{min}. However, only in the TV regularized case the engine tries to continuously extrapolate the response beyond T_{max}. This removes the wiggles in the magnitude of the reconstructed object in the energy domain (Fig. 6.22). The extrapolated time response beyond T_{max} is, however, artificial and comes from the choice of the regularizer. The more pragmatic and stable approach to improving the phase retrieval results is to choose the synchrotron's mode of operation such that T_{max} is long enough to capture the decay of the scattering response of the object, ideally up to at least 3-4 lifetimes of the Mössbauer nuclei.

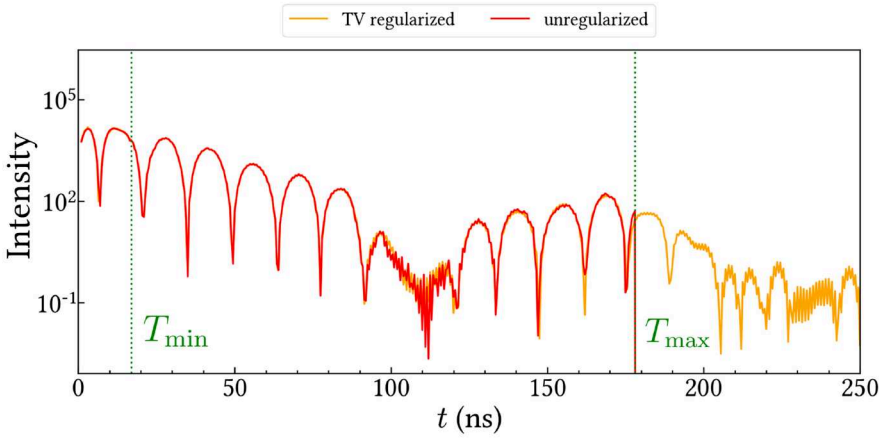

Figure 6.23.: The time response of the object (^{57}**Fe** foil) is reconstructed by the ptychography in the unregularized case and the total variation (TV) regularized case. The data acquisition time window in the experiment is between $T_{\min}$ = 17 ns and $T_{\max}$ = 178 ns.

6.5. Grazing incidence ptychography

In the grazing incidence ptychography setup (Fig. 6.2(b)), specular reflection from the thin film cavity was used to probe the object (^{57}**Fe** foil). We used the cavity as a probe function at two different angles of incidence corresponding to the first-order waveguide mode ($\vartheta = 0.1426°$) and the third-order waveguide mode ($\vartheta = 0.2225°$). An external magnetic field $\mathbf{B} = 0.12$ T was applied to the ^{57}**Fe** foil in the direction of polarization of the X-ray beam ($\mathbf{B} \parallel \sigma$). The measured ptychograms after velocity calibration of the Doppler drive are shown in Fig. 6.24(a) and 6.24(b). The maximum velocity of the drive and the isomer shift between the ^{57}**Fe** foil and the cavity were found to be 20.03(2) mm s^{-1} and $-0.40(3)$ mm s^{-1}, respectively.

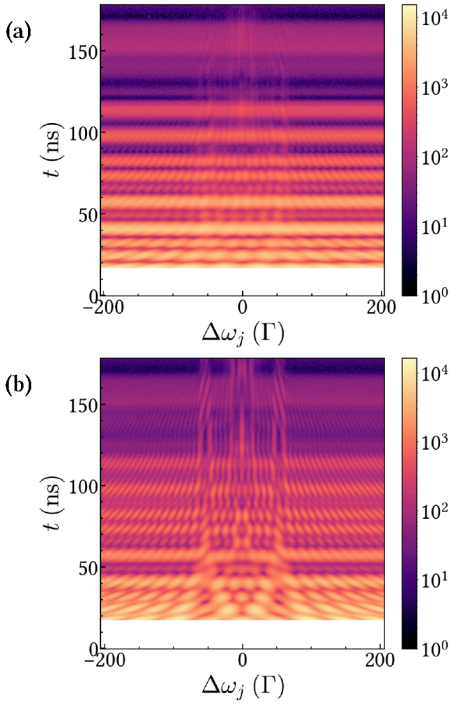

Figure 6.24.: The experimentally measured ptychogram at (a) the first-order waveguide mode ($\vartheta = 0.1426°$) and (b) the third-order waveguide mode ($\vartheta = 0.2225°$).

The input parameters of the ptychography reconstruction are listed in Table 6.9. We always start the phase retrieval with a 4096×1 array of ones as our object guess. The region of interest in the energy domain is between -70 to 70 Γ and we only select the measurements with $\Delta\omega_j \in$ (-70 Γ, 70 Γ) from the ptychogram to retrieve the object.

Parameter	Value
$(\omega_{\text{min}}, \omega_{\text{max}}, \Delta\omega)$	(-886.62, 886.19, 0.43) Γ
M_{factor}	11
Calculation grid size	4096×1
Acquisition time window (T_{min}, T_{max})	(17 ns, 178 ns)
Maximum velocity of the Doppler drive	20.03(1) mm s^{-1}
Algorithm	SGD-NAG
(α, β, batch-size)	(0.01, 0.66, 20)

Table 6.9.: Ptychography engine reconstruction parameters for the grazing incidence ptychography experiment.

6.5.1. Phase retrieval from simulated datasets

In the grazing incidence ptychogaphy experiment, there are also incoherent contributions to the measured data. We simulate them by using a Monte Carlo mechanism to sample a Gaussian distribution of the incidence angles of the X-ray beam on the cavity and the thickness distribution of the ^{57}**Fe** foil. We also include the incoherent counts due to the finite bunch spacing. The X-ray beam was focused using Beryllium lenses which have a beam spot size (vertical × horizontal) of about 40 µm × 1 mm on the sample and a divergence of about 0.003°. However, by comparing the simulation with the experimental data, we find that a Gaussian angular distribution of FWHM ∼ 0.0075° was present in the experiments. This indicates that the angle of the beam could have slightly drifted during the ptychogram measurements. The silicon substrate for the cavity preparation might also not be thick enough and cause slight bending in the cavity while sputtering.

We can see the incoherent effects in Fig. 6.26 by comparing the simulated ptychograms for the coherent and the incoherent case with the experimentally measured ptychograms. The coherent simulation is done by ignoring any angular divergence

in the beam or thickness distribution in the ^{57}Fe foil. We can also compare the integrated time response of the probe-object system from the ptychograms. In Fig. 6.25, we see that the incoherent effects contribute significantly to the experimental data and should be taken into account during phase retrieval. Therefore, from the Gaussian angular distribution around each waveguide mode, we sample 31 equidistant angles with FWHM 0.0075°. The corresponding scattering response functions of the cavity and their weights are shown in Fig. 6.27.

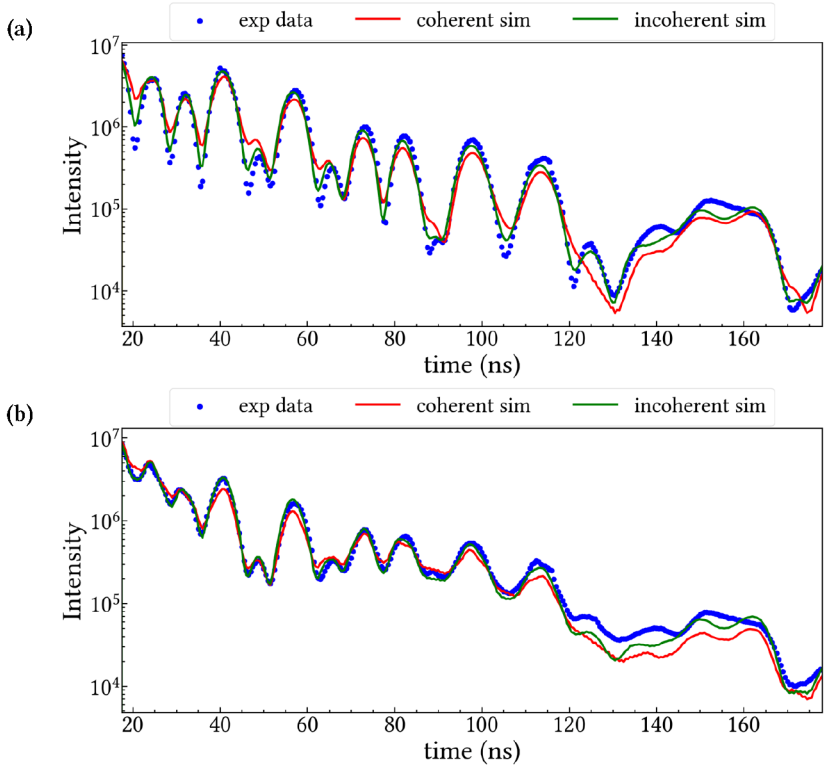

Figure 6.25.: The time response of the object-probe system is integrated along all Doppler detunings at the (a) first and (b) third-order waveguide mode of the cavity.

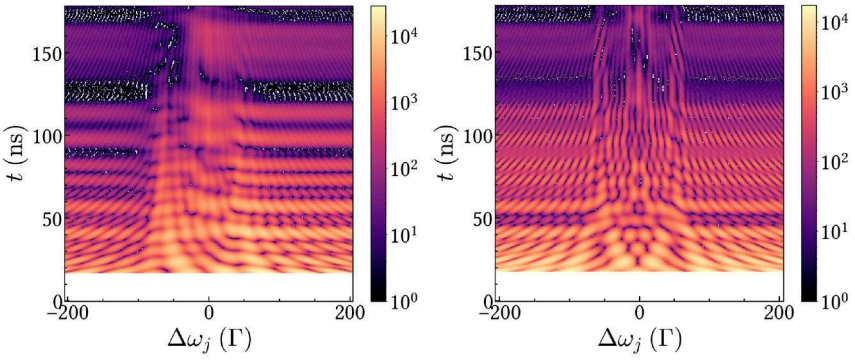

(a) Coherent simulation

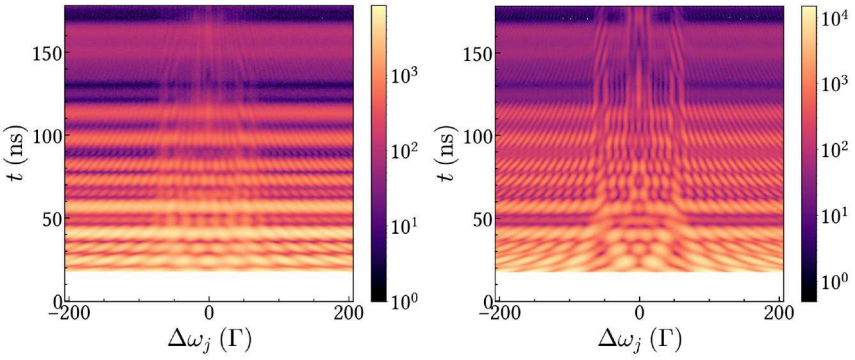

(b) Incoherent simulation

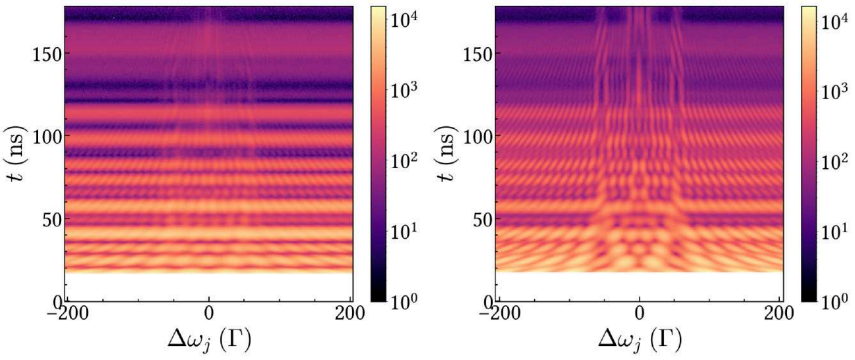

(c) Experimental data

Figure 6.26.: *(see next page)*

Figure 6.26 ***(previous page)***: The (a) coherent and (b) incoherent simulations of the ptychograms are plotted alongside (c) experimental datasets. The left and the right ptychograms in each row correspond to the first and the third-order waveguide modes of the cavity, respectively. At the first-order waveguide modes, the incoherent simulation clearly matches the experimental data better than the coherent simulation. At the third-order waveguide mode, the incoherently simulated ptychogram has a "blurred" effect similar to the experimental data.

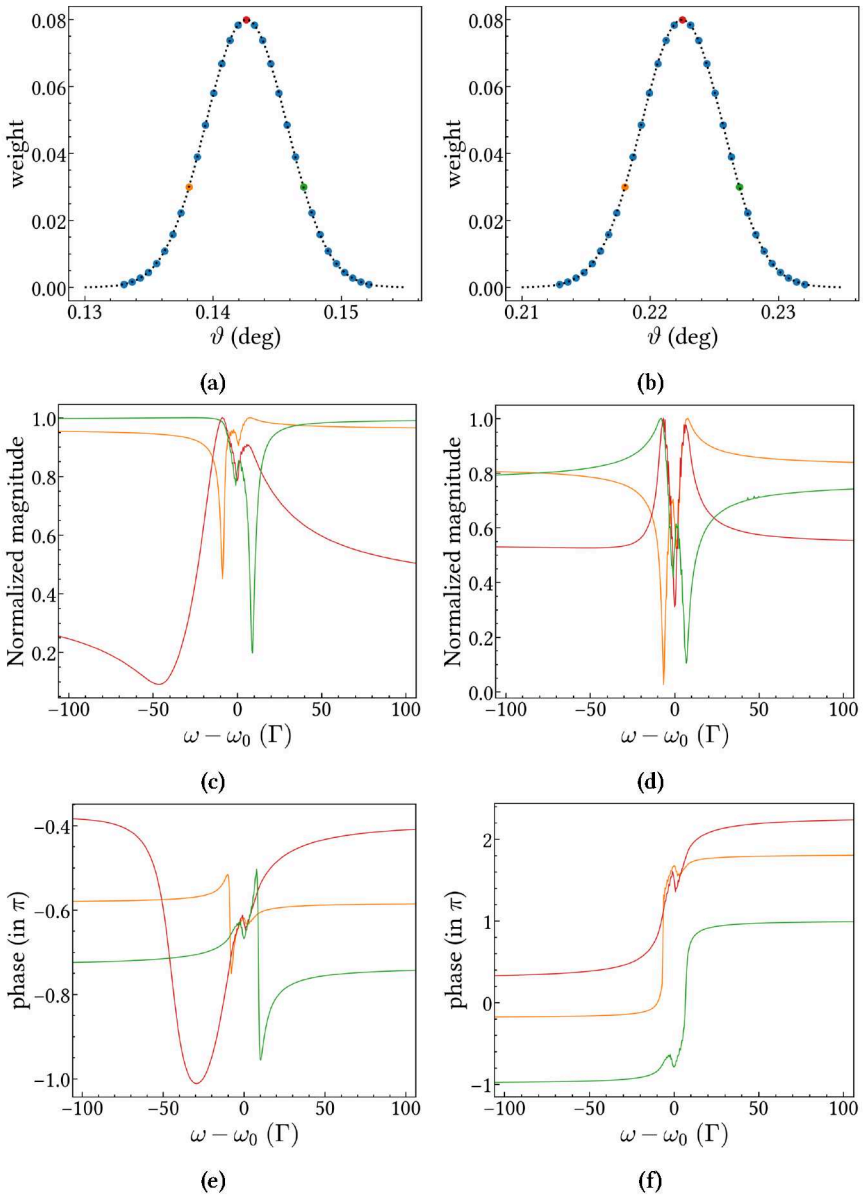

Figure 6.27.: *(see next page)*

Figure 6.27 ***(previous page)***: The angle of reflection of the cavity is chosen from a Gaussian distribution with FWHM 0.0075° for the (a) first and the (b) third-order waveguide mode. The different probe modes $\hat{\boldsymbol{P}}^m$ are used as an input for the ptychography engine. As an example, the energy response of three probe modes sampled from the distribution in (a) are simulated and plotted for the first-order waveguide mode in (c) and (e). The energy response of probe modes sampled around the third-order waveguide mode are plotted in (d) and (f).

We start by testing the ptychographic engine on the coherently simulated ptychograms. As the probe function, we use the scattering response of the cavity at the exact angles corresponding to the waveguide modes. For both waveguide modes of the cavity, we can successfully reconstruct the object response, as shown in Fig. 6.28. Despite the similar results, there are some advantages to using the third-order waveguide mode of the cavity as the probe. First, the convergence to a solution is faster for the third-order waveguide mode - indicating that the ptychography problem might be easier to solve in this case. Secondly, we also find that the angles around the third minimum are more stable to increase in the veto time T_{min}. This is shown in Fig. 6.29. In regions with lower mean squared error, the ptychography engine can extrapolate the time response of the object between 0 and T_{min} very well.

To reconstruct the object from the incoherently simulated ptychograms, we use the incoherent forward model in Eq. (4.29) with 31 probe functions sampled from the angular distribution on the cavity in Fig. 6.27(a) and 6.27(b). We see in Fig. 6.30(a) that the first and third-order waveguide modes have different convergence curves but in both cases, the ptychography engine converges to a solution in about 500 iterations. The reconstructed object for the two waveguide modes of the cavity is shown in Fig. 6.30. The reconstructed object has a global energy shift of 1.5 Γ and 0.6 Γ for the first and the third-order waveguide modes, respectively. In both cases, the reconstructed object also has a global phase shift of -0.33π relative to the true object. These trivial ambiguities are characteristic of the phase retrieval problem and do not change the physical result. At both waveguide modes, we find that the angular divergence in both experiments is so large that the object cannot be perfectly reconstructed in the region of interest (-70 Γ, 70 Γ), even with the incoherent forward model. The baseline of the reconstructed object has fluctuations that mask the true height and shape of the four large resonance peaks, and also introduce slight errors in the peak positions. It could be that in the presence of the large divergence, the object is not illuminated uniformly by the probe and the overlap ratio between the measurements keeps fluctuating. This makes the phase problem ill-conditioned. Since the ptychographic phase retrieval problem is non-convex, the engine is likely stuck in a local minima due to the incoherence.

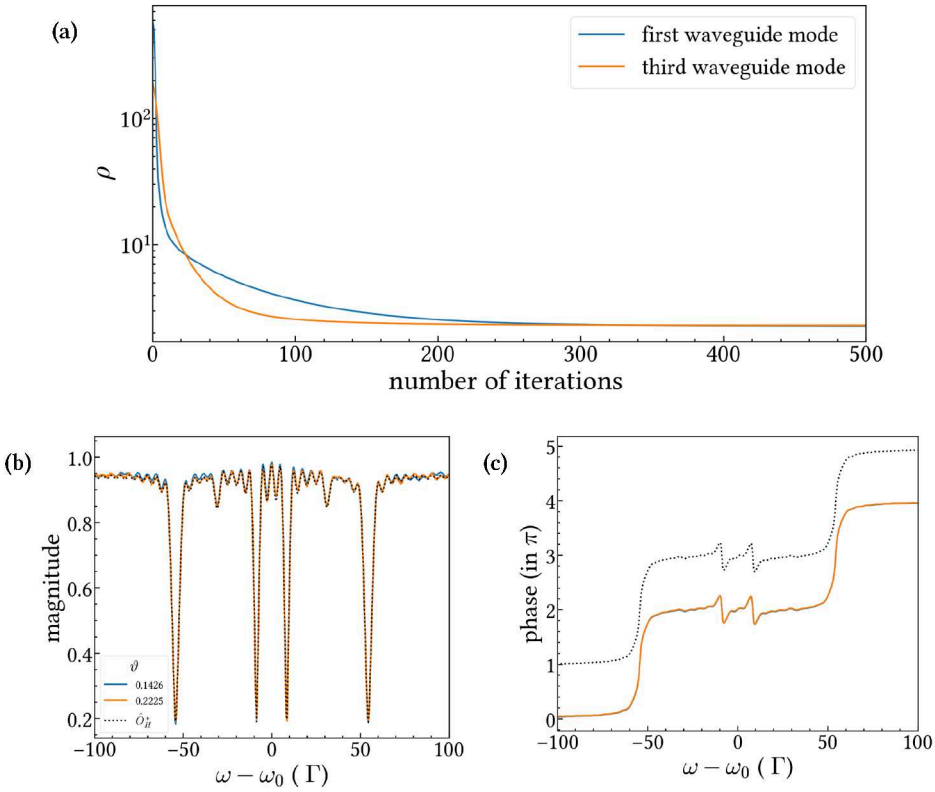

Figure 6.28.: Phase retrieval from the coherent simulations. (a) The convergence curve for the ptychographic reconstruction at the first ($\vartheta = 0.1426$) and the third-order waveguide mode ($\vartheta = 0.2225$) of the cavity. We show the reconstructed (b) magnitude and (c) phase of the energy response of the cavity in both cases. The dotted lines represent the scattering response of the true object in the presence of the time window.

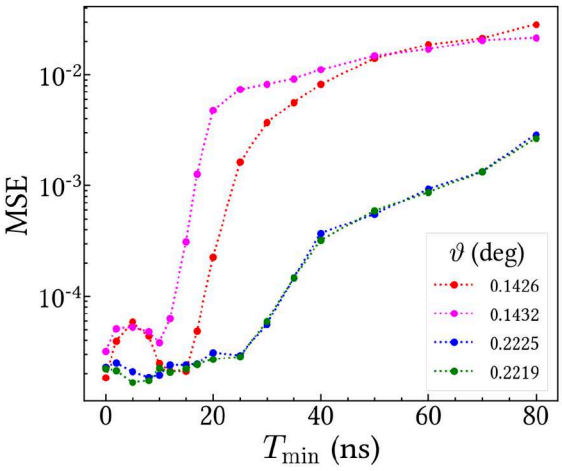

Figure 6.29.: The mean squared error (MSE) of the reconstructed object for different cut off times $T_{\min}$ at different angles of incidence at the cavity.

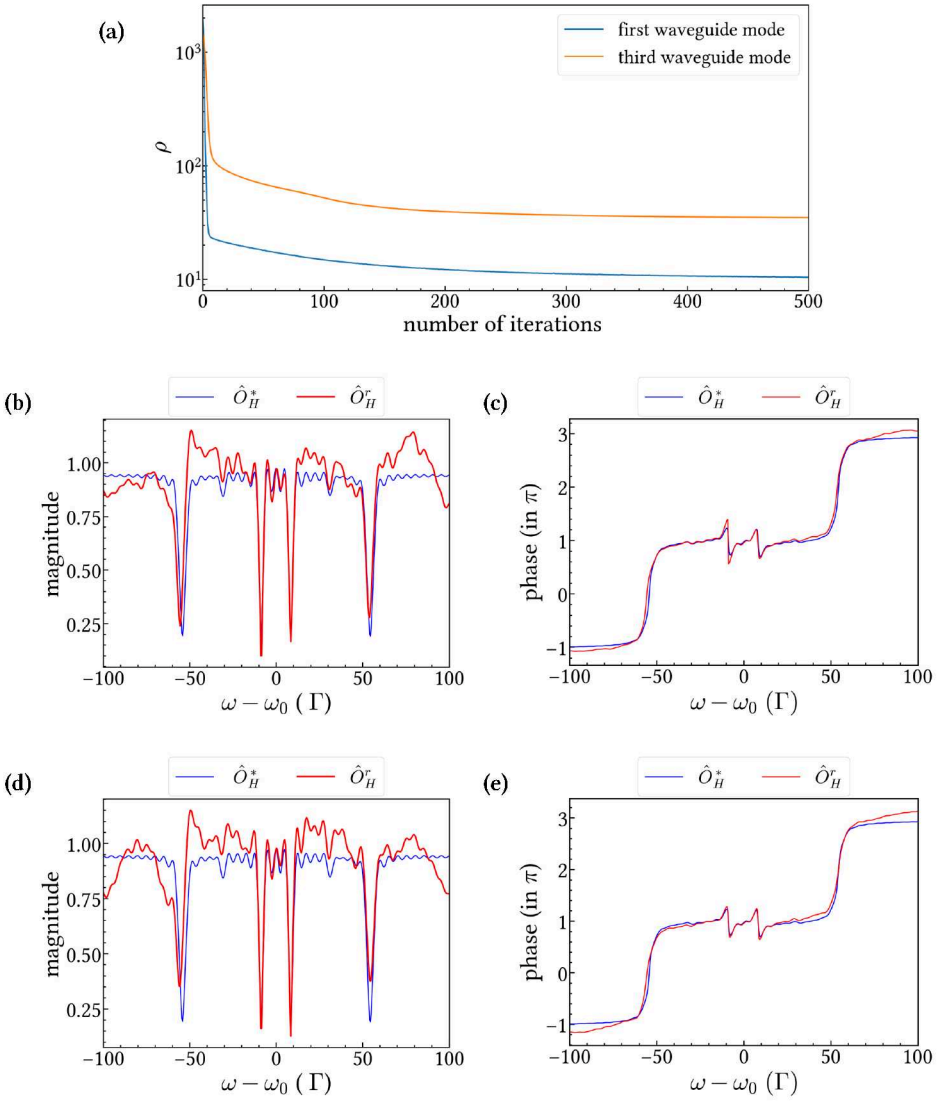

Figure 6.30.: Phase retrieval from the incoherent simulations. (a) The convergence curve of the engine for the ptychographic reconstruction from the first-order and third-order waveguide mode of the cavity. We show the magnitude and phase response of the filtered reconstructed object $\hat{\boldsymbol{O}}_H^r$ (in red) compared to the filtered true object $\hat{\boldsymbol{O}}_H^*$ (in blue) from an angular divergent beam incident at the (b), (c) first-order waveguide mode and the (d), (e) third-order waveguide mode of the cavity. In both cases, the reconstructed object has been scaled by a constant value to match the baseline of the true object. The global energy and phase shift has also been taken into account.

6.5.2. Phase retrieval from experimental datasets

From our tests on simulated ptychograms, we have shown that the incoherent sources of error are rather large in the experiment. We now show the phase retrieval results from the experimentally measured ptychograms. Just like the reconstruction from the incoherent simulation, we make use of the incoherent forward model in the ptychography engine and assume a distribution of probes (Fig. 6.27). For both experimental ptychograms in Fig. 6.24, the external magnetic field (**B**) on the ^{57}**Fe** foil is applied such that $\mathbf{B} \parallel \sigma$.

Figure 6.31(a) shows the convergence curves of the engine for the two ptychograms. The value of ρ decreases for the first 200 iterations and then plateaus to two different solutions. In both cases, the global energy and phase shift of the reconstructed object relative to the true object is -1.1 Γ and 0.33π. We take them into account while plotting the magnitude and phase of the reconstructed object in Fig. 6.31. The reconstructed object $\hat{O}_H^r$ has been filtered in the time domain according to Eq. (6.3) to filter out the error contributions from times beyond $T_{\max} = 178$ ns, and been rescaled to match the height of the peaks of the true object $\hat{O}_H^*$.

After taking the global energy shift into account, we can find the positions of the four largest peaks in the magnitude of the object by fitting Lorentzians. The results of the peak position fits are shown in Table 6.10. The mean squared error in the positions for the first and the third-order waveguide mode is given as 0.15 and 0.23, respectively. In the region of interest $\Delta\omega_j \in (-70, 70)\ \Gamma$, it is not possible to differentiate between the real and the artificial peaks in the magnitude of the object. Due to the time windowing effect and large angular divergence, the two additional smaller resonance peaks present in the SMS energy spectrum of the ^{57}**Fe** foil at around $\pm 31.5\ \Gamma$ (see Fig. 6.12(a)) are not distinguishable in the ptychographic reconstruction.

Peak	a	b	c	d
$\hat{O}_H^*$	-54.22	-8.67	8.49	54.40
$\hat{O}_H^r$ (ϑ = 1436°)	-54.26	-8.72	8.79	53.69
$\hat{O}_H^r$ (ϑ = 2225°)	-55.05	-8.26	8.64	54.58

Table 6.10.: The positions of the peaks marked in Fig. 6.31. All values are given in units of Γ.

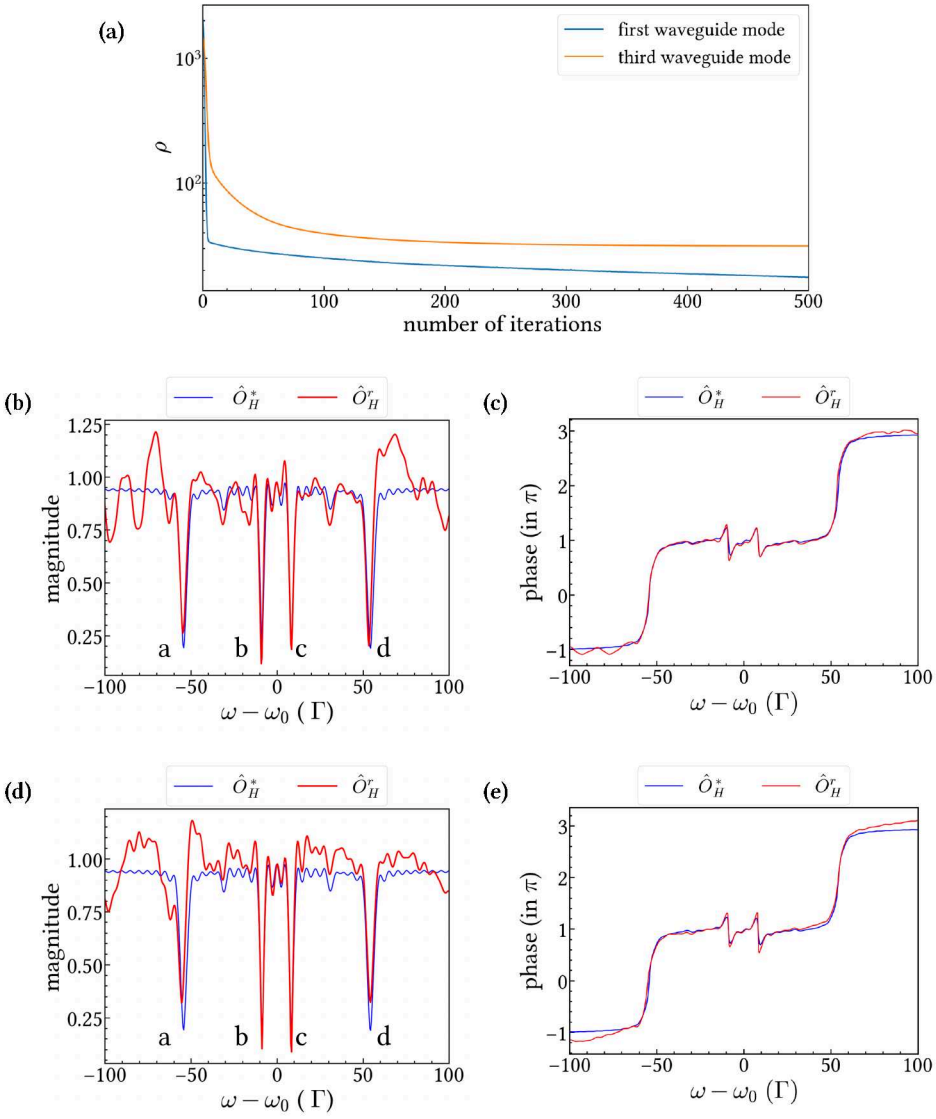

Figure 6.31.: (a) The cost ρ of the object reconstructed by the ptychography engine. Magnitude and phase response of the reconstructed object $\hat{\boldsymbol{O}}_H^r$ (in red) compared to the true object $\hat{\boldsymbol{O}}_H^*$ (in blue) for the (a), (b) first and the (c), (d) third-order waveguide mode of the cavity. The global scaling and trivial shifts have been taken into account while plotting the reconstructed object. Four resonance peaks are prominent in the magnitude of the reconstructed object in the energy domain and are marked as a, b, c, and d.

Finally, we plot the time response of the reconstructed objects in Fig. 6.32. We see that the ptychography engine is unable to smoothly extrapolate the time response between 0 to T_{min} in the presence of the angular incoherence. The time response of the reconstructed object does not match the true object between 120 and 140 ns. This is likely because the ptychography engine does not correct for bunch spacing incoherence in the experimental data due to scattering from the previous X-ray pulses (See Fig. 6.11(b)). Since the ptychographic phase retrieval problem is non-convex, it is likely that the engine is stuck in a local minima due to the incoherence.

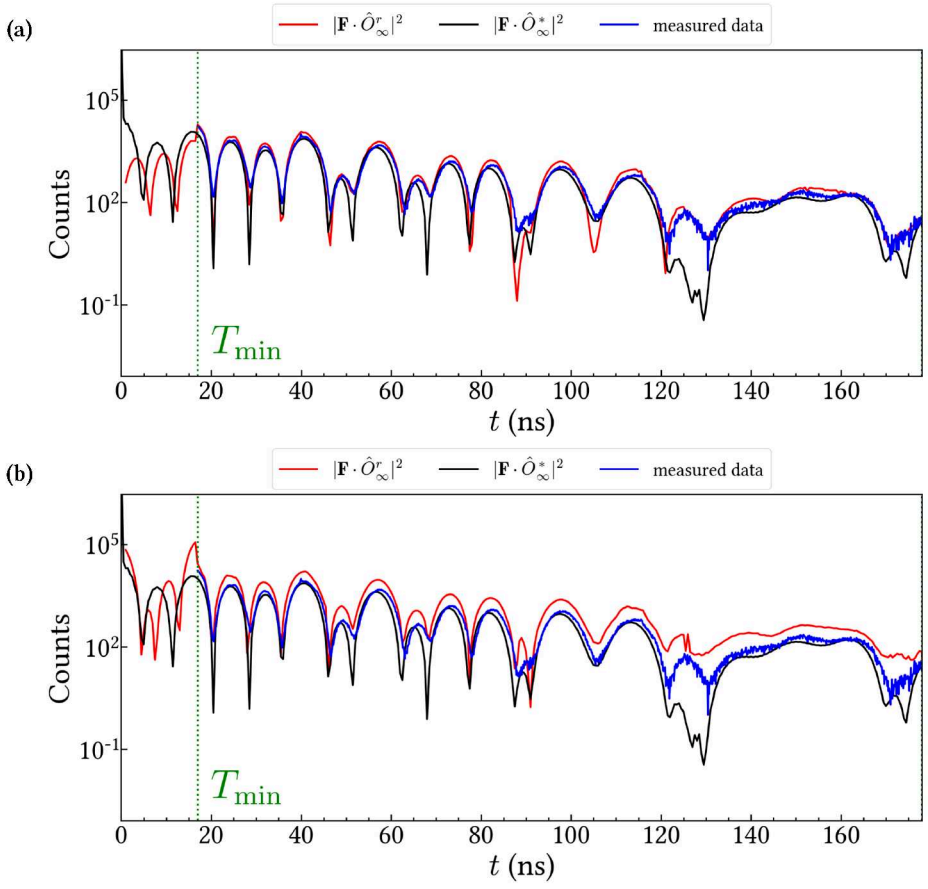

Figure 6.32.: Time response of the object reconstructed with the cavity at the (a) first and (b) third-order waveguide mode (in red). For comparison, the time response of the "true" object, without any incoherence, is plotted in black. The experimentally measured time response of the object ^{57}**Fe** foil (in blue) contains incoherent contributions from previous synchrotron pulses, most prominently seen between 120 to 130 ns.

6.5.3. Conclusion

Firstly, we have demonstrated how a thin film cavity can be designed to be used as a probe for nuclear resonance scattering ptychography. By selecting different waveguide modes of the cavity, we can change the probe/illumination function on the object. Using simulations, we demonstrated the successful reconstruction of the object's energy response for two different waveguide modes of the cavity, assuming full coherence (Fig. 6.28). Notably, the third-order waveguide mode exhibited faster convergence and better stability to an increase in the veto time compared to the first-order waveguide mode. However, in the experimental data, the presence of a large distribution of incidence angles on the cavity led to imperfect ptychographic reconstruction of the object. Fluctuations in the baseline of the reconstructed object were evident due to the corresponding incoherent effects and were too big to be removed by regularization.

It is remarkable how well-conditioned the ptychographic problem is despite the cavity's high angular sensitivity. In Fig. 6.10, we can see how even a minimal change of 0.0006° in the incidence angle results in a noticeable alteration in the energy response of the cavity. Despite the estimated angular divergence in our experiments being almost ten times larger ($\sim 0.0075^\circ$), we could still distinguish between the four major resonance peaks of the ^{57}**Fe** foil. The phase response of the ^{57}**Fe** foil also qualitatively matched the expected value quite well. This suggests that, with future enhancements in experimental conditions in the grazing incidence setup, further improvements in the ptychographic reconstruction could be achieved. For example, the angular divergence of the beam can be controlled by one or more slits positioned after the source, although at the expense of lower photon flux. The distance of the focusing element from the cavity should also be increased. If the high sensitivity to the angle of incidence is not desired, the cavity itself could be redesigned with other materials and layer structures.

7. Conclusion and Outlook

The primary goal of this thesis was to develop a reliable method to retrieve the magnitude and phase shift of an X-ray field scattered by the nuclei in an object at Mössbauer resonances. Our investigation covered both theoretical and experimental aspects of implementing ptychography for nuclear resonant scattering (NRS) - including the physical and mathematical forward models for the measured ptychogram, the inversion algorithms, and their convergence properties.

We implemented a ptychography engine and showed that it is feasible to reconstruct the scattering response of an object in the energy domain using temporal intensity measurements and a known probe. We successfully applied the technique in experiments to reconstruct the complex energy domain response of an iron foil enriched with the Mössbauer isotope ^{57}**Fe**. The Nesterov accelerated stochastic gradient method can efficiently solve the problem by computing the gradient of the "amplitude cost function", which is based on the Poisson likelihood model for the noise in the ptychogram. This is because an array of Avalanche photodiodes (APDs) operated in the photon counting mode are used as the detector in our experiments. The silicon-based APDs can reach dark count rates of only 10s of mHz and the measurements are dominated by Poisson photon counting noise. Trivial ambiguities, such as global energy and phase shifts, are noted in the reconstructed object but are characteristic of the phase retrieval problem and do not alter the physical results.

The phase retrieval scheme is adaptable to different experimental setups - with both transmitting (stainless steel foil) and reflecting (X-ray cavity) probes. In the transmission setup, we reconstruct the scattering amplitude for two different scattering geometries of the ^{57}**Fe** foil. By applying an external magnetic field along the direction σ or π, we investigate two different polarization states of the nuclear exciton-polariton and observe changes in the resonance lines. In the grazing incidence reflection setup, we tune the X-ray beam at two different incidence angles on the cavity to excite different

wave guide modes to probe the ^{57}**Fe** foil. The different wave guide modes have different reflectivity responses, and we compared the object reconstruction at both modes of the cavity.

We can also highlight some challenges encountered in the project, alongside some practical recommendations for future experiments. Firstly, data collected in the NRS experiments is limited in energy resolution by the time structure of the incoming synchrotron radiation. However, the ptychography engine works on an oversampled energy grid to avoid numerical errors due to circular convolutions of the discrete Fast Fourier Transform in the forward model. This introduces side-lobes/"wiggle" artifacts due to spectral leakage in the reconstructed energy response. To circumvent this, we must choose the bunch mode of the synchrotron's operation such that it ensures a sufficiently long time window ($T_{\max}$) to capture the full scattering response. There exist synchrotron sources around the world with the desired time structure as shown in Fig. 7.1. The effective energy resolution for the phase retrieval increases with the number of natural lifetimes of the isotope that can be fit inside the time window between two synchrotron bunches.

Label	Synchrotron	Location	Bunch mode	Bunch spacing (ns)
a	APS[1]	USA	24-bunch	153
b	ESRF	France	16-bunch	176
c	PETRA-III	Germany	40-bunch	192
d	Spring-8	Japan	F-bunch	342
e	Spring-8	Japan	D-bunch	684
f	ESRF	France	4-bunch	704
g	ESRF	France	Hybrid	940
h	Spring-8	Japan	H-bunch	1487

Table 7.1.: The bunch spacing of different modes of operation of synchrotrons with NRS beamlines.

[1]The APS upgrade (2023) has only a 48-bunch timing mode with approximately 88 nanoseconds between the pulses.

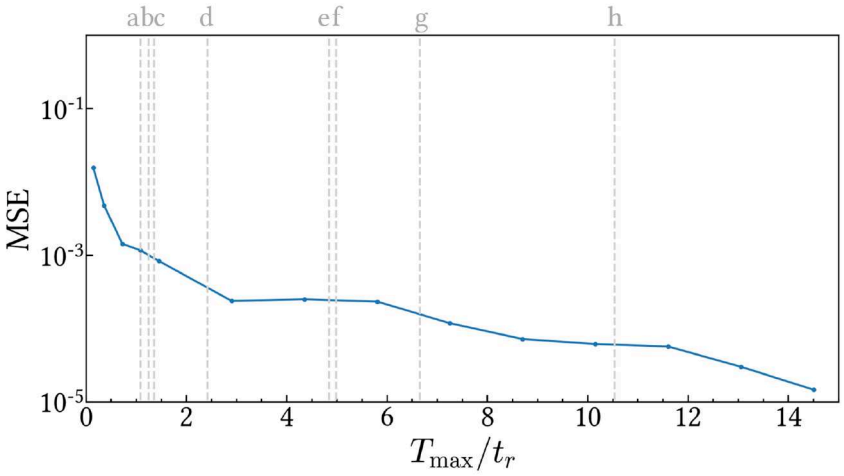

Figure 7.1.: Mean square error (MSE) of the reconstructed object calculated from the simulation tests in Sec. 5.4 plotted against the ratio of the maximum length of the time window ($T_{\max}$) and the natural lifetime of ^{57}**Fe** (t_r = 141.11 ns). The dotted lines mark the maximum time between two pulses for different operation modes of synchrotron around the world given in Table 7.1.

Secondly, the quality of the reconstruction is also affected by the accuracy of the probe detuning. For stability, the Doppler drive is moved with a sinusoidal velocity profile, but this results in a non-constant Doppler detuning difference between two ptychographic measurements, which can range from 0.005 to 6 neV in our experiments. This necessitates precise calibration of the Doppler drive's velocity profile (e.g. by the procedure described in Appendix C.2), ideally both before and after the collection of a ptychogram.

The ptychographic setup assumes only coherent scattering paths in the setup. However, thickness distributions in the transmission geometry and angular distributions in the reflection geometry introduce incoherent contributions in the measured intensities of the scattered X-rays. Taking them into account by considering an incoherent probe model for the engine improves the reconstruction, as emphasized by our tests on both simulated and experimental data. However, if the incoherence is too large or there are beam drifts in the experiments, it can affect the uniformity of the object illumination. The degree of overlap between adjacent probe positions can change during measure-

ments, impacting the accuracy of phase retrieval and making it difficult to regularize the reconstruction. This leads to fluctuations in the baseline of the reconstructed object which obscure the true spectral features. These artifacts occur predominantly in the "flat" regions of the energy response. where there is no resonance. In the reflectivity setup, the angular divergence of the beam contributed to significant incoherent effects in the experimental data. In the future, it can be controlled by decreasing the source size (e.g. with one or more slits positioned after the source), although at the expense of lower photon flux. The distance of the focusing element from the cavity should also be increased.
We also notice that the ptychographic reconstruction from experimental data works best in the Doppler detuning regime of "radiative coupling" between the probe and the object. A reasonable guess for this phenomenon could be a higher information density about the nuclear exciton-polariton in the regime–suppressing the incoherent effects–but this has to be verified by more experimental and numerical tests.

We can also suggest some algorithmic improvements the engine. For example, the phase shift in the reconstructed object is only known modulo 2π and can cause phase wraps. The unwrapped phase can be directly reconstructed using the refractive framework for ptychography (Appendix C.1). Secondly, in our simulations, we demonstrated how total variation regularization can be used to reconstruct the object when the degree of overlap between the measurements is small and the ptychographic phase problem is more ill-conditioned - resulting in a "sparser" object. The regularization term in the reconstruction process artficially extrapolated the time response of the object beyond the measurement time window, reducing the "wiggle" artifacts. However, in experiments, the choice of the phase retrieval algorithm and its sensitivity to incoherent effects impacts the regularization process. Total variation regularization tends to produce piecewise constant regions, leading to "blocky staircase" artifacts in the reconstructed object, especially in regions with high fluctuations. A possible way to avoid these artifacts is to use a total generalized variation regularizer instead [CMM00; NK18], which takes into account higher-order derivatives to accommodate smoothness.

Our ptychography engine relies on an accurate estimation of the probe via fit models. Some probes are more difficult to model than the others. In our experiments, phase retrieval from the nuclear resonating cavity as a probe was more challenging since its scattering response is very sensitive to a precise characterization of the layer structure

and the incident angle of the X-ray beam. An alternative would be to move to a "blind ptychography" approach to simultaneously retrieve the probe along with the object using algorithms employed in two-dimensional problems, like ePIE [Thi+09]. However, in most two-dimensional ptychography setups (e.g., for imaging), the X-ray beam is passed through a slit to probe the object and has compact support. In our case, the probe function is the nuclear-scattered response of another sample and is composed of Lorentzians, which by definition are not compactly supported. Even at large Doppler detunings, the object and probe interfere with each other. This makes deconvolution of the object and the probe more difficult during the reconstruction.

Exploring ptychographic reconstruction for other Mössbauer isotopes presents an intriguing prospect for this research. The tin isotope ^{119}**Sn** stands out as a promising candidate due to its low resonance energy (23.88 keV) and an excited state lifetime of 26 ns. This implies the ability to accommodate around 7 isotope lifetimes within the measurement time window ($T_{\mathrm{max}} \sim 192$ ns) for the 40-bunch mode of Petra III. The hyperfine structure of ^{119}**Sn** closely resembles that of a 'nearly' prototypical two-level quantum state system, adding significant interest from the perspective of nuclear quantum optics [Vel21; RE21]. Ptychography could be useful for energy domain studies of tin or tin-oxide layers in cavity structures to engineer and test their 'clean' hyperfine structure.

Modern X-ray free electron laser sources can also be explored for NRS ptychography experiments, given their high transverse coherence and unique time structure. For example, in the standard mode of operation of the EuXFEL (Fig. 7.2), X-rays arrive as pulse trains with a periodicity of around 100 ms. Each pulse in the pulse train is only a few 10s of femtoseconds long (compared to picoseconds at PETRA III) and is separated from the other pulses with a spacing of 220 ns. However, this time spacing between the pulses, can in principle be tuned in integer numbers. For example, it was tuned to 440 ns for detecting the nuclear resonant X-ray excitation of the scandium isomer ^{45}**Sc** [Shv+23]. Of course, the experimental challenges of radiation damage to the samples and high-resolution monochromatization of the beam to suppress the background noise at the detector have to be overcome first.

As a last remark, we mention that ptychographic phase retrieval in one dimension is also relevant in fields beyond Mössbauer science. For example, the short-time Fourier transform (STFT) is a widely used technique in speech and audio processing to record

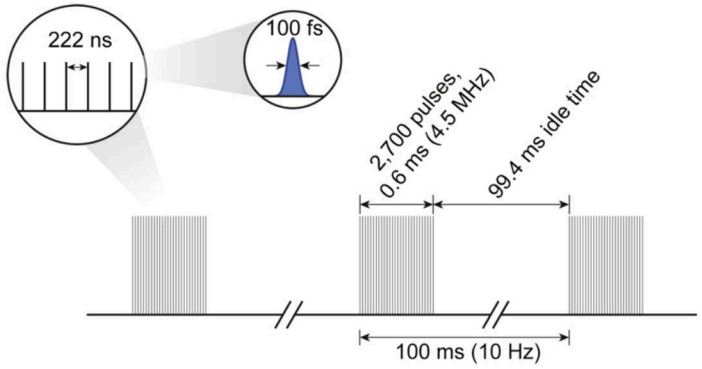

Figure 7.2.: The time structure of the standard mode of operation of the European XFEL, Hamburg, Germany. The figure is adopted from [Mad+13].

a frequency and time-resolved 2-D "spectrogram" of the audio signal. Iterative phase retrieval of an audio signal from its windowed STFT via modified Griffin-Lim [GL84; Wel+22] algorithms is now being employed in speech signal synthesis and enhancement, especially in the presence of noise [GKL15]. Similarly, the Frequency-Resolved Optical Gating (FROG) method is a technique used for measuring the temporal characteristics of ultrafast optical pulses (of femtosecond and attosecond duration) using spectrogram measurements. This is done because the required bandwidth to measure these pulses exceeds the bandwidth of current electronics. Both Griffin-Lim and modern FROG reconstruction algorithms [Spa+15] are close cousins of the PIE [FR04] method employed in CDI ptychography and the gradient methods employed in this thesis. NRS ptychography also mutually benefits from the advancements in these fields. In fact, some demonstrations of semi-blind ptychography for one-dimensional phase retrieval from the FROG spectrogram exist [Sid+16] and the corresponding algorithms can be explored for nuclear resonant scattering.

In conclusion, in this thesis we have highlighted the successes and challenges in the phase retrieval problem for nuclear resonant scattering. We have tested the impact of experimental conditions on the quality of results and shown that phase retrieval requires a comprehensive understanding of the specific incoherent effects present in the experimental setup. In combination with experimental improvements, algorithmic improvements such as the development of regularization techniques tailored to these

challenges can make energy-time ptychography a way to simultaneously characterize an object in the energy and time domain. This would elevate nuclear resonant scattering at synchrotrons as the be-all and end-all method for Mössbauer science.

A. Gradient algorithms

A.1. Accelerated gradient descent

We describe aGD, which is a generalized version of the accelerated gradient descent and includes the object update shown in lines 22 and 23 of Algorithm 4. The algorithm always starts with an update direction $\boldsymbol{d}^{(0)} = -\nabla_{\hat{O}^{(0)}}\rho$ which is the steepest descent direction. For the subsequent iterations, a new update direction $\boldsymbol{d}$ is calculated by applying a gradient-based correction (or 'momentum' in machine learning jargon) to the previous update direction, which is 'damped' by the parameters β and γ. The parameter α gives the step-size of the update for each iteration.

Momentum is most useful in optimization problems where the objective function has a large amount of curvature, meaning that the gradient may change a lot over relatively small regions of the search space. It can also be helpful when the search space has small but consistent gradients, or noisy gradients. Often the effectiveness of this approach is likened to inertia [Qia99].

Figure A.1 shows the three chief variations of the aGD method: (a) the unaccelerated or 'steepest' gradient descent (GD) where $\beta = 0$, (b) classic momentum gradient descent (aGD-CM) where $\gamma = 0$ and (c) Nesterov accelerated gradient descent (aGD-NAG) where $\gamma = \alpha$.

Algorithm 4 aGD

1: $max\_iter \leftarrow$ *maximum number of engine iterations*
2: *Set acceleration parameters:*
3: $\alpha \leftarrow \alpha^0 \in [0, 1]$
4: $\beta \leftarrow \beta^0 \in [0, 1]$
5: $\gamma \leftarrow \gamma^0 \in [0, 1]$
6: $\boldsymbol{b}_0, \boldsymbol{b}_1 \cdots \boldsymbol{b}_{M-1} \leftarrow$ *measurements*

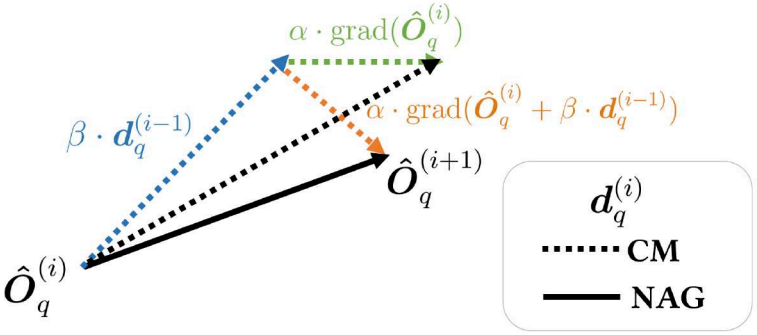

Figure A.1.: Difference between the two types of accelerated gradient descent: classic momentum (aGD-CM) and Nesterov accelerated (aGD-NAG). The update $\boldsymbol{d}_q^{(i)}$ connects the i-th estimate of the object pixel to the next. When the acceleration term $\beta = 0$, the update is in the direction of the steepest gradient, i.e., $\nabla_{\hat{O}_q^{(i)}} \rho$. We denote it as $\mathrm{grad}(\hat{\boldsymbol{O}}_q^i)$ in the diagram. For classical momentum aGD-CM, the update $\boldsymbol{d}_q^{(i)}$ is calculated using the previous update $\boldsymbol{d}_q^{(i-1)}$ and the gradient with respect to the current object $\hat{\boldsymbol{O}}^{(i)}$. For aGD-NAG, the gradient from a 'look-ahead projection' of the object $\hat{\boldsymbol{O}}_q^{(i)} + \beta \boldsymbol{d}^{(i-1)}$ is used. The Nesterov acceleration is typically faster and more stable than the classic momentum update, especially for higher values of β [Sut+13].

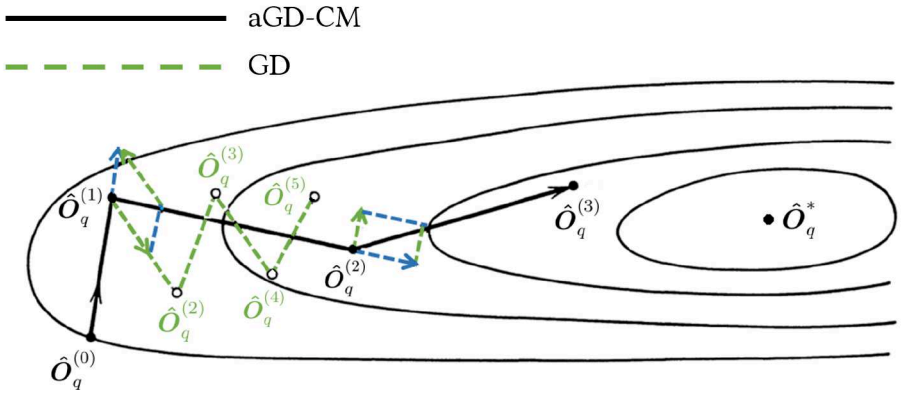

Figure A.2.: Comparison between the accelerated and the simple gradient descent. We illustrate how $\hat{\boldsymbol{O}}_q$ (the q-th pixel of the object) in the complex plane evolves as the iteration number of the algorithm (denoted in brackets) progresses, where $\hat{\boldsymbol{O}}_q^*$ is the true solution. The figure has been adapted from Ref. [Pol87].

$\Delta\omega_0, \Delta\omega_1 \cdots \Delta\omega_{M-1} \leftarrow$ *Dopper detunings*
$\hat{\boldsymbol{P}} \leftarrow$ *probe* $\in \mathbb{C}^N$
Initialize: $\hat{\boldsymbol{O}} \leftarrow \hat{\boldsymbol{O}}^{(0)} \in \mathbb{C}^N$
Initialize: $\nabla_{\hat{\boldsymbol{O}}^{(i-1)}}\rho \leftarrow \mathbf{0} \in \mathbb{C}^N$
$i \leftarrow 0$
repeat
    Initialize: $\rho \leftarrow 0$
    Initialize: $\nabla_{\hat{\boldsymbol{O}}}\rho \leftarrow 0$
    for $j \in \{0, 1, \ldots M-1\}$ **do**
        Forward:
        $\hat{\boldsymbol{P}}_j \leftarrow \mathrm{DETUNE}\ (\hat{\boldsymbol{P}}, \Delta\omega_j)$
        $\hat{\boldsymbol{Z}}_j \leftarrow \mathrm{diag}(\hat{\boldsymbol{P}}_j) \cdot \hat{\boldsymbol{O}}$
        Compare and calculate gradient:
        $\rho \leftarrow \rho + \mathrm{dist}(\boldsymbol{b}_j\ , |\mathbf{F} \cdot \hat{\boldsymbol{Z}}_j|^2)$
        $\nabla_{\hat{\boldsymbol{O}}}\rho \leftarrow \nabla_{\hat{\boldsymbol{O}}}\rho + \nabla_{\hat{\boldsymbol{O}}}\mathrm{dist}(\boldsymbol{b}_j\ , |\mathbf{F} \cdot \hat{\boldsymbol{Z}}_j|^2)$
    end for
    Accelerate:
    $\boldsymbol{d}_{\mathrm{grad}} \leftarrow \nabla_{\hat{\boldsymbol{O}}}\rho - \nabla_{\hat{\boldsymbol{O}}^{(i-1)}}\rho$
    $\boldsymbol{d} \leftarrow -\alpha \cdot \nabla_{\hat{\boldsymbol{O}}}\rho + \beta \cdot (\boldsymbol{d} - \gamma \boldsymbol{d}_{\mathrm{grad}})$
    Update:
    $\hat{\boldsymbol{O}} \leftarrow \hat{\boldsymbol{O}} + \boldsymbol{d}$
    $\nabla_{\hat{\boldsymbol{O}}^{(i-1)}}\rho \leftarrow \nabla_{\hat{\boldsymbol{O}}}\rho$
    $i \leftarrow i + 1$
    if $i = max\_iter$ **then**
        Stop the engine.
    end if
until CONVERGED
return $\hat{\boldsymbol{O}}$

A.2. Gradient descent with step-size selection:

Selecting an appropriate step-size at each iteration is a common strategy to improve the robustness of gradient-based methods. An 'exact' line search to find the step size

is difficult and computationally heavy for our phase retrieval problem. Instead, we perform a non-monotone backtracking line search described in Algorithm 7 which is based on Armijo's condition [Arm66]. The algorithm is adapted from Ref. [ZH04]. We use the parameter $\eta \in [0, 1]$ to control the monotonicity of the algorithm. The monotonic line search ($\eta = 0$) starts with a large initial estimate (α') of the step-size (t) and iteratively shrinks it (i.e., "backtracks") until a decrease of the cost function ρ is observed[1]. For $0 < \eta < 1$, some increase in the value of ρ is permitted. Besides improving the convergence speed, non-monotone schemes can improve the likelihood of finding a global optimum. To further improve the algorithm, we can limit the maximum number of backtracking iterations using the parameter *num_backtracks*. The choice of C can range from extremely small (10^{-4}, encouraging larger steps) to relatively large (0.3, encouraging smaller steps), and typical values of β range from 0.1, (corresponding to a relatively coarse search) to 0.8 (corresponding to a finer search). We fix the values of the backtracking parameters in Algorithm 7 as $(\beta, C, num\_backtracks) = (0.5, 0.25, 10)$.

The common choice for the initial step-size α' to start the backtracking is $\alpha' = 1$. Here, we test two variants of the backtracking scheme with different selection techniques for the initial step-size: GD-backtrack (Algorithm 5) and GD-BB (Algorithm 6. In the first case, we use an empirical guess of the starting stepsize at each engine iteration (Algorithm 8). For GD-BB, however, we use the more sophisticated selection scheme [TZ18] shown in Algorithm 9. At each iteration $i \geq 2$ of the engine, we calculate a convex combination of the classic Barzilai-Borwein [BB88] step-sizes $\alpha_1^{(i)}$ and $\alpha_2^{(i)}$, i.e.,

$$\alpha^{(i)} = w^{(i)} \cdot \alpha_1^{(i)} + (1 - w^{(i)}) \cdot \alpha_2^{(i)}. \tag{A.1}$$

where $0 \leq w^{(i)} \leq 1$ is the weighting factor. The relative weighting of the step sizes is adapted using the rule given in [Haf+21]. This is used as our starting guess for the backtracking.

Algorithm 5 GD-backtrack

1: $max\_iter \leftarrow$ *maximum number of engine iterations*
2: $\eta \leftarrow \eta^0 \in [0, 1]$

[1] The amount of decrease should be according to the Armijo condition

Set backtracking parameters:
$\alpha \leftarrow \alpha^0 \in [0, 1]$
$\beta \leftarrow \beta^0 \in [0, 1]$
$C \leftarrow C^0 \in [0, 1]$
$num\_backtracks \leftarrow 10$
$\boldsymbol{b}_0, \boldsymbol{b}_1 \cdots \boldsymbol{b}_{M-1} \leftarrow$ *measurements*
$\Delta\omega_0, \Delta\omega_1 \cdots \Delta\omega_{M-1} \leftarrow$ *Dopper detunings*
$\hat{\boldsymbol{P}} \leftarrow$ *probe* $\in \mathbb{C}^N$
Initialize: $\hat{\boldsymbol{O}} \leftarrow \hat{\boldsymbol{O}}^{(0)} \in \mathbb{C}^N$
Initialize: $\hat{\boldsymbol{O}}^{(i-1)} \leftarrow \hat{\boldsymbol{O}}^{(0)} \in \mathbb{C}^N$
Initialize: $\nabla_{\hat{\boldsymbol{O}}^{(i-1)}} \rho \leftarrow \mathbf{0} \in \mathbb{C}^N$
Initialize: $Q = 1$
Initialize: $Q^{(i-1)} = 1$
$i \leftarrow 0$
repeat
    Initialize: $\rho \leftarrow 0$
    Initialize: $\nabla_{\hat{\boldsymbol{O}}} \rho \leftarrow 0$
    for $j \in \{0, 1, \ldots M-1\}$ **do**
        Forward:
        $\hat{\boldsymbol{P}}_j \leftarrow \text{DETUNE}\ (\hat{\boldsymbol{P}}, \Delta\omega_j)$
        $\hat{\boldsymbol{Z}}_j \leftarrow \text{diag}(\hat{\boldsymbol{P}}_j) \cdot \hat{\boldsymbol{O}}$
        Compare and calculate gradient:
        $\rho \leftarrow \rho + \text{dist}(\boldsymbol{b}_j\ , |\mathbf{F} \cdot \hat{\boldsymbol{Z}}_j|^2)$
        $\nabla_{\hat{\boldsymbol{O}}} \rho \leftarrow \nabla_{\hat{\boldsymbol{O}}} \rho + \nabla_{\hat{\boldsymbol{O}}} \text{dist}(\boldsymbol{b}_j\ , |\mathbf{F} \cdot \hat{\boldsymbol{Z}}_j|^2)$
    end for
    if i = 0 **then**
        $\rho_c \leftarrow \rho$
    else
        $\rho_c \leftarrow \dfrac{\eta \cdot Q^{(i-1)} \cdot \rho}{Q}$
        $Q \leftarrow \eta \cdot Q^{(i-1)} + 1$
        $Q^{(i-1)} \leftarrow Q$
    end if

if $i \leq 2$ **then**
  $\alpha' \leftarrow \alpha$
else
  $\boldsymbol{d}_{\text{grad}} \leftarrow \nabla_{\hat{\boldsymbol{O}}}\rho - \nabla_{\hat{\boldsymbol{O}}^{(i-1)}}\rho$
  $\alpha' \leftarrow$ ADHOC_STEPSIZE$(\boldsymbol{d}, \boldsymbol{d}_{\text{grad}})$
end if
$t \leftarrow$ ARMIJO_BACKTRACK$(\hat{\boldsymbol{O}}, \rho_c, \nabla_{\hat{\boldsymbol{O}}}\rho, \boldsymbol{d}, \alpha', \beta, C, num_backtracks)$
Update:
$\boldsymbol{d} \leftarrow -\nabla_{\hat{\boldsymbol{O}}}\rho$
$\hat{\boldsymbol{O}} \leftarrow \hat{\boldsymbol{O}} + t \cdot \boldsymbol{d}$
$\nabla_{\hat{\boldsymbol{O}}^{(i-1)}}\rho \leftarrow \nabla_{\hat{\boldsymbol{O}}}\rho$
$i \leftarrow i + 1$
if $i = max\_iter$ **then**
  Stop the engine.
end if
until CONVERGED
return $\hat{\boldsymbol{O}}$

Algorithm 6 GD-BB

$max\_iter \leftarrow$ *maximum number of engine iterations*
$\eta \leftarrow \eta^0 \in [0, 1]$
Set backtracking parameters:
$\alpha \leftarrow \alpha^0 \in [0, 1]$
$\beta \leftarrow \beta^0 \in [0, 1]$
$C \leftarrow C^0 \in [0, 1]$
$num\_backtracks \leftarrow 10$
$\boldsymbol{b}_0, \boldsymbol{b}_1 \cdots \boldsymbol{b}_{M-1} \leftarrow$ *measurements*
$\Delta\omega_0, \Delta\omega_1 \cdots \Delta\omega_{M-1} \leftarrow$ *Dopper detunings*
$\hat{\boldsymbol{P}} \leftarrow$ *probe* $\in \mathbb{C}^N$
Initialize: $\hat{\boldsymbol{O}} \leftarrow \hat{\boldsymbol{O}}^{(0)} \in \mathbb{C}^N$
Initialize: $\hat{\boldsymbol{O}}^{(i-1)} \leftarrow \hat{\boldsymbol{O}}^{(0)} \in \mathbb{C}^N$
Initialize: $\nabla_{\hat{\boldsymbol{O}}^{(i-1)}}\rho \leftarrow \boldsymbol{0} \in \mathbb{C}^N$
Initialize: $Q = 1$

Initialize: $Q^{(i-1)} = 1$
$i \leftarrow 0$
repeat
  Initialize: $\rho \leftarrow 0$
  Initialize: $\nabla_{\hat{\boldsymbol{O}}}\rho \leftarrow 0$
  for $j \in \{0, 1, \ldots M-1\}$ **do**
    Forward:
    $\hat{\boldsymbol{P}}_j \leftarrow \text{DETUNE}\ (\hat{\boldsymbol{P}}, \Delta\omega_j)$
    $\hat{\boldsymbol{Z}}_j \leftarrow \text{diag}(\hat{\boldsymbol{P}}_j) \cdot \hat{\boldsymbol{O}}$
    Compare and calculate gradient:
    $\rho \leftarrow \rho + \text{dist}(\boldsymbol{b}_j\ , |\mathbf{F} \cdot \hat{\boldsymbol{Z}}_j|^2)$
    $\nabla_{\hat{\boldsymbol{O}}}\rho \leftarrow \nabla_{\hat{\boldsymbol{O}}}\rho + \nabla_{\hat{\boldsymbol{O}}}\text{dist}(\boldsymbol{b}_j\ , |\mathbf{F} \cdot \hat{\boldsymbol{Z}}_j|^2)$
  end for
  if i = 0 **then**
    $\rho_c \leftarrow \rho$
  else
    $\rho_c \leftarrow \dfrac{\eta \cdot Q^{(i-1)} \cdot \rho}{Q}$
    $Q \leftarrow \eta \cdot Q^{(i-1)} + 1$
    $Q^{(i-1)} \leftarrow Q$
  end if
  if $i \leq 2$ **then**
    $\alpha' \leftarrow \alpha$
  else
    $\boldsymbol{d}_{\text{grad}} \leftarrow \nabla_{\hat{\boldsymbol{O}}}\rho - \nabla_{\hat{\boldsymbol{O}}^{(i-1)}}\rho$
    $\alpha' \leftarrow \text{BB\_STEPSIZE}(\boldsymbol{d}, \boldsymbol{d}_{\text{grad}})$
  end if
  $t \leftarrow \text{ARMIJO\_BACKTRACK}(\hat{\boldsymbol{O}}, \rho_c, \nabla_{\hat{\boldsymbol{O}}}\rho, \boldsymbol{d}, \alpha', \beta, C, num\_backtracks)$
  Update:
  $\boldsymbol{d} \leftarrow -\nabla_{\hat{\boldsymbol{O}}}\rho$
  $\hat{\boldsymbol{O}} \leftarrow \hat{\boldsymbol{O}} + t \cdot \boldsymbol{d}$
  $\nabla_{\hat{\boldsymbol{O}}^{(i-1)}}\rho \leftarrow \nabla_{\hat{\boldsymbol{O}}}\rho$
  $i \leftarrow i + 1$

if $i = max\_iter$ **then**
    Stop the engine.
end if
until CONVERGED
return $\hat{\boldsymbol{O}}$

Algorithm 7 ARMIJO_BACKTRACK($\hat{\boldsymbol{O}}, \rho_c, \nabla_{\hat{\boldsymbol{O}}}\rho, \boldsymbol{d}, \alpha', \beta, C, num\_backtracks$)

Initialize the step-size: $t \leftarrow \alpha'$
$b \leftarrow 0$
repeat
    if $b = num\_backtracks$ **then**
        break
    end if
    $b \leftarrow b + 1$
    Shrink the step-size: $t \leftarrow \beta \cdot t$
    $\hat{\boldsymbol{O}}' \leftarrow \hat{\boldsymbol{O}} + t \cdot \boldsymbol{d}$
    Initialize: $\rho' \leftarrow 0$
    for $j \in \{0, 1, \ldots M-1\}$ **do**
        Calculate cost:
        $\hat{\boldsymbol{P}}_j \leftarrow \text{DETUNE}\ (\hat{\boldsymbol{P}}, \Delta\omega_j)$
        $\hat{\boldsymbol{Z}}_j \leftarrow \text{diag}(\hat{\boldsymbol{P}}_j) \cdot \hat{\boldsymbol{O}}'$
        $\rho' \leftarrow \rho' + \text{dist}(\boldsymbol{b}_j\ , |\mathbf{F} \cdot \hat{\boldsymbol{Z}}_j|^2)$
    end for
until *Armijo condition is satisfied, i.e.,* $\rho' - \rho \leq C \cdot t \cdot \langle \nabla_{\hat{\boldsymbol{O}}}\rho_c\ ,\ \boldsymbol{d}\rangle_{Real}$
return t

Algorithm 8 ADHOC_STEPSIZE($\boldsymbol{d}, \boldsymbol{d}_{\text{grad}}$)

$\epsilon \leftarrow 10^{-9}$
$\alpha'' \leftarrow \dfrac{\boldsymbol{d}_{\text{grad}}}{\epsilon + \langle \boldsymbol{d}\ ,\ \nabla_{\hat{\boldsymbol{O}}}\rho\rangle_{Real}}$
return $\text{MIN}(1, 2\alpha'')$

Algorithm 9 BB_STEPSIZE($\boldsymbol{d}, \boldsymbol{d}_{\text{grad}}$)

Calculate Barzilai-Borwein step-sizes:

2: $\epsilon \leftarrow 10^{-9}$
3: $\alpha_1 \leftarrow \dfrac{\|\boldsymbol{d}\|^2}{\langle \boldsymbol{d}\ ,\ \boldsymbol{d}_{\text{grad}} \rangle_{Real}}$
4: $\alpha_2 \leftarrow \dfrac{\langle \boldsymbol{d}\ ,\ \boldsymbol{d}_{\text{grad}} \rangle_{Real}}{\left\|\boldsymbol{d}_{\text{grad}}\right\|^2}$
5: *Calculate the weighing factor:*
6: $K_1 \leftarrow \left\|\alpha_1 \cdot \boldsymbol{d}_{\text{grad}} - \boldsymbol{d}\right\|^2$
7: $K_2 \leftarrow \left\|\dfrac{\boldsymbol{d}}{\epsilon + \alpha_1} - \boldsymbol{d}_{\text{grad}}\right\|^2$
8: $w \leftarrow \dfrac{K_2}{\epsilon + K_1 + K_2}$
9: **return** $w \cdot \alpha_1 + (1 - w) \cdot \alpha_2$

A.3. Non-linear conjugate gradient descent (CGD):

Another way to minimize ρ is to not move in the steepest gradient direction but in the 'conjugate' direction [HS52] at each step. The conjugate gradient algorithm was first presented as an approach to solve symmetric, positive-definite linear systems. However, presently, many non-linear variants of the algorithm exist. The object update is shown in lines 28 and 29 in Algorithm 10, i.e.,

$$\boldsymbol{d}^{(i)} = -\nabla_{\hat{\boldsymbol{O}}^{(i)}} \rho + \mu^{(i)} \boldsymbol{d}^{(i-1)} \tag{A.2}$$

$$\hat{\boldsymbol{O}}^{(i+1)} = \hat{\boldsymbol{O}}^{(i)} + t^{(i)} \boldsymbol{d}^{(i)} \tag{A.3}$$

Here, $\boldsymbol{d}$ is the conjugate direction while t is the step-size of the update. We use monotone Armijo-backtracking (Algorithm 7) with $(\beta, C, num\_backtracks) = (0.5, 0.25, 10)$ to calculate t and the Hager-Zhang method (Algorithm 11 adapted from [HZ06]) to calculate the conjugate direction. Since the backtracking line-search for t is expensive, we switch it off after the first 50 iterations of the engine.

Algorithm 10 CGD with Armijo backtracking

1: $max\_iter \leftarrow$ *maximum number of engine iterations*
2: *Set backtracking parameters:*
3: $\alpha \leftarrow \alpha^0 \in [0, 1]$

$\beta \leftarrow \beta^0 \in [0, 1]$
$C \leftarrow C^0 \in [0, 1]$
$num\_backtracks \leftarrow 10$
$\boldsymbol{b}_0, \boldsymbol{b}_1 \cdots \boldsymbol{b}_{M-1} \leftarrow measurements$
$\Delta\omega_0, \Delta\omega_1 \cdots \Delta\omega_{M-1} \leftarrow Dopper\ detunings$
$\hat{\boldsymbol{P}} \leftarrow probe \in \mathbb{C}^N$
Initialize: $\hat{\boldsymbol{O}} \leftarrow \hat{\boldsymbol{O}}^{(0)} \in \mathbb{C}^N$
Initialize: $\nabla_{\hat{\boldsymbol{O}}^{(i-1)}} \rho \leftarrow \mathbf{0} \in \mathbb{C}^N$
Initialize: $\boldsymbol{d} \leftarrow \mathbf{0} \in \mathbb{C}^N$
$i \leftarrow 0$
repeat
    Initialize: $\rho \leftarrow 0$
    Initialize: $\nabla_{\hat{\boldsymbol{O}}} \rho \leftarrow 0$
    for $j \in \{0, 1, \ldots M-1\}$ **do**
        Forward:
        $\hat{\boldsymbol{P}}_j \leftarrow \text{DETUNE}\ (\hat{\boldsymbol{P}}, \Delta\omega_j)$
        $\hat{\boldsymbol{Z}}_j \leftarrow \text{diag}(\hat{\boldsymbol{P}}_j) \cdot \hat{\boldsymbol{O}}$
        Compare and calculate gradient:
        $\rho \leftarrow \rho + \text{dist}(\boldsymbol{b}_j\ , |\mathbf{F} \cdot \hat{\boldsymbol{Z}}_j|^2)$
        $\nabla_{\hat{\boldsymbol{O}}} \rho \leftarrow \nabla_{\hat{\boldsymbol{O}}} \rho + \nabla_{\hat{\boldsymbol{O}}} \text{dist}(\boldsymbol{b}_j\ , |\mathbf{F} \cdot \hat{\boldsymbol{Z}}_j|^2)$
    end for
    $\alpha' \leftarrow \alpha$
    $\rho_c \leftarrow \rho$
    if i < 50 **then**
        $t \leftarrow \text{ARMIJO\_BACKTRACK}(\rho_c, \nabla_{\hat{\boldsymbol{O}}} \rho, \boldsymbol{d}, \alpha', \beta, C, num\_backtracks)$
    end if
    Update:
    $\mu \leftarrow \text{HAGER\_ZHANG}(\nabla_{\hat{\boldsymbol{O}}} \rho, \nabla_{\hat{\boldsymbol{O}}^{(i-1)}} \rho, \boldsymbol{d})$
    $\boldsymbol{d} \leftarrow -\nabla_{\hat{\boldsymbol{O}}} \rho + \mu \cdot \boldsymbol{d}$
    $\hat{\boldsymbol{O}} \leftarrow \hat{\boldsymbol{O}} + t \cdot \boldsymbol{d}$
    $\nabla_{\hat{\boldsymbol{O}}^{(i-1)}} \rho \leftarrow \nabla_{\hat{\boldsymbol{O}}} \rho$
    $i \leftarrow i + 1$
    if $i = max\_iter$ **then**

Stop the engine.
end if
until CONVERGED
return $\hat{O}$

Algorithm 11 HAGER_ZHANG($\nabla_{\hat{O}}\rho, \nabla_{\hat{O}^{(i-1)}}\rho, \boldsymbol{d}$)

$\epsilon \leftarrow 10^{-9}$
$\eta \leftarrow 0.1$
$\eta' \leftarrow -\dfrac{1}{\epsilon + \|\boldsymbol{d}\| \cdot \text{MIN}(\eta, \left\|\nabla_{\hat{O}^{(i-1)}}\rho\right\|)}$
$\boldsymbol{d}_{\text{grad}} \leftarrow \nabla_{\hat{O}}\rho - \nabla_{\hat{O}^{(i-1)}}\rho$
$\boldsymbol{s} \leftarrow \boldsymbol{d}_{\text{grad}} - 2\boldsymbol{d} \cdot \dfrac{\left\|\boldsymbol{d}_{\text{grad}}\right\|^2}{\epsilon + \langle \boldsymbol{d}\ ,\ \boldsymbol{d}_{\text{grad}} \rangle_{Real}}$
$\mu' \leftarrow \dfrac{\langle \boldsymbol{s}\ ,\ \nabla_{\hat{O}}\rho \rangle_{Real}}{\epsilon + \langle \boldsymbol{d}\ ,\ \boldsymbol{d}_{\text{grad}} \rangle_{Real}}$
return $\text{MAX}(\mu', \eta')$

A.4. Stochastic algorithms

We use two stochastic algorithms in the thesis:

1. **Stochastic gradient descent (SGD)**: Stochastic gradient descent is a probabilistic approximation of the gradient descent algorithm. As shown in Algorithm 3, at each iteration of SGD, we calculate the gradient for a random sample from the dataset, instead of calculating the gradient for the entire dataset. It is therefore less computationally expensive than gradient descent, especially for large datasets. Like the steepest gradient descent, it is also possible to use acceleration strategies with SGD. We use the pytorch (*torch.optim.SGD*) implementation[2] of the stochastic gradient descent with Momentum/Nesterov and label them as SGD-CM and SGD-NAG, respectively.

2. **Adaptive moment estimation (ADAM)**[KB14]: The ADAM algorithm is an extension of SGD that uses adaptive learning rates and moment estimation. We use

[2] which slightly differs from the framework in Algorithm 4. See `https://pytorch.org/docs/stable/generated/torch.optim.SGD.html`.

the pytorch implementation of the algorithm (*torch.optim.ADAM*) in the thesis. In its simplest form, the object update at each iteration i can be written as

$$\boldsymbol{m}_1^{(i)} = \beta_1 \boldsymbol{m}_1^{(i-1)} + (1-\beta_1)\nabla_{\hat{\boldsymbol{O}}^{(i)}}\rho \tag{A.4}$$

$$\boldsymbol{m}_2^{(i)} = \beta_2 \boldsymbol{m}_2^{(i-1)} + (1-\beta_2)(\nabla_{\hat{\boldsymbol{O}}^{(i)}}\rho)^2 \tag{A.5}$$

$$\hat{\boldsymbol{O}}^{(i+1)} = \hat{\boldsymbol{O}}^{(i)} - \alpha \frac{\hat{\boldsymbol{m}}_1^{(i)}}{\sqrt{\hat{\boldsymbol{m}}_2^{(i)}} + \epsilon} \tag{A.6}$$

where

$$\hat{\boldsymbol{m}}_1^{(i)} = \frac{\boldsymbol{m}_1^{(i)}}{1-\beta_1} \text{ and } \hat{\boldsymbol{m}}_2^{(i)} = \frac{\boldsymbol{m}_2^{(i)}}{1-\beta_2}. \tag{A.7}$$

Here ϵ is a small constant to prevent division by zero, α is the step-size and (β_1, β_2) are damping parameters for the first and the second moment estimations at each iteration $\boldsymbol{m}_1$ and $\boldsymbol{m}_2$ [3]. While SGD updates the model parameters using a fixed step-size, ADAM adapts the effective step-size for each parameter based on $\boldsymbol{m}_1$ and $\boldsymbol{m}_2$. The algorithm also has an additional step Eq. (A.7) to correct initialization biasing during the initial iterations. ADAM is one of the most successful and widely used algorithms for non-linear optimisation in machine learning and has been included in this thesis for comparison to the more traditional optimisation methods.

[3] The first and the second moment are estimated as moving averages of the gradient and the squared gradient.

B. Coherence

Coherence refers to the degree of correlation between the phases of the electromagnetic waves that make up the X-ray field. It determines how the scattered X-ray waves interfere with each other. Therefore, the detected intensity depends strongly on the coherence of the scattered radiation.

The coherence length is a measure of the degree of coherence of the wave field. It is evaluated by correlating the phases of different points in time and space of the wave field. The correlation calculated along the axis of propagation in space gives the time evolution of the wave field, and thus the longitudinal coherence. The correlation calculated for different points of the wave field perpendicular to the propagation axis at a fixed time gives the transverse coherence. The subsequent discussion follows Refs. [Bar99; Len01].

B.1. Longitudinal coherence length

The longitudinal coherence length is the longitudinal distance between two points where the radiation from a source still has a defined phase relationship. The bandwidth of synchrotron radiation from the monochromator is of the order of 1 meV, which is much larger than the hyperfine splitting of a Mössbauer source ($\sim$ 100 neV). Therefore, all nuclear transitions are excited simultaneously and the resulting time response is a coherent superposition of individual transitions. Throughout the longitudinal coherence length, several transitions of the same nucleus as well as transitions of separate nuclei are simultaneously triggered, and the scattering is coherent. Even in the presence of hyper-fine splitting, the spectral bandwidth of the scattered Mössbauer radiation hitting the detector is very small. We can thus approximate it as a monochromatic wavefield with temporal coherence time $\tau = \tau_N$, where τ_N is the lifetime of the nucleus.

The longitudinal coherence length can thus be given as

$$\xi_L \propto c\tau = c\tau_N = \frac{\hbar c}{\Delta E_\gamma} \tag{B.1}$$

where ΔE_γ is the (full width at half-maximum) linewidth of the Mössbauer radiation. It defines the maximum longitudinal optical path difference between two X-ray waves - coming from a nuclear scattering sample and hitting the same detector pixel - at which the interference is still detectable. For the ^{57}**Fe** resonance, $\tau_N = 141.11$ ns and ξ_L is of the order of 42 m.

B.2. Transverse coherence length

Transverse coherence is defined as the length scale transverse to the beam position at which the phase correlations between different points in the wave field are stable at a given time. It is determined by the angular size of the synchrotron beam, since the individual electrons emit light more or less randomly.

A first-hand calculation of transverse coherence length can be done using Young's double-slit experiment [Bor+99]. The transverse coherence length ξ_T for an extended monochromatic light source of wavelength λ and size σ_0, positioned upstream at a distance S is given as

$$\xi_T \sim \frac{\lambda S}{2\pi\sigma_0}. \tag{B.2}$$

However, in the context of nuclear resonant scattering (NRS), the detector acceptance (or detector size) also needs to be taken into consideration to calculate the transverse coherence length. This is because the detection setup uses APDs rather than the 2-D detectors used in interference experiments. Hence, when we measure the intensity of a sample's response at time t, we are integrating over all of the photons hitting various parts of the detector surface.
Let us consider the time domain analogue of the double slit experiment, as shown in Fig. B.1. We take two scatterers in a sample separated by distance d. Their response functions $G_1(t)$ and $G_2(t)$ are assumed identical upto a global phase shift (e.g. isomer

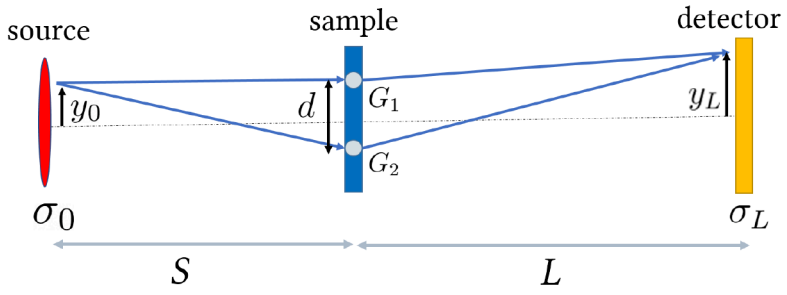

Figure B.1.: The nuclear scattering analogue of Young's double-slit experiment.

shift) such that

$$G_1(t) = |G_0(t)|e^{i\omega_1 t} \tag{B.3}$$

and

$$G_2(t) = |G_0(t)|e^{i\omega_2 t} \tag{B.4}$$

The source-sample distance and the sample-detector distance are given as S and L, respectively. The intensity seen at the point y_L on the detector due to excitation of photons from a source point at y_0 is given as [Bar99]

$$I(t) \propto |G_0(t)|^2 \left[1 + \cos\left\{(\omega_1 - \omega_2)t + 2\pi\frac{d}{\lambda}\left(\frac{y_0}{S} + \frac{y_L}{L}\right)\right\}\right]. \tag{B.5}$$

The $(\omega_1 - \omega_2)t$ part in the cosine (interference) term leads to quantum beats in the resulting intensity spectrum whereas the second part leads to blurring if the source and detector sizes are finite. If both the bunch electron distribution at the synchrotron source and the detector acceptance can be taken as Gaussians, we can integrate Eq. (B.5) with respect to y_0 and y_L to get

$$I(t) \propto |G_0(t)|^2 \left[1 + e^{-(d/\sqrt{2}\xi_{Te})^2} \cos\{(\omega_1 - \omega_2)t\}\right], \tag{B.6}$$

where $\xi_{Te} = \frac{\lambda}{2\pi}\frac{1}{\sigma_{Te}}$ and $\sigma_{Te} = \sqrt{\left(\frac{\sigma_0}{S}\right)^2 + \left(\frac{\sigma_L}{L}\right)^2}$. Here, σ_0 and σ_L are the vertical sizes

of the source and detector, respectively, with $y_0 = 0$ and $y_L = 0$ as their centers.

The 'effective' transverse coherence length, ξ_{Te}, takes into account how the source and detector sizes both constrain the coherent addition of scattering from transversely separated parts of the sample. Depending on whether the KB mirror system or the refractive Beryllium lenses are used for focusing, the beam size for a typical NRS experiment at P01, Petra III is $\sigma_0 = 4 - 400$ µm, while the pixel size of the APD detectors σ_L is in mm. As a result, ξ_{Te} is dominated by the detector size, and is given as

$$\xi_{Te} \sim \frac{\lambda L}{2\pi\sigma_L}. \tag{B.7}$$

The transverse coherence length was calculated to be around 68.5 nm for typical conditions in our ptychography setup ($\lambda = 0.086$ nm, $L \sim 1$ m and $\sigma_L \sim 0.2$ mm). Thickness distributions over this transverse length scale in the samples will result in incoherent effects.

B.3. Bunch spacing incoherence

In nuclear resonant scattering experiments, scattered photons from various X-ray pulses hitting the sample are histogrammed into bins to generate the temporal response. Since the detectors are synchronised with the synchrotron's bunch clock, they always reset to time 0 when a new pulse hits the sample. Photons scattered from an earlier X-ray pulse may scatter at times longer than T_{bs}, which is the bunch clock's time period. The histogram at time $t - T_{\mathrm{bs}}$ contains an incoherent addition of these photons scattered at time $t > T_{\mathrm{bs}}$. This incoherent "bunch-spacing correction" is particularly noticeable in the minima of the measured time response (See Fig. B.2).

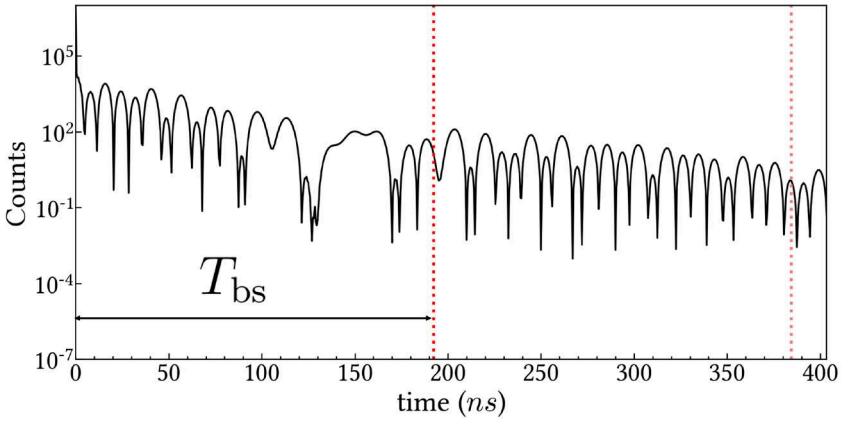

(a)

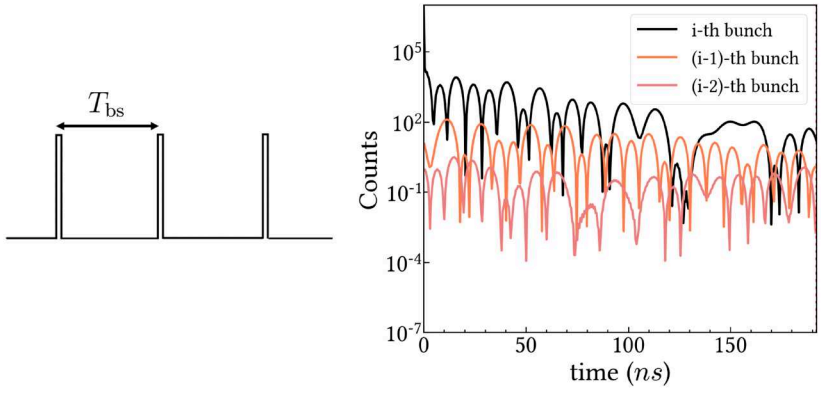

(b)

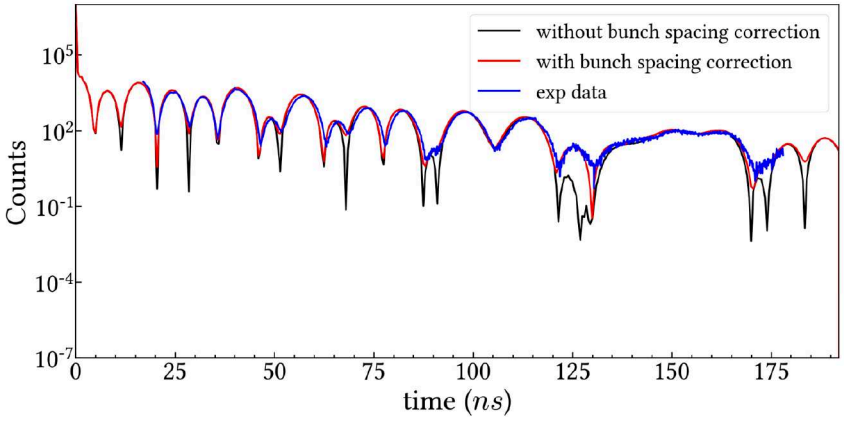

(c)

Figure B.2.: *(see next page)*

Figure B.2 ***(previous page)***: Example of bunch spacing incoherence for the ^{57}**Fe** foil described in Sec. 6.3. (a) The simulated time response of the foil does not decay to zero after T_{bs} which is the spacing between the electron bunches in the synchrotron. (b) The synchrotron pulses coming from the different electron bunches contribute to the measurement at the detector and are added together. (c) The measured time response of the ^{57}**Fe** foil (in blue) versus the fitted model with (in red) and without (in black) the bunch spacing correction.

C. Miscellaneous

C.1. Refractive ptychography

We can rewrite our complex object as

$$\hat{\boldsymbol{O}} = \mathrm{e}^{\mathrm{i}\tilde{\boldsymbol{O}}} \tag{C.1}$$

where $\tilde{\boldsymbol{O}}$ is the 'refractive' object [Wit+22]. From Eq. (2.23), we get

$$\mathrm{phase}(\hat{\boldsymbol{O}}) = \Re(\tilde{\boldsymbol{O}}) = -\boldsymbol{\delta} \cdot K \cdot z \tag{C.2}$$

$$-\log(|\hat{\boldsymbol{O}}|) = \Im(\tilde{\boldsymbol{O}}) = \boldsymbol{\beta} \cdot K \cdot z \tag{C.3}$$

where $\boldsymbol{\delta}$ and $\boldsymbol{\beta}$ are the phase shift and attenuation terms of the refractive index. The incident wave vector K and thickness z of the object can be taken as constant with respect to ω. If we run the ptychography engine to minimize the cost function with respect to the refractive object $\tilde{\boldsymbol{O}}$, we can directly reconstruct the real and imaginary parts of the complex refractive index from the measurements - while avoiding the need for phase unwrapping altogether. The forward model for the intensity at the detector for probe detuning $\Delta\omega_j$ is given as

$$\boldsymbol{I}^{(j)} = |\mathbf{F} \cdot \mathrm{diag}(\hat{\boldsymbol{P}}_j) \cdot \mathrm{e}^{\mathrm{i}\tilde{\boldsymbol{O}}}|^2. \tag{C.4}$$

For example, we show the results of refractive ptychography on the noiseless ptychogram 'A' simulated as described in Sec. 5. The initial guess for the refractive object is taken as an array of zeros. The algorithm SGD-NAG with (α, β, batch-size)=(0.03, 0.66, 20) is used to reconstruct the refractive object. The phase response of the reconstructed object after 500 iterations is shown in Fig. C.1. We compare it to the wrapped phase

that can be reconstructed by the conventional formalism, in the worst case scenario.

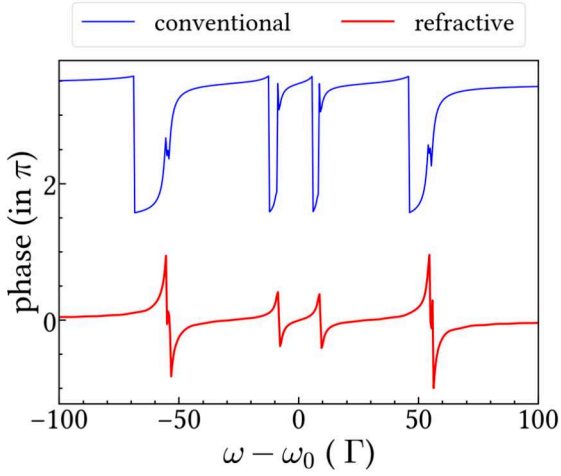

Figure C.1.: The phase response of the object reconstructed by refractive ptychography compared to the wrapped phase response reconstructed by the conventional formalism.

C.2. The velocity calibration

To do phase retrieval from the ptychograms, we need to know the probe detunings in the energy domain relative to the object. Therefore, we first determine the velocity of the Doppler drive at each channel number of the MCS6A. For the velocity calibration, we measure a ptychogram using the energy response of a "known" probe and a "known" object[1]. We assume that the sinusoidal motion of the drive gives the detuning $\Delta\omega_j$ for the j-th channel of the MCS6A as [2]

$$\Delta\omega_j = \frac{\omega_0}{c \cdot \Gamma} \left(\mathrm{v}_{\max} \cos\left(2\pi(j - j_0)/1024\right) + \mathrm{v}_{\mathrm{iso}} \right), \tag{C.5}$$

where $\omega_0 = 14.41$ keV and $\Gamma = 4.66$ neV for ^{57}**Fe**. The channel number where the drive has maximum velocity $\mathrm{v}_{\max}$ is given as j_0. We have also included a term $\mathrm{v}_{\mathrm{iso}}$ to capture the isomer shift between the probe and the object.

[1] i.e., with known hyperfine parameters.
[2] See the first-order Doppler shift formula in Eq. (2.37)).

The velocity can be fitted as shown in Algorithm 12. Here, CALC_DETUNINGS() denotes a calculation of the detunings of the drive at the current guess of v_{max}, v_{iso} using Eq. (C.5). The module SIM_HISTOGRAM() refers to a simulation of the ptychogram from the calculated detunings and the hyperfine parameters of the probe and the object. We also take the data acquisition time window into account (which in our case is given as (T_{min}, T_{max}) = (17 ns, 178 ns)). The simulation is done with Poisson sampling such that we get the same number of total counts as the experiment.

To start the algorithm, we typically initialize (v_{max}, v_{iso}, j_0)= (25 mm s^{-1}, 0 mm s^{-1}, 1). A least square fit LSQFIT() is then performed on the velocity parameters v_{max}, v_{iso} of the drive by comparing the integrated photon counts in the simulated and measured ptychogram at each velocity.

Algorithm 12 Least squares fitting for velocity calibration

1: $\{c_0, c_1 \cdots c_{M-1}\} \leftarrow$ *photon counts per channel of the MCS6A*
2: $\hat{\boldsymbol{O}}^* \leftarrow$ *energy domain response of the object*
3: $\hat{\boldsymbol{P}}^* \leftarrow$ *energy domain response of the probe*
4: $j_0 \leftarrow 1$
5: *Initialize:* $v_{max} \leftarrow 25$ mm s^{-1}
6: *Initialize:* $v_{iso} \leftarrow 0$ mm s^{-1}
7: $\Delta\omega_0, \Delta\omega_1 \cdots \Delta\omega_{M-1} \leftarrow$ CALC_DETUNINGS(v_{max}, v_{iso}, j_0)
8: $\{\boldsymbol{b}'_0, \boldsymbol{b}'_1 \cdots \boldsymbol{b}'_{M-1}\} \leftarrow$ SIM_HISTOGRAM$(\hat{\boldsymbol{O}}^*, \hat{\boldsymbol{P}}^*, \{\Delta\omega_0, \Delta\omega_1 \cdots \Delta\omega_{M-1}\})$
9: $c'_0, c'_1 \cdots c'_{M-1} \leftarrow \sum_q \boldsymbol{b}'_0, \sum_q \boldsymbol{b}'_1 \cdots \sum_q \boldsymbol{b}'_{M-1}$
10: *Fit:* $v'_{max}, v'_{iso} \leftarrow$ LSQFIT$(\{c_0, c_0 \cdots c_{M-1}\}, \{c'_0, c'_1 \cdots c'_{M-1}\}, v_{max}, v_{iso})$
11: *Update:* $v_{max}, v_{iso} \leftarrow v'_{max}, v'_{iso}$

Since we have pre-characterized both the ^{57}SS foil and the ^{57}**Fe** foil as described in Sec. 6.2.1 and 6.3, we use one of their measured ptychogram datasets to do the velocity calibration of the Doppler drive using the procedure described in Appendix C.2. This also forces our validation procedure to be self-consistent. The maximum velocity of the drive and the isomer shift between the two foils were found to be 20.70(3) mm s^{-1} and $-0.10(1)$ mm s^{-1}, respectively. The corresponding Doppler detunings are plotted in Fig. C.2.

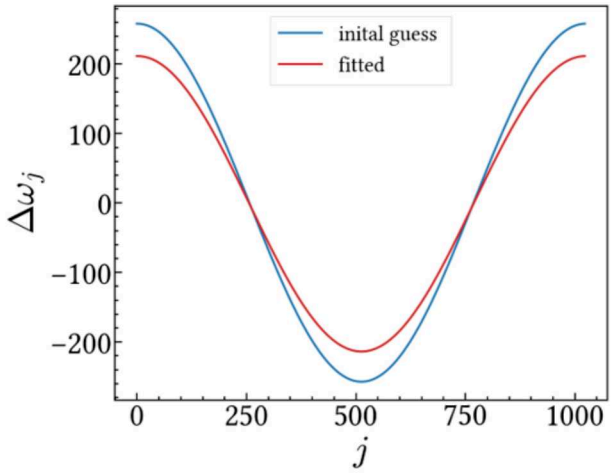

Figure C.2.: The Doppler detunings between the object and the probe at each MCS6A channel, fitted via the calibration procedure described in Appendix C.2.

C.3. The Doppler detuning range for ptychography

In our experiments, we observe that the ptychography engine converges to slightly different reconstructed objects, depending on what range of the data is selected from the ptychogram. For example, we run the engine to reconstruct the ^{57}**Fe** foil complex response from the experimentally measured ptychogram described in Fig. 6.14(a). We repeat the process by taking only data between different maximum ranges of Doppler detunings. In Fig. C.3, we see that the mean square error of the reconstructed object is the minimum when the data is taken between $\Delta\omega_j = \pm 70\,\Gamma$.

The reason behind this is not fully clear, but it might have something to do with the two different interaction regimes in the ptychogram for the object-probe system - the "radiative coupling" regime and the interferometric regime between the object and the probe (see discussion in Sec. 3.2.1). In Fig. C.4, we show how the intensities in the ptychogram change with the Doppler detuning at certain time cuts. We can see a rough separation between the two regimes at $\Delta\omega_j = \pm 70\,\Gamma$. When the probe is detuned relative to the object beyond this value, the samples decouple and one only measures the interference fringes.

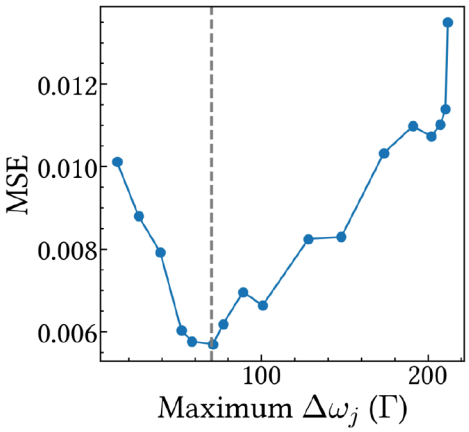

Figure C.3.: The mean square error (MSE) of the reconstructed object for different maximum Doppler detunings of the probe relative to the object. The dotted line marks 70 Γ.

The object reconstructed from the full range of the ptychogram measurements is shown in Fig. C.5. Non-trivial discrepancies between the true and the reconstructed object can be seen in both the complex energy response and the intensities of the time decay. On the other hand, the object reconstructed from the restricted data range of $\Delta\omega_j \in (-70, 70)\ \Gamma$ is shown in the main text in Fig. 6.20.

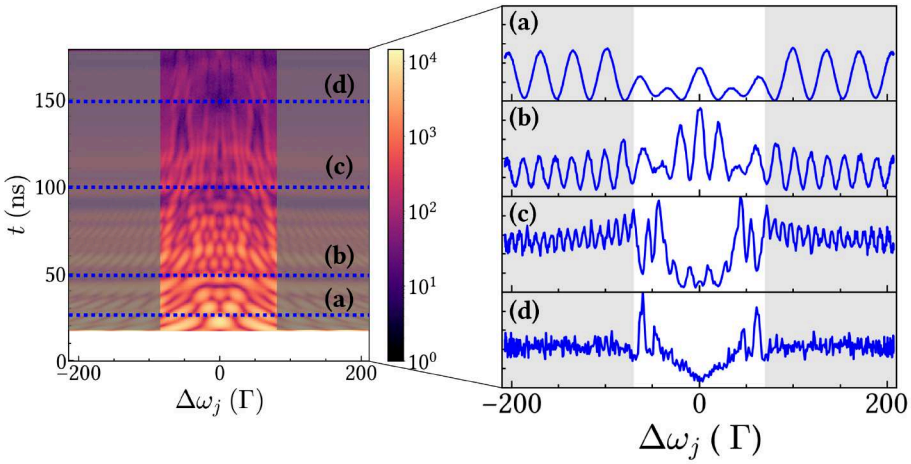

Figure C.4.: The intensity in the ptychogram as a function of the Doppler detuning at t = (a) 25 ns (b) 50 ns (c) 100 ns and (d) 150 ns. The grey area in all the plots marks the regime where the radiative coupling between the object and the probe is negligible.

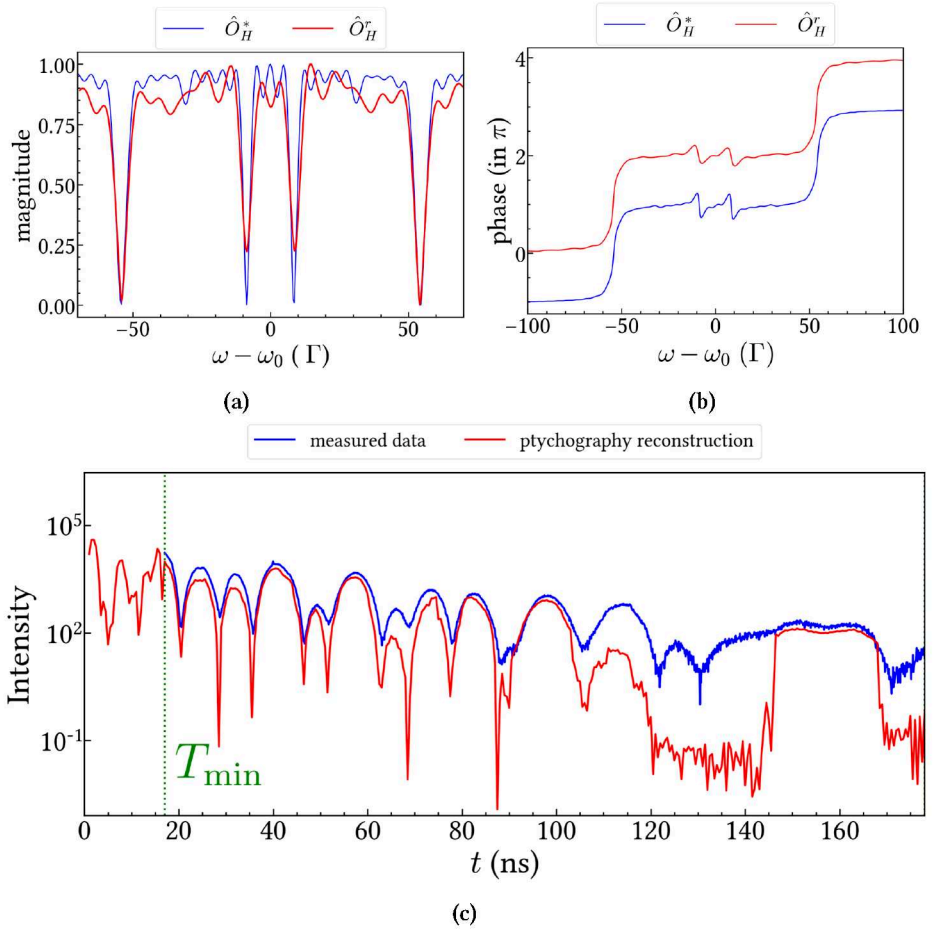

Figure C.5.: Ptychographic reconstruction by taking into account all ptychogram measurements with $\Delta\omega_j \in$ (-212, 212) Γ. (a) Magnitude and (b) phase response of the reconstructed object $\hat{\boldsymbol{O}}_H^r$ (in red) compared to the true object $\hat{\boldsymbol{O}}_H^*$ (in blue) from the ptychogram with $\mathbf{B} \parallel \sigma$. The global energy shift of 0.49 Γ has been taken into account while plotting the reconstructed object. (c) The time response of the reconstructed object is plotted against the experimentally measured time response of the ^{57}**Fe** foil for the same scattering geometry ($\mathbf{B} \parallel \sigma$).

Conference contributions

Here is a list of contributions from this work towards major conferences. The presenting author is underlined.

- **Contributed Talk**
  A. Negi, L. Bocklage, L. M. Lohse, C. Brandt, G. Meier, and R. Röhlsberger, "Ptychography for Nuclear Resonance Scattering", International Conference on the Applications of the Mössbauer Effect, Cartagena de Indias, Colombia (2023)

- **Poster Presentation**
  A. Negi, L. Bocklage, L. M. Lohse, S. Velten, D. Bessas, C. Brandt, G. Meier, and R. Röhlsberger, "Ptychography for phase retrieval in Nuclear Resonance Scattering", German Conference for Research with Synchrotron Radiation, Neutrons and Ion Beams at Large Facilities, Berlin, Germany (2022).

- **Poster Presentation**
  A. Negi, L. Bocklage, L. M. Lohse, S. Sadashivaiah, C. Brandt, G. Meier, and R. Röhlsberger, "Ptychography for phase retrieval in Nuclear Resonance Scattering", 14th International Conference on Synchrotron Radiation Instrumentation, Hamburg, Germany (2021).

Nomenclature

Physics Constants

$\hbar$	Reduced Planck's constant
c	Speed of light in a vacuum

Number Sets

$\mathbb{C}$	Complex numbers
$\mathbb{N}$	Natural numbers
$\mathbb{R}$	Real numbers

Other Symbols

$\boldsymbol{X}^\dagger$	Conjugate transpose of $\boldsymbol{X}$
$\langle \boldsymbol{X}, \boldsymbol{Y} \rangle_{Real}$	Real part of the complex inner product $\boldsymbol{X}^\dagger \cdot \boldsymbol{Y}$
$\lvert \boldsymbol{X} \rvert$	Elementwise absolute value of $\boldsymbol{X}$
$\lVert \boldsymbol{X} \rVert$	Frobenius/L2 norm of $\boldsymbol{X}$
$\mathbb{F}\{\boldsymbol{X}\}$	Discrete Fourier transform of X
$\text{diag}(\boldsymbol{X})$	Diagonal matrix with a vector $\boldsymbol{X}$ along its diagonal
$\overline{\boldsymbol{X}}$	Complex conjugate of $\boldsymbol{X}$

List of Abbreviations

ADAM	Adaptive moment estimation
APD	Avalanche photo-diode
BB	Barzilai-Borwein
CDI	Coherent diffraction imaging
CGD	Conjugate gradient descent
CM	Classic momentum
CONUSS	COherent NUclear resonant Scattering by Single crystals
DCM	Double-crystal monochromator
ePIE	Extended ptychographic iterative engine
ESRF	European synchrotron radiation facility
FFT	Fast Fourier transform
FFC	Frequency frequency correlation
FROG	Frequency resolved optical gating
FWHM	Full width half maximum
GAT	General Anscombe transform
GD	Gradient descent
HIO	Hybrid input output
HRM	High-resolution monochromator
HPR	Heterodyne phase reconstruction
MSE	Mean square error
MTF	Modulation transfer function
NAG	Nesterov accelerated gradient
NEXUS	Nuclear Elastic X-ray scattering Universal Software
NRS	Nuclear resonant scattering

PETRA	Positron electron tandem ring accelerator
PIE	Ptychographic iterative engine
PSF	Point spread function
QS	Quadrupole splitting
RAAR	Relaxed averaged alternating reflections
ROI	Region of interest
SGD	Stochastic gradient descent
SNR	Signal to noise ratio
STFT	Short time Fourier transform
TV	Total variation
XFEL	X-ray free electron laser
XUV	Extreme ultra violet

Bibliography

[Ans48] Anscombe, F. J. The Transformation of Poisson, Binomial and Negative-Binomial Data. *Biometrika* **35**, 246. DOI: 10.2307/2332343 (1948).

[Arm66] Armijo, L. Minimization of functions having Lipschitz continuous first partial derivatives. *Pacific Journal of Mathematics* **16**, 1–3. DOI: 10.2140/pjm.1966.16.1 (1966).

[AS21] Ainsworth, M. & Shin, Y. Plateau Phenomenon in Gradient Descent Training of RELU Networks: Explanation, Quantification, and Avoidance. *SIAM Journal on Scientific Computing* **43**, A3438–A3468. DOI: 10.1137/20m1353010 (2021).

[Ban+14] Bandeira, A. S., Cahill, J., Mixon, D. G. & Nelson, A. A. Saving phase: Injectivity and stability for phase retrieval. *Applied and Computational Harmonic Analysis* **37**, 106–125. DOI: 10.1016/j.acha.2013.10.002 (2014).

[Bar+04] Barla, A. *et al.* Pressure-Induced Magnetic Order in Golden SmS. *Physical Review Letters* **92**, 066401. DOI: 10.1103/physrevlett.92.066401 (2004).

[Bar99] Baron, A. Q. R. Transverse coherence in nuclear resonant scattering of synchrotron radiation. *Hyperfine Interactions* **123/124**, 667–680. DOI: 10.1023/a:1017065100051 (1999).

[BB88] Barzilai, J. & Borwein, J. M. Two-Point Step Size Gradient Methods. *IMA Journal of Numerical Analysis* **8**, 141–148. DOI: 10.1093/imanum/8.1.141 (1988).

[BBE17] Bendory, T., Beinert, R. & Eldar, Y. C. in *Compressed Sensing and its Applications* 55–91 (Springer International Publishing, 2017). DOI: 10.1007/978-3-319-69802-1_2.

[BH65] Bonse, U. & Hart, M. An X-ray Interferometer. *Applied Physics Letters* **6**, 155–156. DOI: 10.1063/1.1754212 (1965).

[Bis+21] Biscani, F. *et al. esa/pagmo2: pagmo 2.17.0* 2021. DOI: 10.5281/ZENODO.4585131.

[Boc+21] Bocklage, L. *et al.* Coherent control of collective nuclear quantum states via transient magnons. *Science Advances* **7**. DOI: 10.1126/sciadv.abc3991 (2021).

[Boc23] Bocklage, L. *Nexus - Nuclear Elastic X-ray scattering Universal Software* 2023. DOI: 10.5281/ZENODO.10074447.

[Bor+99] Born, M. *et al. Principles of Optics: Electromagnetic Theory of Propagation, Interference and Diffraction of Light* ISBN: 9781139644181. DOI: 10.1017/cbo9781139644181 (Cambridge University Press, 1999).

[BP15] Beinert, R. & Plonka, G. Ambiguities in One-Dimensional Discrete Phase Retrieval from Fourier Magnitudes. *Journal of Fourier Analysis and Applications* **21**, 1169–1198. DOI: 10.1007/s00041-015-9405-2 (2015).

[BP17] Beinert, R. & Plonka, G. Sparse Phase Retrieval of One-Dimensional Signals by Prony's Method. *Frontiers in Applied Mathematics and Statistics* **3**. DOI: 10.3389/fams.2017.00005 (2017).

[Bra86] Bracewell, R. N. *The Fourier transform and its applications* ISBN: 9780073039381 (McGraw-Hill New York, 1986).

[Cal+05] Callens, R. *et al.* Phase determination in nuclear resonant scattering using a velocity drive as an interferometer and phase shifter. *Physical Review B* **72**. DOI: 10.1103/physrevb.72.081402 (2005).

[CMM00] Chan, T., Marquina, A. & Mulet, P. High-Order Total Variation-Based Image Restoration. *SIAM Journal on Scientific Computing* **22**, 503–516. DOI: 10.1137/s1064827598344169 (2000).

[Con+15] Conca, A., Edidin, D., Hering, M. & Vinzant, C. An algebraic characterization of injectivity in phase retrieval. *Applied and Computational Harmonic Analysis* **38**, 346–356. DOI: 10.1016/j.acha.2014.06.005 (2015).

[CSW60] Cranshaw, T. E., Schiffer, J. P. & Whitehead, A. B. Measurement of the Gravitational Red Shift Using the Mössbauer Effect in Fe^{57}. *Phys. Rev. Lett.* **4**, 163–164. DOI: 10.1103/PhysRevLett.4.163 (4 1960).

[Dej+24] Dejkameh, A. *et al.* Recovery of spatial frequencies in coherent diffraction imaging in the presence of a central obscuration. *Ultramicroscopy* **258**, 113912. DOI: 10.1016/j.ultramic.2023.113912 (2024).

[Dic54] Dicke, R. H. Coherence in Spontaneous Radiation Processes. *Physical Review* **93**, 99–110. DOI: 10.1103/physrev.93.99 (1954).

[DLE22] Diekmann, O., Lentrodt, D. & Evers, J. Inverse design in nuclear quantum optics: From artificial x-ray multilevel schemes to spectral observables. *Physical Review A* **106**, 053701. DOI: 10.1103/physreva.106.053701 (2022).

[Dwi+18] Dwivedi, P., Konijnenberg, A. P., Pereira, S. F. & Urbach, H. P. Lateral position correction in ptychography using the gradient of intensity patterns. *Ultramicroscopy* **192**, 29–36. DOI: 10.1016/j.ultramic.2018.04.004 (2018).

[Els03] Elser, V. Phase retrieval by iterated projections. *Journal of the Optical Society of America A* **20**, 40. DOI: 10.1364/josaa.20.000040 (2003).

[Fie78] Fienup, J. R. Reconstruction of an object from the modulus of its Fourier transform. *Optics Letters* **3**, 27. DOI: 10.1364/ol.3.000027 (1978).

[Fie82] Fienup, J. R. Phase retrieval algorithms: a comparison. *Applied Optics* **21**, 2758. DOI: 10.1364/ao.21.002758 (1982).

[For+20] Forstner, A., Krahmer, F., Melnyk, O. & Sissouno, N. Well-conditioned ptychographic imaging via lost subspace completion. *Inverse Problems* **36**, 105009. DOI: 10.1088/1361-6420/abaf3a (2020).

[FR04] Faulkner, H. M. L. & Rodenburg, J. M. Movable Aperture Lensless Transmission Microscopy: A Novel Phase Retrieval Algorithm. *Physical Review Letters* **93**. DOI: 10.1103/physrevlett.93.023903 (2004).

[FW23] Fang, Y. & Wu, X. *L2-norm Total Variation Regularization Deconvolution Algorithm for Radar Angular Super-resolution* in *IEEE 3rd International Conference on Information Technology, Big Data and Artificial Intelligence (ICIBA)* (IEEE, 2023). DOI: 10.1109/iciba56860.2023.10164936.

[GB22] Glavic, A. & Björck, M. GenX: the latest generation of an established tool. *Journal of Applied Crystallography* **55**, 1063–1071. DOI: 10 . 1107 / s1600576722006653 (2022).

[Ger+85] Gerdau, E. *et al.* Nuclear Bragg diffraction of synchrotron radiation in yttrium iron garnet. *Physical Review Letters* **54**, 835–838. DOI: 10.1103/physrevlett.54.835 (1985).

[Ger21] Gerharz, M. *Temporal phase and polarization interferometry at x-ray energies: Reconstruction of phase-related observables and temporal pulse shaping*. MA thesis (Ruprecht Karls Universität Heidelberg, 2021). URL: https://hdl.handle.net/21.11116/0000-0009-7D36-F.

[Ger72] Gerchberg, R. W. A practical algorithm for the determination of plane from image and diffraction pictures. *Optik* **35**, 237–246 (1972).

[GKL15] Gerkmann, T., Krawczyk-Becker, M. & Le Roux, J. Phase Processing for Single-Channel Speech Enhancement: History and recent advances. *IEEE Signal Processing Magazine* **32**, 55–66. DOI: 10.1109/MSP.2014.2369251 (2015).

[GKR20] Grohs, P., Koppensteiner, S. & Rathmair, M. Phase Retrieval: Uniqueness and Stability. *SIAM Review* **62**, 301–350. DOI: 10.1137/19m1256865 (2020).

[GL84] Griffin, D. & Lim, J. Signal estimation from modified short-time Fourier transform. *IEEE Transactions on Acoustics, Speech, and Signal Processing* **32**, 236–243. DOI: 10.1109/tassp.1984.1164317 (1984).

[Gol+18] Gollwitzer, J. *et al.* Incoherent Nuclear Resonant Scattering from a Standing Spin Wave. *Scientific Reports* **8**. DOI: 10.1038/s41598-018-29596-z (2018).

[Goo05] Goodman, J. W. *Introduction to Fourier Optics* ISBN: 9780974707723. URL: https://books.google.de/books?id=ow5xs_Rtt9AC (W. H. Freeman, 2005).

[Gre04] Greivenkamp, J. E. *Field guide to geometrical optics* ISBN: 9780819478160 (SPIE Press, Bellingham, Washington, 2004).

[GT21] Guizar-Sicairos, M. & Thibault, P. Ptychography: A solution to the phase problem. *Physics Today* **74**, 42–48. DOI: 10.1063/pt.3.4835 (2021).

[Hab+17] Haber, J. *et al.* Rabi oscillations of X-ray radiation between two nuclear ensembles. *Nature Photonics* **11**, 720–725. DOI: 10.1038/s41566-017-0013-3 (2017).

[Haf+21] Hafshejani, S. F., Gaur, D., Hossain, S. & Benkoczi, R. Barzilai and Borwein conjugate gradient method equipped with a non-monotone line search technique and its application on non-negative matrix factorization. DOI: 10.48550/ARXIV.2109.05685. arXiv: 2109.05685 (2021).

[Has+94] Hasegawa, Y. *et al.* Time-Delayed Interferometry with Nuclear Resonant Scattering of Synchrotron Radiation. *Japanese Journal of Applied Physics* **33**, L772. DOI: 10.1143/jjap.33.1772 (1994).

[HAS24] HASYLAB. *Machine Parameters PETRA III (Design Values)* 2024. URL: https://photon-science.desy.de/facilities/petra_iii/machine/parameters/index_eng.html (2024).

[Hee+15] Heeg, K. P. *et al.* Interferometric phase detection at x-ray energies via Fano resonance control. *Physical Review Letters* **114**, 207401. DOI: 10.1103/physrevlett.114.207401 (2015).

[Hee+21] Heeg, K. P. *et al.* Coherent X-ray-optical control of nuclear excitons. *Nature* **590**, 401–404. DOI: 10.1038/s41586-021-03276-x (2021).

[Hee14] Heeg, K. P. *X-Ray Quantum Optics With Mössbauer Nuclei In Thin-Film Cavities* PhD thesis (Ruprecht Karls Universität Heidelberg, 2014). DOI: 10.11588/HEIDOK.00017869.

[HM82] Hayes, M. H. & McClellan, J. H. Reducible polynomials in more than one variable. *Proceedings of the IEEE* **70**, 197–198. DOI: 10.1109/proc.1982.12262 (1982).

[Hoe20] Hoegen, A. V. *Probing Nonlinear Dynamics in Strongly Driven Quantum Materials* PhD thesis (Universität Hamburg, 2020). URL: https://ediss.sub.uni-hamburg.de/handle/ediss/9066.

[Hop69] Hoppe, W. Beugung im inhomogenen Primärstrahlwellenfeld. I. Prinzip einer Phasenmessung von Elektronenbeugungsinterferenzen. *Acta Crystallographica Section A* **25**, 495–501. DOI: 10.1107/s0567739469001045 (1969).

[HS52] Hestenes, M. R. & Stiefel, E. Methods of conjugate gradients for solving linear systems. *Journal of Research of the National Bureau of Standards* **49**, 409. DOI: 10.6028/jres.049.044 (1952).

[HT99] Hannon, J. P. & Trammell, G. T. Coherent γ-ray optics. *Hyperfine Interactions* **123/124**, 127–274. DOI: 10.1023/a:1017011621007 (1999).

[Hun07] Hunger, R. *An Introduction to Complex Differentials and Complex Differentiability* URL: https://mediatum.ub.tum.de/doc/631019/document.pdf (2007).

[HZ05] Hager, W. W. & Zhang, H. A New Conjugate Gradient Method with Guaranteed Descent and an Efficient Line Search. *SIAM Journal on Optimization* **16**, 170–192. DOI: 10.1137/030601880 (2005).

[HZ06] Hager, W. W. & Zhang, H. Algorithm 851: CG_DESCENT, a conjugate gradient method with guaranteed descent. *ACM Transactions on Mathematical Software* **32**, 113–137. DOI: 10.1145/1132973.1132979 (2006).

[IVW15] Iwen, M., Viswanathan, A. & Wang, Y. *Fast Phase Retrieval from Local Correlation Measurements* 2015. DOI: 10.48550/ARXIV.1501.02377. arXiv: 1501.02377.

[Izu+95] Izumi, K. *et al.* Time Domain Interferometry in X-Ray Region Using Nuclear Resonant Scattering. *Japanese Journal of Applied Physics* **34**, 4258. DOI: 10.1143/jjap.34.4258 (1995).

[Joh70] Johnson, D. P. Resonant Cross Section for 14.4-keV Gamma-Ray Absorption in ^{57}**Fe**. *Physical Review B* **1**, 3551–3554. DOI: 10.1103/physrevb.1.3551 (1970).

[KB14] Kingma, D. P. & Ba, J. *Adam: A Method for Stochastic Optimization* 2014. DOI: 10.48550/ARXIV.1412.6980. arXiv: 1412.6980.

[KCU18] Konijnenberg, A. P., Coene, W. M. J. & Urbach, H. P. Model-independent noise-robust extension of ptychography. *Optics Express* **26**, 5857. DOI: 10.1364/oe.26.005857 (2018).

[KEO17] Kogan, D., Eldar, Y. C. & Oron, D. On the 2-D Phase Retrieval Problem. *IEEE Transactions on Signal Processing* **65**, 1058–1067. DOI: 10.1109/tsp.2016.2631455 (2017).

[Kli+22] Klimova, N., Snigireva, I., Snigirev, A. & Yefanov, O. Using diffraction losses of X-rays in a single crystal for determination of its lattice parameters as well as for monochromator calibration. *Journal of Synchrotron Radiation* **29**, 369–376. DOI: 10.1107/S1600577521013667 (2022).

[KLY18] Kleinberg, B., Li, Y. & Yuan, Y. *An Alternative View: When Does SGD Escape Local Minima?* in *Proceedings of the 35th International Conference on Machine Learning* (eds Dy, J. & Krause, A.) **80** (PMLR, 2018), 2698–2707. URL: https://proceedings.mlr.press/v80/kleinberg18a.html.

[KN29] Klein, O. & Nishina, Y. Über die Streuung von Strahlung durch freie Elektronen nach der neuen relativistischen Quantendynamik von Dirac. *Zeitschrift für Physik* **52**, 853–868. DOI: 10.1007/bf01366453 (1929).

[Len+22] Lengyel, A. *et al.* Synergy effect of temperature, electric and magnetic field on the depth structure of the FeRh/$BaTiO_3$ composite multiferroic. *Materials Science and Engineering: B* **285**, 115939. DOI: 10.1016/j.mseb.2022.115939 (2022).

[Len01] Lengeler, B. Coherence in X-ray physics. *Naturwissenschaften* **88**, 249–260. DOI: 10.1007/s001140100221 (2001).

[Les06] Lessard, C. S. in *Signal Processing of Random Physiological Signals* 175–193 (Springer International Publishing, 2006). DOI: 10.1007/978-3-031-01610-3_16.

[LTP13] Luong, D. A., Thang, T. C. & Pham, A. T. Effect of avalanche photodiode and thermal noises on the performance of binary phase-shift keying-subcarrier-intensity modulation/free-space optical systems over turbulence channels. *IET Communications* **7**, 738–744. DOI: 10.1049/iet-com.2012.0600 (2013).

[Luk04] Luke, D. R. Relaxed averaged alternating reflections for diffraction imaging. *Inverse Problems* **21**, 37–50. DOI: 10.1088/0266-5611/21/1/004 (2004).

[Mad+13] Madsen, A., Hallman, J., Roth, T. & Ansaldi, G. *Technical Design Report of Scientific Instrument Materials Imaging and Dynamics (MID)* 2013. URL: https://www.xfel.eu/sites/sites_custom/site_xfel/content/e35165/e46561/e46883/e46942/e46945/xfel_file46946/TR-2013-005_TDR_MID_eng.pdf (2024).

[MDF63] Margulies, S., Debrunner, P. & Frauenfelder, H. Transmission and line broadening in the Mössbauer effect. II. *Nuclear Instruments and Methods* **21**, 217–231. DOI: 10.1016/0029-554x(63)90119-8 (1963).

[Mel+21] Melnyk, O., Forstner, A., Krahmer, F. & Sissouno, N. *Stable Ptychographic Phase Retrieval via Lost Subspace Completion* in *2020 28th European Signal Processing Conference (EUSIPCO)* (2021), 975–979. DOI: 10.23919/Eusipco47968.2020.9287808.

[MF13] Makitalo, M. & Foi, A. Optimal Inversion of the Generalized Anscombe Transformation for Poisson-Gaussian Noise. *IEEE Transactions on Image Processing* **22**, 91–103. DOI: 10.1109/tip.2012.2202675 (2013).

[Mös76] Mössbauer, R. L. Debye Waller Factors and Lamb Factors in the scattering of X-rays, γ-rays and thermal neutrons. *Le Journal de Physique Colloques* **37**, 11–13. DOI: 10.1051/jphyscol:1976602 (1976).

[MR09] Maiden, A. M. & Rodenburg, J. M. An improved ptychographical phase retrieval algorithm for diffractive imaging. *Ultramicroscopy* **109**, 1256–1262. DOI: 10.1016/j.ultramic.2009.05.012 (2009).

[MSC98] Miao, J., Sayre, D. & Chapman, H. N. Phase retrieval from the magnitude of the Fourier transforms of nonperiodic objects. *Journal of the Optical Society of America A* **15**, 1662. DOI: 10.1364/josaa.15.001662 (1998).

[MUZ21] Mignacco, F., Urbani, P. & Zdeborová, L. Stochasticity helps to navigate rough landscapes: comparing gradient-descent-based algorithms in the phase retrieval problem. *Machine Learning: Science and Technology* **2**, 035029. DOI: 10.1088/2632-2153/ac0615 (2021).

[Nes83] Nesterov, Y. A method for solving the convex programming problem with convergence rate $O(1/k^2)$. *Proceedings of the USSR Academy of Sciences* **269**, 543–547. URL: https://api.semanticscholar.org/CorpusID:145918791 (1983).

[NK18] Nasonov, A. & Krylov, A. *An Improvement of BM3D Image Denoising and Deblurring Algorithm by Generalized Total Variation* in *2018 7th European Workshop on Visual Information Processing (EUVIP)* (IEEE, 2018). DOI: 10.1109/euvip.2018.8611693.

[Pfe17] Pfeiffer, F. X-ray ptychography. *Nature Photonics* **12**, 9–17. DOI: 10.1038/s41566-017-0072-5 (2017).

[PKE09] Pálffy, A., Keitel, C. H. & Evers, J. Single-Photon Entanglement in the keV Regime via Coherent Control of Nuclear Forward Scattering. *Physical Review Letters* **103**, 017401. DOI: 10.1103/physrevlett.103.017401 (2009).

[Pol87] Polyak, B. T. *Introduction to Optimization* ISBN: 9783030687113 (Optimization Software, New York, 1987).

[Pot+01] Potzel, W. *et al.* Investigation of radiative coupling and of enlarged decay rates of nuclear oscillators. *Physical Review A* **63**, 043810. DOI: 10.1103/physreva.63.043810 (2001).

[Pra+22] Prajapat, D. *et al.* Magnetism in four-layered Aurivillius $Bi_5FeTi_3O_{15}$ at high pressures. *Journal of Magnetism and Magnetic Materials* **562**, 169783. DOI: 10.1016/j.jmmm.2022.169783. URL: https://www.sciencedirect.com/science/article/pii/S0304885322006795 (2022).

[PS21] Preskitt, B. & Saab, R. Admissible Measurements and Robust Algorithms for Ptychography. *Journal of Fourier Analysis and Applications* **27**. DOI: 10.1007/s00041-021-09811-8 (2021).

[Qia99] Qian, N. On the momentum term in gradient descent learning algorithms. *Neural Networks* **12**, 145–151. DOI: 10.1016/s0893-6080(98)00116-6 (1999).

[RB92] Rodenburg, J. M. & Bates, R. H. T. The theory of super-resolution electron microscopy via Wigner-distribution deconvolution. *Philosophical Transactions of the Royal Society of London. Series A: Physical and Engineering Sciences* **339**, 521–553. DOI: 10.1098/rsta.1992.0050 (1992).

[RC21] Rüffer, R. & Chumakov, A. I. in *Topics in Applied Physics* 1–55 (Springer Singapore, 2021). DOI: 10.1007/978-981-15-9422-9_1.

[RDN13] Raz, O., Dudovich, N. & Nadler, B. Vectorial Phase Retrieval of 1-D Signals. *IEEE Transactions on Signal Processing* **61**, 1632–1643. DOI: 10.1109/tsp.2013.2239994 (2013).

[RE21] Röhlsberger, R. & Evers, J. in *Modern Mössbauer Spectroscopy* 105–171 (Springer Singapore, 2021). ISBN: 9789811594229. DOI: 10.1007/978-981-15-9422-9_3.

[Rei+17] Reinhardt, J. *et al.* Beamstop-based low-background ptychography to image weakly scattering objects. *Ultramicroscopy* **173**, 52–57. DOI: 10.1016/j.ultramic.2016.11.005 (2017).

[RM19] Rodenburg, J. & Maiden, A. in *Springer Handbook of Microscopy* 819–904 (Springer International Publishing, 2019). DOI: 10.1007/978-3-030-00069-1_17.

[ROF92] Rudin, L. I., Osher, S. & Fatemi, E. Nonlinear total variation based noise removal algorithms. *Physica D: Nonlinear Phenomena* **60**, 259–268. DOI: 10.1016/0167-2789(92)90242-f (1992).

[Röh+10] Röhlsberger, R., Schlage, K., Sahoo, B., Couet, S. & Rüffer, R. Collective Lamb Shift in Single-Photon Superradiance. *Science* **328**, 1248–1251. DOI: 10.1126/science.1187770 (2010).

[Röh+12] Röhlsberger, R., Wille, H.-C., Schlage, K. & Sahoo, B. Electromagnetically induced transparency with resonant nuclei in a cavity. *Nature* **482**, 199–203. DOI: 10.1038/nature10741 (2012).

[Röh05] Röhlsberger, R. *Nuclear Condensed Matter Physics with Synchrotron Radiation* DOI: 10.1007/b86125 (Springer Berlin Heidelberg, 2005).

[Röh99] Röhlsberger, R. Theory of X-ray grazing incidence reflection in the presence of nuclear resonance excitation. *Hyperfine Interactions* **123/124**, 301–325. DOI: 10.1023/a:1017063605078 (1999).

[Rüf+91] Rüffer, R. *et al.* Nuclear Bragg diffraction using synchrotron radiation A new method for hyperfine spectroscopy. *Nuclear Instruments and Methods in Physics Research Section A: Accelerators, Spectrometers, Detectors and Associated Equipment* **303**, 495–502. DOI: 10.1016/0168-9002(91)90286-y (1991).

[Sad+19] Sadashivaiah, S. *et al.* Light-induced spin transition in the spin-crossover complex FePt2 detected by optical pump -coherent resonant nuclear elastic scattering. *Hyperfine Interactions* **241**. DOI: 10.1007/s10751-019-1673-9 (2019).

[Sah+11] Sahoo, B. *et al. Preparation and Characterization of Ultrathin Stainless Steel Films* in *AIP Conference Proceedings* (AIP, 2011). DOI: 10.1063/1.3601785.

[SG94] Sturhahn, W. & Gerdau, E. Evaluation of time-differential measurements of nuclear-resonance scattering of x rays. *Physical Review B* **49**, 9285–9294. DOI: 10.1103/physrevb.49.9285 (1994).

[She+21] Shedligeri, P. *et al. Improving Acquisition Speed of X-Ray Ptychography Through Spatial Undersampling and Regularization* in *2021 IEEE International Conference on Image Processing (ICIP)* (IEEE, 2021). DOI: 10.1109/icip42928.2021.9506086.

[Shi+18] Shi, X., Burdet, N., Batey, D. & Robinson, I. Multi-Modal Ptychography: Recent Developments and Applications. *Applied Sciences* **8**, 1054. DOI: 10.3390/app8071054 (2018).

[Shi+19] Shi, Y., Zhang, X., Rao, Z., Wang, M. & Soleimani, M. Reduction of Staircase Effect With Total Generalized Variation Regularization for Electrical Impedance Tomography. *IEEE Sensors Journal* **19**, 9850–9858. DOI: 10.1109/jsen.2019.2926232 (2019).

[Shv+23] Shvyd'ko, Y. *et al.* Resonant X-ray excitation of the nuclear clock isomer 45Sc. *Nature* **622**, 471–475. DOI: 10.1038/s41586-023-06491-w (2023).

[Shv99] Shvyd'ko, Y. V. *Hyperfine Interactions* **123/124**, 275–299. DOI: 10.1023/a:1017015721916 (1999).

[Sid+16] Sidorenko, P., Lahav, O., Avnat, Z. & Cohen, O. Ptychographic reconstruction algorithm for frequency-resolved optical gating: super-resolution and supreme robustness. *Optica* **3**, 1320. DOI: 10.1364/optica.3.001320 (2016).

[SMB98] Starck, J.-L., Murtagh, F. D. & Bijaoui, A. *Image Processing and Data Analysis* DOI: 10.1017/cbo9780511564352 (Cambridge University Press, 1998).

[Smi+05] Smirnov, G. V. *et al.* Propagation of nuclear polaritons through a two-target system: Effect of inversion of targets. *Physical Review A* **71**. DOI: 10.1103/physreva.71.023804 (2005).

[Smi+97] Smirnov, G. V., van Bürck, U., Chumakov, A. I., Baron, A. Q. R. & Rüffer, R. Synchrotron Mössbauer source. *Physical Review B* **55**, 5811–5815. DOI: 10.1103/physrevb.55.5811 (1997).

[Smi99] Smirnov, G. V. General properties of nuclear resonant scattering. *Hyperfine Interactions* **II-2**, 31–77. DOI: 10.1023/A:1017007520099 (1999).

[Spa+15] Spangenberg, D., Rohwer, E., Brügmann, M. H. & Feurer, T. Ptychographic ultrafast pulse reconstruction. *Optics Letters* **40**, 1002. DOI: 10.1364/ol.40.001002 (2015).

[Stu00] Sturhahn, W. CONUSS and PHOENIX: Evaluation of nuclear resonant scattering data. *Hyperfine Interactions* **125**, 149–172. DOI: 10.1023/a:1012681503686 (2000).

[Stu01] Sturhahn, W. Phase problem in synchrotron Mössbauer spectroscopy. *Physical Review B* **63**. DOI: 10.1103/physrevb.63.094105 (2001).

[Sut+13] Sutskever, I., Martens, J., Dahl, G. & Hinton, G. *On the importance of initialization and momentum in deep learning* in *Proceedings of the 30th International Conference on Machine Learning* **28** (PMLR, 2013), 1139–1147. URL: https://proceedings.mlr.press/v28/sutskever13.html.

[TG12] Thibault, P. & Guizar-Sicairos, M. Maximum-likelihood refinement for coherent diffractive imaging. *New Journal of Physics* **14**, 063004. DOI: 10.1088/1367-2630/14/6/063004 (2012).

[Thi+08] Thibault, P. *et al.* High-Resolution Scanning X-ray Diffraction Microscopy. *Science* **321**, 379–382. DOI: 10.1126/science.1158573 (2008).

[Thi+09] Thibault, P., Dierolf, M., Bunk, O., Menzel, A. & Pfeiffer, F. Probe retrieval in ptychographic coherent diffractive imaging. *Ultramicroscopy* **109**, 338–343. DOI: 10.1016/j.ultramic.2008.12.011 (2009).

[TM13] Thibault, P. & Menzel, A. Reconstructing state mixtures from diffraction measurements. *Nature* **494**, 68–71. DOI: 10.1038/nature11806 (2013).

[Tsa+16] Tsai, E. H. R., Usov, I., Diaz, A., Menzel, A. & Guizar-Sicairos, M. X-ray ptychography with extended depth of field. *Optics Express* **24**, 29089. DOI: 10.1364/oe.24.029089 (2016).

[TZ18] Ting, L. I. & Zhong, W. A. N. New Adaptive Barzilai-Borwein Step Size and Its Application in Solving Large-Scale Optimization Problems. *The ANZIAM Journal* **61**, 76–98. DOI: 10.1017/s1446181118000263 (2018).

[vBür+02] Van Bürck, U. *et al.* Inversion of Target Sequence in Nuclear Forward Scattering of Synchrotron Radiation. *Hyperfine Interactions* **141/142**, 151–155. DOI: 10.1023/a:1021210221375 (2002).

[Vel21] Velten, S. *Phonon engineering in thin tin films for tuning photon-nuclei interaction* PhD thesis (Universität Hamburg, 2021). DOI: 10.3204/PUBDB-2022-01324.

[Vin15] Vinzant, C. *A small frame and a certificate of its injectivity* 2015. DOI: 10.48550/ARXIV.1502.04656.

[Wal63] Walther, A. The Question of Phase Retrieval in Optics. *Optica Acta: International Journal of Optics* **10**, 41–49. DOI: 10.1080/713817747 (1963).

[WE23] Wolff, L. & Evers, J. Unraveling time- and frequency-resolved nuclear resonant scattering spectra. *Phys. Rev. Res.* **5**, 013071. DOI: 10.1103/PhysRevResearch.5.013071. URL: 10.1103/PhysRevResearch.5.013071 (1 2023).

[Wel+22] Welker, S., Peer, T., Chapman, H. N. & Gerkmann, T. *Deep Iterative Phase Retrieval for Ptychography* in *IEEE International Conference on Acoustics, Speech and Signal Processing (ICASSP)* (IEEE, 2022). DOI: 10.1109/icassp43922.2022.9746811.

[Win95] Winick, H. *Synchrotron Radiation Sources - A Primer* DOI: 10.1142/2444 (World Scientific, 1995).

[Wit+22] Wittwer, F., Hagemann, J., Brückner, D., Flenner, S. & Schroer, C. G. Phase retrieval framework for direct reconstruction of the projected refractive index applied to ptychography and holography. *Optica* **9**, 295. DOI: 10.1364/optica.447021 (2022).

[YC22] Yaroslavtsev, S. & Chumakov, A. I. Synchrotron Mössbauer source: trade-off between intensity and linewidth. *Journal of Synchrotron Radiation* **29**, 1329–1337. DOI: 10.1107/s1600577522009316 (2022).

[Yeh+15] Yeh, L.-H. *et al.* Experimental robustness of Fourier ptychography phase retrieval algorithms. *Optics Express* **23**, 33214. DOI: 10.1364/oe.23.033214 (2015).

[ZH04] Zhang, H. & Hager, W. W. A Nonmonotone Line Search Technique and Its Application to Unconstrained Optimization. *SIAM Journal on Optimization* **14**, 1043–1056. DOI: 10.1137/s1052623403428208 (2004).

[Zha15] Zhang, D. *Applications of Nuclear Resonant Scattering to Further Our Understanding of Earth's Interior* PhD thesis (California Institute of Technology, 2015). DOI: 10.7907/Z9SQ8XD5. URL: https://resolver.caltech.edu/CaltechTHESIS:12152014-195321239.

[ZSC16] Zuo, C., Sun, J. & Chen, Q. Adaptive step-size strategy for noise-robust Fourier ptychographic microscopy. *Optics Express* **24**, 20724. DOI: 10.1364/oe.24.020724 (2016).

[ZSD17] Zhang, Y., Song, P. & Dai, Q. Fourier ptychographic microscopy using a generalized Anscombe transform approximation of the mixed Poisson-Gaussian likelihood. *Optics Express* **25**, 168. DOI: 10.1364/oe.25.000168 (2017).

Acknowledgements

The research work in this Ph.D. thesis was mainly carried out at the Department of Photon Science at Deutsches Elektronen-Synchrotron, Hamburg, which is a research centre of the Helmholtz Association, and the Institute of Applied Mathematics at the University of Hamburg. A lot of people have majorly contributed to the completion of this thesis, and it is most important for me to thank everyone.

To begin, I want to express my gratitude to my supervisors: Prof. Dr. Ralf Röhlsberger, Prof. Dr. Christina Brandt and PD Dr. Guido Meier for their expertise, ideas, support, encouragement and constructive comments throughout the three years. They also gave me sufficient freedom to explore the topic. I arrived in Hamburg in the middle of the COVID-19 lockdown, but both Ralf and Christina gave me a warm welcome and the opportunity to integrate into their respective groups. Thank you for also being the official reviewers of the thesis. Major thanks to Guido for guiding me throughout the writing process. Without his rigorous input, the thesis would not have reached its final form. From the examination committee, I also want to thank Prof. Dr. Michael Potthoff and Prof. Dr. Henry Chapman for agreeing to be the Chair and the Deputy Chair in assessing the thesis.

Next, I would like to thank the present and former members of the FS-MCP group: Dr. Lars Bocklage, Dr. Kai Schlage, Dr. Sven Velten, Dr. Anjali Panchwanee, Leon Merten Lohse, Andrey Seimens, Janne Luetjens and Dr. Mehdi Ramin Moayed for the open, friendly and supportive working environment at DESY. My sincere thanks to Lars for being an integral part of the supervision, helping with the samples and experiments, and also, NEXUS. He also took a lot of time from his schedule to help with the revision of the thesis and the German translation of the abstract. I had never done a synchrotron experiment in my life before my Ph.D. Therefore, for the beamtimes at PETRA III and ESRF, the recommendations and participation of Lars, Kai, Anjali, Sven and Leon was invaluable. I again want to thank Lars, Leon and Sven for also taking part in the dis-

cussions about my project. I have interrupted them countless times with my questions and have always been treated with immense patience. Also thanks to the new members of *Area 228* - Dr. Christina Boemer and Dr. Dietrich Krebs, who helped clarify all my doubts about the last steps of the submission process.

For the discussion and support for the beamtime at Petra III, I want to thank Dr. Ilya Sergeev and Dr. Olaf Leupold from the P01 beamline, DESY, and Dr. Sakshath Sadashivaiah from the University of Jena. Similarly, I am grateful to Dr. Dimitrios Bessas at beamline ID14 (formerly ID18) for his help during the beamtime experiments at ESRF.

I also extend my thanks to the group at the University – especially my former officemate Dr. Thi Bich Tram Do for helping me navigate the literature on inverse problems. I also thank her for her advice and friendship.

This Ph.D. project would not be possible without DASHH graduate school - not only as a funding source but also as a center of support and interaction with a diverse group of peers. I want to thank the program coordinators Dr. Christiane Ehrt and Dr. Heike Hufnagel Martinez and my DASHH mentor Dr. Hans Fangohr for organizing and overlooking the progress of the project.

Thank you to all the friends from DASHH: Thea, Ke Li, Surya; friends from Cologne: Atif, Saurabh, Sakshi, (Dr.) Nikhil; and beyond: Sonali, Mansi, Gyanendra, Samridhi and Sarthak. Over the years, I have accumulated lovely words of encouragement from everyone. Janne, thank you for the anti-stress ball. Anjali, thank you for feeding me dinner on several days as I struggled to synchronize my odd sleeping and working hours. Thanks to Lars, Kai and Andrey for their everyday advice on navigating German life and bureaucracy. A note of apology to Leon, who had to listen to my endless complaints for months while I was drafting the thesis – *at last it's over!* Finally, I thank my parents, brother and grandmother for their constant love, support and understanding throughout this challenging endeavor, and well, life in general.

You only write a Ph.D. thesis once. So, heck, let me also thank myself – *in the words of rap legend Snoop Dogg*[3] – for believing in myself and never quitting.

[3] `https://www.youtube.com/watch?v=wGRF3GQ4Wdk`

Eidesstattliche Versicherung

Hiermit erkläre ich an Eides statt, dass ich die vorliegende Dissertationsschrift selbst verfasst und keine anderen als die angegebenen Quellen und Hilfsmittel benutzt habe.

Hamburg, den 19.02.2024

Ankita Negi